# Computational insights into excited state properties of MgO and other nanoparticles with the rocksalt structure

Milena Claudia Charlotte Wobbe

Department of Chemistry

**UCL**

Thesis submitted for the degree of Doctor of Philosophy (PhD)

I, Milena Claudia Charlotte Wobbe, confirm that the work presented in this thesis in my own. Where information has been derived from other sources, I confirm that this has been indicated in the thesis.

Milena Claudia Charlotte Wobbe

May 2016

# Abstract

This work investigates the applicability of (time-dependent) Density Functional Theory, (TD)DFT, for the description of the excited state properties of MgO, and other inorganic nanoparticles exhibiting the rocksalt structure. Firstly, the excitation behaviour of MgO nanoparticles is studied and it is shown that the commonly used exchange-correlation ($xc$)-functional B3LYP severely underestimates the lowest vertical excitation energies (LVEE) in these systems. It is demonstrated that TD-B3LYP erroneously stabilises those excitations with charge-transfer (CT) character. The use of different approximations to the exchange-correlation functional, such as the long-range corrected $xc$-functional CAM-B3LYP or the hybrid $xc$-functional BHLYP, significantly improves the energetic description of excited states with CT character.

Different inorganic nanoparticles exhibiting the rocksalt structure, such as those of the alkaline earth chalcogenides CaO, SrO, BaO, MgS and MgSe as well as CdO and PbS, are investigated and found to behave similarly to MgO in that their localised excited states are poorly described with the TD-B3LYP $xc$-functional. It is demonstrated that the concept of CT character is not binary. Nanoparticles of both the CdO and PbS materials have delocalised excited electrons and a high dielectric constant: in these systems the excited state appears to be suitably described using TD-B3LYP.

The lowest excited states of a series of MgO nanoparticles are optimised and it is found that, despite providing a different description of the excitation character, all investigated $xc$-functionals optimise to a similar lowest lying excited singlet state. The larger particles studied exhibit an excited electron localised on a magnesium corner site and the corresponding hole localised on an oxygen corner site. The magnesium and oxygen corners lie along the same edge of a given particle. TD-B3LYP is found to underestimate the experimentally observed photoluminescence peak, reminiscent of the results obtained for the vertical excitation energies. In contrast to the LVEE results, TD-BHLYP and TD-CAM-B3LYP also underestimate the experimental photoluminescence peak.

Finally, doped MgO nanoparticles are studied. The dopants include alkaline earth elements Be, Ca, Sr and Ba as well as group 12 elements Zn and Cd. It is found that the experimental absorption spectra are not replicated by the computational model of just one dopant present in the system and it is suggested that the experimental absorption peaks attributed to the dopants in the system appear to result from dopant clusters on the particle or that the dopants are not evenly distributed throughout the particle. Furthermore, the preliminary photoluminescence results show that the exciton behaves differently in doped nanoparticles when compared to pure MgO nanoparticles in that the electron and hole remain more localised, yielding higher photoluminescence energies, in-line with experimental observations.

# Acknowledgements

Firstly, I must thank my supervisor Dr. Martijn Zwijnenburg, for sharing his knowledge and providing invaluable feedback and advice along the journey that has culminated in this thesis. My thanks also goes to Nikolas Kaltsoyannis for his support as my second supervisor.

On a more personal note, I would like to thank my amazing parents, who have always supported me throughout my education and in life: I am hugely indebted to them. I also want to thank my husband who had to proof-read more than he bargained for, and without whom I would not have been able to write these pages.

# List of Publications

During my studies, I have published the following peer-reviewed articles:

- Wobbe, M. C. C., Kerridge, A., Zwijnenburg M. A., Optical excitation of MgO nanoparticles; A computational perspective, *Physical Chemistry Chemical Physics,* 2014, **16**, 22052 – 22061.

- Wobbe, M. C. C., Zwijnenburg M. A., Chemical trend in the optical properties of rocksalt nanoparticles, *Physical Chemistry Chemical Physics,* 2015, **17**, 28892 - 28900.

- Guiglion, P., Berardo, E., Butchosa, C., Wobbe, M. C. C., Zwijnenburg, M. A., Modelling materials for solar fuel synthesis by artificial photosynthesis; predicting the optical, electronic and redox properties of photocatalysts, *Journal of Physics: Condensed Matter*, 2016, **28**, 074001 – 074012.

The following manuscript is currently in preparation for publication:

- Wobbe, M. C. C., Zwijnenburg M. A., Photoluminescence in MgO nanoparticles and exciton self-trapping: A computational approach.

# Contents

# List of Figures

# List of Tables

# Commonly used Abbreviations

**ACM** – Adiabatic Connection Method

**B3LYP** – Commonly used hybrid GGA *xc*-functional with 20% Hartree-Fock exchange

**BHLYP** – Hybrid GGA *xc*-functional with 50% Hartree-Fock exchange

**BO** – Born-Oppenheimer (approximation)

**CAM-B3LYP** – Range separated functional, with 19% HFE at short range and 65% HFE at long range

**CC** – Coupled Cluster

**CDE** – Cluster Deformation Energy

**CGTO** – Contracted Gaussian-type Orbitals

**CT** – Charge Transfer

**CVD –** Chemical Vapour Deposition

**def2-TZVP** – triple-$\zeta$ quality, split valence basis set, developed by Ahlrichs and co-workers

**Δ-SCF** – commonly used method to calculate the energy different between two states

**DZC** – double-$\zeta$ double polarisation (single polarisation for oxygen) basis set, developed by Caneto and co-workers

**DZ(D)P** – double-$\zeta$ double polarisation (single polarisation for oxygen) basis set, developed by Ahlrichs and co-workers

**DZS** – same basis set as DZ(D)P

**DFT** – Density Functional Theory

**EA** – Electron Affinity

**ECP** – Effective Core Potential

**ELC** – Exciton Localisation Character

**ESSE** – Excited State Stabilisation Energy

**GGA** – Generalised Gradient Approximation

**GSDE** – Ground State Destabilisation Energy

**GTO** – Gaussian-type Orbitals

**HF** – Hartree-Fock

**HFE** – Hartree-Fock Exchange

**HK** – Hohenberg-Kohn

**HOMO** – Highest Occupied Molecular Orbital

**IP** – Ionisation Potential

**KS** – Kohn-Sham

**LDA** – Local Density Approximation

**LSDA** – Local Spin Density Approximation

**LUMO** – Lowest Unoccupied Molecular Orbital

**LVEE** – Lowest Vertical Excitation Energy

**NAO** – Natural Atomic Orbital

**NBO** – Natural Bond Orbital (model)

**PBE** – GGA *xc*-functional

**PL** – Photoluminescence

**PLE** – Photoluminescence Energy

**PT** – Perturbation Theory; e.g. PT2 for $2^{nd}$ order Perturbation Theory

**QM** – Quantum Mechanics

**QTAIM** – or simply **AIM**: Quantum Theory of Atoms In Molecules

**RPA** – generalised Random Phase Approximation *xc*-functionals

**S**$_n$ – $n^{th}$ singlet state, with $n = 0$ for the ground (singlet) state

**SCF** – Self-consistent Field

**SE** – Schrödinger's equation

**STE** – Self-trapped exciton

**STO** – Slater-type Orbitals

**T$_n$** – $n^{\text{th}}$ triplet state

**(TD-)** – Time-dependent

**TDDFT** – Time-dependent Density Functional Theory

**TDKS** – Time-dependent Kohn-Sham

**TEM** – Transition Electron Microscopy

**TF** – Thomas-Fermi

**TFD** – Thomas-Fermi-Dirac

*xc* – exchange-correlation

# 1. Introduction

The aim of this chapter is to introduce many of the chemical and physical concepts that are important in this study, and to make the reader aware of commonly used notations and ideas discussed in this thesis.

## 1.1    Basic Quantum Chemical Concepts

A key difference between classical mechanics and quantum mechanics is the concept of energy quantisation. In the "macro world" that humans inhabit, any energy level of a system is conceivable and physically possible. On an atomistic and molecular level, however, only certain energy levels are accessible, with these energy levels defined by the environment of a particle. With this in mind, and considering that the excited state properties of molecules are to be studied, the energy levels comprising the states are inherently important properties of systems to be studied.
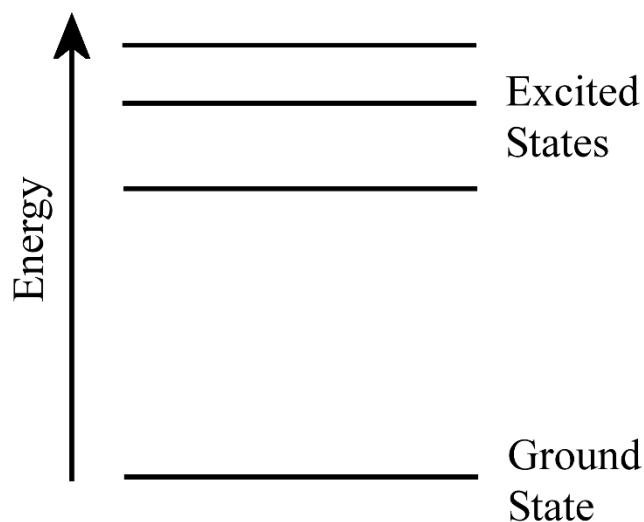


**Figure 1-1:** Qualitative diagram showing the relative energies of the ground and the first three excited electronic states.

When the lowest possible electronic state is occupied, a system is said to be in its 'ground state'. If at least one electron is not at the lowest energy level, then the system is said to be in an excited state, which is higher in energy than the ground state (see figure 1-1). Depending on how much additional energy the electron(s) in question have, the system might be in its first, second, or $n^{\text{th}}$ excited state.

Within each of these electronic energy levels are many more levels which are accessible: Every electronic level has vibrational sub-levels, each of which themselves containing multiple rotational sub-levels. These two sets of sub-levels are not electronic in nature but are instead related to nuclear motion. Within the framework of this study, only electronic levels and their relative energies are considered.

Electronic states can have different spin multiplicities, depending on the number of unpaired electrons. Spin multiplicity is defined as $2S + 1$, where $S$ is the sum of unpaired electron spins, each of which is equal to ½ .When there are no unpaired electrons, $S = 0$, so the multiplicity is one (i.e. a *singlet* state). With one unpaired electron the multiplicity is two (a *doublet* state), two unpaired electrons give rise to a *triplet* state, etc. For a system with no unpaired electrons, the ground state is a singlet state, denoted by a 0 subscript, $S_0$. If, instead, the ground state is a triplet state, the notation $T_0$ is used. The subscript 1 is used to denote the first excited state, etc.

A selection rule that partially determines whether an electronic excitation is optically allowed is that $\Delta S = 0$. This means that if the ground state is a singlet, the excited state must be a singlet state too, i.e. the excited electron cannot change spin. This implies that the excited state is an open-shell singlet. Only when there is significant amount of spin-orbit coupling can there be optical excitations from the formally singlet to the formally triplet state.

## 1.2　The optical gap

The research presented in this thesis focusses on modelling the optical properties of magnesium oxide (MgO) and other inorganic particles. Optical behaviour results from the change in the electronic structure of a system. An 'optical gap' can be defined, and the difference between the fundamental and optical gap is outlined below. Two definitions that need to be discussed first though are the Ionisation Potential (IP) and the Electron Affinity (EA). The former is the energy difference between a system with $N$-1 electrons and $N$ electrons, i.e. the energy associated with removing an electron from the system, whereas the latter is a measure of the energy change when an electron is added to the system, i.e. the energy difference between an $N+1$ electron system and an $N$ electron system:

$$\text{IP} = E_{N-1} - E_N \tag{1-1}$$

and

$$\text{EA} = E_{N+1} - E_N \tag{1-2}$$

where $E_N$ is the energy of the neutral system with $N$ electrons, $E_{N-1}$ the energy of the same system but with one electron removed and $E_{N+1}$ is the energy of the system when an electron has been added.

The fundamental gap, $E_{fund}$ is defined as follows:

$$E_{fund} = \text{IP} - \text{EA} \tag{1-3}$$

To obtain an experimental value for this energy, a combination of photoelectron spectroscopy and electron attachment spectroscopy can be used.[1]

The optical gap, $\Delta_o$, is defined as the lowest possible energy electronic transition of a system into a higher lying state via the absorption of a photon. In some instances, the lowest energy excitation might be forbidden by the selection rules and therefore does not define the optical gap. However, it can generally be referred to as the 'lowest vertical excitation energy' (LVEE), without making the distinction as to whether the transition is

optically allowed or not. The optical gap is lower in energy than the fundamental gap, as the electron-hole pair (or exciton) created by the excitation remains electrostatically bound, whereas in the case of the fundamental gap, the electron-hole pair is assumed to be infinitely separated. It follows that the exciton energy is the energy difference between the fundamental and optical gap.

## 1.3   Photochemistry and Photophysics

The process of photon absorption as discussed in section 1.2 falls under the labels of photochemistry and photophysics. The former encompasses all phenomena occurring when systems interact with light and a subsequent chemical change occurs. The term 'photophysics', on the other hand, implies no net chemical change after a photon is absorbed, i.e.

$$A + h\nu \rightarrow A^* \rightarrow A \tag{1-4}$$

where $A^*$ denotes the electronically excited molecule A and $h\nu$ is a photon of sufficient energy to electronically excite molecule A. After excitation, A* returns to its original state A via internal conversion (or light emission).

In contrast, photochemistry refers to the process when after a photon is absorbed, there is a net chemical change, i.e.

$$A + h\nu \rightarrow A^* \rightarrow B \tag{1-5}$$
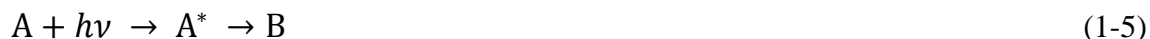
where molecule B is chemically different from molecule A.

There are different processes that can occur within photochemistry and photophysics, as seen in figure 1-2, where process '1' represents light absorption by the particle, '2' represents luminescence (light emission by the particle), '3' is an excited state barrier, '4' is a conical intersection and '5' represents product formation.
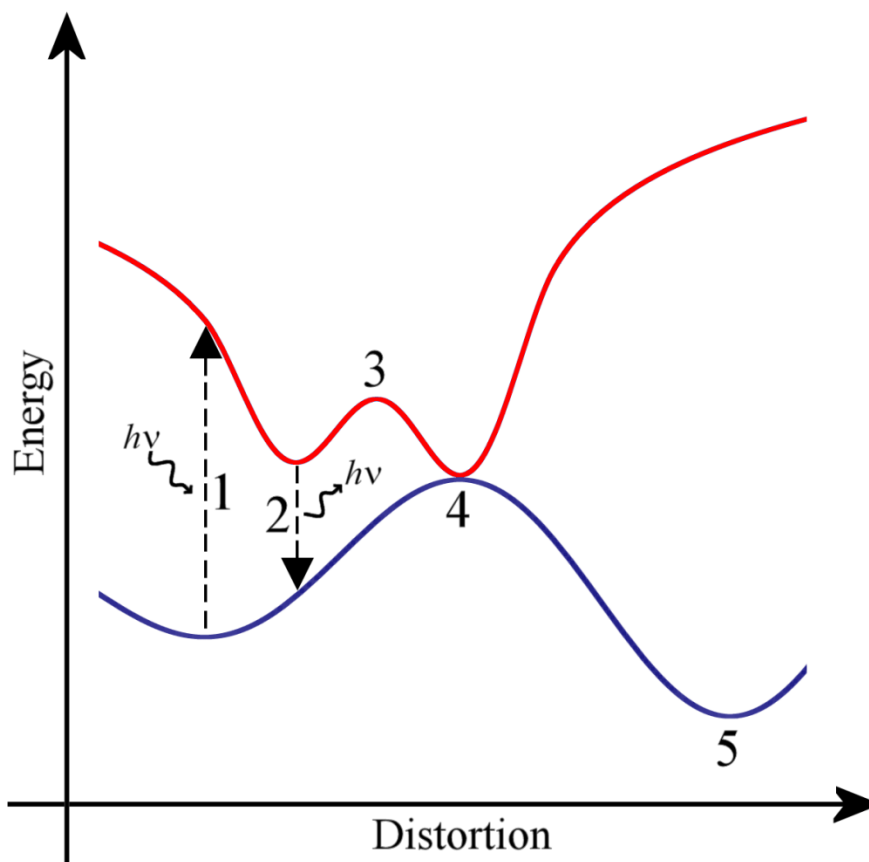
**Figure 1-2:** Ground (blue) and excited (red) potential energy surfaces, showing possible photochemical and photophysical phenomena.

When two potential energy surfaces cross at any point, they are energetically degenerate and this region is called a 'conical intersection' (process '4' in figure 1-2). Very fast, radiationless electronic transitions often occur due to these conical intersections. An alternative explanation for radiationless transitions would be that there is an excited state minimum with the same geometry as a maximum on a lower potential energy surface, but the wavefunctions are not degenerate at that point, so the potential energy surfaces do not touch.

Photon absorption and photon emission (or photoluminescence) can both occur for spin-allowed as well as spin-forbidden processes, although the latter is only possible if intersystem crossing can take place, mediated by e.g. spin-orbit coupling. The spin allowed processes would be from singlet to singlet state or triplet to triplet states: an

example of a spin-allowed absorption process is given below, where $S_0$ is the ground state and $S_1$ the first excited state.

$$S_0 + h\nu \rightarrow S_1 \qquad (1\text{-}6)$$

Similarly, a spin-forbidden transition can be described in the following way:

$$S_0 + h\nu \rightarrow T_1 \qquad (1\text{-}7)$$

where $T_1$ is the first excited triplet state.

The same logic holds for luminescence, although there is a distinction as to which state the photon was emitted from: if it is a singlet state, it is referred to as fluorescence:

$$S_1 \rightarrow S_0 + h\nu \qquad (1\text{-}8)$$

The spin-forbidden counterpart, an emission from a triplet state, is called phosphorescence.

$$T_1 \rightarrow S_0 + h\nu \qquad (1\text{-}9)$$

As a result of the spin selection rule $\Delta S = 0$, fluorescence tends to be a faster process than phosphorescence, although lifetimes are, of course, system dependent: as a general rule, fluorescence occurs within nanoseconds whereas phosphorescence can occur as slowly as seconds after the photon excitation.[2–5]

The energy of the photon emitted during luminescence is lower than that used to excite the system. This is because of the energy dissipated while the excited state relaxes between the absorption and emission of the photon. A measure of this loss of energy is the Stokes shift, which is the difference between the excitation energy (the energy associated with the process of electron absorption) and the photoluminescence energy (the energy associated with the process of electron emission).

A more detailed diagram outlining the different types of energy processes that can occur are shown in figure 1-3, which is generally known as a Jablonski diagram. In this diagram,

the light blue arrow shows absorption, while the dark blue and yellow arrows illustrate luminescence: fluorescence and phosphorescence respectively. The orange arrow shows internal conversion, the green vibrational relaxation and the grey arrow illustrates intersystem crossing.

Internal conversion is a radiationless transition between states with the same spin, whereas an intersystem crossing occurs between states with a different spins, but is also radiationless. Phosphorescence is a special case of intersystem crossing between the lowest triplet state $T_1$ and the ground state $S_0$.

It is noticeable that only the lowest electronically excited states are depicted to emit photons in this diagram and this is due to Kasha's rule.[6] This rule states that photoluminescence occurs in substantial yield only from the lowest excited states of a given multiplicity. This is due to the fact that higher-energy excitation typically results in internal conversion to the $S_1$ and/or $T_1$ states, which then fluoresce or phosphoresce. Internal conversion from higher lying states to $S_1$ or $T_1$ is very fast,[7,8] so that fluorescence/phosphorescence cannot compete with this process kinetically as the $S_1$ or $T_1$ states typically lie further away from $S_0$. This means that the rate of internal conversion is slowed down, and fluorescence/phosphorescence can compete kinetically. There are, however, exceptions to this rule.[9]
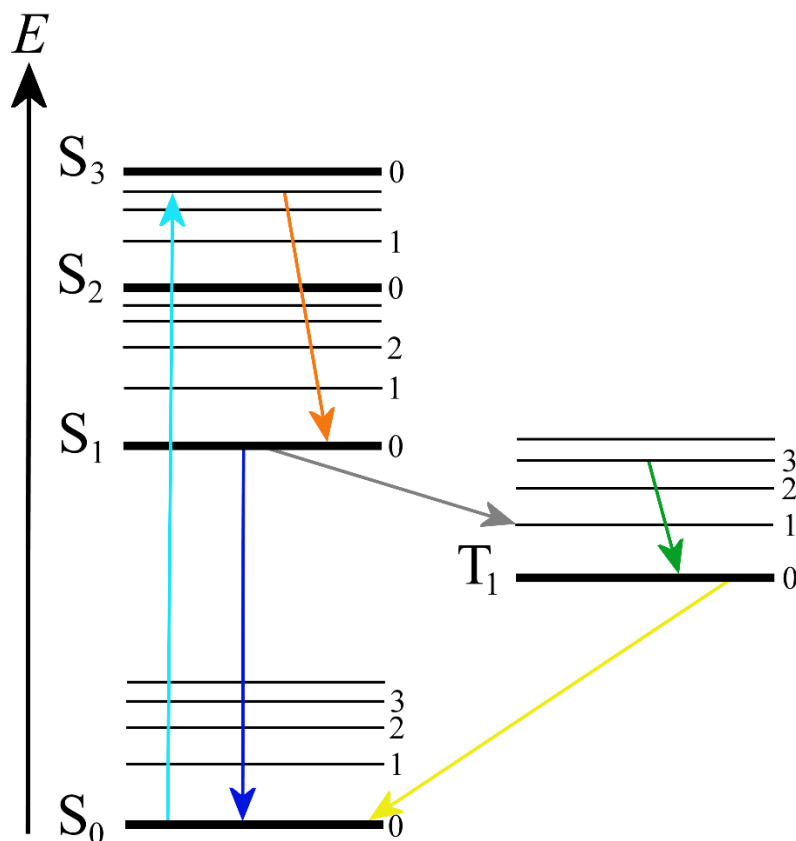
**Figure 1-3:** Jablonski diagram showing ground and excited electronic (thick lines) and vibrational (thin lines, with (some) numbering) states. The light blue arrow shows absorption, the dark blue and yellow arrows illustrate luminescence: fluorescence and phosphorescence respectively. The orange arrow shows internal conversion, the green vibrational relaxation and the grey arrow illustrates intersystem crossing.

## 1.4   Magnesium and Magnesium oxide

Magnesium is the second lightest alkaline earth metal in the periodic table of the elements. It has been used since the time of the ancient Greeks in the form of the mineral talc. The chemistry of the element could be studied after its discovery by Humphrey Davy in 1808. That year was truly fascinating: Davy isolated pure magnesium as well as calcium, strontium and barium by electrolytic methods.[10] It is now known that magnesium is one of the most abundant elements on earth by weight and mainly occurs in the earth's crust in the form of insoluble carbonates, sulfates and silicates.[10,11] The oxides of alkaline earth

metals are relatively easily obtained by calcination of the carbonates or by dehydration of the hydroxides.[10,12,13]

MgO is used in refractory applications, as it is a good thermal conductor and electrical insulator.[14] Crystalline MgO (along with other alkaline earth oxides) is usually found to crystallise in the rocksalt structure, first described for NaCl, and white in colour. Figure 1-4 shows an example of a nanoparticle with the rocksalt structure. Due to the regular ordering of the ions, the lattice energies are very high, which means that the oxides are relatively unreactive. However, it has been shown that, in-line with nanoparticles in general, as the particles become smaller, the more reactive they tend to be.[15] This is due to the fact that there is an increased number of coordinatively unsaturated ions on the surface compared to the number of ions in the bulk. The ions in the bulk have a coordination number of 6, whereas those on the surface have a coordination number of 5. The coordination number is reduced by one for an edge ion and by one more for corner ions, which means that edge ions have a coordination number of just 3.
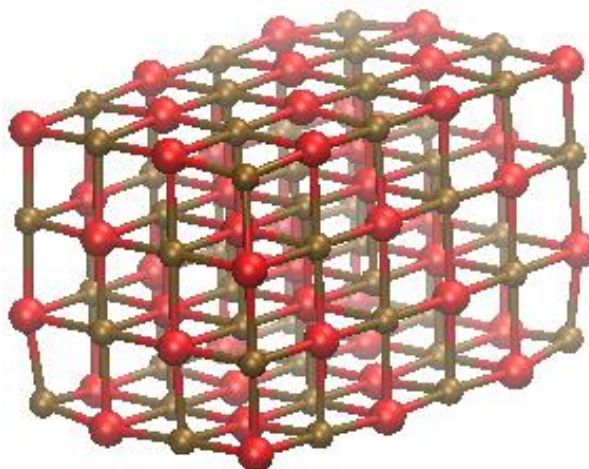


**Figure 1-4:** $(MgO)_{48}$ nanoparticle as an example of the rocksalt structure.

## 1.5  The role of Computational Chemistry

Magnesium oxide is the proverbial guinea pig for inorganic computational chemists due to its low computational cost, closed-shell configuration and the structural similarities between small nanoparticles and the bulk. These are all properties that will prove to be very useful for this project since the material is studied computationally in terms of its photophysical properties and these are then compared to experiment.

Apart from its computational advantages, MgO displays technologically interesting behaviour, such as lithium-doped MgO that is used as a catalyst for the oxidative coupling of methane.[16–18] In addition, it has been found experimentally that MgO nanoparticles absorb ultraviolet light and reemit partially in the visible spectrum[19] and the absorption and photoluminescence properties can be tuned by when varying the particle size[20] or doping nanoparticles, substituting $Mg^{2+}$ ions with other divalent cations, such as $Zn^{2+}$.[21]

The question that arises is whether computational simulation can be used to predict experimental unknowns, rather than focussing solely on explaining experimental observables and trends. MgO is a good candidate with regard to tackling this question: due to its relatively simple electronic structure, computational effort can be spent investigating the complex processes involved in its interaction with radiation, rather than on the optimisation of the electronic structure of a more complex system. The electronic structure of MgO can be described with greater accuracy than if heavier elements were studied, leading to it being an ideal material to begin studying the photophysics of inorganic materials.

The advantage of applying the approximations used in this project (discussed in chapter 2) is that a detailed description of the electron distribution in the particles can be given to explain the processes of interest, such as electronic excitation through photon absorption, excited state relaxation, and photon-emission. Such details cannot be obtained experimentally and it is fascinating to combine the knowledge gained by experiment and computation to paint a complete picture of the process. Experiments can give scientists a wealth of knowledge of a system, such as the characterisation of crystals through their morphology and size distribution, along with the absorption and emission properties of

these crystals. However, only computational models can give detailed microscopic insight into the latter processes. Furthermore, computational chemistry can also investigate the size dependence of properties, such as the already mentioned absorption and emission, or the relative stabilities of different morphologies. The knowledge gained through experiments is substantial and impressive, but computation can give complimentary insight. Only by establishing suitable approximations for chemical systems and testing their validity can the field of computational chemistry move to the realm of predicting chemical properties of systems. When this is achieved successfully, computation could direct aspects of experimental research.

Currently, many approximations must be made when using any computational methodology, which means that the suitability of the chosen approximations need to be tested. For any practical electronic structure method, electron-electron interactions must be modelled approximately. The approximations are incredibly important, as unsuitable approximations can lead to incorrect conclusions. This is further discussed in chapters 5 and 6.

## 1.6   Objectives

The objectives of this thesis are to advance the knowledge of the system of interest, MgO, and its interaction with light. Currently, the details of emission processes of materials are elusive. This is a new field of study and the methodology of choice, Time Dependent Density Functional Theory (TDDFT), needs to be tested rigorously before making trustworthy predictions.

This thesis is structured in the following way: firstly, a discussion of the methodology and computational details is presented in chapter 2. This is followed in chapter 3 by a discussion of previously published experimental and computational studies.

This leads naturally to the four chapters discussing the results obtained by the author during her studies. Firstly, in chapter 5, the ground state structures of MgO nanoparticles are presented and compared, before the excitation behaviour of said particles are discussed

in detail in terms of atomic charges and differences in ground and excited state electron densities. The main focus is on the density functional dependence of the results obtained.

The same density functional dependence has been investigated on different systems exhibiting the rocksalt structure, to investigate whether failures in the prediction of photon absorption energies using certain approximations extend to different materials, such as other alkaline earth oxides, magnesium chalcogens, CdO and PbS nanoparticles, as discussed in chapter 6. These two chapters lead to similar conclusions and it is clear that only certain approximations are appropriate to study the photophysics of (MgO) nanoparticles.

This leaves the question, which is addressed in chapter 7, as to whether the computational approaches that can be used to accurately describe the excitation behaviour of MgO nanoparticles can also be used to model their photoluminescence behaviour. As excited state relaxation is a very complex process, one major simplification had to be made, namely that only the lowest excited singlet state is investigated. The minima on the first excited singlet state surfaces are studied and the corresponding photoluminescence energies are obtained and compared to experiment.

The question arises whether the photoluminescence energies can be tuned, and chapter 8 investigates the effect doping has on the absorption and photoluminescence energies. The chosen dopants are alkaline earth elements beryllium, calcium, strontium and barium as well as group 12 elements zinc and cadmium.

# 2. Methodology

Computational modelling has one aim: obtaining the most accurate electronic structure as cheaply as possible, i.e. at the least computational cost. The perfect solution would, of course, be if realistic systems could be studied with no approximations, but this is far from being possible. Currently, Density Functional Theory[22,23] (DFT) can deal with systems of a few hundreds of atoms, but the largest systems may need smaller basis sets. Quantum chemical calculations, such as those outlined in this thesis, are approximate solutions to the (time-independent) many-electron Schrödinger equation. The fundamental approximations made to solve this equation are outlined in this chapter.

## 2.1 Preliminaries

### 2.1.1 The Schrödinger Equation

The time-independent Schrödinger equation[24] (SE) is one of the most famous quantum mechanical equations, providing together with its time-dependent variant and is relativistic version, the Dirac equation, the quantum mechanical framework underlying Chemistry. In its most general form, the SE can be expressed as follows:

$$\hat{H}\,\Psi = E\,\Psi \tag{2-1}$$

$\Psi$ is the wavefunction, whose square modulus yields the electron density, providing a direct link to a physical observable of the system in question. Equation (2-1) is an example of an eigenvalue equation, which means that, in simplified terms, the results of the Hamiltonian $\hat{H}$ acting on the wavefunction is equal to a multiple of the same wavefunction, where the multiplication factor corresponds to the energy. When the Hamiltonian operator is applied to a wavefunction, the energy of the system, $E$, can be determined.

### 2.1.2  The Many-Body Problem

The wavefunction contains all the information about a system, the only problem is that the SE can merely be solved for one-electron systems without approximations. As soon as more electrons are considered, the description of how they interact with each other becomes too complicated to solve analytically with the complexity increasing with the number of electrons involved. From a chemical perspective, it is fair to say that in any system of real interest (apart from, say, the hydrogen atom, the helium cation, or $H_2^+$) approximations must be made to the SE.

### 2.1.3  The Variational Principle

One very important principle (albeit one not true for all methodologies) is that the energy of any trial wavefunction (i.e. an approximation to the exact solution) must be higher or equal in energy to that of the exact wavefunction. Without this principle, it would be possible for the energy of a trial wavefunction to tend to $-\infty$, which is unphysical. The consequence of this principle is that improving the description of the wavefunction leads to a better description of the energy. The simplest way to improve the description of the wavefunction is to systematically improve the basis set (sections 2.1.7 and 2.2.4.2.2) used. Both Hartree-Fock (HF) theory[25,26] and DFT are methodologies based around this principle.

### 2.1.4  The Born-Oppenheimer Approximation

The Born-Oppenheimer (BO) Approximation[27] is fundamental to most quantum chemistry calculations. It assumes that electronic and nuclear motion can be treated separately due to their very different masses: electrons being much lighter than nuclei adapt their positions with respect to the positions of the nuclei almost instantly, whereas the nuclei move on potential energy surfaces defined by the electronic structure. Application of this BO approximation means that the Hamiltonian used in a quantum

chemical calculation can be a purely electronic one, where the positions of the nuclei can be approximated as being fixed: the nuclei are treated as classical point charges.

The BO approximation is a good assumption to make about chemical systems apart from in specific circumstances and makes the computation of chemical systems considerably less complex. Examples where the BO approximation might break down are conical intersections, where the ground and excited state potential energy surface touch and/or cross, or highly excited rotational states where the orbital angular momentum is decoupled from the nuclear axis.

### 2.1.5  The Orbital Approximation

For reasons of computational tractability the orbital approximation is made, where the wavefunction can be written as a product of one-electron wavefunctions (one-electron orbitals), which is known as the Hartree Product (equation (2-3)). These one-electron orbitals are exact for one electron systems but not for systems with many electrons. This approximation, however, is the underlying assumption of most modern computational chemistry as it makes the modelling of chemical systems a possibility. One should bear in mind that these orbitals, which are a result of these calculations where the degrees of freedom of the electrons have been decoupled for computational feasibility, therefore neglecting some electron-electron interactions, are not in fact chemically meaningful.

The Anti-Symmetry Principle states that the wavefunction must change sign (i.e. antisymmetric) with respect to the interchange of two electrons, which are of fermionic character. One way to insure that the Anti-Symmetry Principle, imposed by the Pauli Exclusion Principle, is obeyed, is to write the wavefunction as a single Slater determinant. This determinant is a linear combination of Hartree Products. This ensures automatic anti-symmetry and the Pauli Exclusion Principle is obeyed, as no two one-electron orbitals are the same.

### 2.1.6  LCAO Approach

The Linear Combination of Atomic Orbitals (LCAO) approach is fundamental to many quantum chemical approaches to describing molecular orbitals (MOs). It is the same thought process behind molecular orbital diagrams: atomic orbitals (AOs) are used to form MOs. The LCAO procedure is formalised in the following way:

$$\varphi_i = \sum_a c_{ai}\, \phi_a \qquad\qquad\qquad (2\text{-}2)$$

where $\varphi_i$ is a molecular orbital, $\phi_a$ are atomic orbitals and $c_{ai}$ are coefficients which are optimised to obtain the lowest energy solution for the system studied.

### 2.1.7  Basis Set Introduction

It is important at this stage to introduce the concept of basis sets. MOs are a linear combination of AOs but how are AOs described? The way this is done is by employing one-electron basis functions, which are centred on the atomic nuclei. One of these functions is not enough to describe any AO properly, therefore a set of basis functions are used to describe each AO. If each set were complete, i.e. an infinite number of basis functions were used, the basis set could describe each AO exactly. However, in practise, any basis set is 'truncated', and only a finite number of functions is used to describe an AO. More detail is given in section (2.2.4.2.2).

### 2.1.8  Self-Consistent Field Procedure

The self-consistent field (SCF) approach is used to solve the Schrödinger equation in DFT and HF theory. The need for this procedure is clear once one realises that in order to determine any given electron orbital, all other orbitals need to be considered. This cannot be done directly, but rather an iterative process needs to be started by using an educated guess to approximate all orbitals. From this initial guess, the MOs can be calculated and an approximation for the wavefunction can be obtained, and this process is repeated and

is only stopped when the total energy of the system (which itself is dependent on the orbitals) does not change within the tolerance of the convergence criteria:

1- Initial guess for the wavefunction/electron density
2- Evaluate effective potential and therefore MOs
3- New electron density is calculated using MOs from step 2
4- Repeat steps 2 and 3 until no more change in MOs.

At step 3, the total energy of the system is calculated, which is used to establish whether self-consistency is reached or not. It should be borne in mind that within this procedure, the orthonormality of the orbitals must be enforced.

### 2.1.9  Correlation Energy

Both DFT and HF theory use a mean-field approach to describing electron-electron interactions: one electron interacts with an average potential defined by the other electrons. If all electrons interacted explicitly with each other, their average separation would be greater than that predicted by HF theory. This avoidance would result in a change in the kinetic energy and the electron-electron repulsion would diminish, hence a variation in the potential energy. If the result of the HF calculation (in the complete basis set limit, section 2.2.4.2.2) were to be compared to the real system, the difference in energy would be precisely the correlation energy, comprising about 1% of the total.[28] Although this might seem small, it is actually important: in Chemistry, energy *differences* are of interest, and as correlation contributes differently to different states, an error significantly larger than 1% may result - therefore correlation energy may be comparable in magnitude to chemically relevant energy scales.

Being able to describe the electron correlation energy is the holy grail of computational chemistry: HF theory does not take electron correlation into account*, Kohn-Sham DFT (which will be described in section 2.2.4.1.2) tries to mimic (dynamic) correlation (and

---

* Strictly speaking, HF theory includes correlation between like-spin electrons, although the origin of this is the exclusion principle, rather than the Coulomb interaction.

neglects static correlation) and post-HF methods sometimes make the distinction between dynamic and static correlation, both described below.

Dynamic correlation, which is the more obvious energy contribution, is normally meant when 'correlation' is discussed. This energy describes the relative motion of the electrons and is important if there is a large number of electrons occupying different orbitals in a similar spatial region. One obvious example are electrons occupying the $p_x$, $p_y$ and $p_z$ orbitals. This type of correlation increases as the number of electrons increases. Dynamic correlation is a direct consequence of making the orbital approximation (section 2.1.5).

Static correlation, on the other hand, is important when there are different possibilities in how electrons can populate different orbitals, with the corresponding electronic configurations having similar energies, i.e. in a multiconfigurational system. This form of correlation energy is normally a smaller contribution to the total correlation of the system, and is only of concern for valence electrons, or a subset thereof. However, to accurately describe this type of correlation, more than one Slater determinant is needed to describe the total wavefunction (as done in post-Hartree-Fock methodologies). The Kohn-Sham approach to DFT does not take static correlation into account, so from this point onwards, when correlation energy is mentioned, it refers to dynamic correlation unless otherwise stated.

## 2.2   Computational Details

As discussed in section 1.6, this work has been performed within the framework of DFT and TDDFT due to the reasonable compromise between the size of the system studied and the accuracy. Before these two methods can be studied in more detail, some background should be given on the Thomas-Fermi model (section 2.2.1) and Hartree-Fock Theory (section 2.2.2), as the former is a 'frontrunner' of DFT and the latter is based on similar concepts and equations, which are the basis on which current implementations of DFT are built up on.

### 2.2.1 The Thomas-Fermi and Thomas-Fermi-Dirac Model

The Thomas-Fermi (TF) model[29,30] is the 'forefather' of DFT as we know it today. In fact, the TF model is *a* density functional theory formulated in 1927, as it was developed to obtain information about a chemical system from a physical observable, namely the electron density (and not from the wavefunction directly). The basic ideas behind the theory is discussed in this section, without going into the (mathematical) details of the theory.

The first assumption behind this model is that the kinetic energy is based on an expression for a uniform electron gas. This kinetic energy in this theory is a function of the density and becomes a *functional*. A functional is a function which itself is dependent on a function, rather than a variable. In this example, the kinetic energy is dependent on the electron density approximated as non-interacting electrons in a homogeneous gas, itself is dependent on the spatial coordinates. Electron correlation and electron exchange† were not taken into account in the original formulation. However, in 1930 Dirac added a term approximating local exchange, which gives rise to the Thomas-Fermi-Dirac Theory[31] (TFD). The name given to this theory is a bit unfortunate, as it was in fact Bloch who first derived a term for including the electron exchange energy in 1929.[32]

The advantage of this approach is its computational simplicity: there are only 4 variables (the three spatial coordinates and the spin), which makes any calculation very fast compared to a calculation which takes every electron into account. However, the approximation of a uniform electron gas in the expression for the kinetic energy, is unphysical: It may sometimes be adequate for the description of valence electrons in metallic systems when they contain a "sea of delocalised electrons", but in general is not suitable. The main issue with this methodology is that neither TF to TFD theory predict any type of bonding, due to the electron gas being assumed to be uniform. The result of this is, of course, that molecules are predicted to not exist, as shown by Teller *et al.*.[33]

---

† The energy associated with electron exchange is the measure of how the energy of a system changes when two electrons are interchanged. This is discussed further in the section on HF and DFT.

### 2.2.2  Hartree-Fock Theory

Hartree-Fock theory is a wavefunction based method, which generally yields satisfactory results but is outperformed by DFT (section 2.2.4) in terms of cost and efficiency.

#### 2.2.2.1    Hartree Theory

Unlike TF and TFD theories (and, ultimately DFT), Hartree-Fock (HF) theory is not a density functional method but rather a wavefunction method. This means that this methodology attempts to solve the (many-electron) Schrödinger equation directly, albeit with some major approximations.

The general approach to solving the Schrödinger equation is to find a solution to equation (2-3). The simplest way to write an *N*-electron wavefunction is to do so as a simple product of one-electron functions, or orbitals:

$$\Psi_{\mathrm{HP}} = \ \psi_1\,\psi_2\,\psi_3 \,...\, \psi_N \tag{2-3}$$

As discussed previously, $\Psi_{HP}$ is the 'Hartree-product' wavefunction with the $\psi_i$ being one-electron functions. Although only exactly solvable for a non-interacting system, this crude approximation forms the basis of Hartree theory. Assuming, in first instance, that the electrons are non-interacting, the Hamiltonian can be separated:

$$\widehat{H} = \ \Sigma_i^N\,\widehat{h}_i \tag{2-4}$$

where $\hat{h}_i$ is the one-electron Hamiltonian which, for non-interacting electrons, can be expressed as:

$$\hat{h}_i = \ -\ \frac{1}{2}\,\nabla_i^2 - \ \Sigma_{k=1}^M \frac{Z_k}{r_{ik}} \tag{2-5}$$

where $\nabla_i^2$ is the kinetic energy operator in atomic units and the second term represents the Coulomb interaction between electron *i* and each nucleus *k*, with *k* ranging from 1 to *M*,

the total number of nuclei. The Coulomb interaction consists of the nuclear charge $Z_k$ and the electron-nuclear separation $r_{ik}$.

To find the energy of the system (equation (2-1)), a series of *N* eigenvalue problems needs to be solved:

$$\hat{h}_i \, \psi_i = \varepsilon_i \, \psi_i \tag{2-6}$$

where $\varepsilon_i$ are the energies of the one-electron orbitals and $\psi_i$ are the one-electron wavefunctions as seen in equation (2-3).

This means that the many-electron Schrödinger equation has been simplified to a series of one-electron eigenvalue problems.

The one-electron Hamiltonian can be improved upon by including an interaction term $V_i\{j\}$, representing the interaction of electron *i* with all other electrons *j*.

$$\hat{h}_i = -\frac{1}{2} \nabla_i^2 - \sum_{k=1}^{M} \frac{Z_k}{r_{ik}} + V_i\{j\} \tag{2-7}$$

The interaction between electron *i* and all other electrons can be expressed in the following way:

$$V_i\{j\} = \sum_{j \neq i} \int \frac{\rho_j}{r_{ij}} \, d\mathbf{r} \tag{2-8}$$

This equation defines the Coulomb interaction between electron *i* and each other electron, *j*, in terms of the charge density $\rho_j$ and the inter-electron separation $r_{ij}$. These interactions are evaluated over all space. This shows that the electron interaction is included as a mean field external potential, i.e. electron *i* is only interacting with the average field of all other electrons. This means that Hartree (and Hartree-Fock, as it uses the same Coulomb potential) theory is a *mean field* theory.

The aim of a quantum chemical calculation is to find the eigenfunction that satisfies the many-electron eigenvalue problem (minimising the energy). As the density $\rho_j$ from

equation (2-8) is equal to $|\psi_j|^2$, and the equations above are linked to each other, the 'self-consistent field' approach (section 2.1.8) is used to solve the set of equations. The total energy is related to the one-electron energies in the following way:

$$E = \sum_i \varepsilon_i - \frac{1}{2} \sum_{i \neq j} \iint \frac{\rho_i \rho_j}{r_{ij}} \, d\mathbf{r}_i d\mathbf{r}_j \qquad (2\text{-}9)$$

The final term in this equations corrects for the fact that every $\hat{h}_i$ contains an electron-electron repulsion term. This repulsion is between electron $i$ and the mean field generated by all other electrons. When another electron $j$ is considered, part of the repulsion it experiences is from electron $i$, but this repulsion has already been accounted for when electron $i$ was considered.

The wavefunction is the final thing that needs to be considered in order to understand how to solve the Schrödinger equation using Hartree Theory. As formalised in Pauli's exclusion principle[34], no two electrons can have the same set of quantum numbers, so in a given molecular orbital, an electron can either have $\alpha$ ("up") or $\beta$ ("down") spin. This means that Hartree theory considers a wavefunction of the following form to create the Hartree Product:

$$^3\Psi_{\text{HP}} = \psi_a(\mathbf{r}_1)\alpha(1) \, \psi_b(\mathbf{r}_2)\alpha(2) \qquad (2\text{-}10)$$

The superscript indicates a triplet electronic state (as there are two electrons with the same spin), and the orbitals $\psi_a$ and $\psi_b$ must differ from each other, as the Pauli Exclusion Principle would be violated otherwise.

The main problem with equation (2-10) is that it does not satisfy the anti-symmetry requirement imposed by QM, so this is not a suitable trial wavefunction. The anti-symmetry requirement imposes that any wavefunction used in quantum chemistry must change sign when the coordinates of two electrons are interchanged. For the purpose of clarity, a wavefunction that would be suitable is shown below. However, this is not a Hartree Product.

$$^3\Psi = \frac{1}{\sqrt{2}} \left[ \psi_a(\mathbf{r}_1)\alpha(1)\psi_b(\mathbf{r}_2)\alpha(2) - \psi_a(\mathbf{r}_2)\alpha(2)\psi_b(\mathbf{r}_1)\alpha(1) \right] \qquad (2\text{-}11)$$

The factor of $\frac{1}{\sqrt{2}}$ is used to satisfy the normalisation requirement:

$$\int |\psi|^2 \, d\tau = 1 \tag{2-12}$$

### 2.2.2.2    The Hartree-Fock Approximation

As described above, the type of wavefunction used in Hartree theory does not obey the anti-symmetry principle, something noted by Fock in 1930.[26] Fock suggested the use of Slater determinant wavefunctions in Hartree's SCF formulation, which is the simplest way to construct a many-electron wavefunction that satisfied the anti-symmetry principle. The anti-symmetrical wavefunction of equation (2-11) would be written in Slater-determinant form as seen below. The wavefunction is being written as the determinant of a matrix, as the horizontal bars indicate:

$$^3\Psi_{SD} = \frac{1}{\sqrt{2}} \begin{vmatrix} \psi_a(\mathbf{r}_1)\alpha(1) & \psi_b(\mathbf{r}_1)\alpha(1) \\ \psi_a(\mathbf{r}_2)\alpha(2) & \psi_b(\mathbf{r}_2)\alpha(2) \end{vmatrix} \tag{2-13}$$

The main underlying assumption in Hartree-Fock (HF) theory is that the wavefunction of an $N$ electron system can be approximated by a single Slater determinant. Inherently in this formulation, the effects of electron exchange are included in the calculations. The electron exchange energy is linked to the anti-symmetry principle, as it is an energy that stems from the fact that all electrons are indistinguishable from each other, which means that the associated wavefunction needs to be anti-symmetric with respect to the exchange of electrons. In essence, HF theory is the extension of Hartree SCF theory to include electron exchange. However, no Coulomb correlation is included in this formalism.

In 1951 Roothaan[35] suggested that any molecular orbital (MO), which is the eigenfunction of a one-electron operators, can be represented using a set of basis functions. This set of one-electron orbitals (basis functions) can be combined using the Linear Combination of Atomic Orbitals (LCAO) method to obtain the characteristics of the MO in question (section 2.1.6). In theory, this is exact as any function of $n$-variables can be decomposed

into a complete set of *n* one-variable functions. In practise, finite basis sets need to be used to approximate orbitals in HF calculations (or any calculation for that matter).

There are two different formalisms of HF theory that can be used, namely "Restricted" and "Unrestricted" HF. The difference between them is that the former can only be used when there are no unpaired electrons, i.e. when all occupied molecular orbitals have exactly two electrons in them. On the other hand, unrestricted HF theory can be used with any orbital occupation.

An interesting note is that HF theory is a variational method (section 2.1.3), which means that with an infinite basis set, the HF energy would be a minimum with respect to the approximations made: this minimum energy is called the Hartree-Fock limit. However, in practise any results obtained from HF calculations are going to be higher in energy than the HF limit. This limiting energy, however, is not that corresponding to the exact eigenvalue to the non-relativistic Schrödinger equation because the approximation of expressing the wavefunction as a single Slater determinant is insufficient since it does not take electron correlation (section 2.1.9) into account. Electron correlation is defined by how all electrons are interacting with one another. HF theory can only approximate this electron-electron interaction by using a mean-field interaction between one electron and all others. This means that the difference between the HF limit and the eigenvalue to the Schrödinger equation are only separated by the correlation energy, which cannot be solved mathematically, as it is a many-body problem.

### 2.2.3  Post-Hartree-Fock Methodologies

Hartree-Fock theory is still widely used as a starting point for further calculations, which aim to correct for the lack of (static or dynamic) correlation in HF theory, by using virtual orbitals to improve the wavefunction and energy. So-called post-HF methods can be very accurate but are computationally expensive, and can only treat small systems. Only one methodology is introduced, as it is used in chapter 5 to compare (TD)DFT results obtained in this study.

### 2.2.3.1   Coupled Cluster Method

Coupled Cluster (CC) methods[36,37] are based on the idea of improving the HF wavefunction with the inclusion of excited configurations. These corrections, whether incorporating single, double or higher excitations, can be added to the reference wave function. CC includes all excitations of a given type to infinite order, as CC can be defined in terms of an exponential operator acting upon the reference wavefunction (the HF wavefunction $\Psi_{HF}$) which can be expanded in an infinite power series:

$$\Psi_{CC} = e^{\hat{T}}\,\Psi_{HF} \tag{2-14}$$

where $\Psi_{CC}$ is the coupled-cluster wavefunction and $\hat{T}$ the cluster operator. The CC wavefunction is in principle exact. However, CC needs to be truncated for computational tractability and the full power series cannot be incorporated. The way the truncation is implemented in CC theory is part of the reason why this theory is so popular. The cluster operator $\hat{T}$ is defined as follows:

$$\hat{T} = \hat{T}_1 + \hat{T}_2 + \hat{T}_3 + \cdots + \hat{T}_n \tag{2-15}$$

where $n$ is the total number of electrons. The $\hat{T}_i$ operators generate all possible determinants with $i$ excitations from the reference wavefunction. The addition of only the singly excited configurations ($\hat{T} = \hat{T}_1$) does not improve on HF results and the lowest useful approximation would be CCD ($\hat{T} = \hat{T}_2$). Incorporating the singly excited configurations to CCD is, in computational terms, only slightly more demanding, yet it describes a more complete model, known as CCSD ($\hat{T} = \hat{T}_1 + \hat{T}_2$): due to the exponential nature of the CC expansion, not only are $\hat{T}_1$ and $\hat{T}_2$ considered but also the rest of the expansion, as shown below:

$$\Psi_{CCSD} = e^{(\hat{T}_1+\hat{T}_2)}\Psi_{HF} = \begin{bmatrix} 1 + \hat{T}_1 + \left(\hat{T}_2 + \frac{1}{2}\hat{T}_1^2\right) + (\hat{T}_1\hat{T}_2 + \frac{1}{6}\hat{T}_1^3 + \\ (\frac{1}{2}\hat{T}_2^2 + \frac{1}{6}\hat{T}_1^2\hat{T}_2 + \frac{1}{24}\hat{T}_1^4 + \cdots \end{bmatrix}\Psi_{HF} \tag{2-16}$$

Both CCD and CCSD methods scale as $M^6$, with $M$ being the number of basis functions. The triplet (and higher) excitations can be included perturbatively, written as e.g. CCSD(T) and if this is done, the scaling is similar to CCSD. If triplets are included non-perturbatively (known as CCSDT), the scaling is $M^8$, so this method can only be used on very small systems. This shows that CCSD and CCSD(T) are the most practically applicable approximations within the coupled cluster model to retrieve part of the dynamic correlation.

To find the excitation energies within CC theory, the equation-of-motion coupled-cluster formalism (EOM-CC) is often used.[38] It is a linear response excited state version of CC theory.

Despite the success of this methodology and its accuracy, it should be borne in mind that CC methods are non-variational.[39]

### 2.2.4  Density Functional Theory

Similarly to Thomas-Fermi Theory (section 2.2.1), DFT uses the fact that the density $\rho(\mathbf{r})$ is sufficient to obtain all the information of a system, as shown by the Hohenberg-Kohn theorems[22] in the 1964. In contrast to HF theory, this means that fewer variables are needed to approximate the solution to the (many-electron) Schrödinger equation, as only the spatial coordinates and the electron spin are needed rather than $4N$ for an $N$ electron system, which makes it a very efficient methodology. However, only after the Kohn-Sham equations were introduced in 1965,[23] meaning that the variables in DFT increase again from 4 to $4N$, by expressing the electron density using a set of molecular orbitals (which are not to be confused with the 'real' set of orbitals), has the method been computationally viable. In principle, DFT is an exact theory. However, introducing Kohn-Sham orbitals means that it no longer is, as it makes the assumption that we can represent our electronic state in terms of a single configuration.

Although the DFT formalism has been in the scientific community since the 1960s, it took 30 years for it to become a popular method in computational chemistry. Work by, e.g.

Becke,[40,41] has played an important role in bringing DFT to the masses. Nowadays, DFT is one of the most widely used methodologies in quantum chemistry and a large amount of research is based on its results. It is probably fair to say that DFT has even driven experimental work (e.g. references 42 and 43 as well as references therein), which is a huge success for any computational modelling tool.

### 2.2.4.1    *Basic Ideas and Formalisms*

#### 2.2.4.1.1        The Hohenberg-Kohn Theorem

DFT is based on two main theorems, known as the Hohenberg-Kohn (HK) theorems. The first states that the ground state electronic structure is determined completely by the electron density, $\rho(\mathbf{r})$.[22] The second theorem demonstrates that there is a variational principle associated with the density, $\rho(\mathbf{r})$.[22]

The first theorem means that the electron density determines the energy of the system and vice versa: There is a one-to-one relationship between the energy and the electron density. It also follows that $\rho(\mathbf{r})$ is sufficient to describe *all* physical observables associated with the system. It means that a system of $N$ electrons, otherwise described by $4N$ variables (the three spatial coordinates and one spin coordinate for each electron in the system) can be described by only four variables: the three spatial coordinates and the spin, as the electron density is no longer separated into that of individual electrons but rather considered as a whole. The only, and substantial, problem is that the functional linking the density and energy is not known.

It follows from the second theorem that *any* trial density used results in an (ground state) expectation energy that is *always* higher or equal to the actual, true energy of the system – i.e. DFT is a variational method (section 2.1.3).

The DFT energy can be expressed, in terms of the density $\rho(\mathbf{r})$, in the following way:

$$E_{\mathrm{DFT}}[\rho(\mathbf{r})] = T[\rho(\mathbf{r})] + E_{\mathrm{ne}}[\rho(\mathbf{r})] + J[\rho(\mathbf{r})] + E_{\mathrm{xc}}[\rho(\mathbf{r})] \tag{2-17}$$

where $T$ is the kinetic energy, $E_{ne}$ the potential energy of the nuclei-electron attraction, $J$ is the Coulomb energy and $E_{xc}$ is the exchange-correlation part of the energy. All these terms are known exactly within the KS-DFT formalism, apart from the $E_{xc}[\rho(\mathbf{r})]$ term, which, in practise, cannot be calculated without approximations as the exact functional form is unknown. This means that any inaccuracies and incorrect predictions are most likely due to this energy term. All energy terms in equation (2-17) are a function of the density, which in itself is a function on the spatial coordinates. This is where the name 'Density Functional Theory' derives from.

### 2.2.4.1.2    The Kohn-Sham Theory

The HK-formalism of DFT strongly resembles Thomas-Fermi theory, in that a suitable expression for the energy based on the electron density is sought. TF theory was shown to be unsuitable to describe any form of chemical system, so a new approach to solving the problem was required. Kohn and Sham did just that: they developed the idea of reintroducing orbitals in order to solve the Schrödinger equation (SE) within the HK formalism.[23] These so-called Kohn-Sham (KS) orbitals are not necessarily physically meaningful orbitals (although some properties can be approximated well by KS orbitals[44]) but instead represent a set of non-interacting electrons in a fictitious system, such that their electron density gives rise to the exact same density as that of the real, interacting system.[23]

The total electron density is obtained as the sum of the square of one-electron functions:

$$\rho(\mathbf{r}) = \sum_i \varphi_i(\mathbf{r})^2 \tag{2-18}$$

The one electron functions form a set of eigenvalue equations, known as the Kohn-Sham equations, where $\hat{h}_i^{KS}$ is the KS operator, $\varphi_i$ the one-electron orbitals, known as the KS orbitals and $e_i$ is the energy of orbital $i$.

$$\hat{h}_i^{KS}\varphi_i(\mathbf{r}) = e_i\varphi_i(\mathbf{r}) \tag{2-19}$$

The KS operator is also defined as:

$$\hat{h}_i^{\text{KS}} = -\frac{1}{2}\nabla_i^2 - \sum_k^m \frac{Z_k}{|\mathbf{r}_i - \mathbf{r}_k|} + \int \frac{\rho(\mathbf{r}')}{|\mathbf{r}_i - \mathbf{r}'|} d\mathbf{r}' + \frac{\partial E_{\text{xc}}}{\partial \rho(\mathbf{r})} \tag{2-20}$$

where $k$ is the label for the $m$ nuclei with effective nuclear charge $Z_k$. The positions $\mathbf{r}$ have the subscript $i$ if the KS orbital is considered, $k$ the nuclei and $\mathbf{r}'$ represents the position in question. The last term is known as the functional derivative of the exchange-correlation energy with respect to the density, i.e. the *xc*-functional. Choices for $E_{\text{xc}}$ are discussed in section (2.2.4.2.1).

The KS formalism means that the simplicity of the electron density being represented by only 4 variables disappears, as the number of variables for an *N*-electron system again becomes 4*N*. However, the accuracy is much improved over the TF model, which suffers from an extremely poor representation of the kinetic energy (section 2.2.1). In KS-DFT, the kinetic energy has been split into two and the component due to correlation has been taken out of the kinetic energy term. This means that the $T[\rho(\mathbf{r})]$ term can be calculated exactly (for the fictitious system) and the term due to correlation is approximated. The latter is a relatively small contribution to the kinetic energy but is chemically important, i.e. on an energy scale which is comparable to those seen in chemistry in e.g. deciding the energy ordering of different conformers or on a similar scale to energy barriers.[45] This energy term, which is the bane of every computational chemist using DFT, consists of two unknowns: the exchange part of the energy, which stems from the fermionic character of the electrons (which have a spin of ½) and describes the variation in energy due to the exchange of two electrons and is accurately described within the HF formalism (section 2.2.2). This non-classical correction to the Coulomb interaction is normally difficult to quantify in an *N*-electron system.

The (dynamic) correlation part of the *xc*-energy has its roots in the electron-electron interaction: KS-DFT uses the average repulsion between the electrons, not allowing the electrons to instantaneously react to each other. This results in DFT being unable to correctly quantify the effect on all other electrons if one single electron moves. In essence, as this is a many-body problem which has been simplified by a mean-field, these effects are not fully accounted for.

Once the electron density is described, a suitable Hamiltonian needs to be found, and the Hamiltonian used in DFT is similar to HF theory:

$$\hat{H}_\lambda = T + V_{\text{ext}}(\lambda) + \lambda V_{\text{ee}} \tag{2-21}$$

where T is the kinetic energy, $V_{\text{ext}}$ the external potential, $V_{\text{ee}}$ the electron-electron potential and $\lambda$ is a measure of how much the system is interacting: $0 \leq \lambda \leq 1$; when $\lambda = 1$ the system is fully interacting and when $\lambda = 0$ the system is non-interacting. For the case of $\lambda = 0$, the exact solution to the SE can be found by using a Slater determinant representing the molecular orbitals to express the kinetic energy.

This is where Kohn and Sham made a breakthrough: if the real, interacting system was replaced by a non-interacting system which gives the same solution to the energy, the mathematical aspect would be simplified: the Hamiltonian would be the sum of one-electron operators, the eigenfunctions are Slater determinants of the one-electron orbitals and the eigenvalue is the sum over all one-electron eigenvalues.

The DFT energy of any system can be divided into several aspects, which can be evaluated separately, as seen in equation (2-22), where the $E_{\text{xc}}[\rho(\mathbf{r})]$ can be expanded further:

$$E_{\text{xc}}[\rho(\mathbf{r})] = \Delta T[\rho(\mathbf{r})] + \Delta V[\rho(\mathbf{r})] \tag{2-22}$$

where $\Delta T$ is the correction to the kinetic energy, which arises due to the fact that the system actually is interacting and $\Delta V$ the term encompassing all quantum effects due to electron-electron interaction. Finding an expression for this $E_{\text{xc}}$ energy is the Holy Grail for DFT, as it is is unknown and therefore cannot be solved exactly.

### 2.2.4.2    DFT Approximations

#### 2.2.4.2.1        Functionals

Currently, $E_{\text{xc}}$ cannot be evaluated without approximations, and these approximations are expressed in terms of 'functionals'. Every functional uses a different approximation to

describe $E_{xc}$ but there are classes of functionals which have similar starting points. The choice of functional is crucial to the accuracy of the results. The exchange-correlation energy is often expressed in terms of the density as seen below:

$$E_{xc}[\rho(\mathbf{r})] = \int \rho(\mathbf{r})\, \varepsilon_{xc}[\rho(\mathbf{r})]d\mathbf{r} \qquad\qquad (2\text{-}23)$$

where $\varepsilon_{xc}$ is the exchange-correlation energy density, which in itself is dependent on the electron density but generally treated as sum of individual exchange and correlation contributions. It should be noted that the energy density is a density calculated in terms of particles and not per unit volume. Generally, $E_{xc}$ is expressed as the sum of the exchange ($E_x$) and the correlation ($E_c$) contributions, as can be seen below.

$$E_{xc} = E_x + E_c \qquad\qquad (2\text{-}24)$$

Unfortunately there is no 'best' functional that yields the most accurate results for all systems. However, there is a broad guideline as to how accurate a certain group of functionals are: Perdew devised the concept of the 'Jacob's ladder', which is a visualisation of how functionals perform and, broadly speaking, their accuracy.[46] The idea behind this classification is that the higher up the ladder a given class of functionals resides, the closer the solution is to the *exact* solution (albeit at increasing computational cost!), which is represented by 'Heaven of chemical accuracy'. The following section is written in such a way that functionals at the bottom rung are discussed first and then the different groups are mentioned, going one rung up at a time.

HEAVEN OF
CHEMICAL ACCURACY
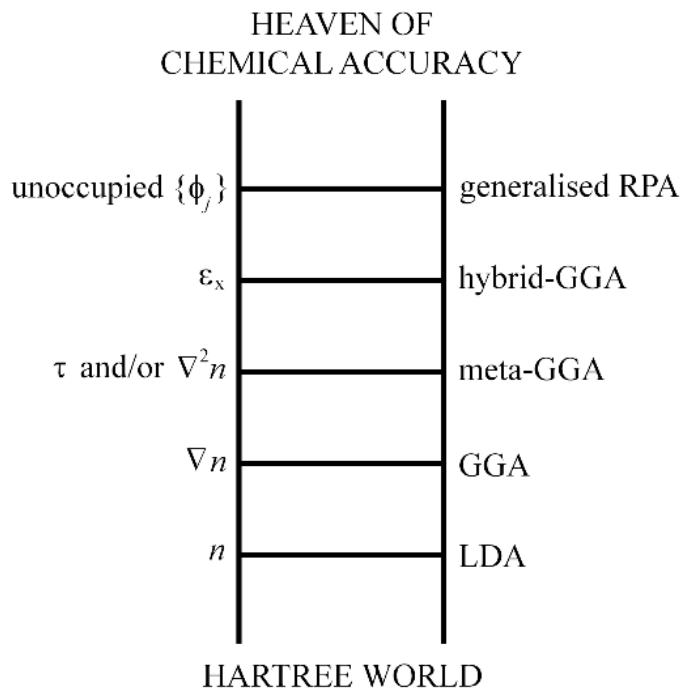


**Figure 2-1:** Jacob's Ladder, adapted from reference 47.

The simplest working approximation to the exchange-correlation functional $E_{xc}$ is the 'Local Density Approximation' (LDA), where the density is treated locally at any given point as a uniform electron gas. In the context of equation (2-23) it would mean that $\varepsilon_{xc}$ would depend solely on the value of $\rho(\mathbf{r})$ at any given point $\mathbf{r}$.

LDA makes use of the following expression for the exchange part of the energy:

$$E_x^{LDA}[\rho(\mathbf{r})] = -C_x \int \rho(\mathbf{r})^{\frac{4}{3}} d\mathbf{r} \tag{2-25}$$

Where $C_x = \frac{3}{4} \left(\frac{3}{\pi}\right)^{\frac{1}{3}}$. This equation can be generalised to take the difference between alpha and beta spin densities into account. When this is done, the approximation is referred to as the 'Local Spin Density Approximation' (LSDA). The density $\rho(\mathbf{r})$ is no longer given as one density but rather as the sum of $\alpha$ and $\beta$ densities, as can be seen from the equation below:

$$E_x^{\text{LDSA}}[\rho(\mathbf{r})] = -2^{\frac{1}{3}}C_x \int \left(\rho_\alpha(\mathbf{r})^{\frac{4}{3}} + \rho_\beta(\mathbf{r})^{\frac{4}{3}}\right) d\mathbf{r} \tag{2-26}$$

In a closed-shell system, i.e. a system without unpaired electrons, the results obtained from LDA and LSDA are equivalent.

A problem with an analytical expression for the correlation energy is that one that is suitable for all cases is not known. There is a need for different expressions for high[48] and low[49] density and functionals are used to interpolate between these two starting points. So, despite the fact that LDA functionals are based on the simple approximation of a uniform electron gas, no analytical expression is known for the correlation energy. This, to some extent, demonstrates just how difficult the quest for suitable functionals is.

As LDA functionals only consider the local density and approximate the *xc*-energy obtained from a uniform electron gas, they are most suited to systems where the electron density varies slowly; valence electrons in metals would be such a system where this would be the case. An example to study these systems using the LDA is the VWN functional.[50]

One rung up on Jacob's ladder, so one step closer to DFT heaven, is the Generalized Gradient Approximation (GGA). The improvement over LDA is that it assumes a non-uniform electron gas and at any given point, does not only take the electron density into account but also the first derivative (the gradient).[51] The name given to LDA is slightly misleading: it implies that all other functionals are not local, but in fact GGA is still a local density approximation, in that it evaluates the *xc*-energy at any given point and describes the local changes to the electron density.

The general approach to GGA functionals is outlined below, i.e. as a correction term to the LDA energy functional:

$$\varepsilon_{xc}^{\text{GGA}}[\rho(\mathbf{r})] = \varepsilon_{xc}^{\text{LDA}}[\rho(\mathbf{r})] + \Delta\varepsilon_{xc}\left[\frac{\nabla\rho(\mathbf{r})}{\rho^{\frac{4}{3}}(\mathbf{r})}\right] \tag{2-27}$$

This approach has been taken in functionals devised by Perdew, such as PBE[52] that is an example of a functional that includes no empirical parametrisation and is rather defined

as an expansion of the reduced gradient. Performing DFT calculations using GGAs rather than LDAs is slightly more expensive. However, results are substantially improved, especially for non-metallic systems.

There are also GGA correlation functionals that do not correct the LDA expression but rather compute the correlation energy in a different way. A commonly used form is that of the LYP correlation functional[53] devised by Lee, Yang and Parr. This functional contains empirical parametrisation (to the Helium atom), so is not an *ab-initio* method but it has the advantage of completely cancelling out the self-interaction error[54] in one-electron systems.‡ When Becke's GGA exchange expression[40] is combined with the LYP GGA correlation expression, the *xc*-functional is called BLYP.

On the third rung of Jacob's ladder (figure 2-1) are meta-GGA (MGGA) functionals, such as B95[55] and TPSS.[46] These functionals are an extension of GGA functionals in that they do not take just the local density and its first derivative into account but also its second derivative the Laplacian. However, the Laplacian is not always numerically stable and the easiest way to circumvent this is to calculate the kinetic energy density, $\tau$, which is still dependent on the Laplacian but numerically more stable and can be expressed as follows:

$$\tau(\mathbf{r}) = \sum_i^{occ} \frac{1}{2} |\nabla \psi_i(\mathbf{r})|^2 \tag{2-28}$$

where $\psi_i$ are self-consistent Kohn-Sham orbitals. Again, meta-GGAs improve results but require slightly more computational resources.

Moving away from the idea of local (LDA) or semi-local (GGA and MGGA) and climbing the next rung on Jacob's ladder, another concept is used for hybrid functionals. These are so-called as they include some percentage of exact exchange from HF theory (discussed in section 2.2.2) in their expression for the *xc*-energy, with the other component being that of either L(S)DA or GGA. These types of functionals are a popular choice for applications to chemical systems. The idea behind this hybridisation of two theories is that if the HF orbitals were the same as the KS orbitals, the HF solution and KS solution would be the

---

‡ The self-interaction error is the unphysical description of an electron interacting with itself.

same and therefore the HF solution would give the exact exchange energy for the KS case. Unfortunately, the HF and KS orbitals are different, but this approximation still seems to be suitable in many cases. Some prefer to say that hybrid functionals contain HF-*like* exchange, as the HF exchange expression is evaluated with the KS orbitals, but it is generally referred to as HF exchange (HFE).

Hybrid functionals are based on the 'adiabatic connection method' (ACM).[56,57] The idea behind this is that an expression needs to be evaluated, which links the non-interacting KS system to the fully interacting system, by varying the electron-electron interaction. Using the Hellman-Feynman theorem,[58,59] the exchange correlation energy can be computed as

$$E_{xc} = \langle \Psi(\lambda)|\hat{V}_{xc}(\lambda)|\Psi(\lambda)\rangle \tag{2-29}$$

where $\lambda$ is an integration variable and the quantitative measure of the electron-electron interaction, ranging from $\lambda = 0$ for no interaction (equivalent to the KS system) and $\lambda = 1$ for fully interacting (the 'real' system) and $\hat{V}_{xc}$ is a 'functional derivative' (a measure relating the change in the functional to the change in the function that the functional depends on), and in this case it would be best described as a one-electron operator which yields the expectation value of $E_{xc}$ for the KS Slater determinant.

Equation (2-29) is an integral to be evaluated; the region of interest is the area under the curve. The end points (at $\lambda = 0$ and $\lambda = 1$), are known/approximated, so it is the curve itself that needs to be established, which can be achieved by including a certain amount of HF-like exchange. The amount of HF-like exchange added is determined by parametrisation to available experimental data, see e.g. B3LYP[40,53,60] as an example, whose definition in given in equation (2-31).

The Half-and-Half method [41,61] defines the *xc*-energy in the following way:

$$E_{xc}^{H+H} = \frac{1}{2}\left(E_x^{exact} + E_x^{LDSA}\right) + E_c^{LDSA} \tag{2-30}$$

It is clear that the exchange term is composed of 50% exact HF exchange and 50% exchange as defined by the LSDA approximation. As HF theory does not take correlation

into account, the correlation contribution to the *xc*-functionals is purely from Kohn-Sham DFT (KS-DFT).

A widely used hybrid functional is the B3LYP functional which includes 20% of exact HF-like exchange($E_x^{HF}$), the Becke 88 GGA-exchange term[62] ($\Delta E_x^B$), the LSDA-exchange term ($E_x^{LSDA}$), the VWN LSDA exchange and correlation[50] term ($E_c^{LSDA}$), the LYP GGA-correlation[53] ($E_c^{LYP}$) and its parametrisation as discussed in the ACM is as follows:

$$E_{xc}^{B3LYP} = 0.8E_x^{LDSA} + 0.2E_x^{HF} + 0.72\Delta E_x^B + 0.19E_c^{LDSA} + 0.81E_c^{LYP} \qquad (2\text{-}31)$$

The BHLYP[40,53,61] functional has 50% exact exchange and, like B3LYP, a GGA expression for the other component of the exchange and the entire correlation energy. It should be noted that the mixing parameters used in hybrid functionals have been fitted to a set of experimental values (different functionals are fitted to different values) from experiment, such as ionisation energies, so care must be taken in their application, as not all elements or properties have been considered in the fitting. The 'optimal' amount of HF exchange depends on the property of interest, and increasing the amount of HF exchange does not necessarily improve results. However, as a general rule, hybrid functionals tend to yield results closer to experimental values, as the self-interaction error commonly found in DFT calculations, is reduced because HF theory is free from self-interaction: in HF theory and more advanced methods (see, e.g. reference 63) the Coulomb self-interaction and exchange self-interaction cancel each other out. However, as DFT only uses an approximate expression for the exchange energy, it no longer cancels with the Coulomb self-interaction, resulting in the self-interaction error.

A class of functionals which offer further improvements over hybrid GGAs (or hybrid functionals in general) are range-separated hybrid functionals. They do not appear on the original Jacob's ladder, as they were devised around the same time as the schematic ladder. These functionals vary the degree of HF exchange, depending on the inter-electronic separation. Using CAM-B3LYP[60,61,64] as an example, 19% of HF exchange is included at small separations and a larger correction of 65% HF exchange is employed at larger separations, in addition to the correlation contribution of B3LYP. This improves the description of both Rydberg states and excitation energies as virtual orbitals can be

highly delocalised and are further from the nucleus: the inclusion of exact exchange improves the description of these higher energy states. In most cases, range-separated functionals have also improved the description of charge transfer (CT) excitations, a problem found in some time dependent density functional theory (TDDFT) calculations.[65]

Another, fairly recent, extension of hybrid functionals are the double hybrid (DH) functionals, first devised in 2004 by Truhlar and co-workers.[66] These are not very widely used, as they require a lot of computational time due to PT2 scaling and the fact that bigger basis sets are needed. These functionals use a certain amount of HF exchange and a certain amount of exact 'PT2' correlation. The latter result is obtained from 2nd order Perturbation Theory, which is a post-HF theory. The expression can generalised as:

$$E_{xc}^{DH} = (1 - a_x)E_x^{DFT} + a_xE_x^{HF} + (1 - b_c)E_c^{DFT} + b_cE_c^{PT2} \qquad (2\text{-}32)$$

where $a_x$ is the amount of HF exchange and $b_c$ the amount of correlation included.

The functionals on the top rung of Jacob's ladder are known as 'Generalized Random Phase Approximation' (RPA) functionals,[67–70] which take not only the occupied but also virtual KS orbitals into account. This is thought to improve the description of dispersion interactions, such as van der Waals interactions. These functionals require large basis sets, are computationally very expensive and therefore not widely used.

### 2.2.4.2.1.1 *Philosophies of Different Functionals*

There are different schools of thoughts in computational chemistry and in the computational chemistry community in general. As it has been shown, different functionals are constructed from different starting points. The parametrisation of hybrid functionals results in not an *ab-initio* but a semi-empirical calculation. Some researchers feel that the latter is somehow worse and arbitrary. However, the results and accuracy, in terms of agreement with experimental data, of these functionals are good, if used well, and often better than more *ab-initio* methods. One reason for this is that GGAs are known to underestimate barrier heights and energetics of ionic bonds[71] for chemical reaction

whereas HF theory tends to overestimate these.[72–75] Some might feel that this accuracy is not real but rather a fortunate cancellation of errors; as although energetics might be improved, geometries and atomisation energies could, for example, be described less accurately using hybrid functionals as pure GGA functionals.[76] This is the issue with parametrisation: One property can be calculated accurately but when the parametrisation has not been optimised for another property, the functional might lead to poorer results. The problem is that there is no one best answer in general: if the atoms and their chemical environment of the system studied were part of a parametrisation process for a certain functional, said function should be a good starting point for calculation. However, if a certain atom in a specific chemical environment was not part of the parametrisation process, then a hybrid functional might not be a very good functional to use. This is particularly true for elements that are not widely studied, such as *f*-elements. In general, scientists who prefer to stay away from empirical parametrisation avoid hybrid functionals (and sometimes GGAs) despite their many advantages, as a more systematic approach to solving the KS equations is favoured. However, in this project, it has been found that (some) hybrid functionals perform well and the predictions of excitation energies agree well with experiment, as discussed later on.

### 2.2.4.2.2 Basis Sets

In DFT (section 2.2.4), the many-electron eigenfunctions are expressed at Slater determinants, which represent the anti-symmetrised product of the (KS) molecular orbitals (MOs) of the system of interest. The aim of this section is to go into more detail (compared to section 2.1.7) as to how these eigenfunctions are constructed. MOs are linear combinations of basis functions (typically, but not always, atomic orbitals, AOs). Theoretically, it is possible to express any MO as a linear combination of known basis functions with only one condition: the basis functions must form a complete set. This one condition, however, is not practically feasible, as only finite basis sets can be used in quantum chemistry calculations. It is obvious that the better, or rather, more accurate one single basis function is in its description of an (atomic) orbital, the fewer such functions are needed to represent the MOs to a certain level of accuracy and therefore the more

efficient the calculation becomes. It is also useful when the atomic orbitals have a chemically meaningful form: the amplitude of the function should be large where the electron density is high (such as near nuclei) and the amplitude should be small where the electron density is small, e.g. in regions furthest away from any nuclei.

This section only considers basis sets that are centred on atoms, and does not discuss plane wave basis sets which are used for periodic calculations due to their delocalised nature. There are two main types of basis functions used in non-periodic DFT calculations: Slater-type orbitals[77] (STO) and Gaussian-type Orbitals[78] (GTO). The choice of basis function type is normally restricted: a quantum chemical code normally only offers STOs or GTOs within its implementation.

### 2.2.4.2.2.1  Slater Type Orbitals

STOs are very accurate basis functions to use, in the sense that their functional form closely resembles that of hydrogenic AOs. Their form is the following:

$$X_{\zeta,n,l,m}(r,\theta,\varphi) = N\, Y_{l,m}(\theta,\varphi)\, r^{n-1}\, e^{-\zeta r} \tag{2-33}$$

where $N$ is a normalisation factor; $Y_{l,m}$ are spherical harmonic functions; $r, \theta, \varphi$ represent the polar coordinates with $r$ being the distance to the atomic nucleus; $n$ the principal quantum number, $l$, the angular quantum number, $m$ the electron spin quantum number and $\zeta$ (greek zeta, which is where the 'zeta' comes from in basis set names) is related to the effective nuclear charge.

STOs represent the exponential decay of electron density with increasing distance from the nucleus, well. Furthermore, the 1s orbital has a cusp at the nucleus, which is the correct interpretation of said orbital. However, these types of functions do not yield radial nodes, although they can be introduced by taking the linear combinations of STOs.

Due to the exponential term in equation (2-33), STOs reach the basis set limit with fewer functions than GTOs. However, integrals involving STOs are complex to solve, which

means that many computational chemistry codes favour GTOs (section below), and therefore the use of STOs is less widespread.

### 2.2.4.2.2.2  *Gaussian Type Orbitals*

GTOs are usually expressed using Cartesian coordinates:

$$X_{\zeta,l_x,l_y,l_z}(x,y,z) = N\, x^{l_x}\, y^{l_y}\, z^{l_z}\, e^{-\zeta \mathbf{r}^2} \tag{2-34}$$

where $N$ is a normalisation factor, and $l$ is the angular moment quantum number. When all $l$ indices are equal to zero, a GTO has spherical symmetry, like an *s* orbital. When only one of these indices is equal to one, the GTOs have an axial symmetry, like a *p* type orbital. When the sum of the $l$ is equal to two we have a *d* orbital, and so on.

Basis functions are said to be 'contracted' when they are represented as a linear combination of 'fixed', or 'primitive' GTOs. Due to the exponential $\mathbf{r}^2$ dependence which is typical of Gaussian functions, GTOs have a zero slope at the nucleus, and not a discontinuous derivative as STOs do. This means that GTOs do not represent the physical behaviour near the nucleus well. In addition, GTO functions fall too rapidly at larger distances from the nucleus (when compared to physical behaviour or to STOs). However, integrals involving GTOs are mathematically much easier to solve, as analytical solutions are available. Another advantage is that the product of GTOs is again a GTO, which means that its application in quantum chemical calculations is much easier. In themselves, GTOs are less accurate than STOs. Their ease of calculation makes GTOs much more widely used than STOs. Due to the fact that STOs mimic the physical behaviour of atoms better, GTOs are combined to behave similarly to STOs, or more often AOs themselves. When this is done, a common notation for such basis sets is STO-*M*G, which means 'STO approximated by *M* GTOs'.[79]

### 2.2.4.2.2.3    Nomenclature and General Notes on Basis Sets

A few more basis set related ideas are worth considering. As mentioned above, the choice between STOs and GTOs is normally made within a code package, so the end user does not have the choice between the two different types of basis sets. However, within every code there is a huge variety of basis sets available and some of the more common distinctions are discussed below.

A 'minimal' basis set is one where the least number of basis functions possible is used, i.e. only one $s$-function is used for H and He, two $s$-functions ($1s$ and $2s$) and one set of $p$-functions ($p_x$, $p_y$, $p_z$) for the first row elements and so on.

As previously stated, when using GTO basis sets, contracted basis functions are typically used. The idea behind this is simple: the basis sets used in quantum chemical calculations are sets of AOs. A linear combination, or contraction, of primitive GTOs can be used to approximate each AO: such orbitals are known as 'Contracted Gaussian Type Orbitals' (CGTO). The contraction coefficients are chosen such that the shape of the CGTOs resemble the AOs. CGTOs are more often used than uncontracted GTOs. So the entire basis set for one atom using contracted basis functions is computationally cheaper to evaluate than the basis set that does not contract basis functions. There are two types of contraction schemes: segmented contraction and general contraction. In the former method each primitive GTOs is used by only one CGTO, whereas the latter uses all primitive GTOs to form all CGTOs, only with different contraction coefficients.

A double zeta (DZ) basis set doubles the amount of functions employed - it uses two $s$-functions for the hydrogen atom and the helium atom ($1s$ and $1s'$) and for $1^{st}$ row elements it uses four $s$-functions ($1s$, $1s'$, $2s$, $2s'$) and two sets of $p$-functions ($2p$ and $2p'$), etc. Triple zeta (TZ) basis sets have three basis functions, and the trend continues to quadruple zeta (QZ) and quintuple or pentuple zeta (5Z or PZ) sets. Typically, a more efficient way of using DZ is by having a split valence basis, so a valence double zeta (VDZ), which means that only the valence orbital functions are doubled and the core orbitals are represented by a single basis function, which makes the calculation more tractable.

Higher angular momentum functions are often considered and are known as polarization functions, so $p$-functions are used to allow an $s$-type orbital to be polarised, $d$ for $p$-type orbitals, $f$ for $d$-type orbitals, etc. Polarisation means that the function distort slightly, e.g. a $p$ polarisation function would allow an $s$-function to distort from its spherical symmetry to allow for stronger bonding or stronger interaction with an external field, like a ligand field. It is also possible to add a second set of higher angular momentum polarisation functions, however the first set is the most chemically important. When polarisation functions are added to, for example, a double zeta basis set, it is referred to as a DZP basis set (double zeta plus polarization). Double polarisation results in a 2P or PP addition to the name of the basis set. Care must be taken to have balanced set of basis functions - when too much polarisation is added then false artefacts may be seen in the results. A rule of thumb says that the number of polarisation functions should be at most one less than the amount of functions used for one lower angular momentum, i.e. a $4s3p2d1f$ basis function would be well-balanced whereas a $4s3p4d3f$ basis function would be considered over-polarised.

It is also possible to use different basis sets for different parts of a molecule - if the molecule is large but only a fraction of it needs to be described accurately, that fraction could have a better basis set than the rest of the molecule.[80] This is particularly useful if the studied molecule is rather large, as the speed of the calculation can be increased dramatically.

Diffuse functions can, and should, be added when there are regions of electron density further away from the nuclei, such as in the case of anions, highly excited states or weakly bound electrons. Without diffuse functions, these kinds of interactions may not be represented well and may not result in very accurate energetics. When basis sets have diffuse functions included, they are known as 'augmented basis sets'.

Adding more functions so as to be able to describe more complex chemical systems is good however, without adaptation, it is not suitable for heavier elements, which have more and more core electrons, needing correspondingly more GTOs. As core electrons do not contribute much to the chemistry but more to the energetics of a system, an alternative solution to contracting orbitals was proposed in 1935.[81] Instead of representing the core

electrons by many GTOs, an analytical function can replace all chemically unimportant core electrons, mimicking their behaviour. These analytical functions are called 'effective core potentials' (ECP).[81] ECPs represent the Coulomb repulsion accurately and can even be used to describe relativistic effects. There is generally a choice between 'large-core' and 'small core' ECPs, the former representing all electrons apart from the valence shell as a pseudopotential and the latter only replacing the deeper lying core orbitals. The small core pseudopotentials are, of course, more computationally demanding but can improve on the chemical model of the system as the shell just below the valence shell in energy can contribute to, for example, polarisation effects.

There is a wide variety of basis sets available, which this section showed. It is quite important to choose a suitable size basis set for a given calculation: what is the point of using a highly developed basis set for a HF calculation, or a small basis set for an expensive post HF calculation? Computational costs can vary hugely between different basis sets, which can have an impact on whether a calculation is tractable. In this study, two main basis sets are used, namely the def2-TZVP[82] basis set, which is a basis set proposed by Ahlrichs and co-workers, with a triple-$\zeta$, split-valence and polarisation functions§ and the DZDP (all-electron, double-$\zeta$ plus double polarisation) for Mg[83] and DZP (all-electron, double-$\zeta$ plus polarisation functions) for O.[83]

### 2.2.5  Excited State Calculations

There are several ways of calculating the excited state properties of a system, i.e. a system where not all electrons are at their lowest possible energy. This is typically associated with a molecule after it has absorbed a photon and before the molecule has had a chance to relax its electronic configuration back to that of the ground state. Modelling this behaviour is very useful, due to the transient nature of the excited state. Excited state calculations tend to be more complex and expensive than ground state calculations and the focus of the next section is mainly on the application of time dependent functional theory (TDDFT)

---

§ The 'def2' stands for 'default 2', to differentiate these basis sets from previously published basis sets with similar names.

and its formalisms, as used in this project to model excited states. As the name suggests, TDDFT is an extension of ground state DFT.

### 2.2.5.1   Delta-SCF (Δ-SCF)

Δ-SCF is an approximate method of obtaining excited state energies within DFT and has been justified for the lowest state for a given set of quantum numbers.[84,85,86] Δ-SCF works as long as one can perform a (constrained) optimisation in a (sub)space that doesn't involve the true SCF minimum (i.e., the ground state). This method works when the true ground state has a different symmetry, or multiplicity, to the state in question. Excitation energies are obtained by subtracting the ground state energy from the excited state energy. Orbital relaxation is taken into account within the limits of DFT. This is a very easy and reliable route for atomic excitation energies and ionisation energies. However, its application in the case of molecules generally, is limited to the lowest excitation energies between triplet and singlet states.[87]

### 2.2.5.2   Time Dependent Density Functional Theory

Time dependent density functional theory is most commonly used for the calculation of excitation energies, as it has a good balance between computational expense and accuracy (of around 0.25 - 0.55 eV compared to experiment, depending on the functional used).[88–90] The calculation of excitation energies is typically based on linear response theory; it calculates the response of a system after perturbation in the electric field. Calculating vertical absorption energies in TDDFT does not necessarily give any information about the electronic excited state density.[15,88]

In DFT, an external potential determines the density. This mapping is possible in the time dependent case as well; the time dependent density is determined by the time dependent potential. It is shown by the Runge-Gross Theorem[91] that the correspondence between a time-dependent density and a time-dependent potential is one-to-one, which forms the

basis of TDDFT. The van Leeuwen theorem [92] then shows that the interacting system can be replaced with an auxiliary non-interacting system. This is the time dependent analogue of the Kohn-Sham approach.

From here, a time dependent version for the Kohn Sham (TDKS) formalism can be produced, which, in principle just like DFT, produces the exact (time dependent) density for the $N$-electron system. In reality, approximations need to be made, mainly to the exchange and correlation term in the functionals used and the perturbation. For the latter, only the linear response approximation has been used in this project. Like DFT, TDDFT is in principle exact, but in practice approximate.[88]

Just like in ground state DFT, there is a problem in TDDFT of finding suitable functionals - (most) functionals do not have a memory; but a time dependent functional should describe the effective potential, which depends on the density at all previous times.[93] This memory dependence is usually ignored (see section 2.2.5.2.4). To the author's knowledge, no memory dependent functional is available in standard quantum chemical codes.

One of the most well-known approximations in TDDFT is the adiabatic approximation. This approximation uses the ground state exchange-correlation functional to approximate the excited state, or rather the excited state *xc*-functional. This is a reasonable approximation if the external potential varies slowly in time and the system studied begins in the ground state.

Despite all the approximations made within the TDDFT framework, TDDFT tends to work well in many cases, especially when calculating excitation energies using the Casida's equation (section 2.2.5.2.5),[94–96] leading to its success in computational chemistry.

### 2.2.5.2.1      The Runge-Gross Theorem

The Runge-Gross Theorem[91] lays the foundations of time dependent density functional theory by showing that there is a one-to-one correspondence between the density and the

external potential for a system: let us assume that there is a many-body state $\psi_0$ with two densities $n(\mathbf{r}, t)$ and $n'(\mathbf{r}, t)$, each influenced by potentials $v(\mathbf{r}, t)$ and $v'(\mathbf{r}, t)$ respectively, with $v'(\mathbf{r}, t) \neq v(\mathbf{r}, t) + c(t)$ and the condition that both potentials are Taylor-expandable around $t_0$. This scenario would lead to the densities becoming different at $t_1$, which is a time infinitesimally later than $t_0$. The consequence of this is that there is a one-to-one correspondence between densities and potentials, when there is a fixed initial many-body state. The function $c(t)$ is a time dependent scalar function, i.e. the two potentials are not linked to each other by a scalar function.

The proof for this theorem is typically performed in two steps: a one-to-one correspondence between the current densities and the potentials is first established, which is achieved by starting from the equation of motion for the current density $\hat{\jmath}(t)$. The second step then shows that having different current densities implies that the corresponding densities are different.

It should be noted that the Runge-Gross theorem only deals with scalar potentials, which means that it does not hold for some phenomena, such as time-varying magnetic fields. Also, the theorem is restricted to finite systems, as there is a surface integral in the second step of the proof which is required to vanish.

### 2.2.5.2.2 The Van Leeuwen Theorem

The Runge-Gross Theorem shows that there is a one-to-one dependence between the density and the potential in the time-dependent case, which is analogous to that shown by Hohenberg and Kohn for the time-independent ground state. What is now needed is a way to calculate the time-dependent densities without having to solve the time-dependent Schrödinger equation; ideally, a time-dependent version of the static Kohn-Sham formalism. The van Leeuwen theorem describes exactly this: an auxiliary set of non-interacting orbitals that produce the exact same density as the interacting system can be found: Any density $n(\mathbf{r}, t)$ of a many-body system with initial state $\psi_0$, external potential $v(\mathbf{r}, t)$ and particle-particle interaction $w(|\mathbf{r} - \mathbf{r}'|)$ can be reproduced by a different

many-body system with a unique external potential $v'(\mathbf{r}, t)$ (up to a time-dependent factor $c(t)$), and interactions $w'(|\mathbf{r} - \mathbf{r}'|)$ with initial state $\psi'_0$ such that the it yields the same density, and time derivative, as $\psi_0$ at $t = 0$. Importantly, the interaction $w'$ can be chosen to equal zero, corresponding to a non-interacting system. Under the condition that there exists a non-interacting initial state $\psi'_0$, the van Leuuwen theorem states that there is a unique potential $v_s(\mathbf{r}, t)$, in addition to the time-dependent function $c(t)$, which gives rise to the density $n(\mathbf{r}, t)$ for $t > t_0$. This is the time-dependent equivalent of the Hohenberg-Kohn theorem in static DFT.

### 2.2.5.2.3      The Time-Dependent Kohn-Sham Equations

A system that is in its ground state until a time $t_0$ and then evolves under a time-dependent external potential can be described using static DFT for the initial state at $t_0$. This means that both the wave function of the interacting and non-interacting systems, $\psi_0$ and $\phi_0$, respectively, define the ground state density.[51] The non-interacting system is evolving under the following effective potential, $v_s$, dependent on the time-dependent density $\rho(\mathbf{r}, t)$, the initial state of the interacting system $\psi_0(\mathbf{r}, t)$ and the initial state of the non-interacting system $\phi_0(\mathbf{r}, t)$.

$$v_s[\rho(\mathbf{r}, t), \psi_0(\mathbf{r}, t), \phi_0(\mathbf{r}, t)] \tag{2-35}$$

and the time-dependent external potential can be written as:

$$v(\mathbf{r}, t) = v_0(\mathbf{r}) + v_1(\mathbf{r}, t)\theta(t - t_0) \tag{2-36}$$

where $\theta(t - t_0)$ is a Heaviside step function, taking the value of 1 for a positive argument and the value of 0 for a negative argument. This means that the effective potential $v_s$ from equation (2-35) can be simplified to a potential which is dependent only on the time-dependent density, as the initial states $\psi_0(\mathbf{r}, t)$ and $\phi_0(\mathbf{r}, t)$ partially define $v_0(\mathbf{r})$.

At any time after $t_0$, the time dependent potential, $v_1$, comes into effect and produces the time dependent density:

$$\rho(\mathbf{r}, t) = \sum_{j=1}^{N}\left|\varphi_j(\mathbf{r}, t)\right|^2 \tag{2-37}$$

with the single-particle orbitals $\varphi_j$ coming from the time-dependent Kohn Sham equation:

$$\left[-\frac{\nabla^2}{2} + v_s[\rho(\mathbf{r}, t)]\right]\varphi_j(\mathbf{r}, t) = i\frac{\partial}{\partial t}\varphi_j(\mathbf{r}, t) \tag{2-38}$$

where the initial condition is $\varphi_j(\mathbf{r}, t_0) = \varphi_j^0(\mathbf{r})$.

The effective potential, as seen in the Time Dependent Kohn-Sham (TDKS) equation is given by:

$$v_s[\rho(\mathbf{r}, t)] = v(\mathbf{r}, t) + \int d^3\mathbf{r}' \frac{n(\mathbf{r}', t)}{|\mathbf{r} - \mathbf{r}'|} + v_{xc}[\rho(\mathbf{r}, t)] \tag{2-39}$$

With the integral being the Hartree potential $v_H(\mathbf{r}, t)$ with the addition of the *xc*-functional (discussed in more detail in section 2.2.4.2.1) $v_{xc}[\rho(\mathbf{r}, t)]$.

In principle, the exact time-dependent density of an *N*-electron system can be reproduced by these equations. However, as in static DFT, approximations must be made. The approximation to the time-dependent *xc*-potential $v_{xc}[n(\mathbf{r}, t)]$ needs to be made to solve the time-independent KS equations. Most commonly, and in this project, the adiabatic approximation is used to find an expression for the time-dependent *xc*-potential, discussed below.

### 2.2.5.2.4     The Adiabatic Approximation

Static DFT is in principle exact. However, an approximation is needed for the exchange correlation potential. The equivalent to the exchange-correlation potential in TDDFT would be $v_{xc}[\rho(\mathbf{r}, t)]$. The adiabatic approximation uses the *xc*-potential $v_{xc}^0$ from static DFT and applies it to the time-dependent Kohn-Sham equations, using, instead of the ground state density $\rho_0(\mathbf{r})$, the time-dependent density $\rho(\mathbf{r}, t)$ and therefore obtaining the adiabatic *xc*-potential $v_{xc}^A$.[45] This is formalised as:

$$v_{xc}^{A}(\mathbf{r}, t) = v_{xc}^{0}[\rho_0(\mathbf{r})]|_{\rho_0(\mathbf{r}) \to \rho(\mathbf{r},t)} \tag{2-40}$$

This approximation is exact when the time-dependent perturbation is slow enough that the system remains in its instantaneous eigenstate. This means that the *xc*-potential at time *t* is only dependent on the density at time *t*, i.e. no previous densities are of interest. It is said that there is 'no memory'. However, the majority of physical systems are non-adiabatic. Nevertheless, the approximation still works in most cases and is the default approximation made in most TDDFT calculations in computational chemistry.[88] However, when simulating the oscillatory motion of the nucleus, the density deforms and the system does not return to its ground state after the external field oscillates once. This means that neither the density nor the correlation potentials agree, which shows that the adiabatic approximation is not suitable in this case.[97] If the oscillation or external potential varies so rapidly that the electronic wave function cannot react fast enough and instead finds itself in quasi-stationary[**] states, then the adiabatic approximation has been shown to yield satisfactory results (even though the system is not adiabatic).[98]

### 2.2.5.2.5 The Casida Equations

Finding the TDDFT excitation energies can be expressed within linear response theory as an eigenvalue problem, as shown by Casida in 1995 and 1996.[95,99] The Casida equations, which is the most common approach to calculating excitation energies within linear response theory, involve moving an electron from an occupied KS orbital to an unoccupied KS orbital and the eigenvalue problem can be solved self-consistently in the form of a matrix problem. Within the adiabatic approximation, the eigenvalue equation is a matrix problem, as shown below:[100]

$$\begin{pmatrix} \mathbf{A} & \mathbf{B} \\ \mathbf{B}^* & \mathbf{A}^* \end{pmatrix} \begin{pmatrix} X \\ Y \end{pmatrix} = \Omega \begin{pmatrix} -1 & 0 \\ 0 & 1 \end{pmatrix} \begin{pmatrix} X \\ Y \end{pmatrix} \tag{2-41}$$

---

[**] Non-equilibrium, time-independent states

A and B are matrixes themselves, also known as the 'Orbital Rotation Hessians'[101] and $\Omega$ the diagonal matrix with the diagonal element being the square of the excitation energies. This equation results in paired excitation ($\Omega > 0$) and de-excitations ($\Omega < 0$).

In practise, the Casida equations would yield the exact excitation energies of any system, but for this to be true, certain conditions must be met, such as obtaining the exact KS ground state of the system. The fact that Casida's equation is infinite-dimensional, also leads to the necessity of approximations, and therefore not exact solutions. One issue with the application of this formalism is that it relies on non-zero transition densities, so excitations without oscillator strength might not be calculated accurately.[102]

The excitation energies obtained through Casida's approach lead to the calculation of excited state properties: the total excited state energy can be obtained by taking the sum of the ground state energy and the excitation energy. As excited state properties are calculated as the derivate of the excited state energy with respect to an external perturbation,[101] it means that any excited state property is the sum of the corresponding ground state property and an excitation part, which is the derivative of the excitation energy.[101,103]

### 2.2.5.2.6      The Tamm-Dancoff Approximation

A useful and rather efficient approximation in TDDFT is the Tamm-Dancoff approximation.[104] This formalism uses a truncated form of the Casida equation (section 2.2.5.2.5) to calculate the excitation energies. The excitation energies from the Casida equation are the square roots of the eigenvalues, which means that there are both positive negative energy solutions. The Tamm-Dancoff approximation ignores the negative energy solution from the excitation energy pair, which in practise involves setting the B matrix (equation (2-41)) to zero. Physically, this approximation neglects the de-excitation part of the excitation energy. This approximation is particularly useful if the calculation suffers from the 'triplet instability' problem.

### 2.2.6 Limitations of DFT and TDDFT

There are many chemical phenomena that (TD)DFT cannot predict accurately enough or where (TD)DFT even fails.[105] The most important issues related to the project discussed in this thesis are outlined below.

- An issue related to excited states is that the excitation energies calculated with TDDFT are usually only accurate to within ~ 0.4 eV of the experimental results, but only when using hybrid functionals – non-hybrid functionals tend to perform worse.[88,90,106,107] In fact, this accuracy typically only holds for valence states, not those involving diffuse orbitals, like Rydberg states. When these states are the basis of a (TD)DFT study, asymptotically corrected functionals such as LB94[108] or range-separated functionals such as CAM-B3LYP[64] ought to be used. This is because the standard exchange correlation functionals generally decay too quickly with inter-electronic separation: Rydberg states are weakly bound, therefore having a greater spatial extent which means that the poor long-range behaviour of the functional has a more pronounced effect, and asymptotic corrected functionals enforce the correct asymptotically behaviour.

- In addition to the above, it has been found that charge transfer (CT) excitations are often predicted by TDDFT to have excitation energies several eV below experimental values. The problem, from a computational perspective, is that electron excitations can be non-local phenomena. However, LDA and GGA functionals are local functionals, depending only on the density and its derivative(s) at a certain point, meaning that non-local excitations, such as charge transfer excitations, are not well described. Tozer and co-workers [65,87,109–111] have shown that if the overlap between the initial and final orbitals associated with the electronic excitation is too small, then TDDFT does not predict the excitation energy accurately. Functionals with high amounts of exact exchange at long distance (such as CAM-B3LYP, which has 65% of exact exchange), significantly improves the description of such CT excitations, as it improves the behaviour of the functional at long-range. The likelihood of having an accurate result with TDDFT increases when this overlap is larger but is still not guaranteed. CT problems are not uncommon and this is one issue that is addressed further within this thesis.

- The adiabatic approximation generally employed in TDDFT and the resulting lack of memory in the calculations mean that double-excited states are fundamentally not well reproduced.[87,112]

- The adiabatic approximation also means that the topology of conical intersections tend not to be very well reproduced by TDDFT. However, their location on the potential energy surface tends to be described rather well.[113–115]

- It should also be noted that (TD)DFT is a formulation of non-relativistic quantum mechanics, so calculations treating heavier elements need to include additional approximations to model relativistic effects, such as spin-orbit coupling.

### 2.2.7  Applied Quantum Chemistry

This section is concerned with the question of what a quantum chemical code actually calculates. As the Born-Oppenheimer approximation (section 2.1.4) is assumed to hold, the calculation always begins with the molecular geometry given in the input file as the coordinates for the nuclei, about which the electron density is evaluated.

#### 2.2.7.1    Single-point energy calculations

Single-point calculations are calculations with the aim of finding out the minimum, or ground state, energy of the system at a given geometry. This is nothing more than going through the SCF cycle (section 2.1.8) at a certain geometry: finding an initial guess of the electron density, and improving it iteratively until self-consistency is achieved

#### 2.2.7.2    Geometry Optimisations

Geometry optimisations are more complicated than a single-point calculation: the starting point is a set of coordinates for the nuclei. The aim of the calculation is to find the

geometry with the lowest possible energy. The starting geometry can be thought of being on a $3M$-dimensional potential energy surface, with $M$ being the number of nuclei. This potential energy surface is defined by the electronic structure, being dependent on the electronic and nuclear degrees of freedom. In the first instance, a single point energy calculation is performed on the input structure, to obtain the potential energy surface. The next step is to evaluate the gradients at the point on the energy surface (which define the internal forces acting upon the nuclei) present at that geometry. Distorting the structure slightly along the most negative gradient should lower the energy. A single point calculation is then performed on this new structure, its gradients evaluated and the structure is modified again according to the gradients. This cycle is repeated until the gradients vanish, (to within a threshold defined by the convergence criteria). There is one issue, however: the structure found might not actually be the lowest energy structure but it may be a 'local minimum' (or, a saddle point).

### 2.2.7.3    Frequency Analysis

As mentioned in the geometry optimisation section, all nuclei have forces acting upon them (however small) apart from at the extrema where the forces exactly vanish. A (vibrational) frequency analysis calculation looks at the second derivatives of the energy with respect to nuclear positions at a stationary point, and determines whether the molecule is truly at a minimum on the potential energy surface or at a different kind of extremum. To calculate the vibrational frequencies, it is assumed that the nuclei interact harmonically; the coordinates are mass-weighted and a set of eigenvalue problems is constructed for the second derivative of the energy. The square-roots of the eigenvalues are related to the vibrational frequencies. Three of these eigenvalue equations describe molecular translation (one in the $x$ direction, one in the $y$ direction, one in the $z$ direction), and three (two for linear molecules) describing molecular rotation. These six (or five for a linear molecules) should all produce an eigenvalue of zero, while all other equations should yield a real (positive) frequency eigenvalue. However, due to the fact that the frequencies are derived from the square-roots of the eigenvalues, imaginary solutions are also possible. The number of imaginary frequencies corresponds to the number of negative

second derivatives of the energy (giving information about the curvature of the potential energy surface). If exactly one imaginary frequency is present, the structure is said to be in a transition state.

### 2.2.8  Analysis Tools

#### 2.2.8.1    Mulliken and Löwdin Population Analysis

To calculate the partial atomic charges in a molecule, Mulliken population analysis [116–119] is often used. To calculate the charges of the atoms, it looks at the density matrix (the way the density is distributed over the whole molecule) and the off-diagonal gives the overlap population of two AOs. Mulliken analysis divides the overlap population in half and attributes half to each contributing AO, giving the atomic populations. To find the total population for each AO, all of the attributed overlap population is summed up for each AO. To find the partial charges, all of the atomic populations corresponding to one atom are added and from that, the nuclear charge is subtracted. Mulliken population analysis suffers from several problems, such as a strong dependence on the basis set used for the calculation, and its result sometimes seem unphysical. However, due to its simplicity of implementation, it is still widely used and usually yields qualitatively correct trends. However, its numerical values should not be trusted.

Löwdin analysis[120] is very similar to Mulliken analysis but its main advantage is that it employs an orthogonal basis set while calculating the partial charges, which improves on the results somewhat. Although both methodologies are dependent on the basis set employed in the calculation.

#### 2.2.8.2    Natural Bond Orbitals Analysis

The idea behind the Natural Bond Orbital (NBO) model [121] is that the density matrix of the system of interest can be divided into atomic blocks, each of which is diagonalised to give a set of natural atomic orbitals, NAOs. Taking a linear combination of these NAOs

is thought of as 'catching the essence of bonding': the density matrix is re-expressed in terms of these NAOs and re-diagonalised in order to obtain the NBOs. The NBOs with the highest occupation can be associated with the localised electron pairs associated with the Lewis model. In this way the electron population associated with each atom can be more accurately described than with Mulliken Population Analysis.

### 2.2.8.3    Quantum Theory of Atoms and Molecules

Quantum Theory of Atoms and Molecules (QTAIM or AIM) is a topological method of analysis derived by Richard Bader[122–124] and is thought to be a very rigorous way of describing the electron density. Orbitals are not considered and the system is only studied in terms of its electron density. Maxima in electron density are called attractors and tend to coincide with nuclei. Bader stated that the only necessary and sufficient condition for a chemical bond to be present is a bond path, so a path of maximum electron density between two 'attractors'. The point of lowest electron density along a bond path is called a 'bond critical point', if it lies on the interatomic surface. Properties of the electron topology are derived for ring and cage critical points (the latter being a minima in the electron density). The bond critical points can give information about the bonding interactions, in particular their degree of covalency.

### 2.2.8.4    Lambda ($\Lambda$) Analysis

This analysis tool was devised by Peach *et al.*[89,125] to identify potentially problematic charge-transfer excitation. It is a measure of the spatial overlap between the occupied and unoccupied Kohn-Sham orbitals contributing to an excitation. A $\Lambda$ value of 0 corresponds to no overlap and 1 to complete overlap. A quantitative measure for CT has been devised using the B3LYP *xc*-functional, with any excitation resulting in a $\Lambda$ value below 0.3 certain to suffer from the CT problem. This means that, using TDDFT, the excitation is problematic to describe using *xc*-functionals with no or low HF exchange. In contrast, any value above 0.3 suggests that the excitation is not problematic due to (lack of) overlap,

but TDDFT might still not describe this excitation accurately. However, this numerical cut-off has been formulated for organic systems, and past studies[126–128] show that this number might need to be adapted depending on the system, including inorganic materials. It should also be noted that this number has only been devised with and for the B3LYP functional; other functionals have been tested and a link between $\Lambda$ and CT character has been established, but this is not investigated, and applied, further in this study.

### 2.2.9  Codes

#### 2.2.9.1    *TURBOMOLE*

TURBOMOLE[129,130] is a quantum chemistry package which offers a range of molecular calculation options, including DFT and TDDFT. It uses Gaussian type orbitals (as discussed in section 2.2.4.2.2.2). This package contains excited state gradients for many commonly used functionals, which is needed for this study.

#### 2.2.9.2    *GAMESS-US*

GAMESS-US[131,132] is, like TURBOMOLE, capable of different types of molecular calculations. However, this code generally required more computing resources than TURBOMOLE. Yet, GAMESS-US was used because it allows for calculations using the range-separated CAM-B3LYP[64] functional (section 2.2.4.2.1) and as well as obtaining $\Lambda$ values, neither being available within the TURBOMOLE package. GAMESS-US uses, like TURBOMOLE, Gaussian type orbitals.

#### 2.2.9.3    *DGrid*

This programme[133] is used to calculate QTAIM properties. It uses slightly modified TURBOMOLE output files as input.

### 2.2.9.4    Others

The VMD (Visual Molecular Dynamics) package[134] is used for visualisation of clusters, orbitals and electron densities. A custom made script by Enrico Berardo has been used to create absorption spectra. This script performs the following task: it takes the excitation energies and their oscillator strengths and describes these in terms of Gaussian function centred on the value of each excitation energy: the width of the Gaussians can be customised.

# 3. Literature Review

The aim of this chapter is to provide a discussion of previous work performed on the systems studied, as well as defining the approach used in tackling outstanding problems.

## 3.1 Previous Work

After the discussion of the basic concepts that this research is founded upon in the introductory chapter, the previous research that has been completed on these and similar systems can be presented. The focus of this work is on computing the photophysical properties of nanoparticles and nanoclusters, so an experimental overview must be given to put this work into context. As MgO, which is the focus of the research described in this thesis, is a computationally well-studied system due to relatively low mass of the constituting atoms (which means fewer electrons to take into account), its closed shell electronic structure and its rocksalt morphology, an overview of previous computational research is also given.

Computational limitations meant that the largest systems that was studied in most detail has the chemical formula $(MgO)_{32}$, which is a cube with approximate side lengths of 0.6 Å, and so the experimental results most relevant to this thesis are those obtained from studies on as small systems as possible since the size of the particle can determine the absorption and emission behaviour.

### 3.1.1 Magnesium oxide

#### 3.1.1.1 Experimental studies

The experimental literature regarding MgO and other nanoparticles is vast and cannot be covered fully here. The interested reader is directed to references 135–145 and references

therein for a more complete review. Here, the focus is on experimental work most amenable to comparison with the simulations reported in this thesis.

Nanoparticles are of particular interest when it comes to their interaction with light. Semiconductors generally adhere to general excitation behaviour as follows: due to the effect of quantum confinement, the excitation energy increases as the size of the particle decreases.[146] This effect only becomes apparent when the electron and hole are confined in a space that is close to the exciton Bohr radius (the separation of the electron-hole pair): in this situation, the valence and conductions bands transition from continuous bands into discrete energy levels, which widens the band gap. However, the excitation behaviour in insulator materials, such as MgO, is different: the energy required to create an exciton (an electron-hole pair) in the bulk is typically much larger than in particles with a high surface-to-volume ratio, due to fewer unsaturated surface atoms in the former. This means that the energy required to photo-excite an electron can be much lower in a nanoparticle.[15] Bulk MgO crystals exhibit absorption starting at only 7.68 eV [147] but this is not the case for MgO nanoparticles. It has been proposed that the energy required to excite an electron from an anion to its immediate surroundings is dependent on the coordination number of the anion ($O^{2-}$ in the case of MgO) - i.e. the more nearest neighbours an anion has, the higher the excitation energy.[148] This also means that corner site anions are the first sites to be excited compared to edge, face or bulk sites.

MgO nanoparticles intended for use in photoluminescence can be produced in two different ways: either through the decomposition of hydroxides and carbonates [148] or via Chemical Vapour Deposition (CVD), both under vacuum conditions (or via annealing under vacuum) so that there are a larger number of under-coordinated surface sites available.[149] CVD is a clean, solvent-free approach that can offer a good amount of control over the particle, its size and potential dopants.[19,21] Furthermore, CVD does not require expensive equipment in itself.

In the case of MgO, CVD can produce particles with the cubic rocksalt structure, which has been shown to be the most stable conformation.[150–153] This demonstrates that MgO takes on its bulk crystalline structure, even in smaller samples. The nanoparticles are created using a flow system:[154] high purity magnesium is added to a carrier gas (often

argon or other inert gas) and is then brought into contact with oxygen gas (or another oxygen carrier). Then, with the aid of the carrier gas, this is added to the reaction chamber where the MgO nanoparticles deposit onto a chemically inert surface. To avoid any surface contamination of the samples themselves, they are annealed to around 1173 K, in a high vacuum of pressure below 1 x $10^{-5}$ mbar.[20] Subsequent photon absorption experiments, such as UV diffuse reflectance spectra and the photoluminescence spectra, are normally performed at room temperature but in vacuum. To test that the recorded spectra do not show any unwanted photoluminescence (i.e. that the light emitted by the particles is not re-absorbed and leads to further photoluminescence), gaseous oxygen is added to the reaction chamber and this quenches the photoluminescence from emitted light. This means that all photoluminescence recorded occurs on surface sites, and no photoluminescence arises from photo-emitted light during the process. Furthermore, gaseous oxygen can also be added at the stage of the photon absorption measurements, to ensure that no photoluminescence is recorded within the absorption spectrum.

Stankic et al.[148,149] find, using CVD methods outlined above, that the average particle size for MgO is about 3 to 5 nm (depending on the experimental conditions), with a cubic morphology (see figure 3-1) and the (*100*) and symmetry equivalent planes usually exposed. Under certain conditions, e.g. with the use of $N_2O$ as an oxidising agent, Stankic et al.[20] show that it is possible to synthesise MgO nanocubes which have edge lengths as short as 2 nm. Despite the fact that these clusters can be synthesised, they are unstable and very reactive due to their high surface area.[15] It is, of course, possible to produce larger particles: Mageshwari et al.[155] use a reflux-condensation approach to synthesising MgO nanoparticles. However, these experiments offer less control over the final product and the optical properties are less defined: the absorption spectra show a peak between 5.39 eV and 6.20 eV (200 - 230 nm) and the photoluminescence spectrum for samples with an average crystalline size of 6 nm show peaks as low as 464 nm (2.67 eV), whereas samples of 8 nm size exhibit peaks from 454 nm (2.73 eV). Both samples exhibit very similar luminescence spectra. However, the authors themselves attribute these peaks with defects sites, such as oxygen vacancies, indicating that these samples are less clean than the CVD samples produced by Stankic et al. This shows that it is imperative to choose the experimental data the computational model is trying to reproduce carefully.
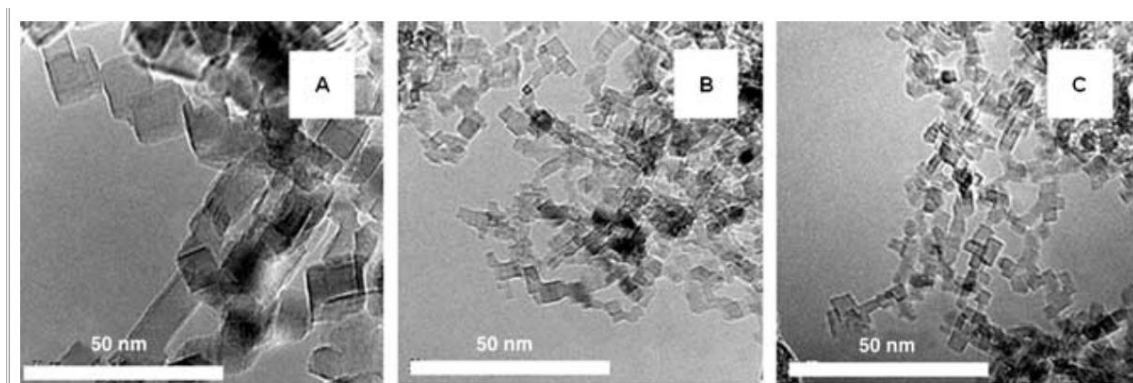
**Figure 3-1:** Transition electron microscope images of differently sized MgO nanoparticles: A shows particles with an average length of 10 nm, B of 5 nm and C of 3 nm. All have cubic morphologies. Reproduced from reference 20.
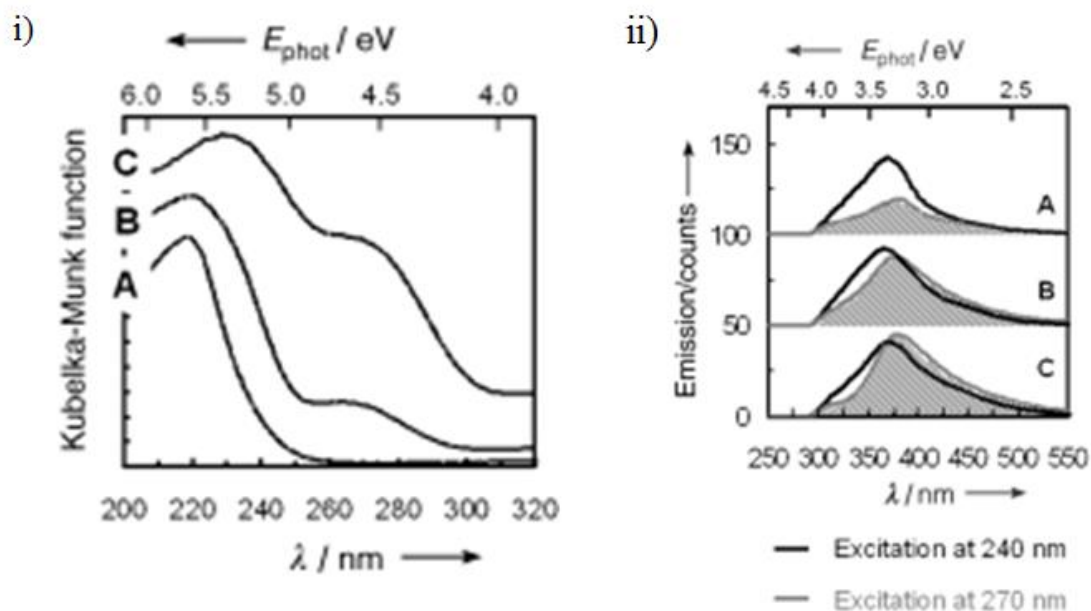


**Figure 3-2:** i) The reflectance spectra and ii) the photoluminescence spectra for three different MgO nanoparticles: sample A is 10 nm long, sample B 5nm and sample C 3nm, at two different excitation energies: 5.2 eV (240 nm) and 4.6 eV (270 nm). Both reproduced from reference 20.

The particles synthesized by Stankic *et al.*[20] with an average length of 3 nm (sample C in figure 3-1), show absorption peaks at both 4.4 eV and 5.4 eV (figure 3-2 i)[20]. The authors

attribute the lower excitation to 'corner' excitations and the higher one to 'edge' excitations, electronic excitations from 3- and 4-coordinated oxygen anions, respectively. This assignment has been inferred from the relative intensities of the peaks on the differently sized particles: the smaller particles have relatively more corner atoms, therefore the peak, which disappears for the larger particles, is presumed to be due to corner excitation, which gets masked as the intensity of the 4-coordinated excitation increases. From a theoretical point of view, this is overly simplistic, as any excitation involves more than one site, as has been shown in computational studies.[127,156]

Stankic et al.[20] found that the 3 nm MgO particles, obtained through CVD, give rise to particular peaks in the photoluminescence spectrum. The photoluminescence spectrum is dependent on the energy of the light used to excite an electron: if an excitation energy of 5.2 eV (240 nm) is used, the resulting photoluminescence spectrum shows a broad emission band which has a full widths at half maximum (FWHMs) of 0.8 eV. The peak value is found at 3.4 eV (370 nm), a value reported previously.[151,157–159] This corresponds to a Stokes shift (the difference between the excitation and luminescence energy) of 1.8 eV. A second luminescence peak can also be observed in these 3 nm - sized particles from Stankic et al.,[20] at 3.3 eV (380 nm), observed when an excitation energy of 4.6 eV (270 nm) is used. This peak is also part of a broad emission band, with FWHM of 0.8 eV. It should be noted that the both photoluminescence spectra are asymmetric, and some luminescence can be detected as low as 500 nm (~ 2.47 eV), which might explain the general low luminescence behaviour discussed in chapter 7.

The broadness of the photoluminescence spectra can be seen in figure 3-2 ii. A fundamental issue here is that computational simulations only give a single value; the value of the lowest possible luminescence energy. This is due to the fact that only the potential energy surface of the lowest excited state can be defined explicitly at all points: if, for example, the surface of the 6$^{th}$ excited state (at the ground state structure) were to be followed and it were to cross with the 5$^{th}$ excited energy surface, then the simulation would then follow the formerly 5$^{th}$-lowest surface, although the formerly 6$^{th}$ lowest (and now 5$^{th}$ lowest surface) should be followed. This problem is not present in excitation energy calculations, as, in principle, any excitation can be calculated, allowing full

absorption spectra to be modelled. So how can a luminescence spectrum be computationally predicted? How can the experimental and computational values be compared? Comparison is extremely difficult: does the broad peak in the experimental luminescence spectrum stem from different excited states (i.e. in a deviation from Kasha's rule) or are there different minima on the lowest potential energy surface from which emission occurs? Throughout this thesis, it will be assumed that Kasha's rule (section 1.3) is applicable to these systems, and results will be considered within the limitations defined by the methodology.

### 3.1.1.2    *Computational Studies*

A number of previous computational studies have been performed on similar clusters. However, the approach taken in previous work has been significantly different to that presented in this thesis: the emphasis has been on maximising cluster size and, to increase this, a methodology often referred to as QM/MM[160] (quantum mechanics/ molecular mechanics), has been used. This methodology has been hugely important in advancing computational chemistry and three of its developers were awarded the Nobel Prize for Chemistry in 2013. The approach has its basis in the fact that the chemically most relevant part of a large system (e.g. the polar region of a protein or the surface of an adsorbing material) can be modelled quantum mechanically (using, e.g. DFT) and the remainder of the system, which is not expected to play a chemically important role, can be modelled using molecular mechanics (a computationally cheaper approach, using empirical or parametrised force fields). As the part of a system treated quantum mechanically can be thought of as a cluster, and this cluster is 'embedded' into a molecular mechanical system, this method is also known as an 'Embedded Cluster' method, as visualised in figure 3-3. One major problem with this approach is that it restricts the description of the excitations modelled: by only modelling one area quantum mechanically, the chemistry is restricted to this part of the cluster (usually a region surrounding a corner site when studying MgO particles); no overall delocalisation of the electron density is possible. It is obvious that this approach is only suitable for systems where the excitation is limited to a region small enough that it can be fully described within the quantum mechanical cluster.

Shluger *et al.*[161] considered different quantum mechanical clusters of up to 12 atoms within a larger molecular mechanical cluster, giving a total of 512 atoms and looked into the effect of changing the site of the quantum cluster within the larger cluster (i.e. comparing corner, edge, etc. sites) and the resulting absorption spectra. The quantum mechanical clusters differ in their location and arrangement within the larger cluster: a cubic edge site was described using 8 atoms, and this same sized cube was also located in the bulk. Further, linear edge sites were described quantum mechanically: terrace sites were also considered. The quantum mechanical clusters were described using the all-electron 6-311+$G$ basis sets within the Hartree-Fock approximation. The rest of the particle was described using pair potentials of non-polarisable ions, with a layer of atoms described by pseudopotential between the quantum cluster and the rest, as to avoid artificial polarisation of the density due to the point charges. Excitation energies were calculated using the Configuration Interaction Singles (CIS) approach, as well as the difference between the triplet and singlet energy states, as calculated using Configuration Interaction Singles and Doubles (CISD). These calculations support the experimental assignment of excitations from 3-coordinated ions at 4.9 eV and 4-coordinated excitations at 5.6 eV, in agreement with Garrone *et al.*[162]

Trevisanutto *et al.*[163] used a QM cluster of 26 atoms, centred on an oxygen corner, using DFT, the 6-31G basis set and the B3LYP exchange-correlation functional. Excitation energies were calculated using TDDFT, as well as the difference between the triplet and singlet state (using Δ-SCF). The authors claimed that the use of a larger QM cluster or more flexible basis sets does not affect the results for excitation energies considerably. The rest of the cluster, which incorporated 1000 ions in total, was modelled using inter-atomic potentials. An interface region was also defined using pseudo-potentials for the 48 Mg ions nearest to the QM cluster. The results showed that the hole is mainly localised on the corner oxygen and the electron is mainly localised on the magnesium ions nearest the oxygen corners. The aim of the paper was to find a process which described the desorption of an oxygen corner atom: the corner oxygen absorbs a photon of energy equal to 4.7 eV, which results in an exciton localised over the corner oxygen and neighbouring ions. This exciton is allowed to relax on the triplet surface, and becomes an asymmetrically localised exciton. After absorption of a second 4.7 eV photon, the oxygen corner desorbs. Of course,

this work is looking at a singlet to triplet excitation (through the Δ-SCF) to model a singlet to singlet excitation, so it should be borne in mind that the numerical solution might not actually yield a correct physical description of the excitation and de-excitation process.

Trevisanutto et al.[164] looked into the desorption properties further using the above mentioned methodology, and also applies the same approach to study CaO clusters. The kinetic energy of the desorbed oxygen is calculated to be about 0.5 eV, after its bond to the cation has been broken through light absorption. The researchers noted that the TDDFT results may not be sufficient in describing all of the properties of the clusters, due to potential issues with charge-transfer transitions, and suggest that more accurate methods should be used when modelling the QM cluster. However, the research by Trevisanutto et al.[164] showed that surface modification in MgO and CaO via relatively low-energy photon absorption is possible.

Müller et al.[156] have performed a combined experimental and computational study into site-specific hydroxylation of MgO nanocubes. Particles of sizes ranging from 3-10 nm have been synthesised using CVD, as described above. The computational approach was the same as described for Trevisanutto et al.[163] and the QM corner oxygen was hydroxylated. Both the clean and hydroxylated particles show absorption at 4.6 eV, which brought the authors to the conclusion that 4-coordinated atoms, i.e. the edge sites directly linked to the corner oxygen, are involved in the absorption. This hypothesis was confirmed by computation. The photoluminescence spectra of hydroxylated and non-hydroxylated MgO was compared, assuming excitation at 4.6 eV: both spectra are asymmetric, but the hydroxylated spectrum is more intense and shows a peak at 2.9 eV compared to 3.2 eV for the clean cluster, but the feature ranges from 2 to 4 eV. The photoluminescence was calculated using the Δ-SCF approach. The non-protonated cluster is predicted to exhibit photoluminescence at 2.6 eV, compared to 2.3 eV for the cluster with protonated corner oxygens. These computed predictions correspond to the lowest transition and not the most intense but seem to be in agreement with experimental observation.

Sushko et al.[165] reported photoluminescence further, using the same experimental and theoretical approach as above, although the QM cluster contained 14 Mg ions and 13 O ions. The QM cluster was also modelled using CIS and corrected using CISD. The

excitation results match experiments rather well, predicting absorption at 4.5 eV for 'corner' (compared to 4.6 eV experimentally) and 5.7 eV for edge excitations (5.7 eV experimentally, although this can decrease to 5.3 eV as the edge length decreases). The photoluminescence was calculated using the Δ-SCF approach, and when the triplet state was allowed to relax symmetrically, photoluminescence was predicted to occur at 2.6 eV (3.2 eV experimentally), but when the corner site is allowed to relax further (anti-symmetrically), the photo-emission lowers to approximately 1 eV. This approach has also been applied to other materials, namely CaO, SrO and BaO (discussed below).

Sternig *et al.*[166] have also compared the experimental photoluminescence spectra to the results obtained from the coupled cluster approach, described above. The photoluminescence energy has been calculated using a delta-SCF type approach (using the difference between $T_1$ and $S_0$) and was found to be 2.6 eV.[165] This has been calculated as the difference between the total energies of the singlet and triplet states. Although the calculated value of 2.6 eV is in reasonable agreement to the experimental peak value of 3.2 eV (based on an excitation energy of 4.6 eV, and photoluminescence can be as low at 2 eV), it does not seem to be a wholly accurate representation of the physics behind the process: the closed-shell nature of this system in addition to the relatively low mass of the atomic components means that little spin-orbit coupling is expected for this material, which means that no, or very little, phosphorescence would occur. However, the excited triplet state (with both unpaired electrons having the same spin) might be similar in energy to the lowest excited singlet state (with electrons having opposite spin), so this is an approximation which might be quantitatively satisfactory.
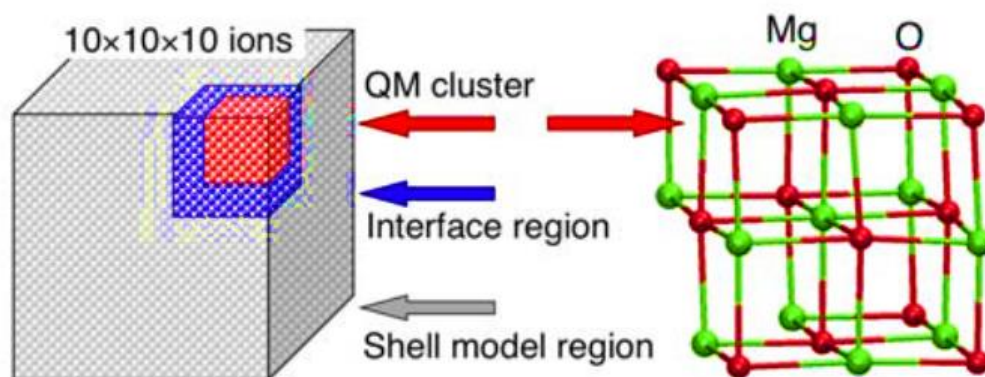
**Figure 3-3:** An example set-up of an embedded cluster calculation: the grey area shows the part of the model which is treated by molecular mechanics, the blue region is an interface region, which is needed to stabilise the calculation, and the red region is the area representing the quantum mechanical cluster. This cluster is shown in more detail on the right. Reproduced from reference 165.

The problem with the embedded cluster calculations described above is that they force the exciton to be localised on just the quantum mechanical cluster comprising of 26 atoms (in figure 3-3). However, when full DFT calculations are performed, it is found that the exciton delocalises over the entire cluster, especially when the B3LYP exchange-correlation functional is used.[127] Furthermore, the proposed match to experimental spectra might not actually be valid: McKenna *et al.*,[167] using the embedded cluster method, with 1000 atoms as described above and a 26-atom QM cluster described using B3LYP and the 6-311G* basis set, predicted, using TDDFT, two major absorption peaks, at 3.7 eV and 4.7 eV (figure 3-4). As the 4.7 eV peak is very close to the experimentally observed peak at 4.6 eV, it was hypothesised that the predicted peak at 3.7 eV is a 'dark' excitation, or is at least too weak to be observed experimentally. However, Wobbe *et al.* have shown that DFT typically underestimates the energy of charge transfer excitations and that MgO excitations, when modelled using B3LYP, suffer from poor overlap, meaning that the agreement with experiment may be coincidental, i.e. the predicted 3.7 eV excitation is actually an under-prediction of the experimental 4.6 eV excitation, further discusses in chapter 5.
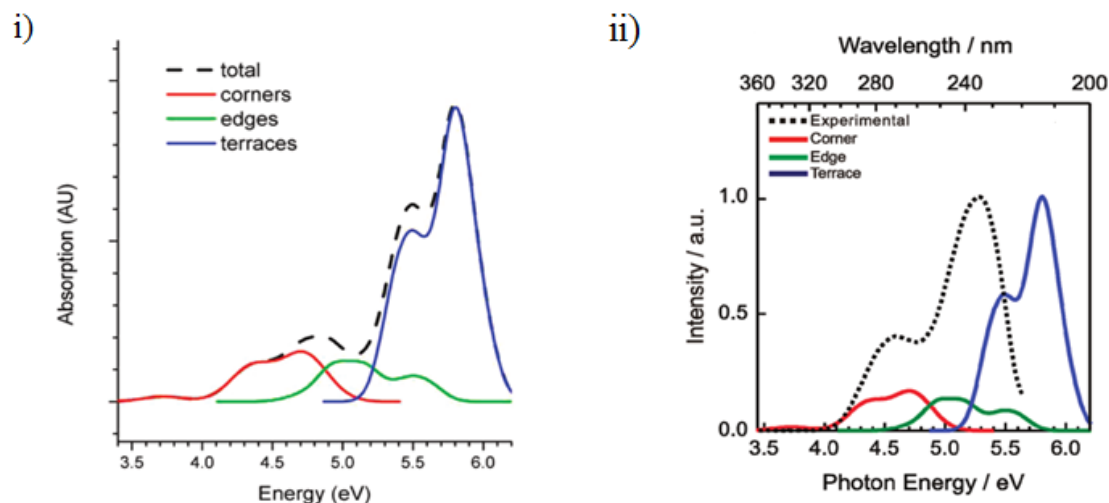
**Figure 3-4:** i) Calculated absorption spectra for MgO nanoparticles, using the embedded cluster method. Reproduced from reference 167, ii) Calculated absorption spectra compared to experimental results. Reproduced from reference 166.

### 3.1.1.3 Other Nanoparticles with the rocksalt structure

This work does not only comprise a study of MgO but also investigates excitations of other nanoparticles which exist in the rocksalt configuration, namely CaO, SrO, BaO, MgS, MgSe, CdO and PbS. Unfortunately, none of these materials exhibit the regular cubic nanoscale structure found in MgO. Below, this is further discussed for each material.

### 3.1.1.4 CaO

Glascock *et al.*[168] have studied the absorption spectrum of thin-film CaO, and have found that the lowest absorption peak, in the energy range of 5.5 − 11.3 eV, is at 7.0 eV. However, the same spectrum showed peaks at higher energy that, according to Whited *et al.*[169] are not reproducible, and the latter team have found that, using crystalline CaO, an absorption peak at room temperature is found at 6.8 eV is found. Zecchina *et al.*[170] have measured the reflectance spectrum of CaO, and have found that fluorescence must be quenched with outgassing of the reaction chambers with molecular oxygen. The

reflectance spectrum shows absorption at energies above 40000 cm$^{-1}$ (4.95 eV), which is in-line with previous work from Whited *et al.*[169] These studies have shown that bulk CaO has an absorption peak at 6.80 eV (compared to 7.68 eV for MgO). On the nanoscale, however, CaO is less easy to study than MgO: unlike the cubic structure found in CVD-MgO, Sternig *et al.*[19] have shown that CVD-CaO undergoes coalescence, resulting in nanoparticles with a diameter of around 27 nm (figure 3-5).[19] The peak of the excitation spectrum is centred around 325 nm (3.81 eV) whereas luminescence after excitation using a 282 nm (4.40 eV) light source is observed around a peak at 416 nm (2.98 eV). This corresponds to a Stokes shift of 0.83 eV. CaO therefore exhibits photoluminescence in the visible spectrum (~ 1.7 – 3.1 eV), showing its potential as a nanomaterial that can be used for optical applications.
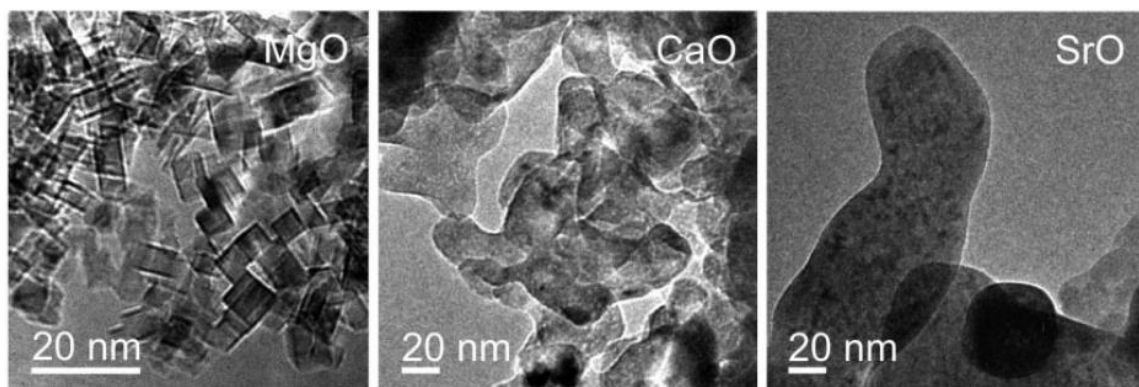


**Figure 3-5:** The difference in morphology between MgO, CaO and SrO. Reproduced from reference 19.

### 3.1.1.5    SrO

Sternig *et al.*[19] have shown that CVD-SrO nanoparticles completely lose the well-defined cubic topology found for MgO, as seen in figure 3-5: the SrO particles are between 20 and 200 nm in size. These SrO particles have been studied using transmission electron miscroscopy (TEM) and it has been shown that the individual grains are made up of several nanocrystals, which have colesced. The lowest absorption peak is centred at 340

nm (3.65 eV), and the photoluminescence spectrum shows a peak at 2.55 eV (486 nm) when incident radiation of 318 nm (3.90 eV) is used. Stankic et al.[171] studied the photoluminescence of the same CVD-SrO nanoparticles (referred to as 'polycrystals'), and have found that use of a lightsource of 3.5 eV also results in an emission peak at 2.55 eV. This work on SrO is an expansion of the work by Coluccia et al.[151], who have prepared SrO samples in vacuum which show an absorption peak at 3.96 eV and photoluminescence at 2.64 eV. Similarly to CaO, the luminescence energies of the nanoparticles are in the visible spectrum, which means that these would also be potential candidates for optical applications. The band gap for bulk SrO is 5.68 eV,[172,173] which is higher than the values obtained for nanoparticles. This follows the same trend as found in MgO and CaO particles.

### 3.1.1.6    BaO

No experimental studies of pure BaO nanoparticles are known to the author, and it has been suggested that these are not thermodynamically stable due to coalescence into millimeter-sized grains, which has been shown using TEM.[19] However, Zecchina et al.[147] have observed absorption maxima at 4.15 eV and 4.34 eV for bulk BaO, which has been prepared by decomposition of $BaCO_3$ (as $Ba(OH)_2$ melts before decomposition can take place). Coluccia et al.[151] have studied BaO samples further, and found that photoluminescene at 2.67 eV occurs when a light source of 4.59 eV (270 nm) is used.

### 3.1.1.7    MgS and MgSe

Another pathway of investigation within this project was to replace the oxygen in MgO by other chalcogens, namely S and Se. One important condition was that, for the sake of comparison,  the clusters should crystallise in the rocksalt structure, as alkaline earth oxides do. Unfortunately, no literature regarding MgS or MgSe nanoparticles small enough for comparison to the calculations performed could be found by the author. However, computational work studying the phase stability of MgS and MgSe is available.

This is interesting in terms of the study discussed in chapter 6: only materials that crystallise in the rocksalt structure are of interest within this thesis. Rabah et al.[174] have computationally studied both MgS and MgSe, using the scalar-relativistic full potential linear-augmented plane wave method (FP-LAPW) within the local spin density approximation (LSDA) and find that the total energies are lower in the rocksalt configuration when compared to the zinc blende structure, although the energy gap between the two topologies is smaller in MgSe (~0.04 eV) than it is for MgS (~0.14 eV). However, under certain conditions, as Okuyama et al.[175] have shown experimentally through epitaxial growth, both materials grow as films with zinc blende structure on GaAs using molecular beam epitaxy. It is obvious then that the energetic differences calculated by Rabah et al. are not definitive in terms of predicting the lowest energy conformation, and care must be taken not to put too much trust into these calculations, especially considering the small energy differences: the result of 0.04 eV difference obtained for MgSe (and arguably also 0.14 eV for MgS) in total energies is not big enough to draw any conclusion. Another computational study by Drief et al.[176] using the LDA and the FP-LAPW model confirmed that for MgS the rocksalt structure is about 0.2 eV more stable than the zinc blende form, but also calculated the energy for the MgSe zinc blende structure to be ~0.15 eV lower in energy when compared to the rocksalt form. Finally, Gökoğlu et al.[177] have investigated the energetics of these systems using DFT with projector augmented waves (PAW) using both GGA and LDA functionals. As with the two previous studies, the case for MgS is simpler, and both LDA- and GGA-DFT predict the rocksalt structure to be lowest in energy, by 0.049 eV and 0.006 eV respectively. The latter energy difference is so small that is neglible. For MgSe, LDA predicts the rocksalt structure to be 0.017 eV lower than the NiAs structure[††], whereas GGA-DFT predicts the wurtzite configuration to be lowest, and lower than the rocksalt one by 0.037 eV. Again, the energy differences are so small, and possibly even smaller than the accuracy of the calculation, that it seems to be challenging to determine the true ground state structure of MgSe. Despite this, MgSe is still included in this study, as, based on the data presented

---

[††] This structure is built in the following way: The anions (arsenide / chalcogen) are arranged in a hexagonal close-packed structure and the centre of these hexagons are filled with the metal (nickel / magnesium).

above, it is not unreasonable to assume that the rocksalt conformation to be a low energy structure for MgSe.

### 3.1.1.8    CdO and PbS

CdO and PbS are both semiconductor materials that crystallise in the rocksalt structure,[178–180] and are therfore interesting materials to contrast the behaviour seen for alkaline earth oxides and magnesium chalcogenides.

Kaviyarasu et al.[181] have synthesised CdO nanoparticles by placing cadmiun nitrate and NaOH into a beaker and dried at 90 ˚C in vacuum in a solvothermal recrystallisation approach. The samples coalesce into an average size of 50 nm. The optical absorption spectrum shows a low intensity peak at $3.35 - 3.75$ eV ($330 - 370$ nm) and several more intense peaks from $4.95$ eV $- 6.19$ eV ($200 - 250$ nm), although these are not seperable from each other and might be, in part at least, from impurities. It does not seem apparent how impure these samples are and what properties are due to these impurities. The author is not aware of any other pure CdO naoparticles study or photoluminescence data.

Lü et al.[182] have synthezised PbS nanoparticles in DMSO solvent, where the particles aggregrate into clusters with a diamater of less than 10 nm, although the particles are then added to polythiourethane (PTU) to form composite films and further analysis has been performed on said film rather than on the particles. However, Pawar et al.[183] have deposited a thin film of PbS onto a soda-lime substrate, via chemical bath deposition. This method works in the following way: a precursor solution is made, in which the substrate is immersed for a set priod of time. The tresulting thin-films obtained in the study by Pawar et al.[183] were at least 712 nm thick, although individual particles of $23 - 34$ nm were seen using scanning electron microscopy. The optical properties of these structures is interesting, as the authors observe the effects of quantum confinement: the thicker the thin-film, the lower the absorption onset measured. The thinnest film exhibits an absorption onset at approximately 1.55 eV (800 nm), whereas the thickest film shows this at 0.99 eV (1250 nm). The photoluminescence spectra is very similar for all samples, and

the only change between the spectra is the intensity of the peaks: excitation with a 2.98 eV (214 nm) photon result in twin peaks at 3.06 eV (405 nm) and 3.15 eV (393 nm), as well as a low intensity peak at 2.69 eV (460 nm), which means that the samples should emit blue light. Similar photoluminescence has been observed previously by Cao *et al.*[184] on particles of aproximately 60 nm.

### 3.1.1.9 General Remarks

As experimental absorption data is not always available, a comparison to the experimental band gap for bulk particles is used to determine whether the simulations presented in chapter 6 are reasonable. We find that as either the anion or cation increases in atomic mass, the band gap decreases. The experimental values used for comparison are as follows: 7.8 eV for MgO,[172,185] 7.1 eV for CaO,[172,186] 5.9 eV for SrO,[172] 4.3 for BaO,[172,187] 4.6 eV for MgS,[175,188] 4.0 eV for MgSe,[189] 2.3 eV for CdO,[178,187] and 0.4 for eV PbS[179]. Furthermore, as Catlow *et al.*[190] have concluded from the work of Penn,[191] Phillips[192–195] and van Vechten,[196] that the values of the optical dielectric constant‡‡ of the bulk material in question, are linked to the electronic band structure and therefore, also the extent of iconicity of the chemical bond. In addition, these constant can also help the prediction on the (de)localisation behaviour of an excitation, as hypothesised in chapter 6: the optical dielectric constant determines the extent of the electronic interaction between electron and hole is screened: alkaline earth oxides have a rather low optical dielectric constant (MgO 3.0; CaO; 3.3; SrO 3.2-3.5)[196,197] and seem to yield a very localised excitation behaviour, whereas magnesium chalcogens have been found to have a higher optical dielectric constant (MgS 5.1; MgSe 5.9)[196] giving rise to more delocalised excitation behaviour, and thus not suffering from the CT-problem as much as alkaline earth oxides. The transition metal chalcogenides and semiconductors CdO and PbS, which exhibit a delocalised excited state and therefore do not seem to suffer from CT-behaviour at all, are made of

---

‡‡ A measure of the coulomb interaction of the point charges, specifically how much the Coulomb interaction of the point charges in a material decreases relative to vacuum.

materials which have a higher optical dielectric constant values at 5.5 – 6.2 and 17.2 for CdO and PbS respectively.[196,198]

## 3.1.2 Doped MgO nanoparticles

Another pathway of investigation are doped MgO particles, where one or more $Mg^{2+}$ cation is replaced by another alkaline earth element (Be, Ca, Sr, Ba) or $Zn^{2+}$ and $Cd^{2+}$, although experimental data is only available for some. A large amount of previous research has focussed on Lithium doped MgO (see, for example, references 16,17,145,199) due to its potential in catalysis but this is not the focus of this thesis: neither are the studies of doped single-crystals[200–203] or ceramic materials[204,205], neither of which are nanoparticles.

Doping is interesting, as it can change the optical properties of a material, which in the case of MgO nanoparticles can be intriguing: MgO particles are cheap to prepare via CVD, but their optical applications are limited as their photoluminescence is not in the visible region. However, MgO particles have advantages over CaO or SrO in that their structure is consistent and relatively easy to predict, whereas the other particles have a less well-defined morphology. Doping can be achieved within CVD by altering the chemical composition of the input into the reaction chamber: in addition to a magnesium and oxygen source, another inlet is needed to carry the dopant into the reaction chamber.[206]

### 3.1.2.1 Ca-doped MgO

Kohan *et al.*[207] have shown that, from a thermodynamic perspective for the infinite bulk, ordered Ca-doped MgO particles are unstable, and Müller *et al.*[208] have studied CaO nanoparticles on top of MgO nanoparticles. However, Stankic *et al.*[149] have shown that Ca-doping of MgO is possible on the nanoscale using CVD. Tran *et al.*[209] have synthesised Ca-doped MgO samples that are highly transparent by spark plasma sintering. A computational study by Sushko *et al.*[165] using the embedded cluster methodology

described previously, reveals that the dopant can occupy 3-coordinates sites (corners), 4-coordinated sites (edges) and 5 coordinate sites, although the dopant tends to aggregate at the lower coordination sites. Sternig *et al.*[19] have produced Ca-doped MgO and have found that up to 10% substitution is possible in nanoparticles, although this results in particles with less regular size distribution compared to pure MgO.

The absorption spectra of the samples made by Stankic *et al.*[149] have been compared to those obtained from pure MgO and CaO (both found in e.g. reference 19): MgO absorption spectra show peaks around 4.6, 5.5 eV and 6.6 eV, whereas for pure CaO three peaks can also be seen, namely at 3.8 eV, 4.4 eV and 5.3 eV. The doped materials with stoichiometry of $Ca_{0.1}Mg_{0.9}O$, share the peak at 5.3 eV with pure CaO particles, but the peak is broad, with no other distinct peaks. The absorption onset is at 3.6 eV, which is lower than that of MgO, so the decrease in excitation energies predicted computationally[165] using embedded cluster (and $\Delta$-SCF)) calculations can also be seen experimentally. The absorption spectra can be seen in figure 3-6.

The photoluminescence of the doped particles synthesised by Stankic *et al.*[149] is more intense than that for pure MgO when an excitation wavelength of 290 nm (4.28 eV) is used. The resulting peak is around 425 nm (2.92 eV) but, as is the case for the pure materials, is broad, ranging from approximately 2.25 – 3.54 eV, overlapping with the visible spectrum and with a photoluminescence onset at approximately 575 nm (2.16 eV).[149]
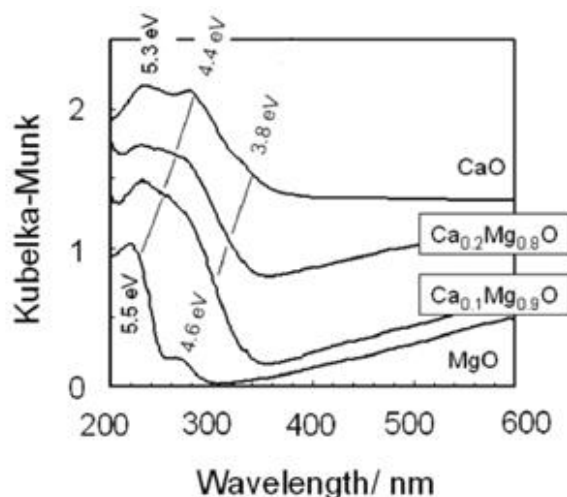
**Figure 3-6:** Showing the absorption spectra for pure MgO, pure CaO and two stoichiometrically different Ca-doped MgO nanoparticles. Adapted from reference 149.

### 3.1.2.2    Sr- and Ba-doped MgO

As well as calcium ions, other alkaline earth oxide ions, such as strontium and barium, are also suitable dopants. These dopants can be used to substitute up to 6% and 3% substitution respectively of magnesium ions, as can be seen in the study by Sternig *et al.*[19] As opposed to calcium dopants,[165] Sr and Ba can only be seen at 3- and 4-coordinated sites, and not at 5-coordinated sites. The singlet to triplet excitation energy, discussed above for calcium-doped and pure MgO, decreases for Sr-doped MgO to 3.87 eV but increases again for BaO-doped MgO to 3.98 eV, as Sushko *et al.*[165] show, using the embedded cluster methodology, described above.

Unfortunately, no experimental photoluminescence data is available for Sr-doped MgO nanoparticles. However, Sternig *et al.*[206] have obtained BaO aggregated on MgO nanoparticles, obtained through CVD. It has been found that these powders are not cubic but hemispherical (due to the growth process; although the bulk is still found to be of rocksalt structure) with an average size of 30 nm, although the size range is broader than for pure MgO particles. According to Sushko *et al.*,[165] only small amounts of $Ba^{2+}$ ends up being used as the dopant, as most of the $Ba^{2+}$ is a surface aggregate, in line with the fact that the energetic cost of replacing a magnesium ion is calculated to be 5.64 eV.

Sternig et al.[210] have also studied the optical properties of BaO nanocubes on MgO clusters: barium oxide dopants add additional peaks to the MgO absorption spectra: at 4.3 eV and 4.8 eV. Using an excitation energy of 5.2 eV, the broad photoluminescence spectrum is observed to contain an additional peak at 2.7 eV, attributed to the barium dopant, as well as the peak at 3.4 eV, which is also observed for pure MgO particles. Similarly, when an excitation energy of 4.6 eV is used to obtain the photoluminescence spectrum, a broad peak at 2.7 eV is observed, which is significantly more intense than the peak observed for pure MgO at 3.3 eV. This means that the MgO luminescence peak is not seen.

Sternig et al.[211] have, as a joint experimental and computational embedded cluster study, substituted $Mg^{2+}$ with $Ba^{2+}$ in MgO nanoparticles, to study the potential application in solid-state lighting. As found previously, samples with 6% substitution exhibit phase separation. However, the study also shows that for samples $Ba_{0.02}Mg_{0.98}O$, phase separation does not occur but the average size increases from 6 nm for pure MgO to 7 nm in addition to slight loss of the definition of the highly cubic morphology seen for pure MgO. The average particle size increases further to 8 nm for samples with stoichiometry $Ba_{0.04}Mg_{0.96}O$. The UV diffuse reflectance spectra of the differently doped particles can be seen in figure 3-7, where the increasing amount of $Ba^{2+}$ redshifts the absorption onset. This is explained theoretically by the fact that the Ba perturbs the electronic states: the holes are more strongly bound and the electron affinity generally increases in features containing Ba meaning that the excitation energies are lower compared to those of pure MgO as the highest occupied molecular orbital (HOMO) increases in energy and the lowest unoccupied molecular orbital (LUMO) decreases in energy.
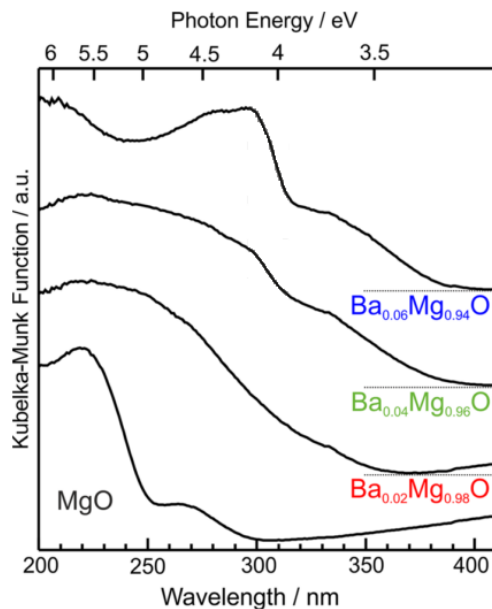
**Figure 3-7:** Showing the UV diffuse reflectance spectra of pure MgO as well as three stoichiometrically different Ba-doped MgO nanoparticles. Adapted from reference 211.

The corresponding photoluminescence spectra obtained by Sternig *et al.*,[211] show the asymmetrical peaks as seen in previous nanoparticles. The luminescence can be recorded to be as low as 1.77 eV with a peak at ~ 2.38 eV, when an excitation photon of 3.20 eV is used. The peak increases in intensity and decreases its luminescence energy to 2.30 eV and the luminescence onset decreases to 1.55 eV when the spectra is not taken at room temperature (298 K) but at 77 K. The same pattern can be found for all different Ba-doped MgO samples. When the excitation photon increases to 3.6 eV, the luminescence peak of 2.70 eV remains unchanged in position but becomes more intense as the temperature is decreased. The luminescence onset is reduced from 1.91 eV to 1.74 eV. Similarly, the spectra remain mostly unchanged as the amount of Ba increases. The photoluminescence has also been modelled but in rather a qualitative way to experiment, as the qualitative change between MgO and Ba-doped MgO luminescence is given meaning. The modelled change is about 1 eV, compared to 0.6 eV seen experimentally. The computational approach to obtaining the photoluminescence was to calculate the difference between the $S_0$ and $T_1$ surface, after allowing for relaxation on the triplet potential energy surface. The potential problems with this approach have previously been discussed.

### 3.1.2.3    Zn-doped MgO

Ohira *et al.*[212]  have shown that doping MgO powders with $Zn^{2+}$ ions is interesting for mainly anti-bacterial applications against e.g. *E.coli*. The problem is that ZnO nanoparticles are toxic to humans but show good anti-bacterial properties, while MgO is non-toxic but neither does it show anti-bacterial properties, so Zn-doped MgO is an interesting alternative. Vidic *et al.*[213] and Stankic *et al.*[21] have demonstrated that preparing nano-sized samples via CVD means that as the amount of zinc increases, so does not only the particle size range but also the average particle size: the size range for $Zn_{0.05}Mg_{0.95}O$ is 5 – 15 nm with an average size of about 8 nm, whereas the particle size ranges from about 8 – 25 nm for $Zn_{0.1}Mg_{0.9}O$ with most particles being found to be about 16 nm in size. Similarly to what is observed for the other doped MgO clusters, the dopant is energetically favoured to occupy low coordination sites, and in the case of $Zn_{0.1}Mg_{0.9}O$ most low coordination sites are occupied by a zinc cation. The advantage of these doped materials is that they are not showing signs of being toxic. The absorption spectrum for Zn-doped MgO is broad but peaks can be identified at 3.7 eV and 5.4 eV, the latter being due to MgO. The photoluminescence spectrum after 4.6 eV excitation exhibits peaks at 3.2 eV, where $Zn_{0.05}Mg_{0.95}O$ samples have one additional peak over pure MgO, namely at 3.9 eV, obtained from 5.2 eV excitation, both with an absorption onset at approximately 650 nm (1.90 eV).[21] When this 5.2 eV photon is used, the peak found for pure MgO at 3.4 eV becomes less intense as the dopant concentration increases, and disappears for $Zn_{0.1}Mg_{0.9}O$. This sample shows additional peaks at 2.4 eV and 3.8 eV in a very broad spectrum ranging from about 1.5 eV to 4 eV.

# 4. This work in context

Research into nanomaterials is very exciting and novel applications have been found, so it is therefore useful to study known materials, comparing their behaviour to the bulk to investigate whether new applications might result. Examples are the anti-bacterial properties of Zn-doped MgO nanoparticles or the potential applications of alkaline earth doped MgO nanoparticles in Light Emitting Diodes (LEDs) or lasers.

As the previous section showed, a lot of work has been performed in this area both experimentally and computationally. However, the approach taken in previous modelling studies may be insufficient to fully understand the excitation behaviour of inorganic nanoparticles. The limitation of simulating only one part of a cluster quantum mechanically has effects on the predicted excitation energies as well as excitation character: e.g. corner to corner excitations cannot be studied appropriately, as the model does not necessarily allow for a complete description of this.

The work performed here aims to describe the entire isolated cluster, giving the methodology more freedom to describe any relevant excitation and luminescence properties of the particles, with the drawback that only smaller particles can be studied. Furthermore, the model employed here can avoid using $T_1$ to $S_0$ transitions which are optically forbidden, rather modelling $S_1$ to $S_0$ transitions, which are predicted to be more prominent in materials such as MgO, due to the lack of spin-orbit coupling. This should give more accurate results, and a better description of the excited state, although the size of the cluster studied is the drawback when using TDDFT (section 2.2.5.2).

To test the validity of TDDFT on these systems, we begin by looking at very small DFT-optimised ground state structures, such as $(MgO)_4$ and $(MgO)_6$, where we can compare results with a very accurate computational method, namely Equation of Motion (EOM) Coupled Cluster (CC) Theory, as discussed in section (2.2.3.1), performed by Dr. Martijn Zwijnenburg, although co-interpreted by the author. As satisfactory agreement has been found (discussed in results section 5.4.1), larger clusters were optimised using DFT (section 5.3), namely $(MgO)_n$ where $n = 9, 12, 18, 24, 32, 40, 50, 108$. Frequencies have

been calculated to confirm ground state structures and from there, vertical excitation energies were obtained by applying TDDFT at these minima.

As the computational modelling of the absorption spectra for MgO nanoparticles has proven to be less straightforward, due to the charge-transfer behaviour of the larger particles, a study has been performed to see whether or not other rocksalt structures suffer from this particular issue as well, as discussed in chapter 6. The materials studied are CaO, SrO, BaO, CdO, PbS, MgS and MgSe.

TDDFT was also used to optimise the excited state geometry on the $S_1$ potential energy surface for each cluster, as shown in chapter 7. This optimisation step simulates the excited state relaxation. Where computationally feasible (up to $n = 12$), the excited state frequencies are calculated to check that the stationary points obtained actually correspond to minima and not another type of extrema, such as saddle points. From the excited state minimum, the cluster is allowed to relax electronically back to the ground state, giving a value for the fluorescence energy.

The excited state geometrical structure is then allowed to relax on the electronic ground state surface, to see if there are any energy barriers, but none have been found: all studied clusters optimise back to the original ground state structure. Due to the absence of ground state barriers, this aspect is not discussed further in this thesis.

Finally, the effects of substituting $Mg^{2+}$ ions by other alkaline earth ions, as well as $Zn^{2+}$ and $Cd^{2+}$, have been investigated and preliminary results are presented in chapter 8. This is of particular interest, as doping is a widely used method to tune optical properties of materials.

# 5. MgO ground state structures and vertical excitation energies

## 5.1 Introduction

The optical properties of MgO nanoclusters have previously been studied computationally, as discussed in section 3.1.1.2. However, the difference in this study is that the whole particle is modelled quantum mechanically, as opposed to a small area which is described quantum mechanically and embedded in a larger cluster of classical point charges.[167,214,215] The problem with the latter approach is that it fails to predict certain low-energy excitations, due to the nature of the assumptions made within the methodology. Treating the whole system quantum mechanically removes this problem. However, it limits the size of the system that can be considered. The largest cluster that has been studied in this project is $(MgO)_{108}$, which is a cubic cluster with approximately 1 nm long sides. However, for calculations to be tractable, some compromises (e.g. with regards to the basis set) have had to be made and, despite these compromises, computational costs remained high. It follows that the systems that can be studied more accurately must be smaller and, because of the tight-packing of the atoms in the rocksalt structure, a lot of the computational cost is associated with modelling bulk atoms (more and more so for the larger computational models). Therefore the largest particle that has been studied in detail is that of $(MgO)_{32}$, a cubic cluster with sides of approximately 0.6 nm. These size limitations mean that the experimental particles these calculations are compared to should be as small as possible to allow for the best possible comparison.

The aim of this project is to study the excited state properties of MgO nanoparticles, which has been done by initially studying the ground state structures, from which the excitation energies have been obtained.

## 5.2    Methodology

Density Functional Theory (DFT) and Time-Dependent Density Functional Theory TDDFT (section 2.2.5.2) have been used to calculate the ground state structures and vertical excitation energies of $(MgO)_n$, respectively. The basis sets utilised to perform this study were DZDP for magnesium in combination with DZP for oxygen: this combination is referred to as DZ(D)P for MgO particles from now on. The basis sets are of double-$\zeta$ quality, and also include double polarisation[§§] for magnesium and single polarisation for oxygen. Furthermore, the calculations have also been performed using the triple-$\zeta$ quality basis set def2-TZVP, which has single polarisation. The latter basis set has only been used for particles with $n \leq 32$. The *xc*-functionals employed were PBE, B3LYP, BHLYP and CAM-B3LYP, which differ in the amount of Hartree-Fock exchange (HFE) included: 0% for PBE, 20% for B3LYP, 50% for BHLYP and 19% at short range in addition to 65% at long range for CAM-B3LYP. The latter xc-functional is only available in the GAMESS-US package, whereas all the other calculations have been performed using the TURBOMOLE suite. The former is a more expensive code to run, which means that the whole range of particles could not be studied. The absorption spectra have been obtained using a custom script, which creates Gaussian functions over every excitation. The standard deviation for these Gaussian functions has been set to 0.1 eV.

## 5.3    Ground state structures

As discussed in chapter 3, MgO nanoclusters have previously been studied computationally and, in general, the most stable isomer for $3n$ clusters (i.e. $(MgO)_3$, $(MgO)_6$, $(MgO)_9$, ...) has a hexagonal tube configuration, for values of $n$ that are smaller than 6.[216] Other structures are found in the rocksalt configuration[14,15,216–218], i.e. cubic structures resembling the bulk crystal structure. Figure 5-1 shows the lowest energy conformations for the MgO clusters studied, namely $n$ = 1, 2, 4, 6, 9, 24, 32, 40, 48, 108 for $(MgO)_n$, as well as the cubic structure for $(MgO)_6$. The ground state structures for

---

§§§§ Polarisation refers to polarisation functions, and the polarisation is applied to each shell.

$(MgO)_{12}$ and $(MgO)_{18}$ are discussed separately (section 5.3.1 and 5.3.2 respectively). The reason for a separate discussion is that no clear ground state global minimum can be determined or that the ground state structure displays unexpected behaviour, as discussed below.
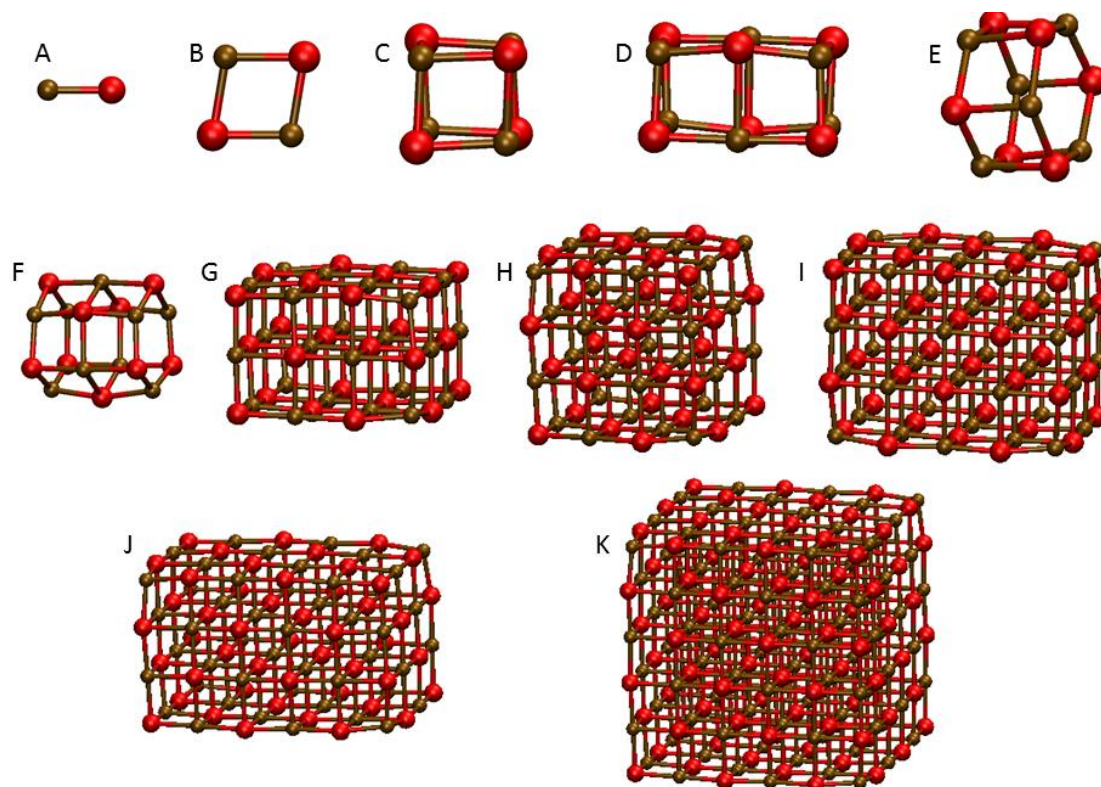


**Figure 5-1:** B3LYP/def2-TZVP optimised ground state (likely) global minimum structures for A $(MgO)_1$, B $(MgO)_2$, C $(MgO)_4$, D $(MgO)_6$ cubic, E $(MgO)_6$ hexagonal, F $(MgO)_9$, G $(MgO)_{24}$, H $(MgO)_{32}$, I $(MgO)_{40}$, J $(MgO)_{48}$ and K $(MgO)_{108}$. The latter is the DZ(D)P optimised struture. Oxygens are the red sphered, magnesium the brown ones.

Figure 5-1 shows that the particles corresponding to the (likely) global ground state minimum are relatively regular, although angles on corner sites are larger than $90°$. Furthermore, it can also be seen that $(MgO)_n$, $n = 24, 32, 40, 48, 108$ all exhibit the rocksalt structure, where $(MgO)_{32}$ and $(MgO)_{108}$ are cubic, and the other clusters are cuboids. The

edge lengths of these rocksalt clusters are tabulated in table 5-1. $(MgO)_{18}$ is not included here, due to its dipole, discussed in section (5.3.2).

**Table 5-1:** Edge lengths of $(MgO)_n$ nanocuboids, optimised at the B3LYP/def2-TZVP level.

| Cluster | Edges /nm | Body diagonal / nm |
|---------|-----------|--------------------|
| $(MgO)_{24}$ | $0.59 \times 0.59 \times 0.40$ | 0.94 |
| $(MgO)_{32}$ | $0.59 \times 0.59 \times 0.59$ | 1.02 |
| $(MgO)_{40}$ | $0.79 \times 0.59 \times 0.59$ | 1.16 |
| $(MgO)_{48}$ | $1.01 \times 0.59 \times 0.59$ | 1.32 |
| $(MgO)_{108}$ | $0.99 \times 0.99 \times 0.99$ | 1.72 |

### 5.3.1  $(MgO)_{12}$ particles

Even in the literature,[216,219–221] the theoretical structure of the global minimum structure $(MgO)_{12}$ is found to be method dependent. In this study, three different structures were initially optimised, namely the rocksalt, hexagonal tube and spherical, bubble-like 'sodalite' structure, as shown in figure 5-2. The 'true' ground state global minimum structure cannot be determined and these clusters are too small to be synthesised but too large to be studied with more accurate post-HF methods.
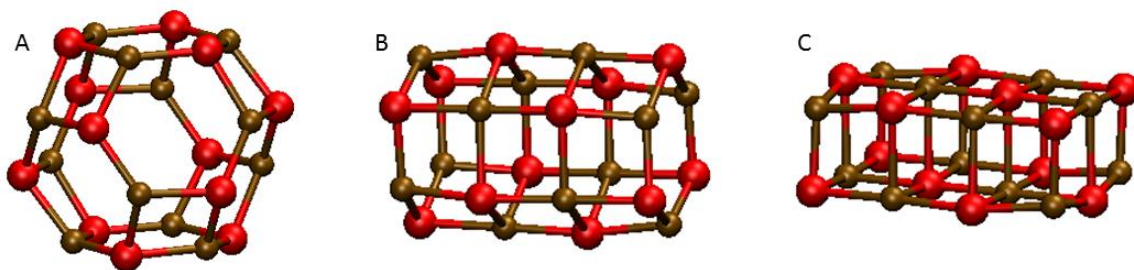
**Figure 5-2:** B3LYP def2-TZVP structures for $(MgO)_{12}$ A sodalite, B hexagonal tube and C rocksalt structure. Oxygens are the red cirles, magnesium the brown ones.

Using the def2-TZVP basis set, table 5-2 shows the relative energies of the different structures that have been studied: each structure has been optimised with each of the three functionals PBE, B3LYP and BHLYP, and the relative energies are tabulated.

**Table 5-2:** Relative energies of the $(MgO)_{12}$ sodalite, hexagonal tube and rocksalt strucutre for xc-functionals PBE, B3LYP and BHLYP. All energies are in eV.

|  | Sodalite | Hexagonal Tube | Rocksalt |
|---|---|---|---|
| PBE | 0.29 | 0.00 | 0.50 |
| B3LYP | 0.00 | 0.03 | 0.73 |
| BHLYP | 0.00 | 0.42 | 2.67 |

It can be seen that neither of these three functionals describes the rocksalt structure as the energetically lowest lying structure, and the differences are larger than that of DFT uncertainty (approximately 0.25 eV,[222–224] although likely to be smaller in this case due to potential error cancellations). When HF exchange is included, the bubble-like structure (sodalite) is predicted to be lowest in energy. However, for B3LYP, the hexagonal tube has a total energy just 0.03 eV above that of the sodalite structure, which means that it is unclear whether the latter truly is the lowest lying structure. BHLYP predicts the

hexagonal tube to be 0.42 eV higher in energy than the sodalite structure, which is a clearer energy difference and just larger than the DFT 'error'. In general, it can be said that increasing the amount of HFE percentage leads to a stabilisation of sodalite relative to the hexagonal tube, as well as a destabilisation of the rocksalt relative to the hexagonal tube. As the sodalite has six 6-membered rings, the hexagonal tube has four 6-membered rings and the rocksalt has no 6-membered rings, it could be said that including (and increasing) HFE stabilises 6-membered rings, leading to the energy variation.

Due to the strong functional dependence, these energy differences should be treated with caution. Furthermore, if these clusters existed experimentally, it would be possible that both the sodalite and hexagonal tube (and possibly even the rocksalt one) isomers would be present. Due to the similar electronic energies of the two structures, both the sodalite and hexagonal tube clusters were taken into account in this work.

### 5.3.2  $(MgO)_{18}$ particles

The study of $(MgO)_{18}$ revealed some unexpected behaviour. Energy differences between different clusters have been calculated (hexagonal tube, rocksalt and 'slab': a more elongated rocksalt structure (see figure 5-3 C). The rocksalt structure was found to be the lowest energy structure for all *xc*-functionals, which was also previously found in the literature.[15,216,219] Yet, we have found that this structure exhibits a considerable dipole moment of 17 Debye.[***] Looking at the images of the two faces (figure 5-4) between which the dipole is defined, it can be seen that both faces are made up of 9 ions, with either a $Mg^{2+}$ or $O^{2-}$ ion at the centre. The total charge on these faces creates said dipole. This effect can even be increased when the distance between the two faces is increased, and this results in the rocksalt cluster $(MgO)_{27}$, which has a dipole of 31 Debye. For the latter particle, a further study to find a lower conformation has not been undertaken. It is, of course, possible that there is a lower energy structure for $(MgO)_{18}$, which is as yet unknown. Due to the dipole moment, the $(MgO)_{18}$ cluster gives anomalous results in

---

[***] For comparison, $(MgO)_1$ (in the gas phase) has a dipole moment of 9.0 Debye, and CaO has a dipole of 10 Deybe.[263]

context of the data obtained from the other clusters, but this cluster is still taken into account for the rest of the study.

While these faces seen in figure 5-4 are non-polar in the traditional sense[225] and this structure cannot be describes as a classically polar surface, as this dipole would not exist in a periodic system, the fact that the surfaces are comprised of an odd number of atoms makes them effectively behave as if polar;  similar to an effect induced by polar surfaces, as described by Melnikov *et al*.[226]
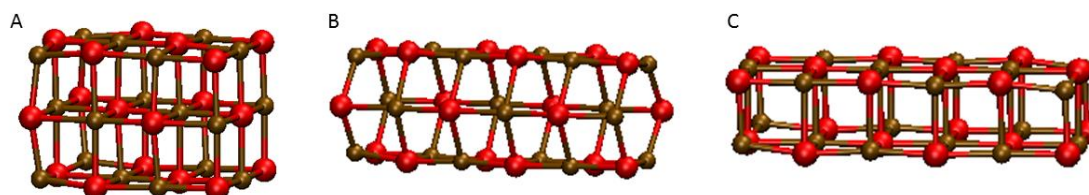


**Figure 5-3:** B3LYP/def2-TZVP optimised structuresof $(MgO)_{18}$.  A rocksalt (cuboid), B hexagonal tube and C 'slab' structure. Oxygens are the red spheres, magnesium the brown ones.
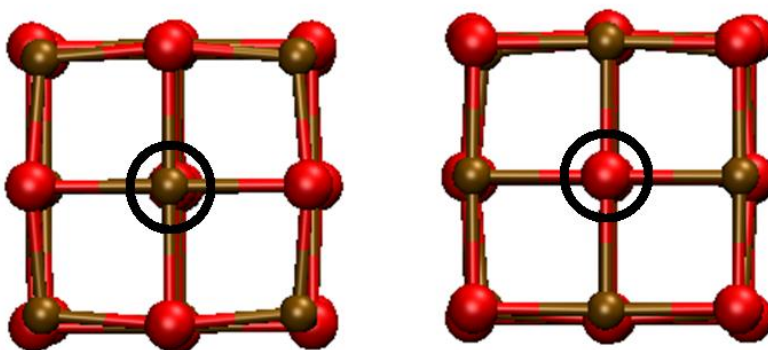


**Figure 5-4:** Opposite faces of the B3LYP/def2-TZVP optimised $(MgO)_{18}$ rocksalt structure, the centre atoms of which generate the dipole moment of the structure, highlighted by black circles. Oxygens are the red spheres, magnesium the brown ones.

## 5.4 Validation of TDDFT

This project is looking at modelling gas-phase clusters and their optical properties. The methodology of choice is TDDFT, as already discussed, as it offers a good compromise between accuracy and computational efficiency. To validate the quality of TDDFT, two comparisons have been made: one for small clusters, which can also be modelled with inherently more accurate (coupled cluster) methods. These small clusters are, of course, unrealistic, as clusters of this size have never been synthesised (and probably never will). In addition, the comparison of the results obtained with the bigger particles (($MgO)_{24}$ and larger) and experiment has been made. Unfortunately the experimental data is based on particles that are larger than the ones used in this study, but this comparison can still be useful.

### 5.4.1 Comparison of TDDFT with CC

A common issue in computational chemistry is the size of the cluster that can be modelled and the level of theory that can be applied to it. In this particular case, a comparison with high-level CC calculations, performed by Dr. M. Zwijnenburg, can be made for the small clusters ($n = 1, 2, 4, 6$), and as the larger clusters approach experimental size, experimental absorption spectra may be used for comparison. However, clusters with sizes in between these two extremes cannot practically be compared to other methods. It is therefore important to make sure that the approach taken for the clusters where no comparison is feasible, is reasonable. This can be achieved by applying the *xc*-functional approximations which yield good agreement with CC calculation. It is not unreasonable to assume that the *xc*-functionals that were found to be suitable for the smaller clusters, can be equally well applied to the larger ones.

The approach to comparing these TDDFT results with EOM-CC is to focus on five small clusters, namely $(MgO)_1$, $(MgO)_2$, $(MgO)_4$ and $(MgO)_6$, the latter being studied both in its cubic and hexagonal configurations (see figures 5-1 A - E). For this part of the study, the structures used for the excited state calculations are those of the B3LYP/def2-TZVP

optimised ground state geometry: the same basis set has been used for both the CC and TDDFT calculations. Clusters $(MgO)_1$ and $(MgO)_2$ have been studied at the EOM-CCSDT as well as EOM-CCSD level of theory, whereas only the latter has been used for the $(MgO)_4$ and $(MgO)_6$ clusters, due to computational expense of the methodology. The TDDFT calculations have been performed with four different *xc*-functionals, namely PBE, B3LYP, BHLYP and CAM-B3LYP.

Firstly, a detailed study of the first five excitations of $(MgO)_2$ was undertaken, as seen in figure 5-5. This is so that the suitability of TDDFT can be established via comparison to high level coupled cluster calculations. $(MgO)_2$ is found to be in the abelian $D_{2h}$ point group, and is therefore suitable to study. What can be seen is that all methods agree on the energetic ordering of the lowest two excited states, as well as a gap of $0.5 - 0.7$ eV between these and the next set of excited states. There is some disagreement with regards to the character of the third and fourth excited states, which most likely stems from the fact that there are many excited states present, all of which lie within 0.1 eV of each other. The values show that the TD-CAM-B3LYP values agree best with the EOM-CCSDT results, with an average error of approximately 0.1 eV, compared to a difference of ~ 0.4 eV for TD-BHLYP and TD-B3LYP, where the former lies higher and the latter lower with respect to the EOM-CCSDT results. The TD-PBE values are calculated to be considerably lower than the reference result (EOM-CCSDT), with a discrepancy of ~ 0.7 eV. These results are representative of all other clusters considered, as the comparison between *xc*-functionals and the EOM-CC results follow the same trend: a corresponding analysis has been made for the $(MgO)_4$ and both $(MgO)_6$ clusters, and the same conclusions can be drawn. These data are not shown here, as they do not offer any further insight. It should be noted that the results presented in figure 5-5 are obtained using the frozen core approximation where the $1s$ core electrons are frozen, although a small investigation performed by Dr. M. Zwijnenburg suggests that an all-electron calculation for $(MgO)_2$ lowers the excitation energies by up to 0.1 eV of those reported here, justifying the use of the approximation.
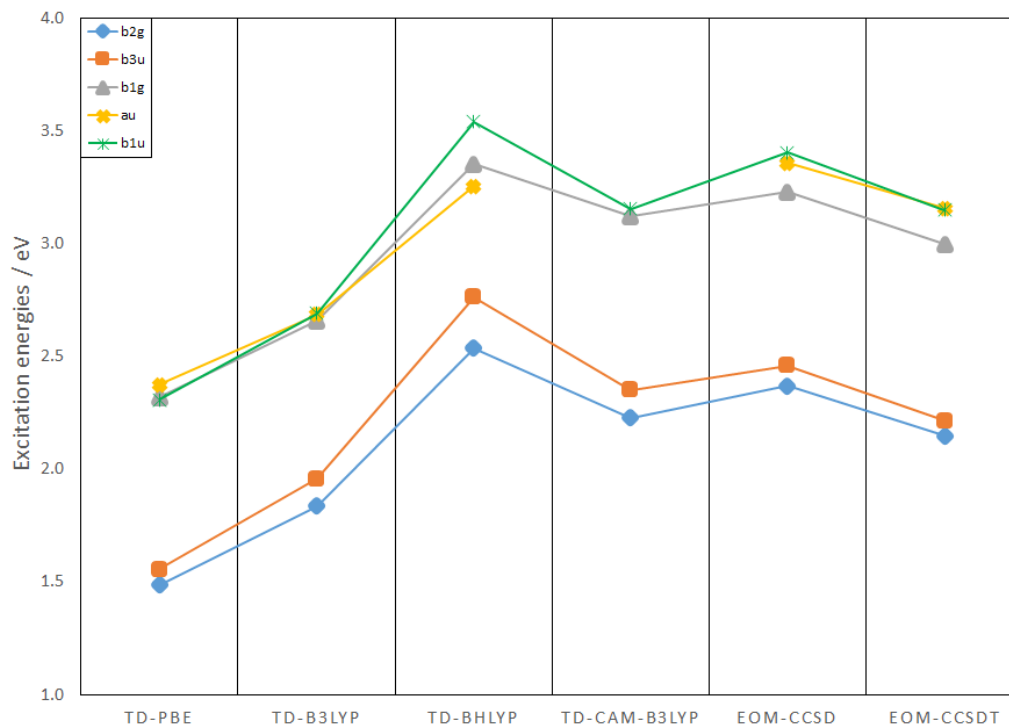
**Figure 5-5:** Excitation energies of the five lowest vertical excitations of the $(MgO)_2$ cluster as calculated using TD-DFT and EOM-CC. Blue diamonds correspond to the excitation to the lowest $^1b_{1g}$ state, orange squares to the lowest $^1b_{3u}$ state, green crosses to the lowest $^1b_{1u}$ state, yellow circles to the lowest $^1a_u$ state, and grey triangles to the lowest $^1b_{1g}$ state.

Further to analysis of the individual clusters, figure 5-6 shows the trend of the lowest vertical excitation energy (LVEE) for the five small clusters, indicating that both EOM-CCSD and TDDFT agree that the LVEE increases smoothly as the size of the cluster ($n$) increases and, furthermore, in the case of the cubic $(MgO)_6$ cluster, the LVEE lies below that of the $(MgO)_6$ hexagonal cluster. Due to computational expense, which meant that the EOM-CCSDT methodology could be applied to clusters where $n < 2$, and the fact that a consistent methodology is sought for comparison, only the EOM-CCSD data is considered here. The EOM-CCSD data lies between that of the TD-BHLYP and TD-CAM-B3LYP data (above and below, respectively), showing that TDDFT using these *xc*-functionals, is a reasonable approach to describing the excitation energies of the small clusters.
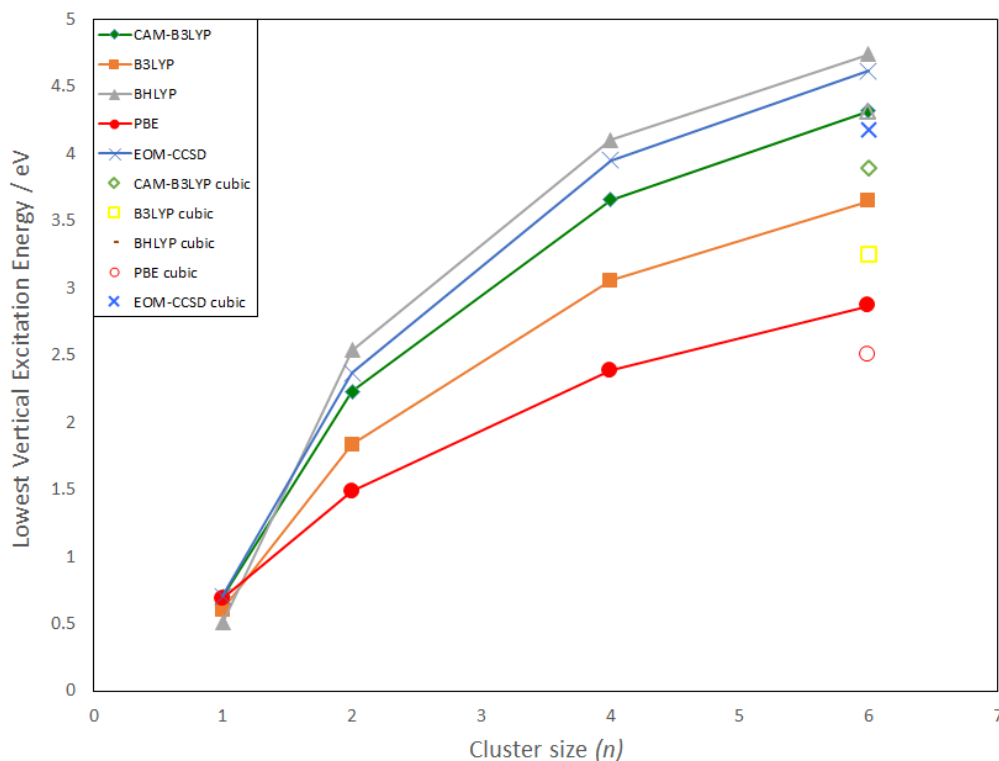
**Figure 5-6:** Lowest vertical excitation energies as a function of cluster size and *xc*-functional (or EOM-CCSD).

### 5.4.2 Comparison of TDDFT with experiment

As established above, TDDFT is a good method for calculating vertical excitation energies for very small clusters, although they are unlikely to be realised experimentally due to their small size. At the other end of the scale are the experimental structures, which TDDFT cannot currently model. However, TDDFT results for particles that approach the experimental size-range can be compared to experimental absorption spectra. The properties of experimentally realised particles are discussed in more detail in section 3.1.1, but the particles most suitable for comparing the TDDFT results with particles that have an average size of 3 nm. The experimental sample does contain smaller particles, possibly as small as 2 or even 1 nm.[19,20] This experimental data has been compared to the absorption onset of particles $(MgO)_{24}$, $(MgO)_{32}$ and $(MgO)_{40}$. For those four particles, the lowest vertical excitation energy (LVEE) corresponds to the theoretically predicted absorption

onset, as the lowest excitation is dipole-allowed in all cases. Figure 5-7 shows the dependence of the LVEE on the particle size $n$ for the range of $xc$-functionals used above, as well as the experimental absorption onset. In this figure, the cubic cluster for $n = 6$ is represented, as only cuboid clusters are displayed in this figure. This has been done to show the LVEE trend with particle size, and not have potentially different trends for different structures in the same figure. Furthermore, only the results for clusters up to $n = 32$ are included for TD-CAM-B3LYP, as the $xc$-functional is not implemented in a computationally cost effective code, which means that the computational cost using (TD-)CAM-B3LYP is considerably higher than that the equivalent calculation with (TD-)PBE, (TD-)B3LYP or (TD-)BHLYP.
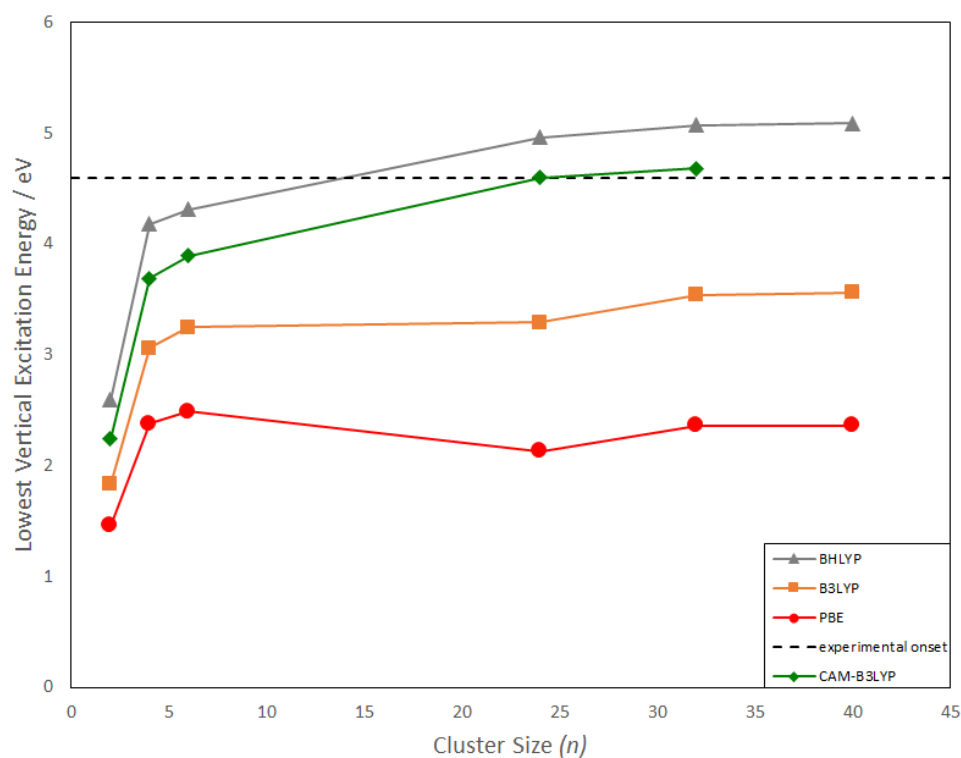


**Figure 5-7:** Lowest vertical excitation energy (LVEE) of (MgO)$_n$ ($n$ = 2, 4, 6, 24, 32, 40) nanocuboids calculated using TD-DFT with different $xc$-functionals. Red circles represent TD-PBE results, orange squares TD-B3LYP results, green diamonds TD-CAM-B3LYP results, grey triangles TD-BHLYP results and the dashed line the experimental absorption onset of 3 nm particles.

The behaviour of the *xc*-functionals seen in figure 5-7 can be divided up into two different groups: both *xc*-functionals with no or low percentage of HFE, i.e. TD-PBE and TD-B3LYP, fail to show a smooth trend as *n* increases, where there is a dip in the value of the LVEE for $(MgO)_{24}$. Also, the apparent converged value of the LVEE is considerably below the dashed line, which represents the experimental value. On the other hand, the two *xc*-functionals with either high percentage of HFE or range-separated HFE, BHLYP and CAM-B3LYP, show a smooth trend and a convergence to the values of 5.1 eV and 4.7 eV respectively, matching the experimental value of 4.6 eV relatively well, and do not show the dip in value for $(MgO)_{24}$. However, it should be borne in mind that the largest particle studied within this context, $(MgO)_{40}$, is only approximately 0.8 nm in its largest dimension, so it still considerably smaller than the experimental particles, although the plateau calculated for n ≥ 24 would suggest that the comparison is valid. Furthermore, when using a smaller basis set (namely DZDP), the LVEE increases by only 0.01 eV for TD-B3LYP and 0.09 eV for TD-BHLYP when comparing the values of $(MgO)_{32}$ and $(MgO)_{108}$ (going from a cube with lengths of 0.6 nm to 1 nm).

It appears that TD-CAM-B3LYP gives the best match to both the coupled cluster results as well as the experimental absorption on-set for larger particles. TD-BHLYP, when compared to the TD-CAMB3LYP values, predicts LVEEs blue-shifted (i.e. higher in energy) by about 0.4 – 0.5 eV over the whole size range. This is different from the behaviour of TD-PBE and TD-B3LYP, where the difference in the predicted LVEE values to TD-CAMB-3LYP increases with particle size. For example, in the case of the small clusters, the difference in the LVEE between TD-CAM-B3LYP and TD-B3LYP is similar in magnitude (~ 0.4 eV) to that between TD-CAM-B3LYP and TD-BHLYP but opposite in sign, while for the larger particles, the difference between TD-CAM-B3LYP and TD-B3LYP increases to more than 1 eV. In the case of TD-PBE the difference increases from 0.7 eV to over 2 eV. Both TD-B3LYP and TD-PBE also severely underestimate the experimental absorption on-set (at 4.6 eV). This underestimation, as well as the mismatch to the TD-CAM-B3LYP values for larger clusters, suggests that the accuracy of TD-B3LYP and TD-PBE declines dramatically with increasing particle size, further discussed below.

## 5.5 Origin of the problematic description of excitations in MgO nanocuboids

As discussed above, the use of TD-PBE and TD-B3LYP yields excitation energies that are consistently too low. A potential origin for this underestimation may lie in the nature of the excitation process. It has previously been found that charge transfer (CT) excitations occur in organic molecules[89,109,110] and also in $TiO_2$ nanoparticles.[227] These CT excitations result when (i) only a small overlap exists between the initial and the final orbitals involved in the electronic excitation and (ii) *xc*-functionals are used that are either non-hybrid functionals (such as PBE) or a hybrid functional with a low percentage of HFE (such as B3LYP). When both (i) and (ii) are present in the same calculation, it is possible that the excited states, accessed by an excitation described by (i), are spuriously stabilized, relative to more local excitations. Typically, the use of hybrid *xc*-functionals with a larger percentage of HFE (such as BHLYP) or range separated *xc*-functionals (such as CAM-B3LYP) minimize the problems related to the description of CT-excitations.[65,87,89,125] It is possible that the larger MgO systems studied here exhibit this spurious stabilization.

A suitable diagnostic test to probe potential CT-excitations is in terms of the $\Lambda$ diagnostic of Peach *et al*.[89] and selected systems are studied in terms of this. Application of this test gives a diagnostic numerical value ranging from 0 (no overlap between the initial and final orbitals involved in the excitations) to 1 (complete overlap). Low values of this $\Lambda$ diagnostic[†††] suggest that the excitation studied has strong CT character, and therefore might be underestimated when using *xc*-functionals with no or low amounts of HFE.

---

[†††] It should be noted that the low values, referred to in this work as 'cut-off' values are dependent on the *xc*-functional used. The cut-off for B3LYP is 0.3 and 0.4 for PBE, as devised by Peach *et al*. In this work, only B3LYP results have been studied in terms of their $\Lambda$ value.

**Table 5-3:** TD-B3LYP calculated $\Lambda$ values of the lowest vertical excitation for a range of particles, [a] denotes cubic structure, [b] hexagonal structure, [c] sodalite structure.

|  | $(MgO)_2$ | $(MgO)_4$ | $(MgO)_6$ | $(MgO)_{12}$ | $(MgO)_{24}$ | $(MgO)_{32}$ |
|---|---|---|---|---|---|---|
| $\Lambda$ | 0.30 | 0.32 | $0.34^b$ ($0.33^a$) | $0.35^b$ ($0.34^c$) | 0.15 | 0.13 |

Table 5-3 shows that the $\Lambda$ value is approximately 0.3 for the small clusters, but this value decreases considerably to about 0.14 for the larger particles $(MgO)_{24}$ and $(MgO)_{32}$. The $\Lambda$ value below which the CT character of a system may lead to spuriously low excitation energies, has been proposed by Peach *et al.* to be about 0.3.[109] However, the studies that underlie this value have been performed on organic systems and studies of $TiO_2$ nanoparticles suggest that a lower cut-off value might be more suitable for these particular inorganic systems.[227] Without providing insight into which cut-off value is more suitable for MgO systems, table 5-3 shows a clear trend: the smaller particles (up to $(MgO)_{12}$) do not show enough CT character to lead to significantly underestimated excitation energies, whereas the value obtained for the larger, more bulk-like particles are suggestive of a CT-problem being the origin of the low vertical excitation energies found when employing TD-B3LYP (and presumably TD-PBE). It can be seen, therefore, that the TD-PBE and TD-B3LYP results may be unreliable in predicting the excitation behavior in MgO nanoparticles. For this reason, the focus for the remainder of this work is on (TD-)BHLYP and (TD-)CAM-B3LYP. Some results obtained with TD-B3LYP are reported, but only with the purpose of portraying the differences between a CT and non-CT excitation.

## 5.6   Calculated optical absorption spectra

After studying the more technical aspects of the lowest excitations, the next step was to simulate the absorption spectra and compare these to experiment. To model the absorption spectra, only the larger clusters were studied, namely $(MgO)_{24}$, $(MgO)_{32}$, $(MgO)_{40}$ and $(MgO)_{48}$, using the TD-BHLYP *xc*-functional and the def2-TZVP basis set. The simulated

spectra are shown in figure 5-8. The spectra in figure 5-8 include a Gaussian smearing of 0.1 eV and a rigid red-shift of 0.5 eV. This red-shift (lowering of the energy) is included since, as seen in figure 5-7 the TD-BHLYP predicted LVEE is overestimated by about 0.5 eV in comparison to the experimental absorption on-set. The experimental spectrum shown in figure 5-8 is the absorption spectrum measured for MgO particles with an average size of 3 nm.[20] The un-shifted spectra shown are in figure 5-9.
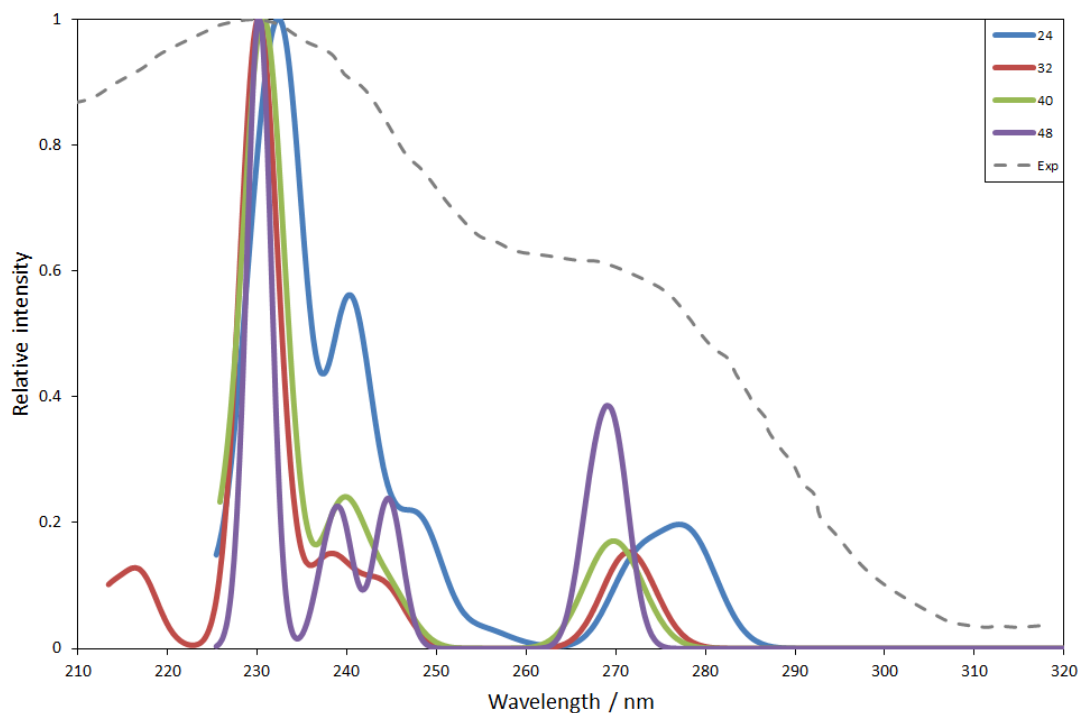


**Figure 5-8:** TD-BHLYP/def2-TZVP calculated absorption spectra (including a 0.5 eV rigid red-shift) of (MgO)$_n$ particles ($n = 24, 32, 40, 48$). The intensity of the peaks has been normalised to the largest intensity peak. Experimental absorption spectrum (dashed line) taken from reference 20.
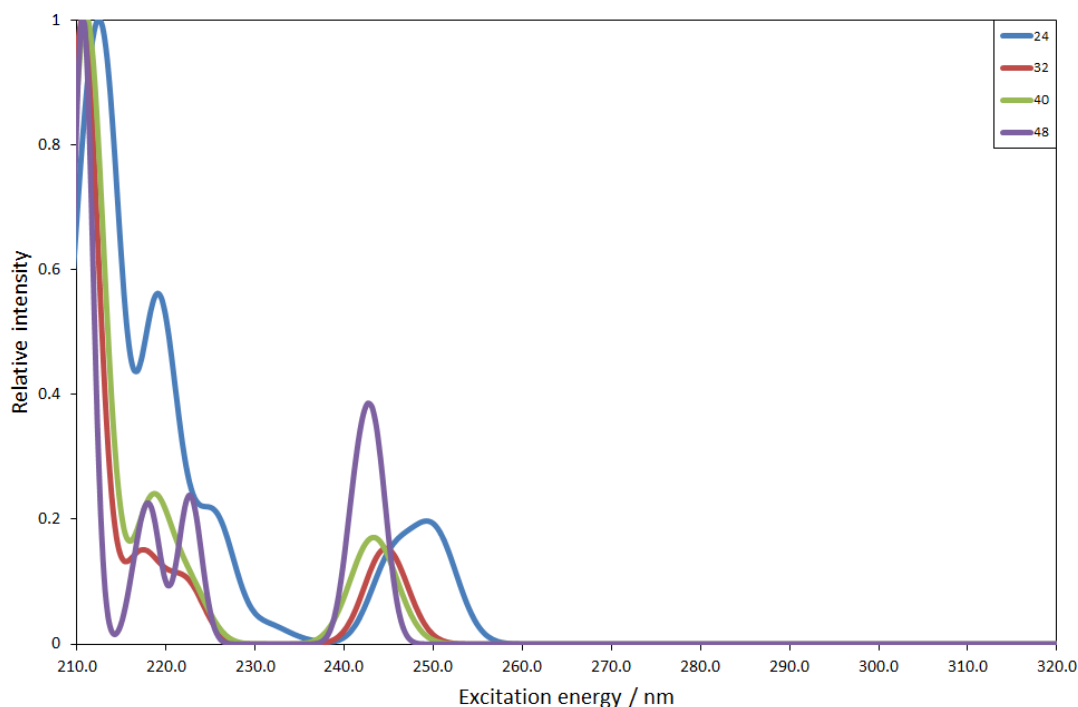
**Figure 5-9:** Unshifted TD-BHLYP/def2-TZVP calculated absorption spectra of (MgO)$_n$ particles for $n$ = 24, 32, 40, 48. The intensity of the peaks has been normalised to the largest intensity peak.

The spectra seen in figure 5-8 agree well with the experimentally obtained absorption spectra; a peak around ~ 265 – 285 nm (4.4 – 4.7 eV) and a more intense peak around ~ 220 – 240 nm (5.2 – 5.6 eV). The calculated spectra shows more fine structure, such as the shoulders between ~ 240 – 255 nm (4.9 – 5.2 eV), although this is dependent on the degree of Gaussian smearing used. It was thought that a higher amount of smearing might replicate the experimentally obtained absorption spectra better but it would also lead to the loss of some detail: the experimental spectrum is, after all, the absorption measured from a wide range of particles which average 3 nm, but the size range is considerably larger than that of the calculated spectra, i.e. the finer structure may well be present if it were possible to record the experimental spectrum of just one particle, or an ensemble of particles of the same size. The inhomogeneous broadening observed experimentally stems from the wide range of particles observed. For these reasons, it was decided that the Gaussian smearing of 0.1 was a good compromise.

125

As with the LVEE, the calculated spectra of the different particles show that there is a slight blue shift of the whole spectrum as the particle size increases: the peak maximum of the first low-intensity peak around ∼ 265 – 285 nm (4.4 – 4.7 eV) shifts to shorter wavelength (higher energy), with increasing particle size.

The relative intensities of the shoulders in the ∼ 235 – 250 nm (5.0 – 5.3 eV) region of the spectra compared to the main peak around ∼ 225 – 235 nm (5.3 – 5.5 eV) decreases from $(MgO)_{24}$ to $(MgO)_{40}$ to $(MgO)_{48}$ to $(MgO)_{32}$. This decrease in relative intensity for $(MgO)_{32}$ seems to be, at least in part, due to symmetry constraints: all particles considered here have $D_{2h}$ symmetry, with the exception of $(MgO)_{32}$, which has (higher) $T_d$ symmetry. The result of this is that the lower symmetry have a greater variety of excitations that are symmetry- (and potentially dipole-) allowed.

The data displayed in figure 5-8 shows that the absorption spectra are size- dependent. Therefore, further investigation into the effect of particle size on the absorption spectrum was undertaken and was achieved by comparing $(MgO)_{32}$ and $(MgO)_{108}$ clusters, both of $T_d$ symmetry. In these calculations the DZ(D)P basis set was used instead of def2-TZVP, because the $(MgO)_{108}$ calculation was not computationally tractable with the larger basis set. Both spectra have been obtained using the BHLYP *xc*-functional. The spectra seen for $(MgO)_{32}$ and $(MgO)_{108}$ with the DZ(D)P basis set would be expected to be representative of the def2-TZVP basis, since the $(MgO)_{32}$ DZ(D)P and def2-TZVP spectra are very similar, as seen from figure 5-10.
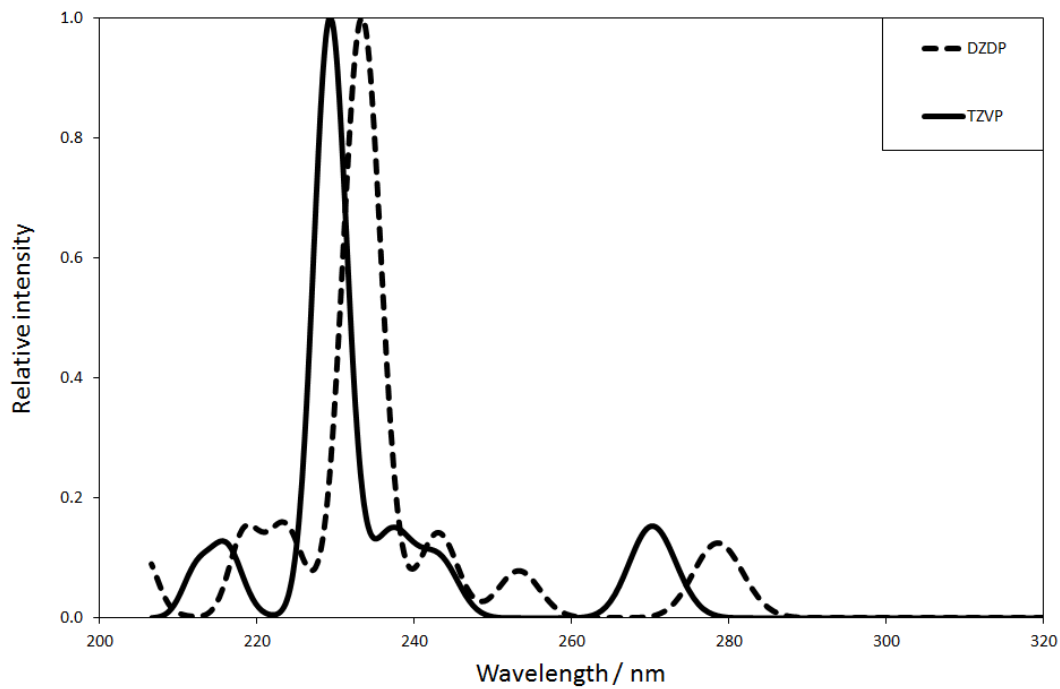
**Figure 5-10:** A comparison between TD-BHLYP/def2-TZVP (solid line) and TD-BHLYP/DZ(DP) (dashed line) absorption spectra for $(MgO)_{32}$. Both spectra include a 0.5 eV rigid red-shift and the intensity of the peaks has been normalised to the largest intensity peak.
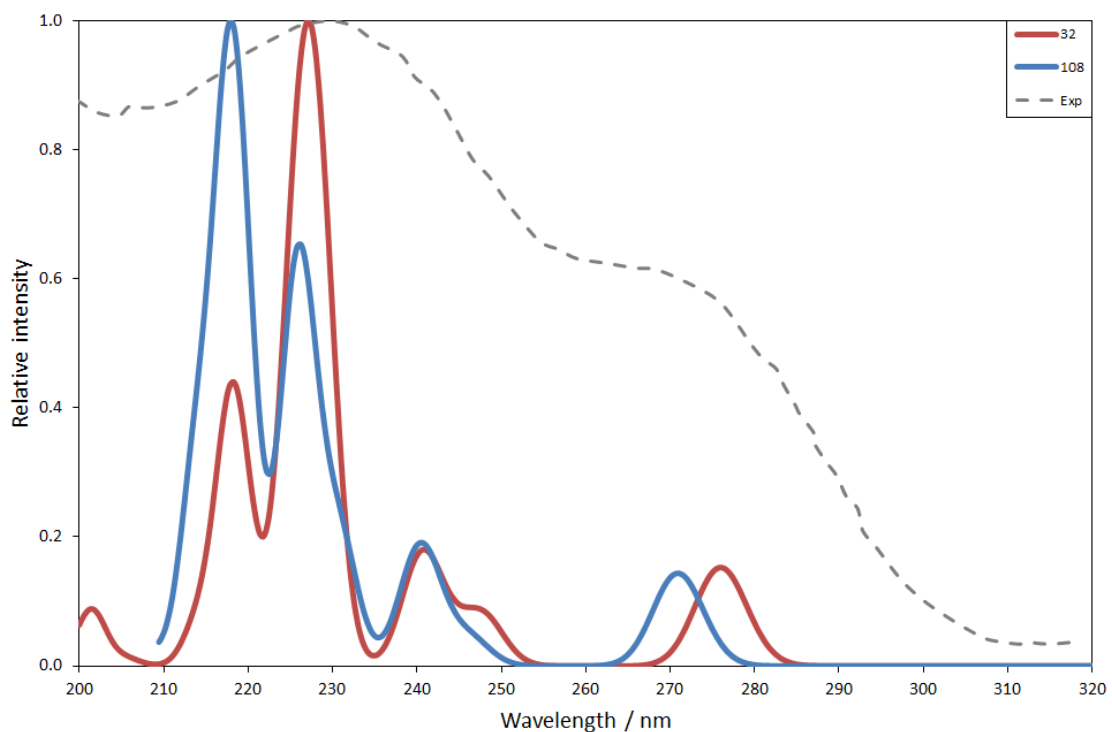
**Figure 5-11:** TD-BHLYP/DZ(D)P calculated absorption spectra for $(MgO)_{32}$ (red line) and $(MgO)_{108}$ (blue line), including a 0.5 eV rigid red-shift. The intensity of the peaks has been normalised to the largest intensity peak. Experimental absorption spectrum (grey dashed line) from reference 20.

Figure 5-11 shows the TD-BHLYP/DZ(D)P spectra for $(MgO)_{32}$ and $(MgO)_{108}$. The low intensity peak in the $265 - 285$ nm ($4.4 - 4.7$ eV) region is blue-shifted when going from $(MgO)_{32}$ to $(MgO)_{108}$. The $235 - 255$ nm ($4.9 - 5.3$ eV) region is similar in both spectra, with the shoulder of the peak decreasing in intensity for $(MgO)_{108}$. When going from $n = 32$ to 108, the low energy peak in the region of $265 - 285$ nm ($4.4 - 4.7$ eV) seems to gain relative intensity to the high energy peaks in the region of $220 - 235$ nm ($5.3 - 5.7$ eV). This, however, is an artifact of the normalization of the peak heights to the largest intensity peak: when the ratio, R, of the sum of oscillator strengths above and below 4.8 eV (260 nm) is taken for $(MgO)_{32}$ and $(MgO)_{108}$, it decreases as the particle size increases, in line with experimental results.[20] R is defined as follows:

$$R = \frac{\sum_{\nu_i > 260\text{nm}} f(\lambda_i)}{\sum_{\nu_i < 260\text{nm}} f(\lambda_i)} \qquad\qquad (5\text{-}1)$$

where $f(\lambda_i)$ is the oscillator strength of the transition with wavelength $\lambda_i$.

The advantage of evaluating the ratios of the oscillator strengths is that this value is independent of the choice of Gaussian broadening parameter. The ratios can be found in table 5-4.

**Table 5-4:** Ratios of summed oscillator strength above and below 260 nm (R) as calculated with TD-BHLYP/DZ(D)P.

|   | $(MgO)_{32}$ | $(MgO)_{108}$ |
|---|---|---|
| R | 0.072 | 0.062 |

As mentioned in section 3.1.1.2, previous studies have employed the B3LYP *xc*-functional, so it is interesting to compare the unshifted TD-B3LYP spectrum with the red-shifted TD-BHLYP spectrum, as seen in figure 5-12. The $(MgO)_{32}$ spectrum calculated with TD-B3LYP is similar to that reported by McKenna and co-workers[166,167] using the embedded cluster methodology to model a cluster centered on an oxygen corner atom. McKenna and co-workers spectrum shows a low peak around ~ 335 nm (3.7 eV) and a more intense peak at ~ 270 nm (4.6 eV). As the more intense peak is centered at the same energy as the experimental shoulder (270 nm, 4.6 eV), the conclusion was made by McKenna and co-workers that the calculated peak is the same as the experimental shoulder and that the experimentally observed peak at 230 nm (5.4 eV) results from purely edge-based excitations. An additional hypothesis was also made, namely that the ~ 335 nm (3.7 eV) peak was too weak to be observed experimentally. However, from the results presented above using an isolated cluster approach, it appears that TD-B3LYP may not describe certain excitations well, potentially lowering the energy of charge-transfer excitations. McKenna and co-workers have labelled both calculated excitations at 3.7 eV and 4.6 eV as local excitations, based around the corner oxygen. However, due to the

small size of the region that is described quantum mechanically, the exciton has to be localised around the corner atom. Therefore, it might be more accurate to say that the calculated peak position at ~ 335 nm (3.7 eV) is a CT artifact. In light of the CT character of the excitation, it seems more accurate to say that the calculated low intensity 3.7 eV peak corresponds to the erroneously stabilised experimental 4.6 eV peak, and not a potential dark excitation, as suggested by McKenna and co-workers.
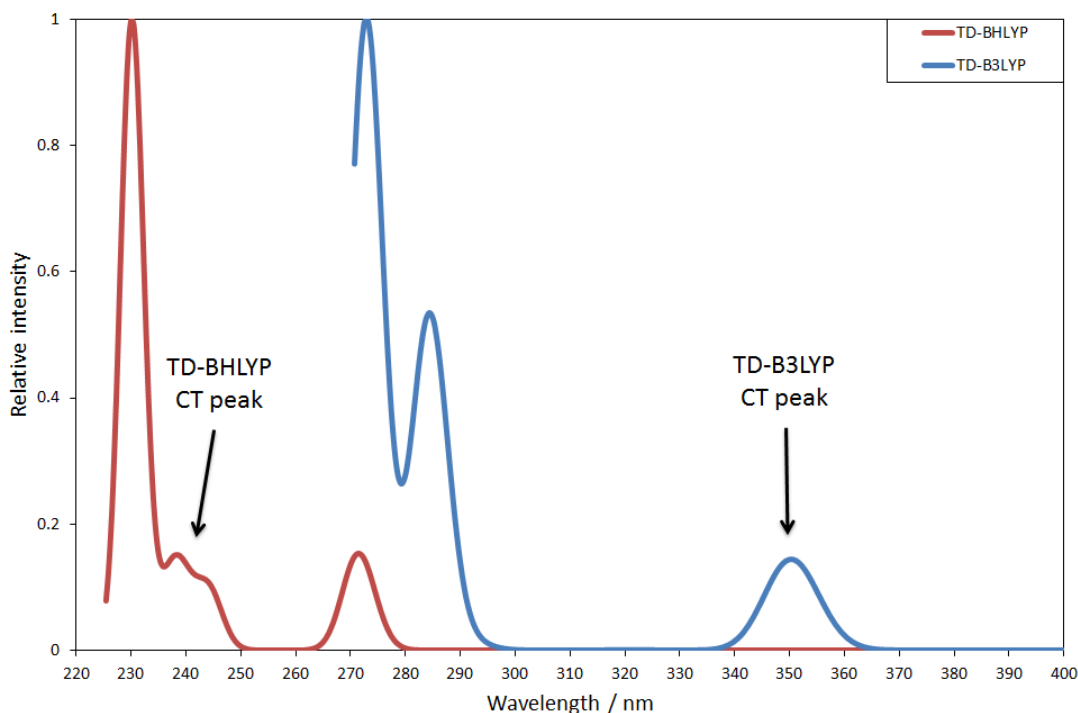


**Figure 5-12:** Comparison of the absorption spectrum of $(MgO)_{32}$, as calculated with TD-B3LYP/def2-TZVP (blue line) and TD-BHLYP/def2-TZVP (red line). The TD-BHLYP spectrum is red-shifted by 0.5 eV.

## 5.7    Character of the excitations

Having investigated the important aspects of electronic excitations in these MgO nanoparticles, and the ability of TDDFT to produce spectra in satisfactory agreement with experiment (subject to appropriate choice of *xc*-functional), it is of interest to study the

character of the excitations at an atomistic level, i.e. to investigate which atoms are involved in a given excitation. To obtain a quantitative measure of the change in electron density upon excitation, it is useful to compare the ground and excited state charges for any given excitation. Here, charges have been obtained from Natural Bonding Order (NBO) analysis (section 2.2.8.1), as Mulliken charges have been shown to be unreliable for MgO by previous tests by the author, especially for $(MgO)_{18}$: atomic charges of unrealistic proportions (~ 18 a.u.) were attributed to the atoms responsible for the dipole moment. The NBO charges are obtained for each atom, and the charges can also be analysed in terms of how much they contribute to the total charge difference in their sub-lattice $\left(\Delta_{Mg}= \sum_{i=1}^{n_{Mg}} \Delta q_i , \Delta_O= \sum_{j=1}^{n_O} \Delta q_j\right)$. Furthermore, density difference plots, describing the redistribution of electronic charge upon excitation, have been generated for the different particles. Here, only the character of optically allowed excitations have been studied, so as to understand and interpret the absorption spectra more accurately.

### 5.7.1  Cubic $(MgO)_{32}$ and $(MgO)_{108}$

Both $(MgO)_{32}$ and $(MgO)_{108}$ are cubic particles and therefore provide an interesting place to begin studying the atomic contribution to the excitations. The ~ 270 nm (4.6 eV) peak for $(MgO)_{32}$ can be attributed to an electronic excitation from the four oxygen corner atoms (90% of $\Delta_O$) to the twelve magnesium edge atoms coordinated directly to the oxygen corners (72% of $\Delta_{Mg}$), along with a small contribution (18% of $\Delta_{Mg}$) from the four magnesium corner atoms. This excitation has been visualised in figure 5-13-A, showing the electron density difference between the ground and excited states. Both analysis methods suggest similar excitation behaviour, although the magnesium density differences are less apparent. This is due to the fact that no individual Mg atom contributes significantly but the 12 edge and 4 corner Mg atoms combined provide a significant contribution to the density difference.

The higher energy $(MgO)_{32}$ excitation at ~ 240 nm (5.2 eV) shows a different character to the 270 nm (4.6 eV) excitation: an electron is excited mainly from the oxygen corner

atoms (84% of $\Delta_O$) to the magnesium corners (60% of $\Delta_{Mg}$), with contributions from edge atoms being considerably reduced (11% of $\Delta_O$ and 35% of $\Delta_{Mg}$). This excitation exhibits CT- characteristics, with a 0.6 nm separation between the corner sites, i.e. the charge accumulation and depletion are spatially separated by the entire length of the cluster.

The ~ 230 nm (5.4 eV) peak is different in that the electron is excited from oxygen edge atoms (70% of $\Delta_O$) to magnesium corner atoms (88% of $\Delta_{Mg}$), with a minor contribution from the four bulk oxygen atoms in the particle (18% of $\Delta_O$). This density difference associated with this excitation is visualized in figure 5-13-B. This analysis method is, as previously, in agreement with the quantitative NBO data obtained for this excitation.

The lower energy peak excitations seem to be associated with an excited electron that is localised over more atoms than the corresponding hole. In contrast, the higher energy peak results from excitations that are based on an excited electron that is localised over fewer atoms than the corresponding hole. Apart from the CT character excitation, most of the optically allowed excitations for $(MgO)_{32}$ are local, i.e. the exciton is localized on neighbouring atoms, rather than delocalized over spatially well-separated atoms.
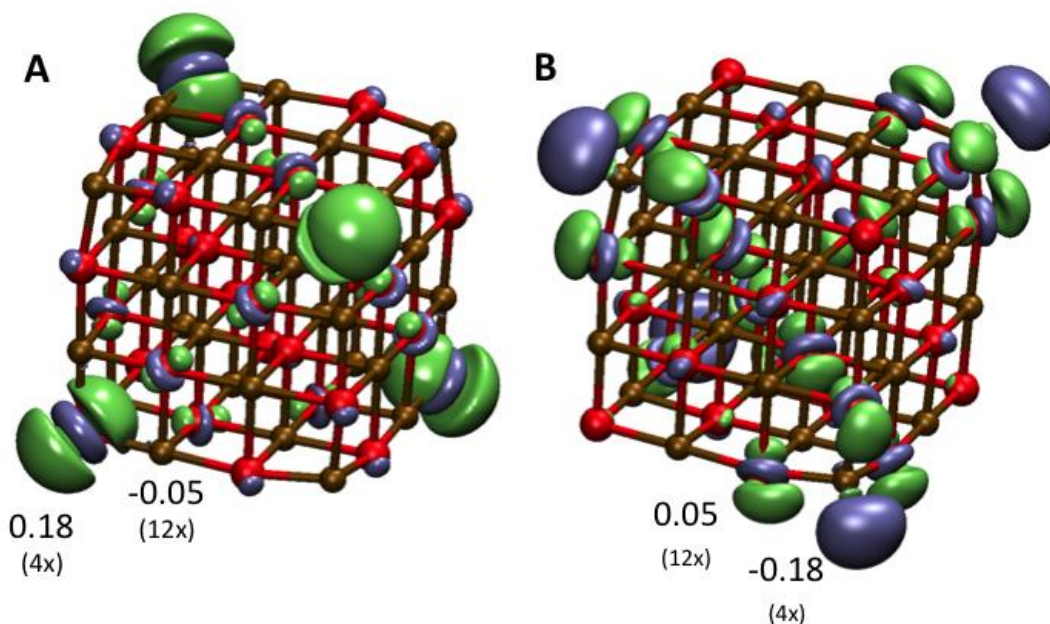
**Figure 5-13:** TD-BHLYP/def2-TZVP calculated ground and excited state electron density difference for the excitation at 4.6 eV (A) and 5.4 eV (B) of the $(MgO)_{32}$ particle: blue shows charge accumulation (excess of electron density in the excited state), and green shows charge depletion (deficit of electron density in the excited state) when an isosurface of 0.01 a.u. is used. The numbers indicate the most significant differences in NBO charge of the excited state and ground state charge, as well as the multiplicity of each site. Red spheres represent oxygen atoms, brown magnesium atoms.

The larger $(MgO)_{108}$ cluster shows similar excitation behaviour to $(MgO)_{32}$: the ~ 270 nm (4.6 eV) peak results from an electronic excitation from the four oxygen corner atoms (86% of $\Delta_O$) to the twelve magnesium edge atoms (77% of $\Delta_{Mg}$) directly bonded to the oxygen corner atoms. The same behaviour can be attributed to the ~ 240 nm (5.2 eV) peak. Looking at the ~ 210 – 240 nm (5.2 – 5.9 eV) part of the spectrum, two distinct peaks can be seen. The lower energy peak corresponds to an excitation from the twelve oxygen edge atoms bonded to the magnesium corner atoms (60% of $\Delta_O$) to the four magnesium corner atoms (86% of $\Delta_{Mg}$), as well as a small but noticeable contribution (20% of $\Delta_O$) of bulk-like oxygen atoms near the magnesium corners. The higher energy peak is less well defined; it is a combination of different excitations close in energy, although they all have the same underlying feature: an electron is excited from a number of oxygen corner (10 – 30% of $\Delta_O$) and edge atoms (~ 60% of $\Delta_O$) to magnesium corner (40 – 50% of $\Delta_{Mg}$) and edge atoms (30 – 40% of $\Delta_{Mg}$). These excitations are the ones with the most CT character,

and appear to be the equivalent to the CT-excitation seen for $(MgO)_{32}$, although both the oxygen as well and magnesium corner atoms contribute more towards the excitations.

### 5.7.1.1   Cuboid $(MgO)_n$ particles and general remarks

The above analysis has also been performed on other rocksalt particles of cuboid structure, i.e. where not all particle sides are equally long. The analysis of charge differences for $(MgO)_{24}$ suggests that the ~ 265 – 285 nm (4.4 – 4.7 eV) peak results from an excitation in which an electron is excited from the four corner oxygen atoms (91% of $\Delta_O$) to magnesium corner (45% of $\Delta_{Mg}$) and edge (44% of $\Delta_{Mg}$) atoms. Comparing this result with that of $(MgO)_{32}$, it can be seen that the magnesium corner atoms are considerably more involved at 45%, compared to 18% in the case of $(MgO)_{32}$.

The ~ 240 nm (5.2 eV) peak as well as the ~230 nm (5.4 eV) peak correspond to excitations in which an electron is transferred from the oxygen corner (30 – 55% of $\Delta_O$) and edge (30 – 45% of $\Delta_O$) atoms to magnesium corner atoms (80 – 95% of $\Delta_{Mg}$). This is again different to the excitation for $(MgO)_{32}$, where the contribution of the oxygen corner atoms is reduced form 84% of $\Delta_O$ to 30 – 55% of $\Delta_O$.

The charge differences for $(MgO)_{40}$ and $(MgO)_{48}$ are very similar to that of $(MgO)_{24}$. Nanocuboids, in comparison to $(MgO)_{32}$ and $(MgO)_{108}$, are more difficult to characterise as one edge site is not symmetry equivalent to another edge site, making the results less obvious. What all clusters have in common is that the low energy excitations have the electron delocalised over more atoms than the corresponding hole, whereas for the higher energy excitations the excited electron is localised over fewer atoms compared to the corresponding hole. Furthermore, an interesting observation is that in none of the particles studied do the symmetry allowed excitations correspond to pure corner or edge excitations, i.e. excitations in which an electron is excited from a corner to a corner (or from an edge to an edge) without any other major contributions. In higher energy excitations, the edge contributions do increase when going from $(MgO)_{32}$ to $(MgO)_{108}$, so it would be possible that for considerably larger clusters (>> 1 nm), these become the

dominant - and possibly only sites - involved these in excitations. As already stated, this cannot be tested with the methodology applied here and is also not very likely as the corner involvement might get substituted for face (5-coordinated) atoms or even atoms below the surface. Experimental data[20,148,228] leads to the conclusion that, on the basis of the evolution of the shape of the absorption spectra with particle size, the ~ 270 nm (4.6 eV) peak is the result of an excitation from a corner (3-coordinated) atom and the ~ 220 – 240 nm (5.2 – 5.6 eV) peak is due to excitation from an oxygen edge (4-coordinated) atom. As the lower energy peak become less intense, in agreement with the fact that as the particle size increases, the relative amount of edge sites decreases. The analysis presented above agrees with the experimental analysis. However, from the charge differences, it seems that the experimental conclusions are too simplistic: at least for particles up to 1 nm, it would be misleading to identify these features as exclusively corner or edge excitations, depending on the coordination environment of the oxygen atoms involved. This work has shown that the centre(s) associated with an electronic excitation tend to differ in coordination number, and an excitation involved a mixture of such sites. This has previously been hypothesized to explain the experimental luminescence spectrum of MgO nanoparticles exposed to $H_2$,[156] but was not demonstrated conclusively. Furthermore, it is important to remember that any peak in an absorption spectrum is made out of several individual excitations, each varying from the other by a small degree.

### 5.7.1.2　B3LYP excitation behaviour

As previous computational work has been performed using the B3LYP *xc*-functional, it is interesting to compare the above analysis of the BHLYP excitations to those obtained with B3LYP. In line with the $\Lambda$ value of 0.13 from table 5-3, the lowest excitation is a CT-excitation, where an electron is transferred from the oxygen corner atoms (89% of $\Delta_O$) to the magnesium corner atoms (71% of $\Delta_{Mg}$), as visualized in figure 5-14.
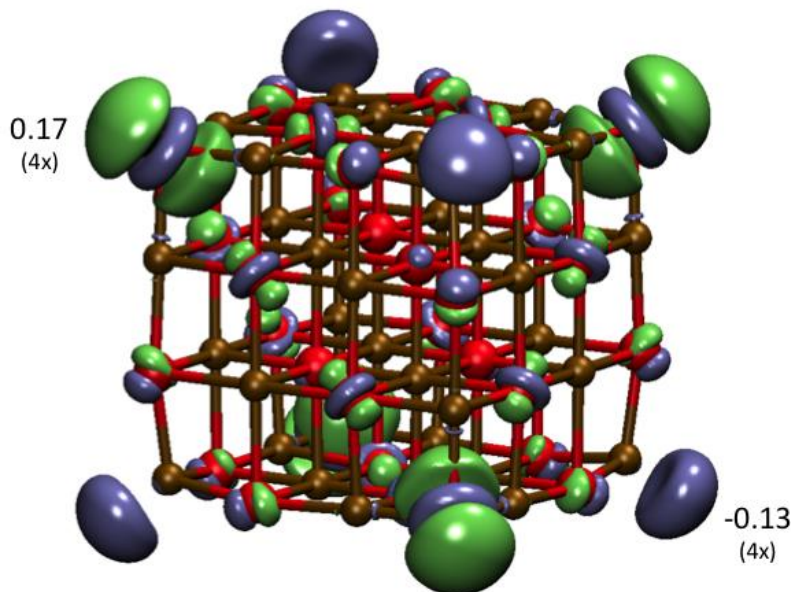
**Figure 5-14:** TD-B3LYP excited state – ground state density difference for the excitation corresponding to the 350 nm charge-transfer peak of $(MgO)_{32}$ (blue, excess of electrons in the excited state; excited electron/ green, deficit of electrons in the excited state; hole) with isovalue of 0.01 a.u.. The numbers indicate the most significant differences in NBO charge of the excited state and ground state charge, as well as the multiplicity of each site. Red spheres represent oxygen atoms, brown magnesium atoms.

As mentioned previously, TD-BHLYP also predicts an excitation with CT character, but this is not the lowest excitation. This means that there is a change in character of the lowest optically allowed excited state, as well as a change in the ordering of excited states when comparing TD-B3LYP and TD-BHLYP. This is further evidence that TD-B3LYP fails in correctly describing the excitation spectra for MgO nanocuboids, as it is unable to assign accurate energies to locate excited states with CT character.

To return to previous work performed on MgO excitation via embedded cluster calculations centered on an oxygen corner atom, it is impossible for this approximation to yield the sort of CT-excited state that can be found in isolated $(MgO)_{32}$ with TD-B3LYP, as the embedded cluster approach does not have any quantum mechanically described magnesium corner atoms. It is therefore not surprising that, although the same *xc*-functional has been used, the lowest excitation is found to have a different character,[156,163,166,167] where the corner and the neighbouring oxygen atoms are the main

contributors to the excitation. This embedded cluster excitation leads to a peak around 3.6 − 3.8 eV, i.e. it takes the character of the lowest TD-BHLYP excitation but at energies similar to those obtained from TD-B3LYP for $(MgO)_{32}$. This shows that embedded cluster calculations yield an accurate description of the excitation but at spuriously stabilized energies. This is presumably due to the fact that the electron in the embedded cluster calculation cannot delocalise from corner to corner atom, as only one corner atom is described quantum mechanically.

## 5.8    Beyond Nanocuboids

As shown in figure 3-1, Transmission Electron Microscopy (TEM) images of MgO nanoparticles show mainly nanocuboids. However, in principle, particles with different crystal cuts to the above studied (*100*) are possible. One such example would be a cuboctahedral particle, which exhibits a mixture of (*100*) and (*111*) surfaces, as shown in figure 5-15-A. Atoms on a (*111*) surface are 3-coordinated, and therefore particles exhibiting such surfaces have a much higher concentration of 3-coordinated sites compared to nanocuboids.

To obtain some insight into the effect a different surface can have, the cuboctahedral $(MgO)_{28}$ particle was optimised using the *xc*-functional BHLYP and the def2-TZVP basis set, and vertical excitation energies have been obtained from TD-BHLYP, from the BHLYP-optimised geometry. The LVEE for the cuboctahedral $(MgO)_{28}$ particle is at 3.60 eV, lower than the LVEE of similar sized nanocuboids (4.96 eV for $(MgO)_{24}$ and 5.07 for $(MgO)_{32}$). The nature of the excitation of the cuboctahedral particle is also fundamentally different compared to that of the cuboid particles, as it involves all atoms on the (*111*) face, as seen in figure 5-15-B. This delocalisation is (presumably) inherently linked to the lowering of the excitation energy.
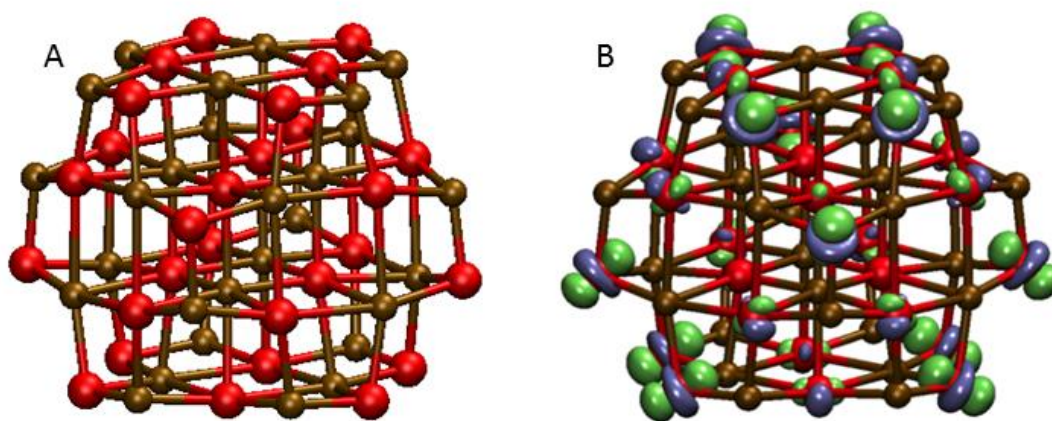
**Figure 5-15:** A shows a BHLYP/def2-TZVP optimized structure of the $(MgO)_{28}$ cuboctrahedral particle and B its TD-BHLYP excited state – ground state density difference for the lowest optically allowed excitation (blue, excess of electrons in the excited state; excited electron/ green, deficit of electrons in the excited state; hole) with isovalue of 0.01 a.u..

An increase of 3-coordinated surface sites decreases the LVEE dramatically and it can be seen that different morphologies have a considerable effect on the excitation energies. Figure 5-16 shows that the previously mentioned hexagonal tube-like clusters ($(MgO)_6$, $(MgO)_9$, $(MgO)_{12}$ and $(MgO)_{18}$) behave in a similar way to the cuboids in that the LVEE increase with particle size, and the LVEE appears to reach a plateau above 5 eV. Figure 5-16 also shows that the bubble-like clusters exhibit a very different behaviour, which has previously been seen for ZnS [229]: the LVEE increase from $(MgO)_8$ to $(MgO)_{12}$, only to decrease again when going from $(MgO)_{12}$ to $(MgO)_{16}$. Both the ground state geometries of the bubble-like structures $(MgO)_8$ and $(MgO)_{16}$ are shown in figure 5-17.
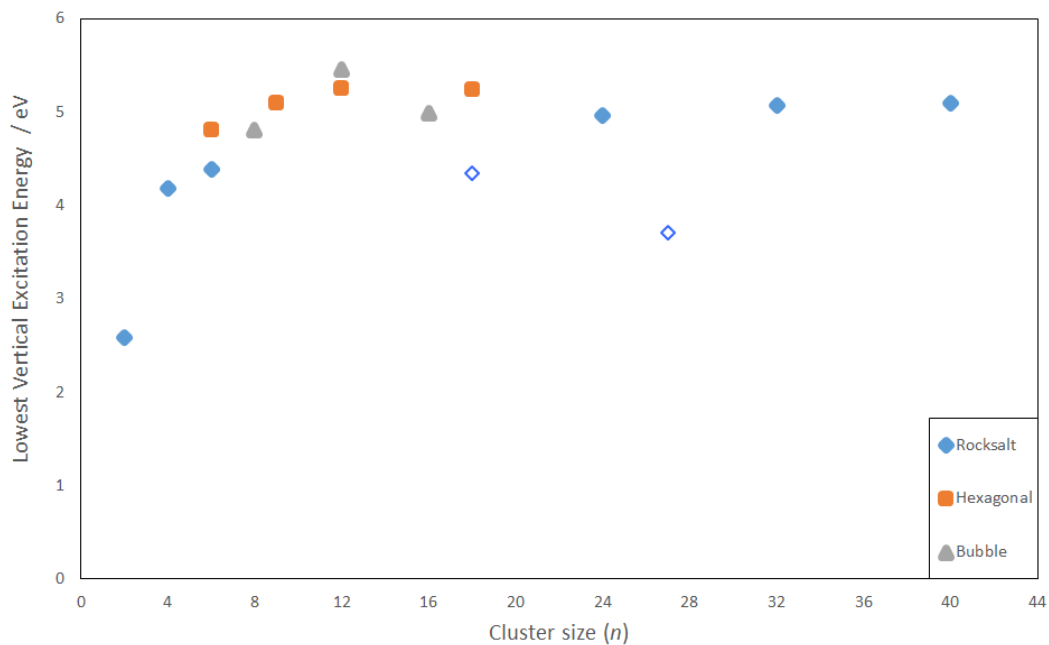
**Figure 5-16:** Lowest vertical excitation energy (LVEE) of $(MgO)_1$ to $(MgO)_{40}$ calculated using TD-BHLYP/def2-TZVP. Blue diamonds show rocksalt structures particles, orange square hexagonal tubes, grey triangles bubble-like structures. Open symbols correspond to particles with faces containing odd number of atoms, i.e. $(MgO)_{18}$ and $(MgO)_{27}$.
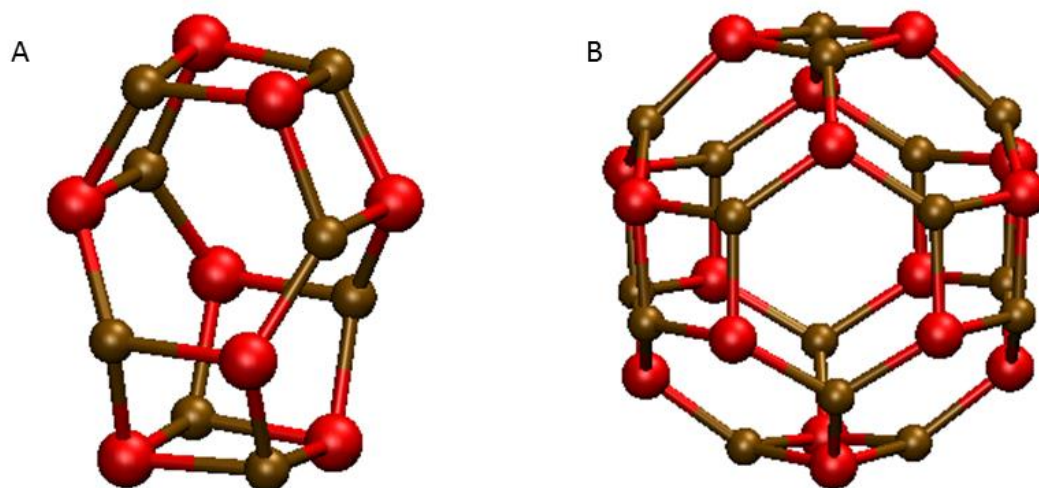


**Figure 5-17:** B3LYP/def2-TZVP optimised structures of A $(MgO)_8$ and B $(MgO)_{16}$.

## 5.9   Conclusions

The work presented here is a study of the suitability of TDDFT to predict and rationalise the optical absorption spectra of cubic and cuboid MgO nanoparticles. It can be concluded that vertical excitations are not as straightforward to predict as previously thought: TD-B3LYP offers a poor description by underestimating the absorption onset, which is most likely due to the fact that the lowest excitation is an erroneously stabilized corner to corner excitation which therefore exhibits CT character, which *xc*-functionals with low HFE struggle to describe properly. However, the use of TD-BHLYP, a hybrid *xc*-functional with a high percentage of HFE, seems to predict the absorption spectra of the studied $(MgO)_n$ particles more reliably, albeit a rigid 0.5 eV red-shift appears to be required to obtain good agreement with experiment. The range-separated CAM-B3LYP *xc*-functional also yields good agreement with experiment. The problem with this functional, however, is that it is only implemented in less efficient quantum chemistry codes.

As the character of the excitations were studied in more detail, an atomistic picture was obtained for the excitations that contribute most to the absorption peaks between the range of $\sim 200 - 300$ nm ($\sim 4 - 6$ eV). These excitations typically comprise an exciton that is delocalized over 3-coordinated corner and 4-coordinated edge sites. It therefore seems overly simplistic to label excitations as simply 'corner' or 'edge' excitations, as some previous experimental studies have done, although it is worth nothing that, for the $(MgO)_{108}$ particle, edge contributions to the excitations become more pronounced.

Further investigation led to the discovery that particles with different morphologies, such as the cuboctahedral particle $(MgO)_{28}$, have considerably different absorption energies and behaviour. This is not studied further in this thesis, although it provides an interesting avenue for future investigations.

This study naturally leads to further questions. Do other rocksalt-structured nanoparticles comprised of different materials also exhibit CT-excitations? Is MgO really a useful computational model, giving insight into the properties of other similar materials, or is MgO the only material in which the accurate description of the excited state needs the use

of an *xc*-functional with high percentage of HF exchange? These questions are considered in the next chapter.

# 6. Optical properties of other particles with rocksalt structure

Before the results of this chapter are discussed, it should be noted that all alkaline earth oxide calculations, as well as those of magnesium chalcogenides, have been performed by the author. However, the optimised geometries of cadmium oxide (CdO) and lead sulphide (PbS) have been obtained from Dr. Martijn Zwjnenburg.

## 6.1   Introduction

Chapter 5 showed that the absorption spectra of MgO nanoparticles are red-shifted when compared to the absorption spectra of the bulk. For semiconductor materials, however, the opposite is true: generally, the absorption spectra of the nanoparticles are blue-shifted with respect to the absorption spectra of the bulk. This is due to quantum confinement[146,230–233]: the exciton (electron-hole pair) is delocalised over the entire particle, which means that as the particle size decreases, the excited state is spatially more and more constrained, which results in an increase of the excitation energy.

The excited state localisation is, as discussed in detail in chapter 5, very different in MgO particles: the exciton gets localised on corners (3-coordinated sites) and edges (4-coordinated sites), resulting in a lowering of the excitation energies to about 4.6 eV for the 3 nm particles synthesised by Stankic *et al.*,[20] compared with 7.8 eV in the bulk.[186]

The issue with describing the MgO excited states is that the use of the commonly employed *xc*-functional B3LYP (as well as other *xc*-functionals with no or low amounts of HFE), in TDDFT calculations is problematic due to charge transfer (CT) excitations that get erroneously stabilised. A CT excitation is characterised by there being no, or limited, overlap between the orbitals involved in the excitation. The solution to this problem seems to be to employ *xc*-functionals with an increased amount of HFE, such as

BHLYP, or the use of CAM-B3LYP, a range-separated $xc$-functional, as found in chapter 5.

To extend the work from chapter 5, the focus here is on other materials that crystallise experimentally in the rocksalt structure, namely calcium oxide (CaO), strontium oxide (SrO), barium oxide (BaO), magnesium sulphide (MgS), magnesium selenide (MgSe), cadmium oxide (CdO) and lead sulphide (PbS). In this chapter, these materials are studied as cubic $(MX)_{32}$ structures, approximately $0.6 - 0.7$ nm in size. These nanoparticles are considered in terms of their excitation localisation, as well as the connection between the optical properties and surface pinning of the excited state. Furthermore, the theoretically predicted absorption spectra are compared to the measured absorption spectrum for experimentally well-defined CaO and SrO nanoparticles.[19]

## 6.2 Methodology

The $(MX)_{32}$ nanoparticles (MX = BaO, CaO, CdO, MgS, MgSe, SrO, PbS) have been optimised using DFT, and the singlet vertical excitation energies have subsequently been calculated using TDDFT on the DFT-optimised ground state geometries.

The $xc$-functionals used were B3LYP and BHLYP, to outline the differences between the use of low (20%) and high (50%) amounts of HFE. The basis set used in all calculations is the triple-$\zeta$ quality def2-TZVP basis set, as was used in the study of the excitation behaviour of MgO nanoparticles in the previous chapter. The basis set includes effective core potentials (ECP) for barium, strontium and lead.[234,235]

The standard deviation of the Gaussian function used in the custom script to create the absorption spectra is 0.1 eV, which has been chosen to approximate experimental peak shapes for MgO, as discussed in chapter 5.

Similarly to previous analysis on MgO discussed in chapter 5, the character of the excitation has been analysed by evaluating the difference in the natural bond order (NBO)

charges[236] between the ground and excited states. The $\Lambda$ diagnostic of Peach *et al.*[89] has been employed to identify potential CT excitations.

All calculations have been performed using the TURBOMOLE 6.4 code, apart from the TD-B3LYP calculations of $\Lambda$, where the GAMESS-US (1 CT 2010 – R1) code has been used. Visualisation has been performed using VMD.

## 6.3 Results

After the ground state structure determination, the optical properties of these particles are studied and a link between the dielectric constants of the corresponding bulk materials and the degree to which the Coulombic interaction between the excited electron and the excited electron-hole is screened in the different nanoparticles is established.

### 6.3.1 Ground state structures

It is useful to examine the general features of the ground state structures of the $(MO)_{32}$ (M = Mg, Ca, Sr, Ba), $(MgX)_{32}$ (X= O, S, Se), $(CdO)_{32}$ and $(PbS)_{32}$ particles, before analysing the optical properties.
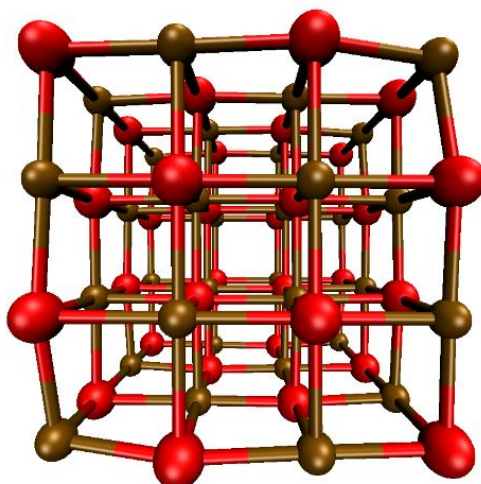
**Figure 6-1:** B3LYP/def2-TZVP optimised structure of the $(MgO)_{32}$ nanoparticle as an example; all other $(MX)_{32}$ particles studied have the same structure and morphology.

As seen in figure 6-1, the $(MX)_{32}$ nanoparticles are cubic with high ($T_d$) symmetry. The edges consist of four ions and the faces contain sixteen ions. Table 6-1 illustrates the particle sizes in terms of the edge lengths, as well as the $M - M$ and $X - X$ body diagonals. The values obtained with BHLYP and B3LYP are in good agreement with each other. As the magnesium or oxygen ions are replaced by heavier ions, edge lengths and body diagonals increase in size, as would be expected based on trends in the ionic radii.

**Table 6-1:** Distances between corner ions on the same face, as calculated for structures optimised using the BHLYP *xc*-functional (B3LYP results in brackets). All values given in Å.

|  | MgO | CaO | SrO | BaO | MgS | MgSe | CdO | PbS |
|---|---|---|---|---|---|---|---|---|
| M – X edge | 5.87 (5.93) | 6.76 (6.79) | 7.24 (7.29) | 7.70 (7.76) | 7.29 (7.33) | 7.68 (7.73) | 6.52 (6.60) | 8.97 (8.96) |
| X – X diagonal | 8.42 (8.52) | 9.52 (9.57) | 10.13 (10.20) | 10.67 (10.75) | 10.69 (10.77) | 11.32 (11.40) | 9.28 (9.41) | 12.71 (12.73) |
| M – M diagonal | 8.17 (8.26) | 9.59 (9.64) | 10.34 (10.41) | 11.11 (11.19) | 9.89 (9.94) | 10.35 (10.41) | 9.16 (9.26) | 12.67 (12.62) |

### 6.3.2  Optical gap

Table 6-2 shows the lowest vertical excitation energies of $t_2$ symmetry for the different particles, predicted by TD-B3LYP and TD-BHLYP, in addition to the $\Lambda$ diagnostic values obtained from TD-B3LYP. Unfortunately, convergence could not be reached in the $\Lambda$ calculation for BaO, and so no value is reported. The $t_2$ excitations corresponds to the optical gap $\Delta_o$ of the respective particles, as excitations belonging to all other irreducible representations are optically forbidden (i.e. are dark excitations) for the electric dipole of the transition moment operator. Similarly to what was found for MgO, TD-B3LYP calculated $\Delta_o$ values are always lower than those obtained using TD-BHLYP. Interestingly, the $\Delta_o$ and $\Lambda$ values obtained vary considerably between the different nanoparticles under consideration.

**Table 6-2:** Optical gap ($\Delta_o$) for $(MX)_{32}$ particles calculated using TD-BHLYP and TD-B3LYP, as well as the TD-B3LYP $\Lambda$ values for the lowest $t_2$ excitation. In the case of PbS, the calculation was performed with the def2-SVP basis-set by Dr. Berardo. $\Delta_o$ values are in eV.

| | MgO | CaO | SrO | BaO | MgS | MgSe | CdO | PbS |
|---|---|---|---|---|---|---|---|---|
| $\Delta_{o,\ B3LYP}$ | 3.55 | 3.30 | 2.89 | 2.91 | 3.62 | 3.21 | 1.48 | 2.71 |
| $\Delta_{o,\ BHLYP}$ | 5.08 | 4.35 | 3.91 | 3.86 | 4.82 | 4.37 | 3.01 | 3.39 |
| $\Lambda_{\ B3LYP}$ | 0.130 | 0.168 | 0.174 | - | 0.240 | 0.373 | 0.429 | *0.476* |

In the case of the $(MO)_{32}$ particles, $\Delta_o$ also corresponds to the overall lowest vertical excitation energy for each of the particles, i.e. all dark excitation have higher excitation energies. From table 6-2, it is clear that for both *xc*-functionals, as magnesium is replaced by heavier alkaline earth metals, $\Delta_o$ decreases, in line with what is experimentally observed for both bulk systems[172,237] and nanoparticles.[19] The difference in the optical gap between SrO and BaO for TD-B3LYP is so small that the slight increase for BaO is within the uncertainty of the methodology. The overall change in $\Delta_o$ when going from MgO to BaO is more pronounced when using the *xc*-functional BHLYP, which includes a greater percentage of HFE. The largest variation in the TD-BHLYP $(MO)_{32}$ data set is between MgO and CaO (0.73 eV), whereas the TD-B3LYP data set shows the largest variation to be between CaO and SrO (0.41 eV). As already mentioned, $\Delta_o$ is always larger for TD-BHLYP than it is for TD-B3LYP but the difference between the two decreases as the cation mass increases: the value of $\Delta_o$ calculated for MgO with TD-BHLYP is 1.53 eV larger than its TD-B3LYP counterpart, while the difference decreases to 1.05 eV for CaO, 1.02 eV for SrO and 0.95 eV for BaO.

The $(MgX)_{32}$ series in table 6-2 shows that the TD-BHLYP prediction of $\Delta_o$ smoothly decreases as the anion becomes heavier, similar to what is found when varying the cation in the $(MO)_{32}$ series. The largest change is between MgS and MgSe, at 0.45 eV (compared

to 0.26 eV between MgO and MgS). The predicted values for $\Delta_o$ using TD-B3LYP, however, exhibit different behaviour: $\Delta_o$ increases slightly (by 0.07 eV) when going from MgO to MgS and then decreases by 0.41 eV when going from MgS to MgSe. It is possible that the increase in $\Delta_o$ when going from MgO to MgS is an artefact of TDDFT, as the increase is so small. However, it is clear that TD-B3LYP does not follow the same pattern as TD-BHLYP. In line with the $(MgX)_{32}$ TD-BHLYP data, the biggest change in $\Delta_o$ is between MgS and MgSe. Interestingly, the lowest $t_2$ excitation for the $(MgX)_{32}$ materials is not always the lowest vertical excitation. In both the TD-BHLYP and TD-B3LYP calculations, the lowest $a_2$ excitation decreases in energy when going along the MgX series, and becomes lower than the $t_2$ excitation for MgSe in the TD-B3LYP calculations (at 3.16 eV for the $a_2$ excitation) and for MgS and MgSe in the TD-BHLYP calculation (at 4.57 eV and 4.05 eV respectively for the $a_2$ excitation). The author is not aware of any study of MgX nanoparticles or absorption spectra of all (bulk) MgX materials, so it is difficult to assess the different trends, as the experimental work has focussed on zinc blende structures rather than rocksalt materials.[188,238–240]

The $\Delta_o$ for CdO is predicted to be smallest in both the TD-BHLYP and TD-B3LYP series and is also the most red-shifted of the $(MX)_{32}$ series. The difference between the TD-BHLYP and TD-B3LYP calculated optical gap is similar to that predicted for MgO, both at 1.53 eV. The author is, again, not aware of an internally consistent experimental study of MgO and CdO nanoparticles, but the calculated red-shift in the optical gap for CdO is similar to the red-shift in the experimental absorption onset between bulk MgO at 7.67 eV and bulk CdO at 5.9 eV.[178]

Finally, the $\Delta_o$ in PbS is predicted both by TD-BHLYP and TD-B3LYP to be second lowest of all the $(MX)_{32}$ particles studied here, with a 0.68 eV difference between the calculated values. It should be noted that no spin-orbit coupling effects have been included in the calculations, which might be significant in materials containing lead. Although the values obtained in this study are consistent within the set of particles studied, it is possible that the experimental $\Delta_o$, and indeed those obtained from calculations including spin-orbit coupling, would be significantly lower than predicted here. The lowering of excitation

energies upon inclusion of spin-orbit coupling is expected as mixing of singlet and triplet excitations could occur.

The $\Lambda$ value, as devised by Peach *et al.*,[89,109] is a diagnostic test of the spatial overlap between the Kohn-Sham orbitals contributing to the TDDFT excitation. The cut-off value below which an excitation is most likely to have CT character is 0.3 for TD-B3LYP, as previously mentioned. From the $\Lambda$ values shown in table 6-2, it can be seen that the $\Lambda$ values for all $(MO)_{32}$ particles fall below the cut-off value proposed by Peach *et al.*[89] The $\Lambda$ values increases ever so slightly down the series MgO < CaO < SrO but the variation in the $\Lambda$ values between particles with different chemical composition is actually smaller than the variation seen in table 5-3, where the $\Lambda$ values were presented for differently sized MgO nanoparticles. In the case of $(MgX)_{32}$, the link between $\Lambda$ values and chemical composition seems stronger, as the $\Lambda$ value increases down the series MgO < MgS < MgSe, actually becoming slightly larger than the 0.3 cut-off for MgSe. Selenium is a softer ion than sulphur, which in turn is softer than oxygen, which leads to a less pronounced CT character in any excitation, as the electron density spreads more for a softer ion, and therefore increases the orbital overlap (although the bond distance increases from oxygen to sulphur to selenium, which potentially reduces the orbital overlap). Both the $(CdO)_{32}$ and $(PbS)_{32}$ $\Lambda$ values lie clearly above the cut-off. The $\Lambda$ value for $(PbS)_{32}$ reported in table 6-2 was calculated by Dr. Enrico Berardo using the smaller def2-SVP basis set[82] because of convergence issues when using the def2-TZVP basis set. However, the def2-TZVP value is likely to be similar to that obtained using the smaller basis set, as the TD-B3LYP predicted $\Delta_o$ values are very similar (and still within the accuracy of TDDFT), at 2.64 eV for def2-SVP and at 2.71 eV for def2-TZVP. This analysis of the orbital overlap suggests that for $(CaO)_{32}$, $(SrO)_{32}$, $(BaO)_{32}$ and $(MgS)_{32}$ particles, the $t_2$ excitation, as described by TD-B3LYP, is a spuriously stabilised CT excitation. Without the spurious stabilisation of the CT excitation, a local excitation would possibly have been the lowest energy excitation, as has been observed for MgO. It is therefore not unreasonable to say that the $\Delta_o$ predicted by TD-B3LYP is severely underestimated for these particles. In contrast, the TD-B3LYP $\Delta_o$ values for $(MgSe)_{32}$, $(CdO)_{32}$ and $(PbS)_{32}$ and the description of these excitations obtained from TD-B3LYP calculations should be more trustworthy.

### 6.3.3   Absorption Spectra for (CaO)$_{32}$ and (SrO)$_{32}$

Before the localisation of the lowest optically allowed excitation is analysed in more detail, it is useful to compare the absorption spectra of (CaO)$_{32}$ and (SrO)$_{32}$ particles with experimental data obtained from reference 19, shown in figure 6-2. This comparison can only be done for these two materials, as only for nanoparticles of these systems is experimental optical data of comparable quality to that of MgO nanoparticles available. Furthermore, this builds on the work on MgO nanoparticles, which shows that TD-BHLYP predicts the absorption spectra very well after a rigid downwards shift of 0.5 eV is applied to the obtained spectrum. This shift is based on the findings in chapter 5 (specifically figure 5-7), which show that as the HFE is increased to 50% in TD-BHLYP, the non-problematic excitations are shifted up in energy by approximately 0.5 eV, while correcting the description of CT states. It is interesting to investigate whether this ad-hoc shift of 0.5 eV can be applied to other alkaline earth oxides apart from MgO.
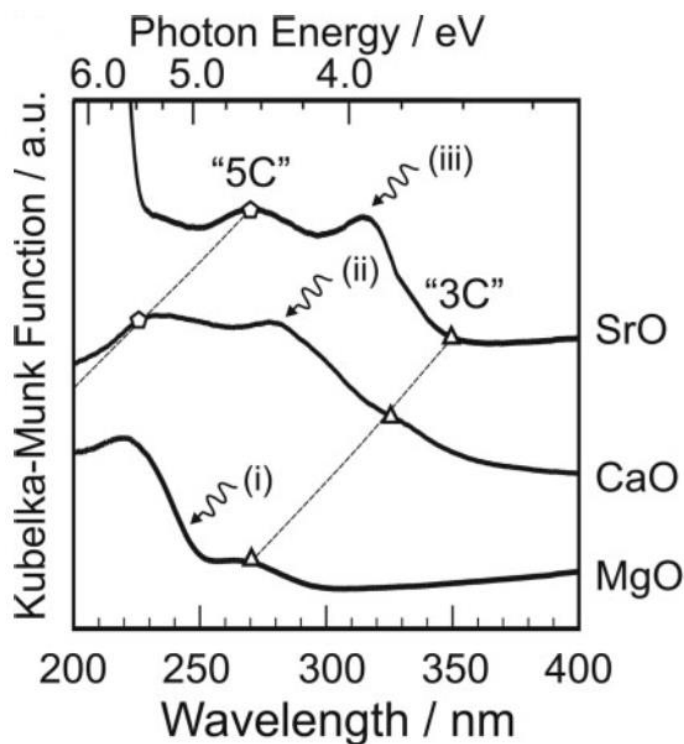
**Figure 6-2:** Experimental UV diffuse reflectance spectra for MgO, CaO and SrO CVD-grown nanoparticles with average sizes of 6 nm for MgO and average diameters of ≈ 27 nm for CaO and diameters between 20 and 200 nm for SrO, obtained from reference 19. The labels ''3C'' and ''5C'' show the excitation energies of 3-coordinated and 5-coordinated surface anions, respectively. (i), (ii) and (iii) mark the energies chosen to probe photoluminescence emission of MgO, CaO and SrO nanoparticles, respectively.

From the experimental absorption spectra for MgO, CaO and SrO nanoparticles, shown in figure 6-2, it can be seen that MgO nanoparticles have the highest absorption energy onset, at approximately 270 nm (4.59 eV), followed by CaO with an absorption onset at approximately 320 nm (3.87 eV) and an absorption onset which is lower in energy than the peak at 340 nm (3.65 eV) but a more accurate absorption onset cannot be determined from the experimental data provided. This shows that SrO nanoparticles can be optically excited at lower energies than CaO nanoparticles, which in turn can be optically excited at lower energies than MgO nanoparticles. This ordering is based on the approximation that the absorption spectra of the particles are the same if all different particles has the same size distribution, which is not the case in the experimental data.

The calculated absorption spectra for $(MgO)_{32}$, $(CaO)_{32}$ and $(SrO)_{32}$ can be seen in figure 6-3. Upon comparing the red-shifted spectra in the range of 200 – 400 nm with the experimental spectra, the same trend in absorption onset can be seen: SrO nanoparticles have the lowest absorption onset, followed by CaO and then MgO nanoparticles. The calculated longest wavelength peaks are predicted to be at 270 nm (4.59 eV), 320 nm (3.87 eV) and 360 nm (3.44 eV) for $(MgO)_{32}$, $(CaO)_{32}$ and $(SrO)_{32}$ respectively. This trend shows the same relative ordering as the optical gap values discussed above; with absorption spectra showing excitations that have significant oscillator strength, and not the lowest possible bright excitation.
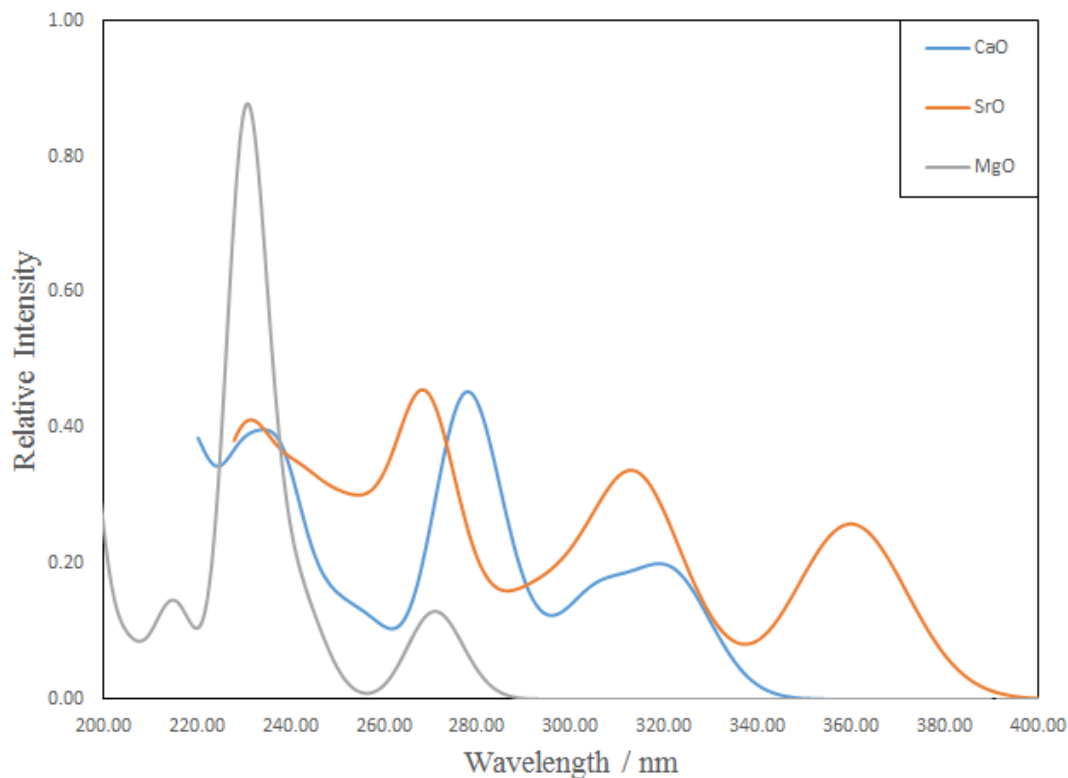


**Figure 6-3:** TD-BHLYP calculated absorption spectra for $(MgO)_{32}$ (grey line), $(CaO)_{32}$ (blue line) and $(SrO)_{32}$ (orange line), including a rigid red-shift of 0.5 eV.

In terms of absolute values, the rigidly red-shifted spectrum for $(MgO)_{32}$ is, as expected, in excellent agreement with the experimental spectrum for MgO nanoparticles. The agreement between experimental and predicted spectra in terms of peak positions is also good for the other two particles, as can be seen in table 6-3.

**Table 6-3:** Experimentally determined lowest peak position, obtained from reference 19, as well as the TD-BHLYP (rigidly red-shifted values in brackets) and TD-B3LYP calculated values.

| Material | Experimental / nm | BHLYP / nm | B3LYP / nm |
|---|---|---|---|
| MgO | 270 | 245 (273) | 350 |
| CaO | 320 | 287 (325) | 380 |
| SrO | 340 | 315 (360) | 425 |

The predicted shifted position of the longest wavelength peak of $(CaO)_{32}$ at 325 nm (3.81 eV) is in good agreement with the experimental peak at 320 nm (3.87 eV). For $(SrO)_{32}$, the predicted shifted peak at ~ 360 nm (3.44 eV) agrees well with the experimental value of ~ 350 nm (3.54 eV) for the lowest energy absorption peak. The good agreement continues for the shorter wavelength features: the experimental shoulders at ~ 270 nm (4.59 eV) and ~ 220 nm (5.64 eV) for CaO and the shoulders at ~ 320 nm (3.87 eV) and ~ 270 nm (4.59 eV) for SrO are mirrored in the calculated spectra in figure 6-3. It appears that the empirical red-shifted spectra yield good agreement to experimental absorption spectra of CaO and SrO nanoparticles. However, one should be careful with over-interpreting the good agreement between calculated and measured peak: the CaO and SrO nanoparticles synthesised were considerably larger at ~27 nm and 20 – 200 nm, respectively, compared to MgO nanoparticles (6 nm) in the same study.
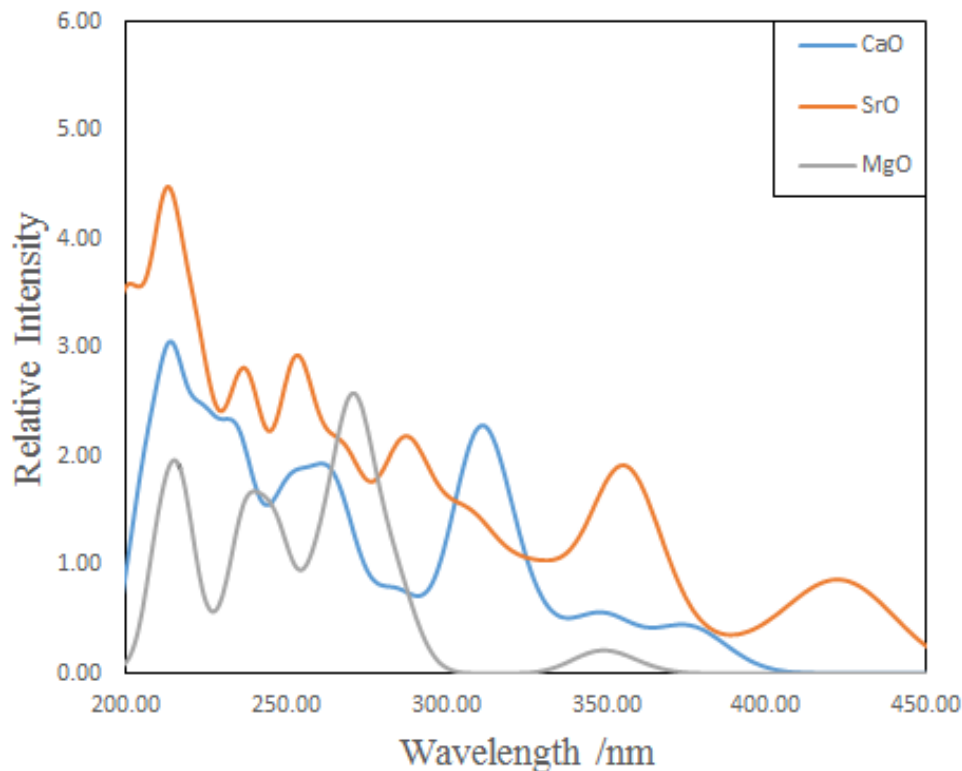
**Figure 6-4:** TD-B3LYP calculated absorption spectra for $(MgO)_{32}$ (grey line), $(CaO)_{32}$ (blue line) and $(SrO)_{32}$ (orange line).

The absorption spectra predicted using the B3LYP *xc*-functional can be seen in figure 6-4. Similarly to what has been observed for the optical gap values discussed previously, the use of TD-B3LYP results in a significant underestimation of the excitation energies of the first peak in the absorption spectra, summarised in table 6-3. The lowest absorption peak for $(MgO)_{32}$ lies at 350 nm (3.55 eV) instead of ~ 265 nm (4.68 eV), for CaO at 380 nm (3.25 eV) instead of ~ 325 nm (3.81 eV) and for SrO at 425 nm (2.91 eV) instead of ~ 350 nm (3.54 eV). Another difference between the TD-B3LYP and TD-BHLYP predicted spectra is that for the former, no single (blue-)shift can be applied to consistently bring the values closer to their experimental counterparts. This is not in itself problematic, but it does show that there is no systematic approach to obtaining a better fit to experiment, as there is with TD-BHLYP.

### 6.3.4 Excited state localisation

As seen above with the optical gap and the absorption spectra for the $(MO)_{32}$ and $(MgX)_{32}$ particles, there is some discrepancy between the energies of the excited state as obtained from TD-BHLYP and TD-B3LYP. To ascertain whether or not this is due to the CT character of the TD-B3LYP excitation, the spatial character of the lowest energy to a $t_2$ state responsible for the optical gap must be considered. Similarly to the analysis on MgO, the character of the excitation is considered in terms of the difference in NBO charges between the ground and $t_2$-symmetry excited state charges for every atom in the particle. All atoms can be labelled as 'corner' (3-coordinated), 'edge' (4-coordinated), 'face' (5-coordinated), or 'bulk' (6-coordinated). Contributions are determined in terms of the percentage of the excited electron (hole) localised on a metal (chalcogen) atom, and are summed per atom type (e.g. metal corner atom, chalcogen edge atom).

Tables 6-4, 6-5 and 6-6 show the percentage of the electron (on M / Cd / Pb sites) and hole (on O / X sites) that are localised on each of the sites (corner / edge / face / bulk). The exciton arises from excitation from the ground state to the lowest state of $t_2$ symmetry, in the alkaline earth oxide $(MO)_{32}$ particles (table 6-4), the magnesium chalcogenide $(MgX)_{32}$ particles (table 6-5) and the post-transition metal chalcogenides $(CdO)_{32}$ and $(PbS)_{32}$ (table 6-6). Figures 6-5 and 6-6 show the corresponding density differences between ground and excited states.

**Table 6-4:** Percentage localisation of the electron (on M sites) and hole (on O sites) of the lowest energy $t_2$ TD-BHLYP / TD-B3LYP excitation (corresponding to the optical gap) for the different $(MO)_{32}$ particles.

|  | M = Mg | M = Ca | M = Sr | M = Ba |
|---|---|---|---|---|
| O corner % | 89.52 / 83.51 | 77.63 / 65.85 | 71.47 / 59.03 | 51.24 / 48.62 |
| O edge % | 0.96 / 4.28 | 4.24 / 1.37 | 3.49 / 1.46 | 25.99 / 11.55 |
| O face % | 3.10 / 3.62 | 9.84 / 16.49 | 14.34 / 19.05 | 14.74 / 22.30 |
| O bulk % | 6.42 / 8.59 | 8.28 / 16.29 | 10.70 / 20.47 | 8.03 / 17.53 |
| M corner % | 17.68 / 75.65 | 7.75 / 76.85 | 4.19 / 70.12 | 14.32 / 62.03 |
| M edge % | 72.24 / 7.37 | 81.25 / 0.29 | 80.57 / 4.00 | 73.52 / 9.07 |
| M face % | 5.36 / 9.07 | 0.52 / 0.37 | 6.66 / 12.86 | 7.69 / 12.45 |
| M bulk % | 4.72 / 7.90 | 10.48 / 22.49 | 8.58 / 13.02 | 4.46 / 16.45 |

Focussing on table 6-4 first, it can be seen that, as for MgO, all alkaline earth oxides have different localisation patterns predicted by TD-BHLYP and TD-B3LYP. The lowest energy $t_2$ excitations have clear CT character when using the latter *xc*-functional, with the electron-hole predominantly localised on the oxygen corner atoms and the excited electron mainly localised on the metal corner atoms. The CT character decreases as the alkaline earth metal increases in size. Use of TD-BHLYP leads to a different picture in which the electron hole is still localised on the oxygen corner atoms but the excited electron now localises on the edge atoms adjacent to these oxygen corners. As magnesium is replaced by its heavier alkaline earth analogues, an increased delocalisation of the electron hole over the entire particle can again be observed: in the case of $(BaO)_{32}$, the electron hole is delocalised mostly on oxygen corner atoms (51%), and half of the charge again (26%) is delocalised over oxygen edge atoms, compared to $(MgO)_{32}$, where 91% of the hole is localised on oxygen corners.

**Table 6-5:** Percentage localisation of the electron (on M sites) and hole (on O sites) of the lowest energy $t_2$ TD-BHLYP / TD-B3LYP excitation (corresponding to the optical gap) for the different $(MgX)_{32}$ particles.

| | X = O | X = S | X = Se |
|---|---|---|---|
| X corner % | 89.52 / 83.51 | 72.09 / 64.26 | 56.51 / 52.27 |
| X edge % | 0.96 / 4.28 | 1.99 / 1.12 | 6.01 / 2.07 |
| X face % | 3.10 / 3.62 | 25.73 / 33.96 | 35.67 / 42.08 |
| X bulk % | 6.42 / 8.59 | 0.19 / 0.66 | 1.81 / 3.58 |
| Mg corner % | 17.68 / 75.65 | 26.22 / 64.96 | 36.36 / 58.18 |
| Mg edge % | 72.24 / 7.37 | 65.97 / 24.77 | 56.17 / 32.34 |
| Mg face % | 5.36 / 9.07 | 3.57 / 9.52 | 4.70 / 9.22 |
| Mg bulk % | 4.72 / 7.90 | 4.24 / 0.75 | 2.78 / 0.26 |

Focussing on table 6-5, TD-B3LYP predicts that the lowest $t_2$ excitation for the magnesium chalcogenide particles is a CT excitation that predominantly involves electron transfer from chalcogen corner sites to magnesium corner sites, similarly to that found for alkaline earth oxides. TD-BHLYP predicts a more local behaviour for the lowest $t_2$ excitation, where the electron transfer occurs mainly from the chalcogen corners to the adjacent magnesium edge atoms. The difference between this data set and that for $(MO)_{32}$ particles is that the effect of replacing oxygen with the heavier chalcogens leads to an increased delocalisation of the excited state electron, in addition to an increased delocalisation of the electron hole: for both TD-BHLYP and TD-B3LYP in $(MgS)_{32}$ and $(MgSe)_{32}$, the hole is delocalised over the corner and face chalcogen atoms, whereas the excited electron delocalises over the edge and corner magnesium atoms. This gradual delocalisation of the hole seen with both the TD-BHLYP and TD-B3LYP results, means that the localisation results become more similar to each other when going from MgO to

MgSe, which is something that does not occur in the alkaline oxide series (with the exception of BaO).

**Table 6-6:** Percentage localisation of the electron (on M sites) and hole (on O sites) of the lowest energy $t_2$ TD-BHLYP / TD-B3LYP excitation (corresponding to the optical gap) for the post-transition metal particles $(CdO)_{32}$ and $(PbS)_{32}$ particles.

|  | CdO | PbS |
|---|---|---|
| X corner % | 22.97 / 24.56 | 8.73 / 14.40 |
| X edge % | 35.35 / 23.20 | 40.24 / 35.38 |
| X face % | 40.40 / 50.62 | 36.69 / 42.70 |
| X bulk % | 1.28 / 1.61 | 14.33 / 7.52 |
| M corner % | 49.24 / 53.00 | 2.87 / 2.56 |
| M edge % | 29.61 / 27.04 | 25.55 / 19.32 |
| M face % | 19.24 / 17.84 | 54.30 / 55.04 |
| M bulk % | 1.91 / 2.13 | 17.28 / 23.08 |

The data for the post-transition metal chalcogenide nanoparticles in table 6-6 show a dramatically different picture to the particles in the $(MO)_{32}$ and $(MgX)_{32}$ series. For both $(CdO)_{32}$ and $(PbS)_{32}$, TD-BHLYP and TD-B3LYP give essentially the same description of the localisation of the lowest energy $t_2$ excitation, and the data shows that the excited state is predicted to be essentially delocalised, in stark contrast to the results obtained for the alkaline earth chalcogenides. The difference between the $(CdO)_{32}$ and $(PbS)_{32}$ results is that the electron and hole of the former are predicted to delocalise over the surface of the particle, mainly over edge and face atoms, whereas the $(PbS)_{32}$ excited state is

predicted to also, in addition to delocalisation over surface sites, have significant contribution from bulk atoms in the centre of the particle.
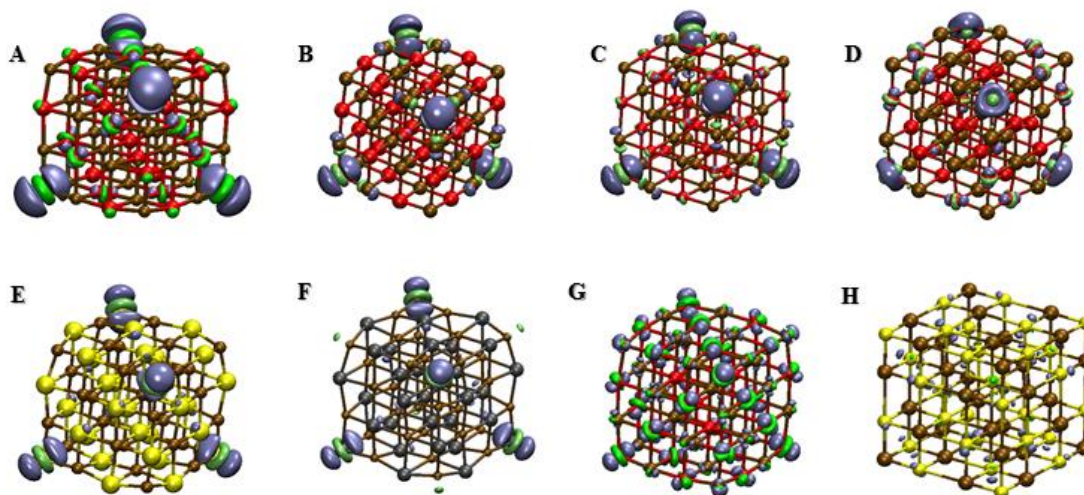


**Figure 6-5:** TD-BHLYP-calculated electron density differences between the ground and lowest t2 excited state for A: MgO, B: CaO, C: SrO, D: BaO, E: MgS, F: MgSe, G: CdO, and H: PbS. Red spheres are oxygen atoms, brown are magnesium /calcium/ strontium/ barium/ cadmium/ lead atoms, yellow are sulphur atoms, black are selenium atoms. Green signifies accumulation of electron density (excited electron), blue signifies depletion of electron density (hole). An isosurface of 0.01 a.u. is used in all figures.
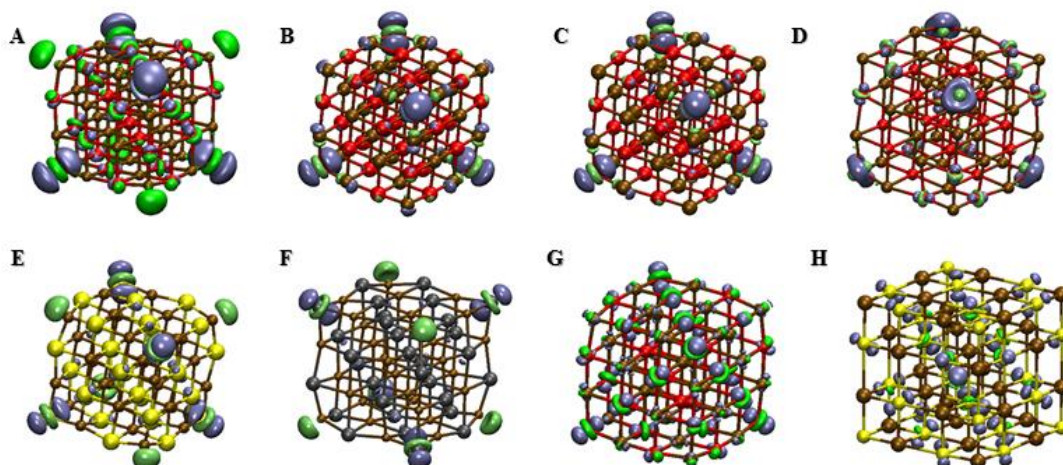
**Figure 6-6:** TD-B3LYP-calculated electron density differences between the ground and lowest t2 excited state for A: MgO, B: CaO, C: SrO, D: BaO, E: MgS, F: MgSe, G: CdO, and H: PbS. Red spheres are oxygen atoms, brown are magnesium / calcium / strontium / barium / cadmium / lead atoms, yellow are sulphur atoms, black are selenium atoms. Green signifies accumulation of electron density (excited electron), blue signifies depletion of electron density (hole). An isosurface of 0.01 a.u. is used in all figures.

The electron density differences between the ground and lowest $t_2$ excited state are visualised in figures 6-5 and 6-6, for TD-BHLYP and TD-B3LYP, respectively. The trend seen in these images is similar to that summarised in tables 6-4, 6-5 and 6-6. There are minor discrepancies, one of them being that the delocalisation of the electron and hole on the $(PbS)_{32}$ particles is not clearly visible at the contour value used. Furthermore, the increase in electron density on the corner metal atoms on the alkaline earth nanoparticles does not show up as clearly as the hole in the same image. This has already been discussed in the case for MgO and stems from the fact that there are four oxygen corner atoms, with twelve adjacent metal edge atoms, and the density difference per unit volume at a metal edge atom is approximately a third of what it is at a corner oxygen atom.

The difference in localisation pattern between the $(MX)_{32}$ series and the post-transition chalcogenides is possibly better seen in HOMO-LUMO images, as seen in figures 6-7 and 6-8. As both TD-BHLYP and TD-B3LYP produce the same HOMO-LUMO images, only one set (TD-BHLYP) is shown. Figures 6-7 and 6-8 shows that the HOMOs and LUMOs are most localised for the $(MO)_{32}$ particles, less so for $(MgX)_{32}$ and even less for $(CdO)_{32}$

160

and $(PbS)_{32}$. It should be noted that the excitations discussed above are not simply HOMO to LUMO excitations but those orbitals do play an important role in the excitation: the HOMO to LUMO transition accounts for over 50% of the lowest vertical $t_2$ excitation.
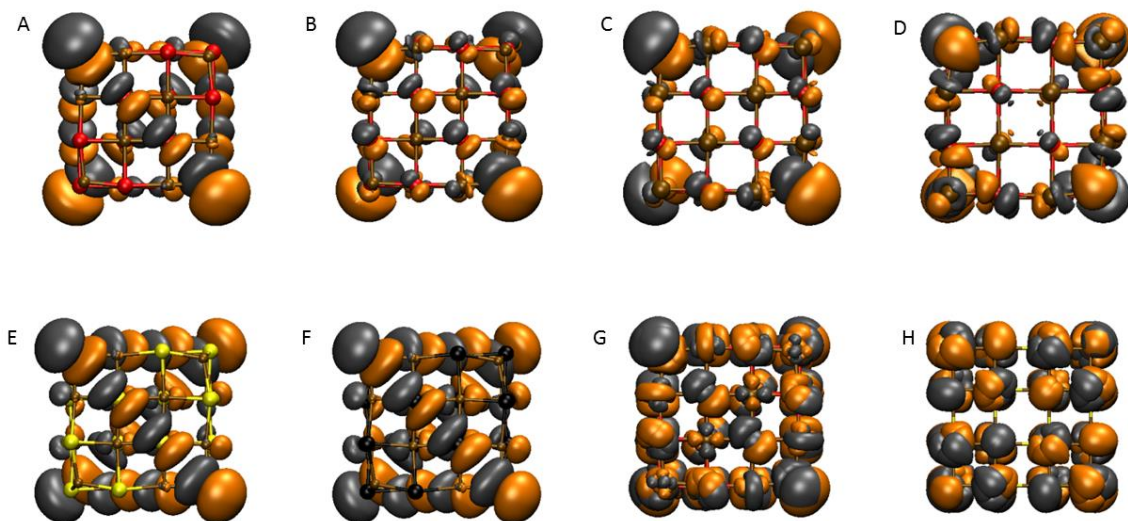


**Figure 6-7:** TD-BHLYP-calculated HOMO for A: MgO, B: CaO, C: SrO, D: BaO, E: MgS, F: MgSe, G: CdO, and H: PbS. Red spheres are oxygen atoms, brown are magnesium / calcium/ strontium / barium/ cadmium / lead) atoms, yellow spheres are sulphur atoms, black spheres are selenium atoms. The same contour value (0.01 a.u.) used in all figures.
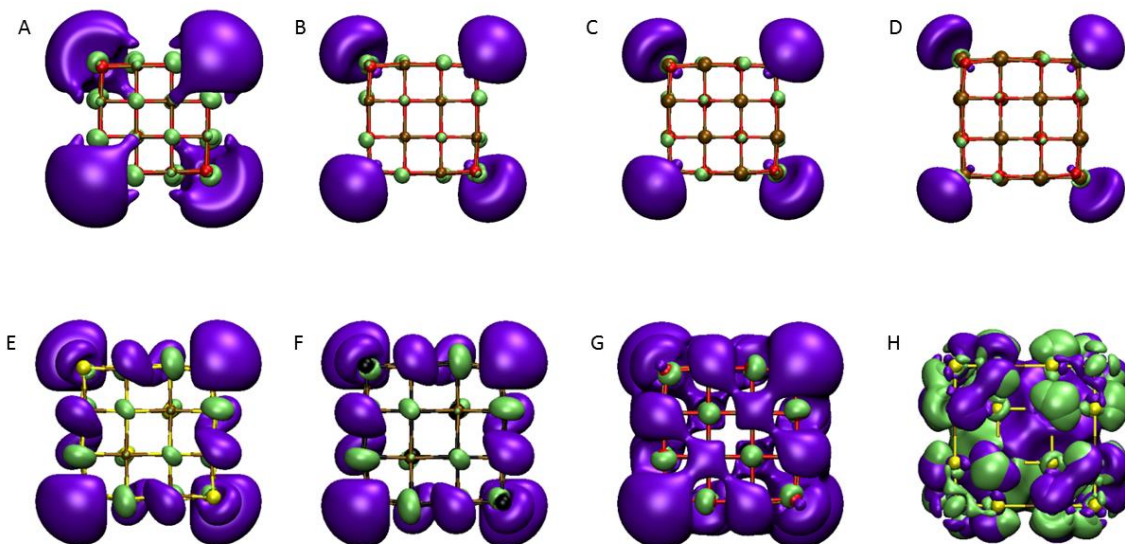
**Figure 6-8:** TD-BHLYP-calculated LUMO for A: MgO, B: CaO, C: SrO, D: BaO, E: MgS, F: MgSe, G: CdO, and H: PbS. Red spheres are oxygen atoms, brown are magnesium / calcium/ strontium / barium/ cadmium / lead) atoms, yellow spheres are sulphur atoms, black spheres are selenium atoms. The same contour value (0.01 a.u.) used in all figures.

## 6.4   Discussion

As seen above, rocksalt structured nanoparticles with different composition have distinctly different optical properties. The clearest contrast is between $(MgO)_{32}$, having a very localised excited state, and $(CdO)_{32}$ and $(PbS)_{32}$, with excited states that are very delocalised. The change in the optical gap between $(MgO)_{32}$ and $(PbS)_{32}$ is nearly 2 eV, which is also seen in the bulk.[179,237]

Of course, the (de)localisation of the particles (apart from $(CdO)_{32}$ and $(PbS)_{32}$) differs substantially between the predicted TD-BHLYP and TD-B3LYP results, which raises the question as to which *xc*-functional is to be trusted to describe these nanoparticles most accurately. As discussed in chapter 5, the case for MgO is clear-cut: the optical gap and overall absorption spectrum predicted by TD-B3LYP is severely red-shifted relative to that measured experimentally, albeit the experimental particles are larger in size than those used for calculating the computational absorption spectrum.

There has been some work suggesting that the $\Lambda$ cut-off value below which an excitation most likely has CT character can be as low as 0.15 for inorganic systems,[241] rather than the value of 0.3 determined for organic systems. Although the most suitable cut-off for inorganic systems has not been tested much, the $\Lambda$ values obtained for MgO particles are rather low (and decrease with increasing particle size): 0.15 for $(MgO)_{24}$ and 0.13 for $(MgO)_{32}$. In addition to this, the excited state localisation predicted by TD-B3LYP has all the characteristics of the CT-excitation (unlike the excited state predicted from TD-BHLYP), which is sufficient evidence to classify the lowest excitation into a $t_2$ state (resulting in the optical gap), as predicted by TD-B3LYP, as a charge transfer state, which is spuriously stabilised. This means that TD-B3LYP cannot reliably be used to study the optical properties of MgO nanoparticles accurately. This is the conclusion from the results of chapter 5. The same reasoning can be applied to the other alkaline earth oxide nanoparticles studied in this chapter: $(CaO)_{32}$, $(SrO)_{32}$ and, to some extent, $(BaO)_{32}$. The use of TD-B3LYP is clearly problematic for these systems based on the $\Lambda$ analysis, so it is advisable to use an *xc*-functional with a high percentage of HFE, such as TD-BHLYP. A range-separated functional, such as CAM-B3LYP, is also a very good alternative in describing the optical properties of alkaline earth nanoparticles, assuming that the behaviour seen for MgO in chapter 5 can be extrapolated to other alkaline earth nanoparticles. Furthermore, in the case of TD-BHLYP, the ad-hoc recipe developed for MgO and applied to the absorption spectra of SrO and CaO nanoparticles, i.e. rigidly shifting the spectra downwards by 0.5 eV, yields excellent agreement with experiment. However, it is possible that another *xc*-functional, such as CAM-B3LYP, predicts better agreement with the experimental data, without the need for correcting the overestimation seen for TD-BHLYP.

The results obtained for $(MgS)_{32}$ are similar to those obtained for the alkaline earth metals: The $\Lambda$ value is slightly larger than those obtained for the $(MO)_{32}$ particles, although still below the cut-off of 0.3. Furthermore, the excited state localisation picture for the lowest excitation into a $t_2$ state is very similar to that of the $(MO)_{32}$ particles, so it can be concluded that TD-B3LYP may also be unsuitable to study this material at sizes similar to those studied here (or, indeed, larger). Slightly different behaviour can be seen for $(MgSe)_{32}$, which appears to be a material which lies between two extremes: a TD-B3LYP

calculated $\Lambda$ value above 0.3, and a similar (but not identical) excited state localisation pattern predicted by TD-B3LYP and TD-BHLYP. It shows that the CT character is not 'black or white' behaviour, but is rather a scale on which $(MgSe)_{32}$ has less CT character than $(MgS)_{32}$, which itself has less CT character than $(MgO)_{32}$. Furthermore, the trend for the optical gap in the $(MgX)_{32}$ series, where $\Delta_o$ increases when going from $(MgO)_{32}$ to $(MgS)_{32}$ and then decreases again from $(MgS)_{32}$ to $(MgSe)_{32}$, could arise from two competing trends in this series of structures. On one hand is the already discussed behaviour, the reduction of the CT character, which means that the spurious energetic stabilisation of the CT state is less severe and TD-B3LYP is a better approximation for $(MgSe)_{32}$ than for $(MgO)_{32}$. On the other hand is the decrease in optical gap when going from $(MgO)_{32}$ to $(MgSe)_{32}$, as seen with TD-BHLYP.

At the opposite end of the spectrum from the $(MO)_{32}$ materials are $(CdO)_{32}$ and $(PbS)_{32}$, for which TD-BHLYP and TD-B3LYP predict a very similar excited state localisation of the lowest $t_2$ excitation. Furthermore, these post-transition metal oxides also exhibit large TD-B3LYP $\Lambda$ values, which are considerably larger than the 0.3 cut-off. In theory, this means that there should be no issue describing the $t_2$ excitation with either *xc*-functional, and both should work equally well. However, for the remainder of the discussion, only TD-BHLYP results are considered, to give a consistent approach for comparison with the other particles.

The trend in the excited state (de)localisation in these nanoparticles possibly stems from the differences in the extent to which the excited electron and the hole are screened from each other. To a first approximation, this can be understood in term of the dielectric constants ($\varepsilon$) of the bulk materials the nanoparticles are composed of. The dielectric constant, also known as relative permittivity, is a property of a material and can be measured as the decrease of the Coulomb forces in the material relative to vacuum, i.e. the degree to which electrostatic interactions are screened in the material.

The $(MO)_{32}$ series is made up of materials with low dielectric constants ($\varepsilon_{MgO}= 3.0$; $\varepsilon_{CaO}= 3.3$; $\varepsilon_{SrO}= 3.2 - 3.5$; $\varepsilon_{BaO}= 3.9 - 4.2$ ),[196,197,242] and also have very localised excited states, with the excited electron and the hole being clearly separated in space. As the dielectric

constant increases, so does the exciton delocalisation: the dielectric constants are higher for the post-transition chalcogenide particles ($\varepsilon_{CdO}$= 5.4-6.2; $\varepsilon_{PbS}$= 17.2)[196,198], and the excited state is much more delocalised, especially for PbS. Both MgS and MgSe are materials that have dielectric constants that lie in between hose of alkaline earth oxides and post-transition metal chalcogenides, ($\varepsilon_{MgS}$= 5.1; $\varepsilon_{MgSe}$= 5.9),[196] and also display intermediate localisation in the excited state.

The (de)localisation thus seems to depend on the combination of two competing trends. The first is due to the potential energy term, which arises from the electrostatic interaction between the excited electron and the electron hole and therefore favours a localised excited state, where the electron and hole are in close proximity. The second competing factor is the kinetic energy term, which favours a delocalised excited state. This means that the degree of screening (and therefore the dielectric constant) between the electron and hole is crucial in determining the extent of localisation: the larger the dielectric constant, the more the charges are screened and the potential energy term therefore decreases: the balance between localisation and delocalisation of the excited state is therefore inherently linked to this constant.

As shown by the works of Penn,[191] Phillips[192–195] and van Vechten,[196] the dielectric constant values of the bulk materials are inherently connected to the electronic band structure and the degree of covalency and ionicity.[190,195] It is therefore not surprising that the trend between the bulk dielectric constant and the excited state (de)localisation in the nanoparticle also maps onto trends between the bulk band gap and excited state (de)localisation in the nanoparticle, with nanoparticles of materials with a smaller band gap having more delocalised excited states. Quantum dots, where quantum confinement is exploited to tune the optical properties of materials by varying particle size, need a delocalised excited state and are, unsurprisingly, often made from materials such as CdSe and PbS, which have a small band gap in the bulk.

Furthermore, the trend shows that the degree of ionic bonding in the bulk material and excited state (de)localisation in the nanoparticles is linked, with more ionic materials having a more localised excited state. Problems when describing CT excitations by TD-

B3LYP are most likely to occur in particles with localised excited states, which is likely to occur only in nanoparticles of ionic materials with a large band gap.

**Table 6-7:** Rigidly-red-shifted by 0.5 eVoptical gap ($\Delta_{o,rs}$) values for the $(MX)_{32}$ particles of the different compositions calculated using TD-BHLYP.

|  | MgO | CaO | SrO | BaO | MgS | MgSe | CdO | PbS |
|---|---|---|---|---|---|---|---|---|
| $\Delta_{o,rs}$ | 4.58 | 3.85 | 3.41 | 3.36 | 4.32 | 3.87 | 2.51 | 2.89 |

Assuming the 0.5 eV red-shift applied to TD-BHLYP computed absorption spectra for MgO (and works well for reproducing the absorption spectra for $(CdO)_{32}$ and $(PbS)_{32}$) is accurate, then a good approximation to the optical gap for all studied materials would be to also red-shift them by 0.5 eV, as seen in table 6-7. The $\Delta_{o,rs}$ values consistently lie below the experimentally determined lowest excitation energies (7.67 eV for MgO, 6.93 eV for CaO, 5.68 eV for SrO and 3.73 eV for BaO)[172,237] of the corresponding bulk material. This shows that, in line with the calculated excited state localisation, the $\Delta_{o,rs}$ values for the materials show a red- rather than a blue-shifted optical gap as the particle size is reduced from the bulk to nano-sized. The comparison with experimental data for the magnesium chalcogenides is more difficult due to the sparsity of experimental data for rocksalt particles.[188,238–240] However, the $\Delta_{o,rs}$ is below the light absorption onset for the bulk at 4.78 eV for MgS and at 5.60 eV for MgSe. However, for $(CdO)_{32}$ and $(PbS)_{32}$, the predicted $\Delta_{o,rs}$ values lie above the experimental absorption onset (2.37 eV for CdO and 0.44 eV for PbS).[178,179] In the case of PbS, this could be related to the lack of spin-orbit coupling in these calculations but in the case of $(CdO)_{32}$ it is in line with the kind of blue-shift, or the hypothesis that such particles would display quantum confinement, seen when the excited state is delocalised.

## 6.5 Conclusions

In conclusion, the question as to whether the problematic description of charge transfer excitations occurring in MgO nanoparticles is also present in $(MX)_{32}$ materials (CaO, SrO, BaO, MgS, MgSe, CdO and PbS) has been investigated in terms of the magnitude and nature of their optical gap in the rocksalt configuration.

The lowest $t_2$ excitations calculated with TD-B3LYP are, as previously found for MgO, CT excitations for all nanoparticles considered bar $(CdO)_{32}$ and $(PbS)_{32}$. These CT excitations are spuriously energetically stabilised relative to local excitations, although the CT character is really more of a sliding scale that can vary from system to system: as either the metal or chalcogen in $(MgO)_{32}$ is replaced by a heavier counterpart, the CT character decreases for the lowest $t_2$ excitation as the excitation becomes more delocalised.

Similarly to the case of MgO nanoparticles, hybrid (GGA) *xc*-functionals with a high percentage of HFE are assumed to correct the description of such CT excitation, similarly to the BHLYP *xc*-functional used in this work. Range-separated *xc*-functionals such as CAM-B3LYP are also known to help alleviate the problematic description of CT artefacts.

The results obtained using TD-BHLYP show that the magnitude and nature of the optical gap varies between the different rocksalt particles. The particles in the $(MO)_{32}$ group are predicted to exhibit large optical gaps, with a very localised excited state involving oxygen corner and the metal edge sites adjacent to these corners. On the other hand, the post-transition metal chalcogenide nanoparticles have a much smaller optical gap and a delocalised excited state. The magnesium chalcogenides display an intermediate behaviour, albeit closer to that of the alkaline earth oxides.

The difference in the optical gap and excited state localisation can, furthermore, be understood in terms of the dielectric screening of the Coulomb interaction between the excited electron and the corresponding electron hole. The larger bulk dielectric constants of CdO and PbS mean that the potential energy term favouring exited state localisation is much reduced, as the charges are better screened from each other.

Finally, taking into account the apparent role played by the dielectric constant, a future avenue of this research is to explore *xc*-functionals where the amount of HFE is treated as an explicit function of the dielectric constant (rather than an empirical constant) [243–245] and their suitability in describing these particles and their corresponding excited states.

# 7. Photoluminescence in MgO nanoparticles

## 7.1   Introduction

Photoluminescence (PL) properties of materials can be very desirable if the emitted light is in the visible spectrum, as it is for e.g. light-emitting diodes (LEDs).[246–250] It is clear that materials with useful PL properties are sought after. The intrinsic processes behind PL are interesting and useful to study computationally: as the light emitting processes occur on very short timescales, the underlying physics and chemistry is extremely difficult to study by experiment alone, let alone at an atomistic level. Computational studies that look at the fundamentals of PL are therefore crucial in expanding the knowledge of these processes – and can potentially even drive experimental studies.

MgO (nano)particles are not currently considered for industrial PL applications, due to the fact that they do not photo-emit light in the visible spectrum. However, MgO nanoparticles are good model systems to study PL computationally, as - in contrast to many other inorganic nanoparticles - even relatively small particles exhibit the rocksalt structure, which is found experimentally.

Experimental studies[20,228] have measured PL spectra of small MgO nanoparticles with an average size of 3 nm that show a broad peak between ~520 – 300 nm (~ 2.4 – 4.1 eV), with the peak maximum at 375 nm (3.3 eV), produced using an incident light source of 270 nm (4.6 eV). The peak maximum shifts to 365 nm (3.4 eV) when a light source of 240 nm (5.2 eV) is used. Experimentally, this shift is rationalised by characterising the photoluminescence in terms of de-excitation from corner (3-coordinated) and edge (4-coordinated) oxygen atoms respectively: as the average particle size increases from 3 to 5 to 10 nm, the peak at 375 nm (3.3 eV) becomes less intense, as proportionally fewer corner sites are available.

This chapter focusses on extending the work on vertical excitations in MgO nanoparticles presented in chapter 5 by studying the excited state behaviour of these particles, obtaining the photoluminescence energies (PLEs) and comparing the different excited state minima

on the $S_1$ surface. As only $S_1$ to $S_0$ transitions are considered here, the PLEs are all technically fluorescence energies. However, as fluorescence and phosphorescence are distinguished experimentally through their respective lifetimes, and this is a property that cannot be easily calculated, photoluminescence is considered to be a more encompassing label for these de-excitation processes.

The previous work presented in chapters 5 and 6, has shown that to model electronic excitations of MgO nanoparticles, the choice of either the BHLYP or the CAM-B3LYP *xc*-functional is most suitable. However, it is not clear whether these *xc*-functionals are also suitable for describing the excited state relaxation process of these nanoparticles. This chapter aims to answer these questions.

## 7.2    Methodology

Different nanoparticles of MgO are studied, namely $(MgO)_n$ where $n = 4, 6, 9, 12, 18, 24,$ 32, 40. The optimised ground state structures, and their vertical excitation energies, have been obtained using Density Functional Theory (DFT) and Time Dependent Density Functional Theory (TDDFT) respectively, as discussed in chapter 5. Here, the optimised structure in the $S_1$ state is obtained starting from the ground state starting structure. The PLE associated with the vertical de-excitation at the excited state energy minimum is also found.

The calculations employ three different *xc*-functionals; the hybrid-GGA BHLYP and B3LYP *xc*-functionals and the Coulomb-attenuated CAM-B3LYP *xc*-functional. Furthermore, three different basis sets were used in these calculations; the triple-$\zeta$ quality def2-TZVP basis set[251] and two variants of a double-$\zeta$ basis set; the DZ(D)P basis-set available in Turbomole by Schäfer *et al.*[83] and the DZP basis-set of Canal Neto *et al.*[252] For simplicity, we shall from now on refer to the DZ(D)P basis-set by Schaefer *et al.* as DZS and the Canal-Neto basis-set as DZC. The DZS basis set has also been used previously in this work. The DZS results can mainly be found in Appendix A. The

advantage of using the smaller basis set is that it allows the study of slightly larger particles compared to the def2-TZVP basis set.

Finally, where computationally tractable (n ≤ 12), analytical frequencies at the excited state stationary points were calculated and only results which show there to be no imaginary frequencies present are discussed. As an exception to this, two analytical frequency calculations have been performed on $(MgO)_{32}$ particle, at very high computational expense. This was deemed necessary as a structure had been optimised that exhibited a larger PLE than the other structures, and it was found that this increased PLE was linked to a non-minimum structure.

The localisation of the excited state at both the ground and relaxed excited state geometry is analysed in terms of the difference between Natural Bond Order (NBO) charges in the case of calculations employing the B3LYP and BHLYP *xc*-functionals, and Löwdin charges in the case of calculations employing the CAM-B3LYP *xc*-functional. The latter is used as NBO charges are not available in the computational package that employed for the CAM-B3LYP calculations. Furthermore, the Λ diagnostic of Peach *et al.*[109,110] was employed to identify potentially problematic charge-transfer (CT)-excitations.

The (TD-)BHLYP and (TD-)B3LYP calculations were generally performed using the TURBOMOLE 6.4 code, whereas the CAM-B3LYP calculations used the GAMESS-US code (version 1 OCT 2010 − R1), as did the TD-B3LYP Λ diagnostic calculations. Visualisation of molecular structures has been performed using the VMD package.

## 7.3   Excited state properties

The vertical excitation spectra of MgO nanoparticles have been discussed previously in chapter 5. It was found that to accurately describe the excitation, the use of an *xc*-functional with a large amount of Hartree-Fock exchange (HFE), such as BHLYP, or a range-separated *xc*-functional such as CAM-B3LYP, is required. This is in contrast to the results obtained using B3LYP, which contains only 20% HFE and fails to correctly

describe the excitation behaviour of MgO and other rocksalt materials, as shown in chapter 6. However, the latter *xc*-functional is included as it has previously been used to study MgO vertical excitations in chapters 5 and 6, and serves to highlight the functional dependence of the PL results.

### 7.3.1  Photoluminescence energies
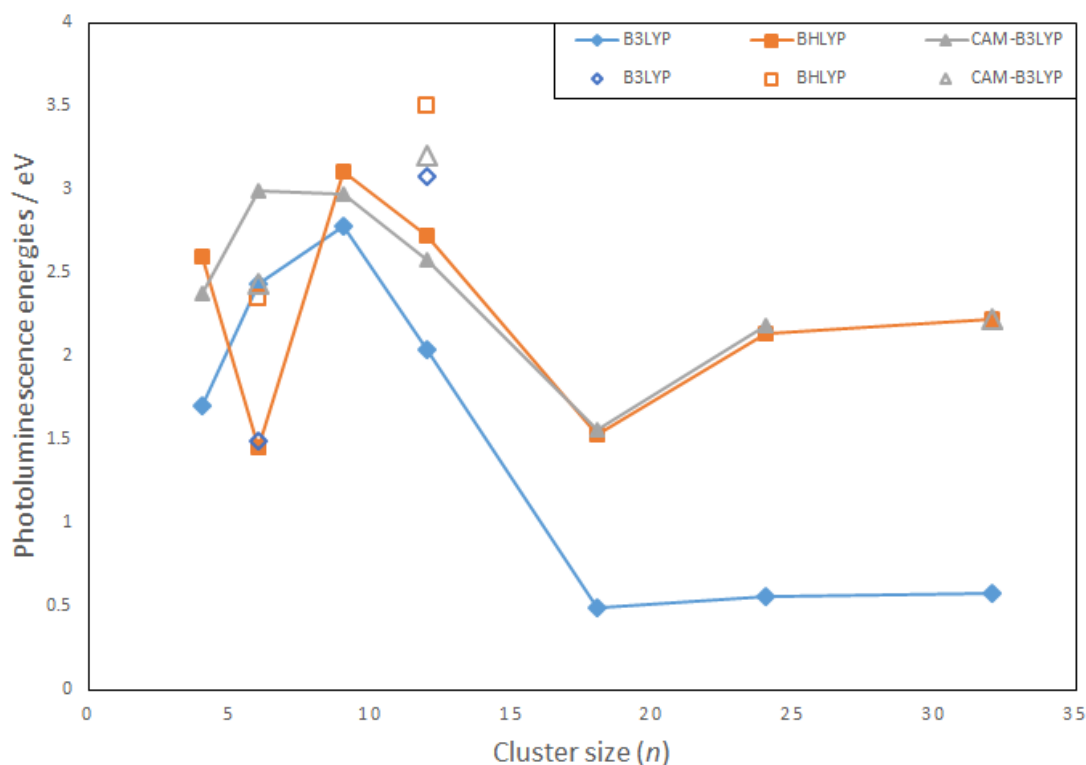


**Figure 7-1:** def2-TZVP calculated photoluminescence energies, obtained using the B3LYP (blue diamonds), BHLYP (orange squares) and CAM-B3LYP (grey triangles) *xc*-functionals. Open symbols correspond to the PLE of the cubic $(MgO)_6$ and the sodalite $(MgO)_{12}$ structures. In the case of CAM-B3LYP, for $(MgO)_{32}$, the open triangle corresponds to the CAM-B3LYP single-point calculation on the TD-BHLYP/def2-TZVP $S_1$ optimised geometry.

**Table 7-1:** def2-TZVP and DZC calculated photoluminescence energies, obtained using the B3LYP, BHLYP and CAM-B3LYP *xc*-functionals (DZC results between parentheses). All energies are in eV.

| | B3LYP | BHLYP | CAM-B3LYP |
|---|---|---|---|
| $(MgO)_4$ | 1.70 (1.53) | 2.60 (2.40) | 2.38 (2.33) |
| $(MgO)_6$ hexagonal | 2.43 (1.37) | 1.45 (2.28) | 2.99 (2.75) |
| $(MgO)_6$ cubic | 1.49 (2.14) | 2.35 (1.32) | 2.43 (2.21) |
| $(MgO)_9$ | 2.78 (2.64) | 3.11 (2.61) | 2.97 (2.71) |
| $(MgO)_{12}$ hexagonal | 2.04 (1.90) | 2.72 (2.57) | 2.58 (2.40) |
| $(MgO)_{12}$ sodalite | 3.08 (2.99) | 3.50 (3.34) | 3.20 (3.08) |
| $(MgO)_{18}$ | 0.49 (0.17) | 1.53 (1.44) | 1.56 (1.46) |
| $(MgO)_{24}$ | 0.56 (0.76) | 2.14 (2.05) | 2.18 (2.08) |
| $(MgO)_{32}$ | 0.58 (0.55) | 2.22 (2.16) | 2.22* (2.25) |
| $(MgO)_{40}$ | - (0.51) | - (2.08) | - (*2.12*)[†] |

*CAM-B3LYP single-point calculation on the TD-BHLYP/def2-TZVP $S_1$ optimised geometry.

[†]optimisation using the ground state TD-BHLYP/DZC structure as a starting point.

Table 7-1, figure 7-1 and figures 7-5, 7-6 and 7-7 show the PLE for all considered $(MgO)_n$ particles, and it can be seen that for all $(MgO)_n$ particles (except $n = 6$), the def2-TZVP PL value obtained using the B3LYP *xc*-functional is considerably lower than that obtained from TD-BHLYP or TD-CAM-B3LYP, with the difference between the calculated PLEs using this and the other two functionals widening as *n* increases. This trend has also been observed for the lowest vertical excitation energy (LVEE), discussed in chapter 5. This underestimation of the PLEs, similarly to what has been seen with the LVEE, is possibly linked to the CT-character of the lowest TD-B3LYP excitation and the underlying issue of why TD-B3LYP cannot predict these excitation processes in MgO nanoparticles

accurately. As the particle size ($n$) increases, the overlap of the orbitals involved in the excitation (and possibly de-excitation) decreases, meaning that the CT-character increases and the description of the process, as obtained from TD-B3LYP, worsens.

The def2-TZVP-calculated PL data presents a varied picture for the smaller particles: both TD-B3LYP and TD-CAM-B3LYP predict an increase in the PLE going from $n = 4$ to $n = 6$ by 0.73 eV and 0.61 eV respectively, but TD-CAM-B3LYP then predicts a decrease in PLE from $n = 6$ to $n = 9$ by 0.02 eV, whereas TD-B3LYP predicts an increase of 0.35 eV. These differences in PLE are all above the uncertainty of the methodology (approximately $0.3 - 0.5$ eV, as discussed in section 2.2.6), apart from the 0.02 eV for TD-CAM-B3LYP. On the other hand, TD-BHLYP predicts a dip in PLE from $n = 4$ to $n = 6$ of 1.15 eV, and an increase by 1.66 eV from $n = 6$ to $n = 9$. Both these differences are significantly larger than the TDDFT uncertainties.

It can be seen that the def2-TZVP calculations with all three *xc*-functionals display the same trend from $n = 9$ onwards: the PLE decreases from $n = 9$ to $n = 12$ and $n = 18$, then increases between $n = 18$ and $n = 24$, before finally plateauing for $n = 32$, which shows the same behaviour as the LVEE values discussed in chapter 5. The variability in the PLEs between the particles with $n \leq 9$ is possibly due to the fact that the smaller particles appear less rigid and so a larger number of excited state minima on the $S_1$ surface are low in energy: this is further discussed in section 7.3.6.

The TD-CAM-B3LYP calculated value for $n = 32$ is only approximate: due to the increased cost of the computational code required, no value could be obtained for the TD-CAM-B3LYP optimised $S_1$ structure. However, a single point calculation was performed on the TD-BHLYP/def2-TZVP optimised structure, as can be seen in table 7-2 below. This approach appears to be a good approximation to the TD-CAM-B3LYP PLE.

**Table 7-2:** Comparison of photoluminescence energies obtained with the def2-TZVP basis set for particles $(MgO)_n$ ($n$ = 18, 24, 32). The first column shows the result of an $S_1$ TD-BHLYP optimisation starting from the BHLYP $S_0$ ground state structure, the second column shows the result of an $S_1$ TD-CAM-B3LYP optimisation using the CAM-B3LYP $S_0$ ground state, and the third column shows the result of a single-point TD-CAM-B3LYP calculation on the TD-BHLYP optimised $S_1$ structure (labelled 'CAM'). All energies are in eV.

|  | BHLYP | CAM-B3LYP | CAM / BHLYP |
|---|---|---|---|
| $(MgO)_{18}$ | 1.53 | 1.56 | 1.55 |
| $(MgO)_{24}$ | 2.14 | 2.18 | 2.13 |
| $(MgO)_{32}$ | 2.22 | - | 2.22 |
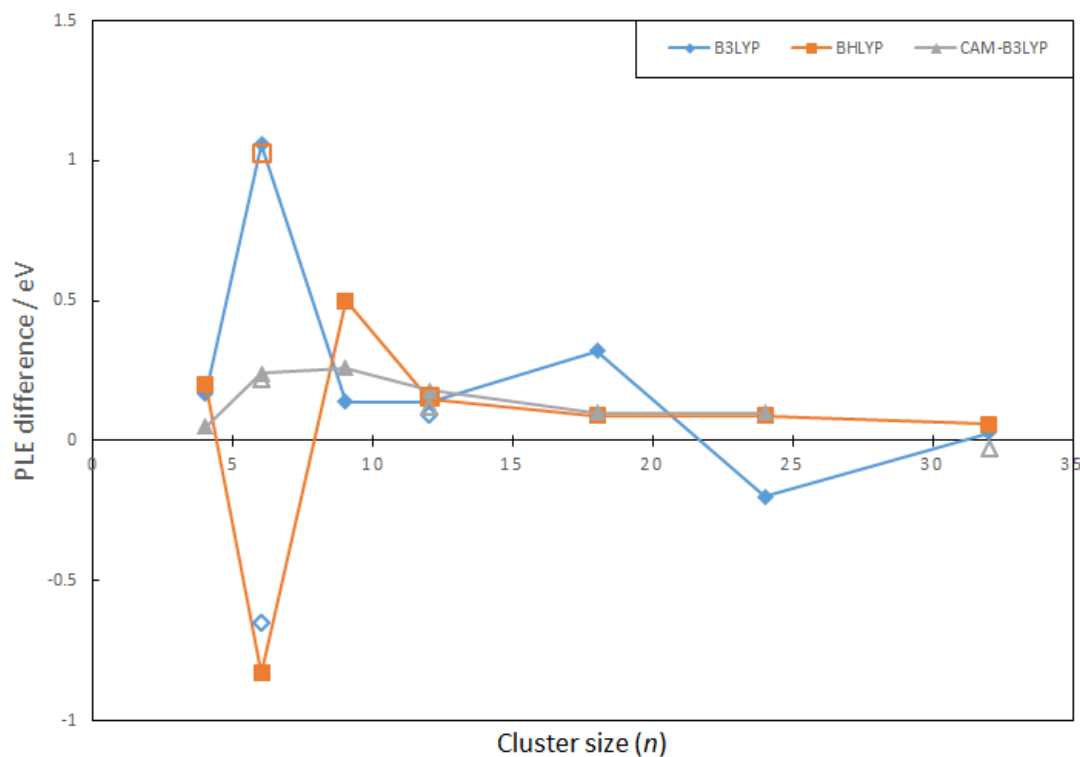


**Figure 7-2:** Difference between def2-TZVP calculated PLE and DZC PLE, obtained using the B3LYP (blue diamonds), BHLYP (orange squares) and CAM-B3LYP (grey triangles) *xc*-functionals. Open symbols correspond to the difference in PLE of the cubic $(MgO)_6$ and the sodalite $(MgO)_{12}$ structures. In the case of CAM-B3LYP, for $(MgO)_{32}$, the open triangle corresponds to the CAM-B3LYP single-point calculation on the TD-BHLYP/def2-TZVP $S_1$ optimised geometry.

The main difference in PLEs (table 7-1 and figure 7-2) calculated with different basis sets can be seen for $n = 6$ (hexagonal) using TD-BHLYP, where the def2-TZVP PLE is 0.83 eV smaller than the DZC result, but in general the DZC PLEs are lower than their def2-TZVP counterparts, and both basis sets exhibit the same general trend. However, especially for the larger particles, the results obtained from the smaller basis set seem to be a good approximation to the PLE calculated with the def2-TZVP basis set. Results obtained with the DZS basis can be found in Appendix A.

For values up to and including $n = 9$, the results obtained using the three $xc$-functionals vary and this is due to the fact that the particles optimise to different structural minima (discussed below). Both the TD-BHLYP/DZC and TD-B3LYP/DZC model chemistries predict a decrease in PLE going from $n = 4$ to $n = 6$, and then an increase going to $n = 9$, although the increase is much larger for TD-B3LYP: the PLE values for $n = 6$ are 2.28 eV for TD-BHLYP/DZC and 1.37 eV for TD-B3LYP/DZC but for $n = 9$, the values are 2.61 eV and 2.64 eV, respectively. TD-CAM-B3LYP/DZC shows a very similar picture for these particular particles, as it does with def2-TZVP: the PLE increases from $n = 4$ to $n = 6$, and drops slightly for $n = 9$.

Going from $n = 9$ to $n = 12$, TD-B3LYP/DZC and TD-CAM-B3LYP/DZC predict a lower PLE value, whereas TD-BHLYP/DZC predicts a slight increase. Going to $n = 18$, all functionals predict a considerable drop in PLEs, before increasing again going to $n = 24$. Both TD-BHLYP/DZC and TD-CAM-B3LYP/DZC approximate a plateau from $n = 24$ to $n = 40$, with only small variations in the PLE and converging around $2.1 - 2.2$ eV, whereas TD-B3LYP/DZC predicts a drop of 0.25 eV from $n = 24$ to $n = 40$. This drop could be related to the CT-excitation issue discussed in previous chapters; as the particle size increases, the orbital overlap within the excitation decreases, resulting in a stronger CT-character of the excitation. This is investigated further later in this chapter.

The above data shows that, especially with the larger basis set, the PLEs of the rocksalt structures ($n > 12$) are similarly described using TD-BHLYP and TD-CAM-B3LYP, and both $xc$-functionals approach the experimental PL onset of 2.4 eV, whereas TD-B3LYP consistently underestimates the PLEs, just as it does excitation energies, as shown in chapter 5.

### 7.3.2 Stokes shifts

The Stokes shift, which is the difference between the LVEE and PLE for a given particle, has been calculated for these particles. The Stokes shift is a measure of energy lost during the relaxation processes occurring in the excited state. It is, in some sense, an indication of the steepness of the potential energy surfaces: a high Stokes shift would mean that the $S_0$ and/or $S_1$ energy surface change significantly between the ground state and excited state optimised geometries.
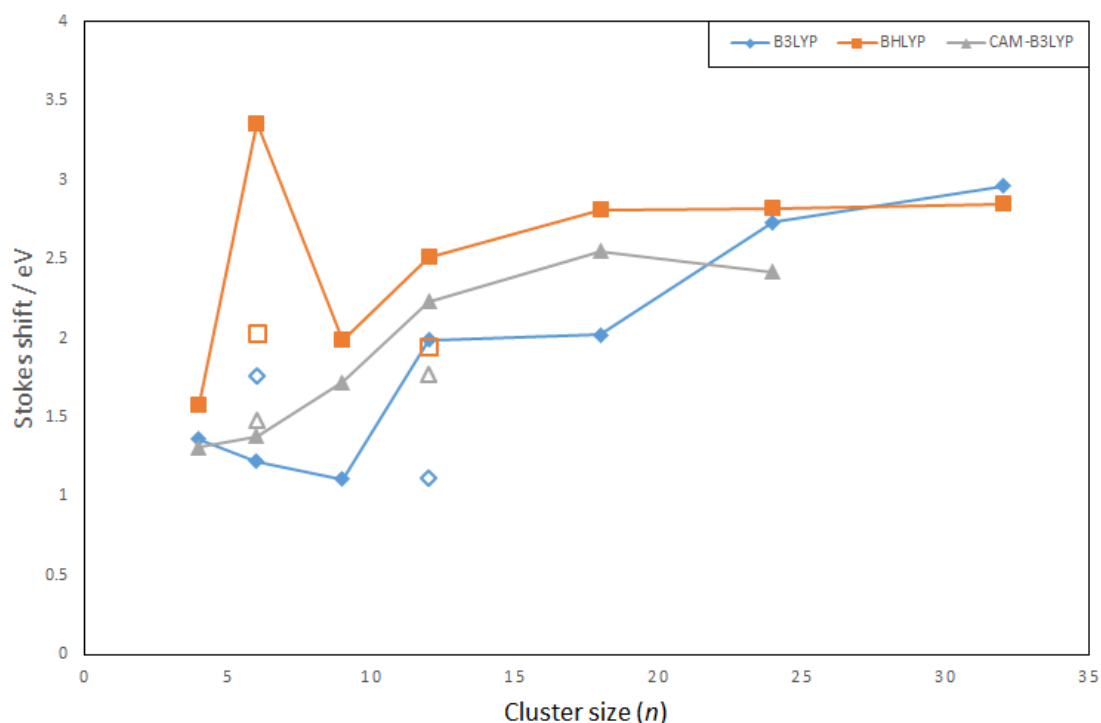


**Figure 7-3:** Stokes shifts, calculated using the def2-TZVP basis sets and the B3LYP (blue diamonds), BHLYP (orange squares) and CAM-B3LYP (grey triangles) *xc*-functionals. Empty symbols represent Stokes shifts for $(MgO)_6$ cubic and $(MgO)_{12}$ sodalite structures. All energies are in eV.

**Table 7-3:** Stokes shifts, calculated using the def2-TZVP and DZC basis sets and the B3LYP, BHLYP and CAM-B3LYP *xc*-functionals (DZC results between parentheses). All energies are in eV.

| | B3LYP | BHLYP | CAM-B3LYP |
|---|---|---|---|
| $(MgO)_4$ | 1.36 (1.26) | 1.58 (1.50) | 1.31 (1.30) |
| $(MgO)_6$ hexagonal | 1.22 (1.12) | 3.36 (3.21) | 1.38 (1.57) |
| $(MgO)_6$ cubic | 1.76 (1.68) | 2.03 (1.99) | 1.48 (1.64) |
| $(MgO)_9$ | 1.11 (1.05) | 1.99 (2.30) | 1.72 (1.96) |
| $(MgO)_{12}$ hexagonal | 1.99 (1.93) | 2.51 (2.46) | 2.23 (2.20) |
| $(MgO)_{12}$ sodalite | 1.12 (1.03) | 1.95 (1.94) | 1.77 (1.95) |
| $(MgO)_{18}$ | 2.02 (2.14) | 2.81 (2.69) | 2.55 (2.58) |
| $(MgO)_{24}$ | 2.73 (2.35) | 2.82 (2.75) | 2.42 (2.43) |
| $(MgO)_{32}$ | 2.96 (2.84) | 2.85 (2.81) | 2.47* (2.28) |
| $(MgO)_{40}$ | − (2.86) | − (2.87) | − (−) |

*CAM-B3LYP single-point calculation on the TD-BHLYP/def2-TZVP $S_1$ optimised geometry used as an approximation to the PL energy.

Table 7-3 and figure 7-3, as well as figures 7-5, 7-6 and 7-7 illustrate the trend in Stokes shifts found for the different MgO nanoparticles. The data can again be separated into two different classes: the smaller, more flexible particles that tend not to follow a clear trend, and the larger particles that tend to converge towards a limiting value, with the TD-CAM-B3LYP/DZC Stokes shift values for $(MgO)_{24}$ and $(MgO)_{32}$ possibly decreasing. No value for $(MgO)_{40}$ is given for the CAM-B3LYP *xc*-functional, as due to the computational costs of the calculation, the starting point for the excited state optimisation was the BHLYP ground state structure, rather than the CAM-B3LYP ground state structure. This means that the Stokes shift cannot be derived. Equally, the TD-CAM-B3LYP/def2-TZVP value

for $(MgO)_{32}$ could potentially be misleading, as the PLE obtained is from a single point calculation on the TD-BHLYP-optimised $S_1$ structure, although table 7-2 shows that the approximation is suitable to approximate PLEs.

The TD-B3LYP predicted Stokes shift values are similar to those predicted by TD-BHLYP and TD-CAM-B3LYP. However, as the B3LYP excitation energies are known to suffer from CT problems as, presumably, do the corresponding PLEs, it is very likely that the numerical values are similar to the values obtained from TD-BHLYP and TD-CAM-B3LYP due to error cancellation rather than an accurate description of the phenomena. Such behaviour has also been seen in $TiO_2$ and ZnS nanoparticles.[241,253–255] The CT character is probed by considering $\Lambda$ values: the TD-B3LYP $\Lambda$ value for $(MgO)_{24}$ at the ground state geometry is 0.15 (as shown in table 5-3) and 0.09 at the $S_1$ minimum, a clear sign of low orbital overlap and therefore a high probability that the $S_1$ surface and PLE at the $S_1$ minimum is poorly described by TD-B3LYP. From the $\Lambda$ values obtained for the $(MgO)_{24}$ system, it appears that TD-B3LYP underestimates the vertical excitation energy from the $S_0$ minimum to $S_1$ (as already discussed in chapter 5), and the orbital overlap decreases as the excited state structure is being optimised, which means that the de-excitation energy from the $S_1$ minimum to $S_0$ and it also underestimated. Due to computational inefficiency of the GAMESS-US package, no $\Lambda$ value for the $S_1$ $(MgO)_{32}$ particle could be obtained.

The difference in Stokes shift values between the TD-BHLYP and TD-CAM-B3LYP values (of approximately 0.3 eV) is possibly due to the overestimation of excitation energies of about 0.5 eV when TD-BHLYP is used, also discussed in chapter 5.

### 7.3.3  Stokes shift components

The difference in the excitation and de-excitation energies has two different components: namely the Ground State Destabilisation Energy (GSDE) and the Excited State Stabilisation Energy (ESSE). The former stems from the fact that as $S_1$ minimises its energy through geometry optimisation, i.e. the excited state stabilises, $S_0$ increases in

energy, as the geometry moves away from that of the ground state minimum. A schematic of the energy differences are pictured in figure 7-4.
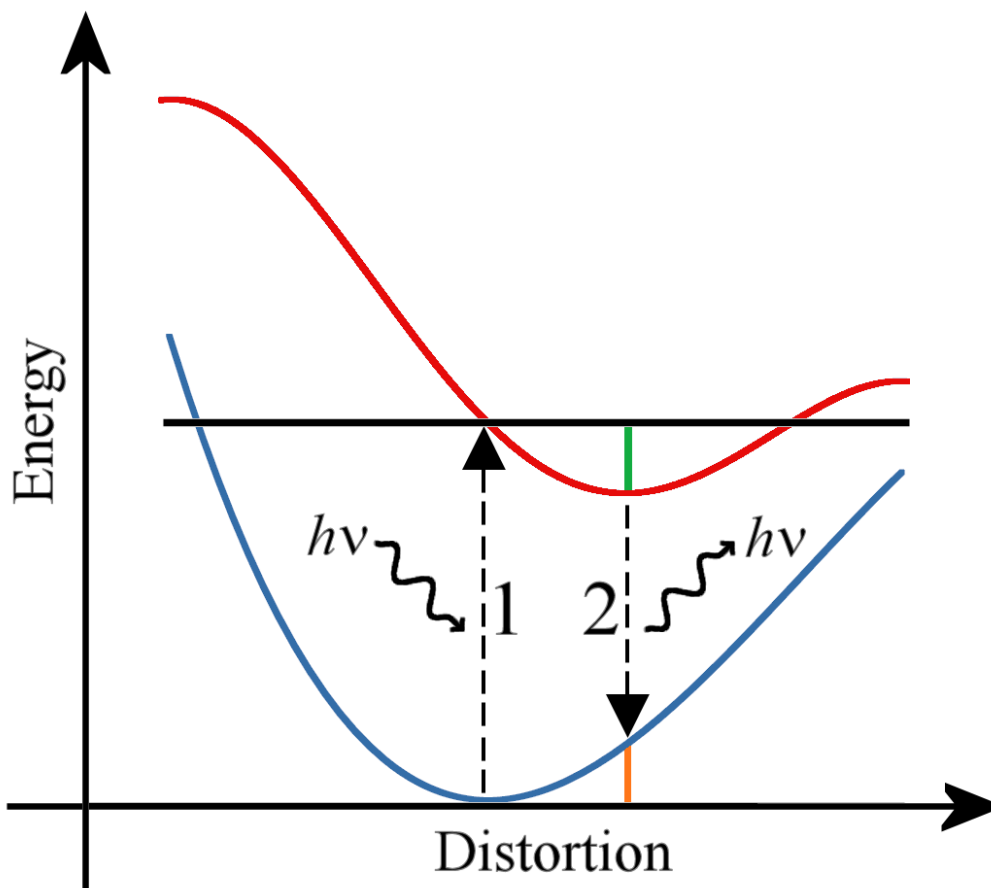


**Figure 7-4:** Conceptual figure of the $S_0$ potential energy surface (blue line), vertical excitation (dashed line labelled 1), the $S_1$ potential energy surface (red line), the excited state stabilisation energy, ESSE, (green line), the vertical de-excitation (black dashed line labelled 2) and the ground state destabilisation energy, GSDE, orange line). The horizontal black line is a guide to the eye, showing the energy of the state after vertical excitation ($S_0$ energy + vertical excitation energy).

**Table 7-4:** The def2-TZVP GSDE for the B3LYP, BHLYP and CAM-B3LYP (denoted by 'CAM') *xc*-functionals. All values are in eV.

|  | B3LYP GSDE | BHLYP GSDE | CAM GSDE |
|---|---|---|---|
| $(MgO)_4$ | 0.78 | 0.94 | 0.79 |
| $(MgO)_6$ hexagonal | 0.73 | 2.30 | 0.86 |
| $(MgO)_6$ cubic | 1.16 | 1.31 | 0.91 |
| $(MgO)_9$ | 0.67 | 1.35 | 1.15 |
| $(MgO)_{12}$ hexagonal | 1.37 | 1.71 | 1.49 |
| $(MgO)_{12}$ sodalite | 0.70 | 1.40 | 1.32 |
| $(MgO)_{18}$ | 0.99 | 1.62 | 1.53 |
| $(MgO)_{24}$ | 1.49 | 1.69 | 1.55 |
| $(MgO)_{32}$ | 1.61 | 1.78 | – |

**Table 7-5:** The def2-TZVP ESSE for the B3LYP, BHLYP and CAM-B3LYP (denoted by 'CAM') *xc*-functionals. All values are in eV.

|  | B3LYP ESSE | BHLYP ESSE | CAM ESSE |
|---|---|---|---|
| $(MgO)_4$ | - 0.58 | - 0.64 | - 0.52 |
| $(MgO)_6$ hexagonal | - 0.49 | - 1.06 | - 0.53 |
| $(MgO)_6$ cubic | - 0.31 | - 0.72 | - 0.57 |
| $(MgO)_9$ | - 0.44 | - 0.64 | - 0.58 |
| $(MgO)_{12}$ hexagonal | - 0.62 | - 0.80 | - 0.74 |
| $(MgO)_{12}$ sodalite | - 0.42 | - 0.55 | - 0.45 |
| $(MgO)_{18}$ | - 1.03 | - 1.28 | - 1.02 |
| $(MgO)_{24}$ | - 1.24 | - 1.13 | - 0.87 |
| $(MgO)_{32}$ | - 1.35 | - 1.07 | – |
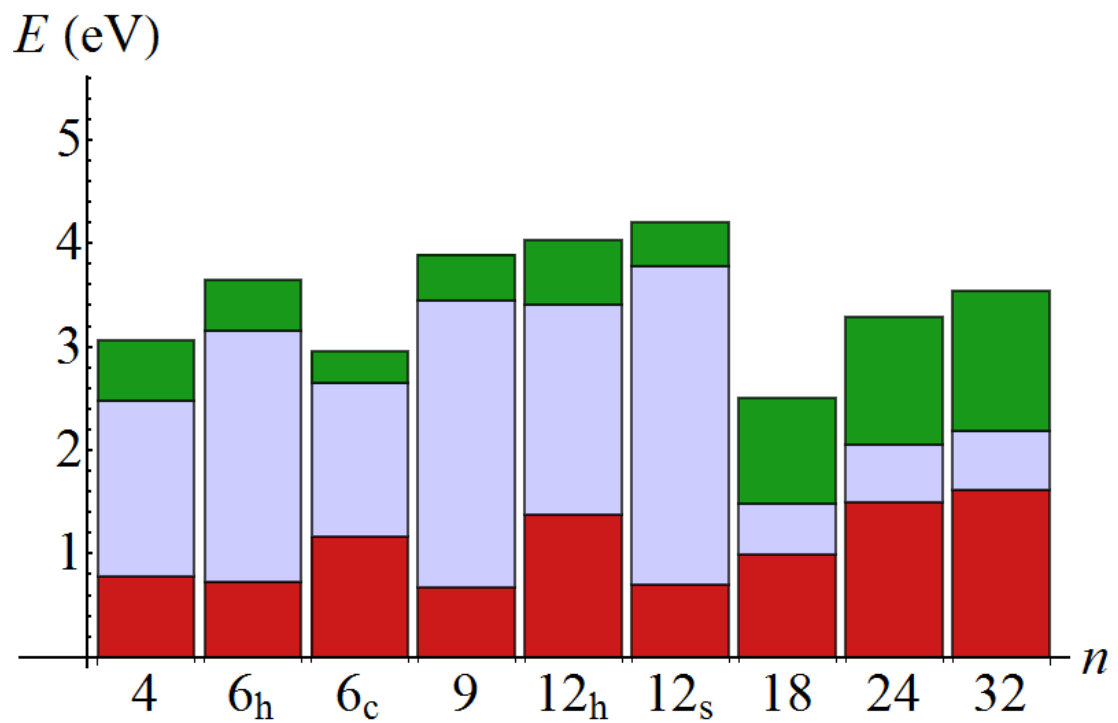
**Figure 7-5:** The TD-B3LYP/def2-TZVP GSDE (red), PLE (light blue) and ESSE (green) results. The 'h' subscript denotes the hexagonal particles, 'c' the cubic one, and 's' the sodalite type particler. All values are in eV.
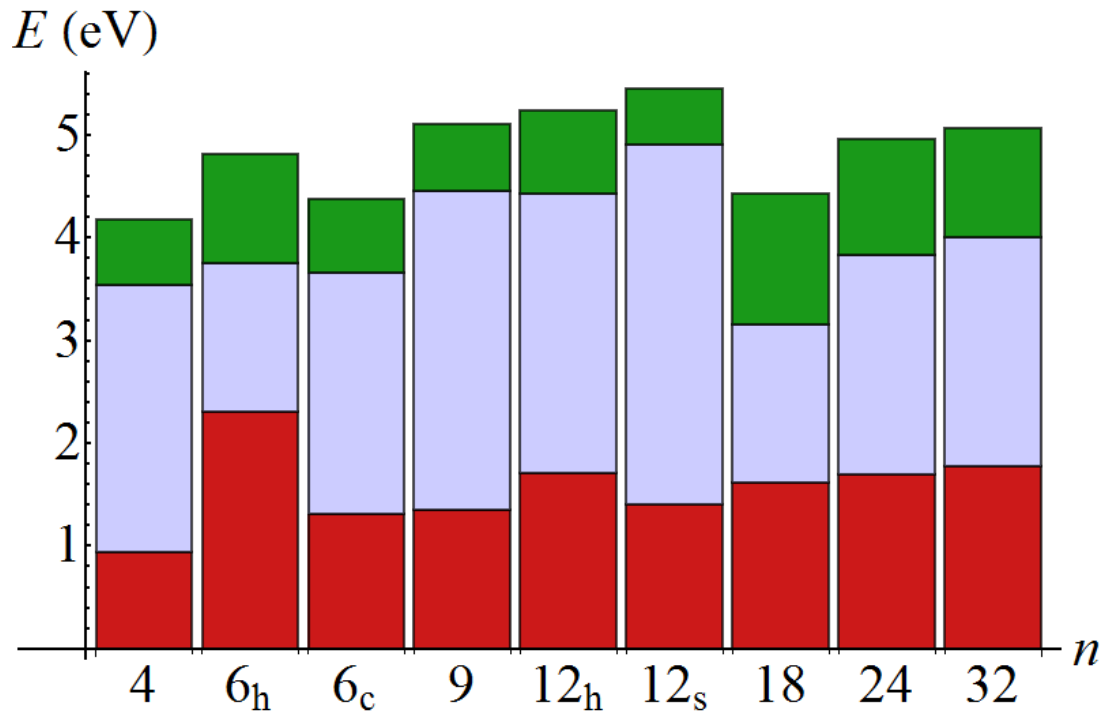
**Figure 7-6:** The TD-BHLYP/def2-TZVP GSDE (red), PLE (light blue) and ESSE (green) results. The 'h' subscript denotes the hexagonal particles, 'c' the cubic one, and 's' the sodalite type particle. All values are in eV.
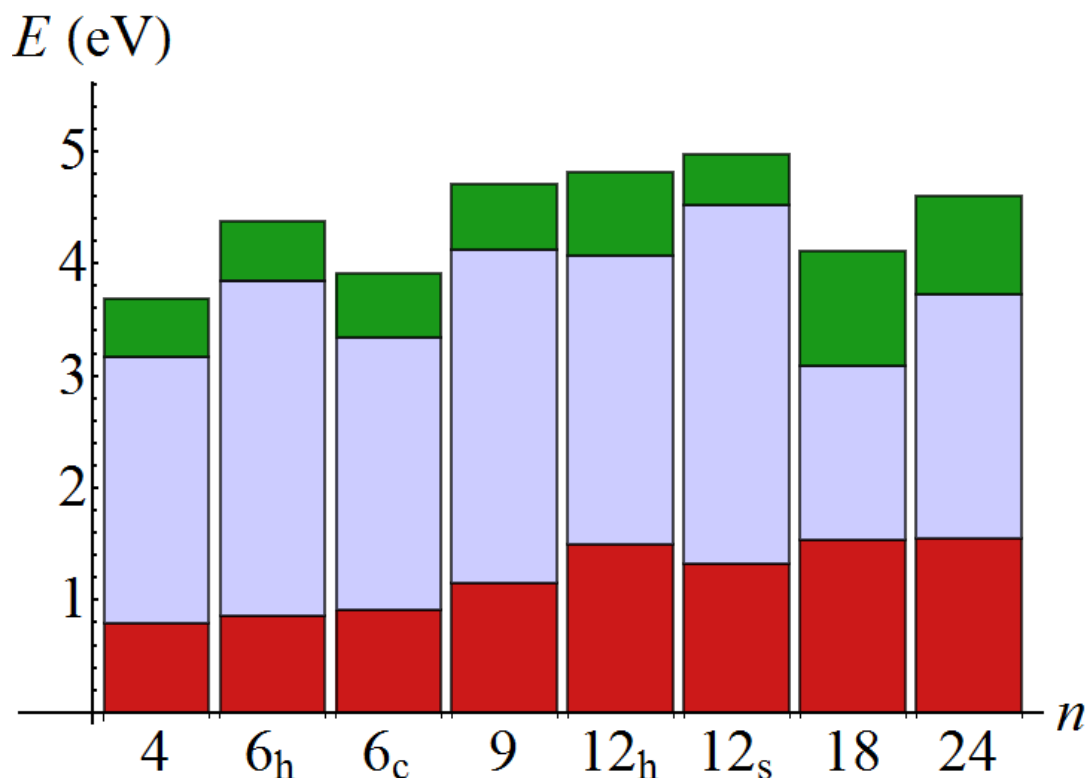
**Figure 7-7:** The TD-CAM-B3LYP/def2-TZVP GSDE (red), PLE (light blue) and ESSE (green) results. The 'h' subscript denotes the hexagonal particles, 'c' the cubic one, and 's' the sodalite type particle. All values are in eV.

From the data presented in tables 7-4 and 7-5 and figures 7-5, 7-6 and 7-7, it can be seen that generally for a given particle the GSDE has a larger absolute value than the ESSE, with the B3LYP-calculated $(MgO)_{18}$ energies being the only exception. The latter might be due to the dipole present in the system, discussed in section 5.3.2.

The fact that the GSDE is larger than the ESSE means that the $S_0$ surface changes more dramatically than the $S_1$ surface, although the ESSEs increase for the larger particles ($n = $ 18, 24, 32). Interestingly, all $xc$-functionals show a similar trend in the energies, which is further evidence for error cancellation (discussed above in the context of Stokes shifts) occurring in the TD-B3LYP data. From previous data discussed in chapter 5, it is obvious that TD-B3LYP does not describe energies on the $S_1$ surface at the $S_0$ minimum energy

structure accurately due to the CT character of the excitations, and it appears that the $S_1$ energies at the $S_1$ structure are also poorly described using TD-B3LYP.

The B3LYP/def2-TZVP $(MgO)_9$ GSDE is very low in in comparison to the GSDE of the other particles, which is presumably due to the fact that the B3LYP/def2-TZVP $(MgO)_9$ particle is  predicted to have a different exciton localisation character, discussed further in section 7.3.4.

**Table 7-6:** GSDE calculated with the B3LYP, BHLYP and CAM-B3LYP (denoted by 'CAM') $xc$-functionals and the DZC basis set for $(MgO)_n$ where $n =$ 24, 32, 40. All values are in eV.

|  | B3LYP  GSDE | BHLYP  GSDE | CAM  GSDE |
| --- | --- | --- | --- |
| $(MgO)_{24}$ | 1.19 | 1.62 | 1.53 |
| $(MgO)_{32}$ | 1.50 | 0.55 | 0.45 |
| $(MgO)_{40}$ | 1.49 | 0.60 | – |

**Table 7-7:** ESSE calculated with the B3LYP, BHLYP and CAM-B3LYP (denoted by 'CAM') $xc$-functionals and the DZC basis set for $(MgO)_n$ where $n =$  24, 32, 40. All values are in eV.

|  | B3LYP ESSE | BHLYP  ESSE | CAM  ESSE |
| --- | --- | --- | --- |
| $(MgO)_{24}$ | - 1.15 | - 1.13 | - 0.91 |
| $(MgO)_{32}$ | - 1.34 | - 2.27 | - 0.71 |
| $(MgO)_{40}$ | -  1.37 | - 2.27 | – |

The DZC equivalent ESDE and ESSE results for the larger particles are presented in tables 7-6 and 7-7, to highlight some differences between these results and the results obtained with the def2-TZVP basis set, shown in tables 7-4 and 7-5. The results obtained from both the B3LYP and CAM-B3LYP $xc$-functionals are not basis set dependent but in the case

of the BHLYP *xc*-functional, some clear differences can be seen: the ESSE becomes larger than the GSDE for both the $(MgO)_{32}$ and the $(MgO)_{40}$ particles when decreasing the size of the basis set. This means that, when using the smaller basis set, the $S_0$ potential energy surface is shallower than the $S_1$ surface. However, it is possible that the $S_1$ surface is sufficiently badly described with the smaller basis set, and described worse than the ground state surface, as, broadly speaking, the excited state density is more diffuse. This increased diffuse nature arises from the fact that the electron is less strongly bound when excited. This then results in an excited state that is more difficult to describe with a smaller basis set.

### 7.3.4  Exciton localisation

It can be difficult to characterise excited state minima, however Zwijnenburg[256,257] has developed a useful approach to describing different types of $S_1$ minima through their exciton localisation character (ELC), and a similar notation is adopted here. The different types of minima are labelled as $(n_e - n_h)$ where $n_e$ = the number of excited electron centres and $n_h$ = the number of hole centres. As, an example, when one electron is localised over two centres and the corresponding hole is localised over one centre, the notation $(2 - 1)$ is used. When the excited electron and/or hole are delocalised over the entire particle, N (for 'nulla', zero in Latin) is used instead of a numerical value. The number of electron and hole centres has been obtained by taking the difference of the ground state $(S_0)$ charges and the excited state $(S_1)$ charges, both obtained at the optimised excited state geometry. When using (TD-)BHLYP and (TD-)B3LYP, NBO charges have been used to evaluate the charge difference, whereas Löwdin charges have been used for calculations with (TD-)CAM-B3LYP.

The localisation data is a set of charge differences, evaluated at every atom, so on every atom, the resulting charge difference could range from zero to one. A charge difference of zero would mean that none of the excited electron or hole is localised on that atom and a charge difference of one would mean that the entire electron or hole is localised on that atom. However, as (TD)DFT describes electrons as wave-like particles (or rather, it

describes the electron density), the charge difference is never zero or one. This means that a cut-off value had to be determined to classify the electron and hole localisation.

Typically, a cut-off value of 0.1 has been used. However, in the case of the TD-B3LYP/def2-TZVP $(MgO)_9$ result, this was not the case: the hole was localised on one oxygen atom by approximately 62% (i.e. the oxygen on which the hole was localised on had a charge difference of 0.62, with the other oxygens having charge differences ranging from 0.03 to 0.08). The corresponding excited electron, however, was delocalised over several magnesium atoms: two atoms had a charge difference of 0.1, two atoms showed a charge difference of 0.09, two atoms showed a charge difference of 0.07, two further atoms had 0.04 of the electron and the final atom had 3% of the electron localised on that atom (corresponding to a charge difference of 0.03). It could be argued that, instead of a $(N - 1)$ localisation, a $(2 - 1)$ localisation would be more suitable. However, as a charge difference of 0.10 is so small compared to one of 0.6 and 0.10 is so similar to a charge difference of 0.09, which in turn is more similar to 0.07 than it is to 0.6, it was felt that a localisation of $(N - 1)$ would be a more suitable description of the relative delocalisation of the electron compared to that of the hole. For all other systems, the case of cut-off values was very clear, and two examples are given to demonstrate this point further. An example particle with $(1 - 2)$ ELC is the cubic $(MgO)_6$ particle with the TD-BHLYP/def2-TZVP model chemistry: the electron is localised on one magnesium atom, seen by a charge difference of 0.72, and the hole is delocalised over two oxygen atoms, with a charge difference of 0.35 each. The TD-BHLYP/def2-TZVP $(MgO)_9$ particle, in contrast, shows a very clear $(1 - 1)$ ELC, with an excited electron localised on one oxygen atom by 76% and the corresponding hole being localised on one magnesium atom of 67%. The ELCs obtained for all $(MgO)_n$ systems are shown in table 7-8, below.

**Table 7-8:** Exciton localisation character (ELC) from the difference in NBO charges derived from calculations using the B3LYP and BHLYP- *xc*-functionals and the def2-TZVP and DZC basis sets.

| | B3LYP | | BHLYP | |
|---|---|---|---|---|
| | def2-TZVP | DZC | def2-TZVP | DZC |
| $(MgO)_4$ | $(2-2)$ | $(2-2)$ | $(2-2)$ | $(2-2)$ |
| $(MgO)_6$ hexagonal | $(2-2)$ | $(2-2)$ | $(1-1)$ | $(1-1)$ |
| $(MgO)_6$ cubic | $(1-2)$ | $(1-2)$ | $(1-2)$ | $(1-2)$ |
| $(MgO)_9$ | $(N-1)$ | $(1-2)$ | $(1-1)$ | $(1-2)$ |
| $(MgO)_{12}$ hexagonal | $(1-1)$ | $(1-1)$ | $(1-2)$ | $(1-2)$ |
| $(MgO)_{12}$ sodalite | $(2-2)$ | $(2-2)$ | $(1-2)$ | $(1-2)$ |
| $(MgO)_{18}$ | $(1-1)$ | $(1-1)$ | $(1-1)$ | $(1-1)$ |
| $(MgO)_{24}$ | $(1-1)$ | $(1-1)$ | $(1-1)$ | $(1-1)$ |
| $(MgO)_{32}$ | $(1-1)$ | $(1-1)$ | $(1-1)$ | $(1-1)$ |
| $(MgO)_{40}$ | – | $(1-1)$ | – | $(1-1)$ |

The results based on the NBO data show that as the particle size increases, the excited electron and hole each become more localised at the $S_1$ minimum energy geometry, as seen in figure 7-8. The localised character of the exciton is most apparent in the calculations for larger particles ($n = 18, 24, 32, 40$), which all have an ELC of $(1-1)$, i.e. the excited electron and hole are localised on one atomic centre each: this is predicted with both the DZC and def2-TZVP basis sets. In these larger rocksalt systems, the excited electron is localised on a corner magnesium atom, whereas the hole is localised on a corner oxygen atom, with some of the excited electron and hole density also accumulating on the edge atoms adjacent to the corner sites.

It sounds contradictory that the optimised $S_1$ exciton appears to be so similar for both TD-B3LYP and TD-BHLYP, considering the different vertical excitation behaviour discussed in chapter 5. Taking the $(MgO)_{32}$ particle as an example, the analysis of the LVEE, discussed in the previous chapters, showed that TD-B3LYP predicts the LVEE to arise from an electron that is excited from a corner oxygen atom to a corner magnesium atom, whereas TD-BHLYP predicts the LVEE involves instead a corner oxygen atom and neighbouring magnesium edge atoms.

It appears that during the $S_1$ relaxation, the TD-B3LYP exciton delocalises slightly, with the NBO charge differences decreasing in absolute terms on the corner atom: the excited electron is localised 75.65% on corner magnesium atoms at the ground state geometry and 74.06% at the $S_1$ minimum. The hole delocalises more, with 83.51% of it being localised on oxygen corner atoms before the exciton relaxes, but only 61.11% of the hole is localised on oxygen corner atoms in the $S_1$ minimum. On the other hand, the TD-BHLYP exciton changes from an electron-hole pair that is in close proximity to each other, to an electron-hole pair that is separated along an edge of the rocksalt particle. TD-BHLYP $S_1$ relaxation therefore is a process where the an electron is excited from magnesium edge atoms coordinating the oxygen corner atom on which the hole is localised to a magnesium corner atom that shares a common edge the a corner hole centre. The excited electron is localised for only 17.24% on magnesium corner atoms before excited state relaxation, but this increases to 81.30% afterwards, whereas the hole delocalises slightly in the process, from 89.52% localisation on corner atoms before the excited state relation, to 67.20% after. A density difference plot, showing the optimised self-trapped exciton (STE)[‡‡‡] calculated with TD-B3LYP and TD-BHLYP can be seen in figure 7-8 for the $(MgO)_{32}$ particle.

In addition to the well-defined trend for the larger particle, good agreement between the different model chemistries (referring to both basis sets and *xc*-functionals) can be seen for some of the smaller particles, such as $(MgO)_4$ and the cubic $(MgO)_6$ structure.

Some model chemistries lead to results that differ from those predicted by the other method combinations: for example, the hexagonal $(MgO)_6$ structure is predicted to have

---

[‡‡‡] A self-trapped exciton is an exciton that traps itself by distorting the geometry around it.

an $(1-1)$ ELC by (TD-)BHLYP, which is in contrast to the (TD-)B3LYP prediction of a $(2-2)$ type ELC. This difference is apparent regardless of which basis set is used. A similar result is found for the $(MgO)_{12}$ particles: (TD-)BHLYP predicts a $(1-2)$ type ELC for both particles but (TD-)B3LYP predicts an ELC of $(2-2)$ for the sodalite particle and an $(1-1)$ ELC for the hexagonal particle. The previously discussed $(MgO)_9$ particle is interesting, as although the DZC basis set yields the same ELC for (TD-)BHLYP and (TD-)B3LYP of $(1-2)$, the def2-TZVP basis set shows a different localisation for the (TD-)BHLYP and (TD-)B3LYP densities: the former showing an $(1-1)$ ELC but the latter a $(N-1)$ ELC, i.e. with the excited electron delocalised over all magnesium sites. $(MgO)_9$ is the only particle where $n_e$ is larger than $n_h$. For all other particles where $n_e \neq n_h$, the electron is localised on one centre, whereas the hole is delocalised over two centres.
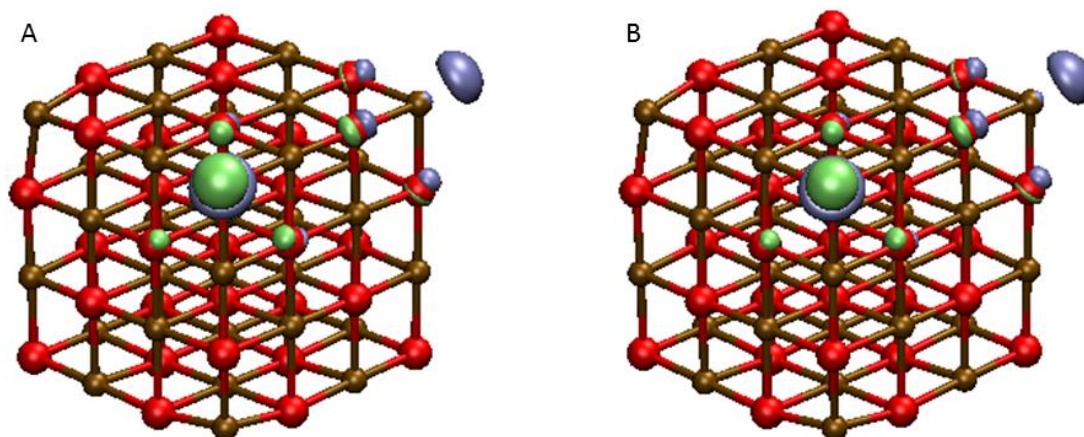


**Figure 7-8:** Ground and excited state electron density differences for the $S_1$ minima of the $(MgO)_{32}$ particle calculated using A. the TD-BHLYP/def2-TZVP and B. the TD-B3LYP/def2-TZVP model chemistries. Blue surfaces show charge accumulation (excess of electron density in the excited state), and green show charge depletion (deficit of electron density in the excited state). Isosurfaces are generated with a contour value of 0.01 a.u. Red spheres represent oxygen atoms, brown magnesium atoms.

**Table 7-9:** CAM-B3LYP/DZC exciton localisation characterisation values for the $S_1$ minima, based on the difference in Löwdin charges.

| | CAM-B3LYP | |
| --- | --- | --- |
| | def2-TZVP | DZC |
| $(MgO)_4$ | $(2-2)$ | $(3-1)$ |
| $(MgO)_6$ cubic | $(2-2)$ | $(2-2)$ |
| $(MgO)_6$ hex | $(1-1)$ | $(1-1)$ |
| $(MgO)_9$ | $(1-1)$ | $(1-1)$ |
| $(MgO)_{12}$ sodalite | $(1-2)$ | $(1-2)$ |
| $(MgO)_{12}$ hexagonal | $(1-2)$ | $(1-2)$ |
| $(MgO)_{18}$ | $(1-2)$ | $(1-2)$ |
| $(MgO)_{24}$ | $(1-1)$ | $(1-1)$ |
| $(MgO)_{32}$ | $-$ | $(1-1)$ |

Due to the unavailability of NBO population analysis in GAMESS-US, localisation characterisation based on Löwdin charges was performed instead for CAM-B3LYP generated densities and is shown in table 7-9. In contrast to the analysis based on NBO charges, Löwdin ELC are the same, irrespective of the basis set used for all particles apart from $(MgO)_4$, where the def2-TZVP basis set gives a $(2-2)$ localisation for the smallest particle, compared to a $(1-3)$ ELC obtained from the DZC generated data. The absolute charge differences obtained for the different basis sets are different: the $(2-2)$ ELC obtained from the def2-TZVP calculation results from the excited electron an hole centres having approximately the same amount of localisation on each of the centres, with an absolute charge of approximately 0.14 per centre, whereas the ELC from the DZC basis set arises from a 23% electron localisation and a 9% localisation of approximately on each

of the hole centres. This strong basis set dependence can only be seen for the smallest particle in this set of results.

Similarly to the NBO results in table 7-8, Löwdin analysis predicts a $(1 - 1)$ localisation for the larger particles studied. It should be noted that the $(MgO)_{40}$ particle has not been included in this analysis, due to previously discussed computational limitations. Both $(MgO)_{24}$ and $(MgO)_{32}$ are discussed in more depth below.

When considering the $(MgO)_{24}$ particle, the CAM-B3LYP *xc*-functional with both the DZC and def2-TZVP basis sets predicts an ELC of $(1 - 1)$, with the electron localised on one magnesium corner and the hole on one oxygen corner. The corner sites are common to one edge. It could be argued that the exciton localisation at the $S_1$ minimum is actually one with an $(1 - 4)$ ELC, as the Löwdin charge differences suggest that the magnesium edge atoms around the oxygen corner (where the hole is localised) also contribute to the hole. The fact that magnesium atoms are predicted to be hole centres is counter-intuitive: MgO is an ionic material, with magnesium being a di-cation and oxygen a di-anion, so the excited electron would move from the negatively charged ion to the positively charged ion, and the excited electron would not move from a positively charged ion. It is possible that localising the hole on magnesium sites is an error that arises from the Löwdin analysis: Löwdin analysis is basis-set dependent, and uses atomic orbitals to analyse charges. The diffuse functions in the magnesium atoms might contribute to the description of charge on the oxygen corner, which would lead to spurious (positive) charges on magnesium. When both optimised $S_1$ CAM-B3LYP geometries (def2-TZVP and DZC optimised) have been studied with NBO analysis (albeit with the BHLYP *xc*-functional), the magnesium edge sites can no longer be identified as hole centres. It was therefore decided that the ELC of $(1 - 1)$ was more suitable.

The $(1 - 1)$ ELC for $(MgO)_{32}$ obtained from Löwdin charges found for CAM-B3LYP/DZC calculations could, similarly to $(MgO)_{24}$, be described as having $(1 - 4)$ ELC. As this is a tetrahedral particle, and all edges contain the same number of atoms, each magnesium edge site neighbouring the hole centre show approximately a third of the charge difference of the oxygen corner site. For comparison, a Löwdin analysis performed on the TD-BHLYP structure (with a photoluminescence energy of 2.22 eV) yields an ELC

of $(1-1)$, although it could be argued that this is a localisation of $(1-2)$, with the magnesium edge site between the electron and hole having some hole characteristics. This is not found when using NBO charges (where only the corner sites show significant electron and hole localisation).

From comparison of the (TD-)CAM-B3LYP and (TD-)BHLYP Löwdin charge analysis, it appears that (TD-)BHLYP localises charges more than (TD-)CAM-B3LYP. Secondly, it seems that the hole localisation on magnesium edge sites adjacent to the oxygen corner hole centre is only apparent when analysing Löwdin charges and not those of NBO. This means that, if NBO analysis were available for the (TD-)CAM-B3LYP densities, an $(1-1)$ ELC would most likely result, with little evidence of a possible $(1-4)$ ELC for $(MgO)_{24}$ or $(MgO)_{32}$.

### 7.3.5  Structural characterisation

A comparison of $S_0$ and $S_1$ structures calculated with the B3LYP/def2-TZVP *xc*-functional are shown in figure 7-9. The $(MgO)_9$ structure is discussed in more detail below, and its TD-B3LYP structures are compared to the TD-BHLYP structures in figure 7-10, showing further evidence that the structural distortion can be directly linked to the ELC.

On the one hand, the larger particles ($n = 18, 24, 32$; structures F, G and H in figure 7-9) show the same, and very clear, structural distortion: one magnesium corner atom (shown as the top left corner) distorts outwards, lengthening the bonds with the neighbouring oxygen atoms. This can be rationalised in the following, simplistic way: all larger particles show a $(1-1)$ ELC, and the excited electron is localised on a corner magnesium. That corner magnesium changes its +2 charge to a +1 charge, meaning that the bond becomes more covalent (less ionic), with a weaker Coulombic interaction, and therefore the bond length increases. Comparing the absolute distortion between the larger particles and the others, it can be seen that the overall distortion appears to be smaller in the larger particles, due to their rigid rocksalt structure.

On the other hand are the smaller particles, where the individual distortions are not clearly visible, such as the $(MgO)_4$, hexagonal $(MgO)_6$ and the bubble-like sodalite $(MgO)_{12}$ (TD-)B3LYP/def2-TZVP particles (structures A, C and E in figure 7-9). This subtle excited state distortion can be explained through its ELC of $(2-2)$: two of the magnesium atoms gain electron density, and two of the oxygen atoms lose electron density. This means that the electron density is distributed over more than one atom and the individual distortions are not as clearly visible, as only smaller parts of the excited electron are localised on each of the two magnesium atoms. As two magnesium atoms distort slightly, the other atoms in the particle rearrange to accommodate the distortion.

The cubic $(MgO)_6$ particle (structure A in figure 7-9) displays different behaviour: one magnesium corner (top left) is distorted more than any other atom. This can be rationalised with the ELC of $(1-2)$, meaning that the excited electron localises mainly on one corner magnesium atom. The main oxygen distortion appears to be on the oxygen atoms directly bonded to the magnesium corner that localises the excited electron and not on the atoms where the hole is located on. This shows that the hole does not distort the atoms as much as the electron does.

Similarly to the cubic $(MgO)_6$ particle, the hexagonal $(MgO)_{12}$ particle (structure D in figure 7-9) displays one very distorted magnesium atom (top right). This arises from the fact that the particle displays $(1-1)$ ELC and the excited electron is localised on the most distorted magnesium atom.
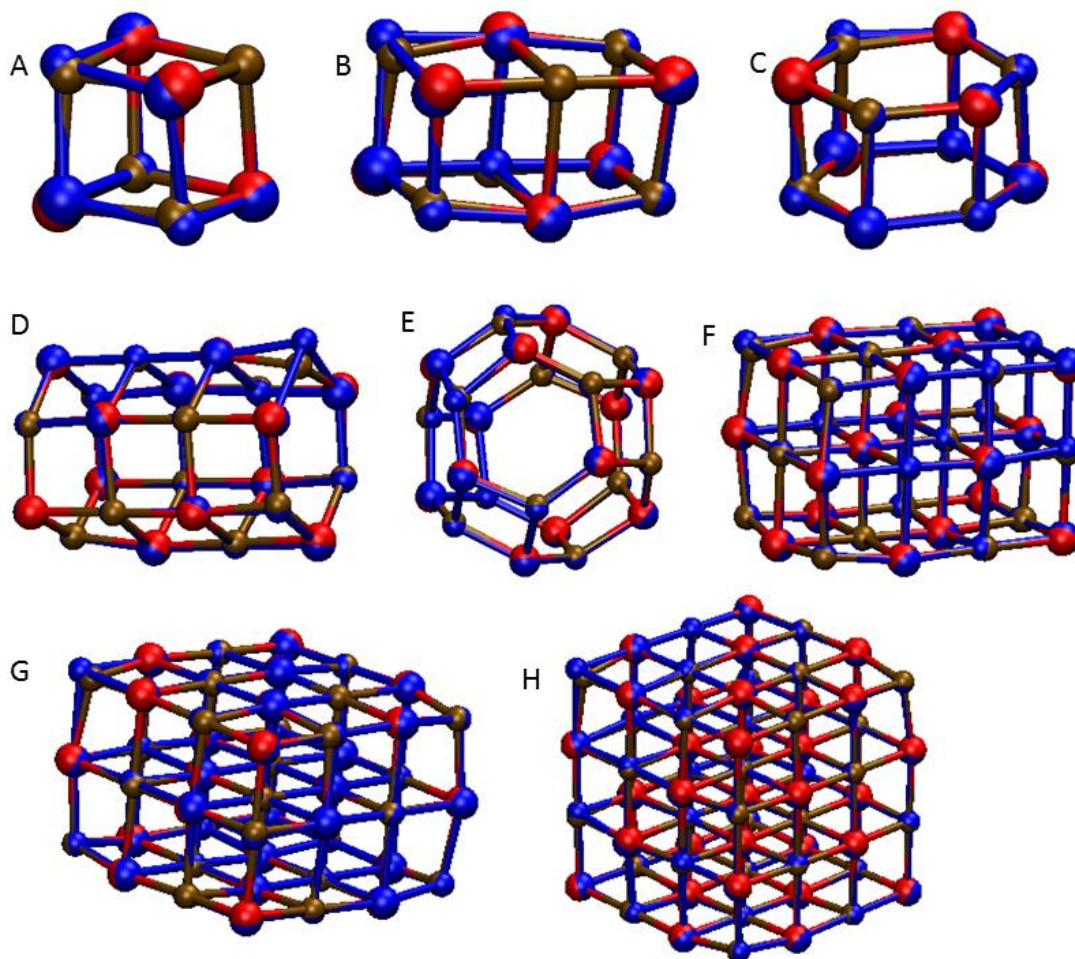
**Figure 7-9:** Overlaid TD-B3LYP/def2-TZVP calculated ground and excited state structures d of A. $(MgO)_4$, B. cubic $(MgO)_6$, C. hexagonal $(MgO)_6$, D. hexagonal $(MgO)_{12}$, E. sodalite $(MgO)_{12}$, F. $(MgO)_{18}$, G. $(MgO)_{24}$, H. $(MgO)_{32}$. Red (brown) spheres represent oxygen (magnesium) atoms in the ground state geometry and the blue spheres represent both species of in the excited state geometry.

The one particle where there is a significant difference between the TD-B3LYP and TD-BHLYP $S_1$ structures is $(MgO)_9$. Figure 7-10 shows that the optimised TD-B3LYP $S_1$ structure is more similar to the B3LYP ground state minimum (figure 7-10 A), whereas the TD-BHLYP optimised $S_1$ structure shows a magnesium atom that is strongly displaced from that of the optimised BHLYP ground state in comparison to the rest of the atoms (figure 7-10 B). This difference can be explained by the difference in ELC: analysis of the TD-B3LYP density gives a minimum with $(N - 1)$ ELC, i.e. the electron is delocalised

over the entire particle and therefore only minor distortions on every atom can be observed, rather than one atom distorting significantly more than the rest, whereas TD-BHLYP predicts a $(1 - 1)$ ELC, which means that the electron is localised on a single magnesium atom, which in turn moves further away from neighbouring oxygens, resulting in a stronger distortion.
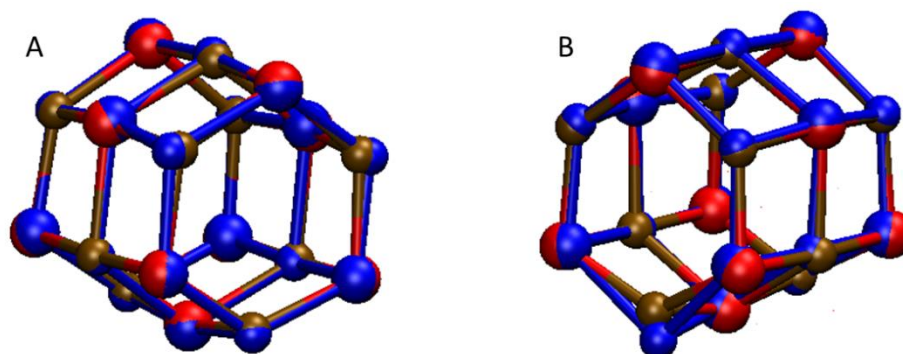


**Figure 7-10:** $(MgO)_9$ TD-B3LYP/def2-TZVP (A) and TD-BHLYP/def2-TZVP (B) calculated ground and excited state structures overlaid. Red (brown) spheres represent oxygen (magnesium) atoms in the ground state geometry and the blue spheres represent both species in the excited state geometry. Black circle highlights the different distortion behaviour.

### 7.3.6 The flexibility of smaller particles

All the above presented work has been done under the assumption that starting the $S_1$ optimisation from the $S_0$ optimised structure is a reliable way to finding the $S_1$ minimum responsible for fluorescence. To test this assumption, the smaller particles have been chosen and the $S_1$ optimisation has been performed with a different starting structure. Not only are the optimisation calculations tractable for these clusters, but the frequency analysis can also be performed with reasonable computational expense. Furthermore, from the behaviour of the smaller particles, extrapolating the validity of the $S_1$ minima of the larger particles (which cannot be studied in the same way due to computational costs involved) might be possible. Only actual minima with no imaginary frequencies are discussed below.

The flexibility of the clusters is illustrated in greater detail in this section using the BHLYP and B3LYP $xc$-functionals, along with the DZS and the def2-TZVP basis sets. Here the focus is on the $(MgO)_n$ particles with $n = 4, 6, 9$. The approach to investigating this flexibility has been the following: the excited state structure of a particle optimised with one functional and one basis set is taken and then re-optimised with either the other functional or basis set. This means that the starting point of the $S_1$ re-optimisation is not the optimised $S_0$ structure, but some non-optimal structure. This allows further exploration of the excited state surface from a different starting point, potentially leading to other local minima on the $S_1$ surface. The different minima are characterised by their PLE and their ELC. Further data on the DZS results can be found in Appendix A.

**Table 7-10:** Calculated photoluminescence energies for the cubic $(MgO)_4$ particle, obtained from different combinations of $xc$-functional and basis set: the model chemistry for the starting structure of the calculation is listed on the left hand side, whereas the model chemistry used for the re-optimisation is listed at the top. Italicised values are for the reference minima, the '−' sign means that this combination of model chemistries has not been tested. All values are in eV.

| $(MgO)_4$ | BHLYP / def2-TZVP | B3LYP / def2-TZVP | BHLYP / DZS | B3LYP/ DZS |
|---|---|---|---|---|
| BHLYP / def2-TZVP | *2.60* | 1.70 | 2.29 | − |
| B3LYP / def2-TZVP | 2.60 | *1.70* | − | 1.44 |
| BHLYP / DZS | 2.60 | − | *2.29* | 1.44 |
| B3LYP / DZS | − | 1.70 | 2.29 | *1.44* |

As table 7-10 shows, $(MgO)_4$ does not have any other accessible minima in close proximity to the minima already found. As previously discussed and shown in table 7-8, the def2-TZVP minima are of $(2 − 2)$ ELC, with a PLE of 2.60 eV and 1.70 eV for TD-

BHLYP and TD-B3LYP, respectively. The DZS basis set also predicts a $(2-2)$ ELC at the $S_1$ minima for both *xc*-functionals. The PLEs from DZS the found minima is 2.29 eV and 1.44 eV from TD-BHLYP and TD-B3LYP, respectively.

Through the use of different starting structures, several transition states were identified, although the only minima found are those reported above. The fact that several transition states are present shows that the $S_1$ potential energy surface is not composed of just one minimum, but rather that the $S_1$ surface has several extrema.

**Table 7-11:** Calculated photoluminescence energies for the hexagonal $(MgO)_6$ particle, obtained from different combinations of *xc*-functional and basis set: the model chemistry for the starting structure of the calculation is listed on the left hand side, whereas the model chemistry used for the re-optimisation is listed at the top. Italicised values are for the reference minima, the '−' sign means that this combination of model chemistries has not been tested. All values are in eV.

| $(MgO)_6$ hex. | BHLYP / def2-TZVP | B3LYP / def2-TZVP | BHLYP / DZS | B3LYP / DZS |
|---|---|---|---|---|
| BHLYP / def2-TZVP | *1.45* | 0.73 | 1.23 | − |
| B3LYP / def2-TZVP | 1.45 | *2.43* | − | 1.88 |
| BHLYP / DZS | 1.45 | − | *2.60* | 1.88 |
| B3LYP / DZS | − | 0.73 | 2.60 | *1.88* |

The hexagonal $(MgO)_6$ particle shows more complicated behaviour than $(MgO)_4$, as shown in table 7-11. The $S_1$ minima predicted by TD-BHLYP/def2-TZVP and TD-B3LYP/DZS do not appear to be dependent on the starting structure.

However, the TD-B3LYP/def2-TZVP model chemistry predicts a second minima in addition to the minima with a PLE of 2.43 eV and an ELC of $(2-2)$, discussed previously

in this chapter. The second TD-B3LYP/def2-TZVP minima with PLE of 0.73 eV has an ELC of $(1-1)$. This minimum is actually 0.6 eV more stable[§§§] than the previously found minima with PLE 2.43 eV, showing that the more localised exciton stabilises the $S_1$ surface more. However, it is unclear whether the lower energy minima would be accessible from the TD-B3LYP/def2-TZVP ground state structure, as this study does not investigate energy barriers between minima

Furthermore, a second minimum has been found for the TD-BHLYP/DZS model chemistry, with a PLE of 1.23 eV and an $(1-3)$ ELC. This minima 3.60 eV higher in $S_1$ total energy to $(1-2)$ minima with a PLE of 2.60 eV. Despite the higher energy of the minima with a PLE of 1.23 eV, this minima is closer in PLE to the def2-TZVP PLE (with a difference of 0.22 eV) than the DZS minimum of 2.60 eV (with a difference of (1.15 eV), or the previously discussed DZC minimum with PLE 2.28 eV (with a difference of 0.83 eV).

It can be seen that TD-BHLYP energetically favours more localised excitons.

---

[§§§] The statement in this context refers to the total excited state energy. No comments about GSDE and ESSE are made, which could influence the PLE. In these cases, no Stokes shift, GSDE or ESSE have be calculated, as the model chemistries describing the starting structure and the final structure is different.

**Table 7-12:** Calculated photoluminescence energies for the cubic $(MgO)_6$ particle, obtained from different combinations of *xc*-functional and basis set: the model chemistry for the starting structure of the calculation is listed on the left hand side, whereas the model chemistry used for the re-optimisation is listed at the top. Italicised values are for the reference minima. Italicised values are for the reference minima, the '–' sign means that this combination of model chemistries has not been tested. All values are in eV.

| $(MgO)_6$ cub. | BHLYP / def2-TZVP | B3LYP / def2-TZVP | BHLYP / DZS | B3LYP / DZS |
|---|---|---|---|---|
| BHLYP / def2-TZVP | *2.35* | 1.48 | 2.08 | – |
| B3LYP / def2-TZVP | 2.35 | *1.49* | – | 1.31 |
| BHLYP / DZS | 2.35 | – | *2.08* | 1.30 |
| B3LYP / DZS | – | 1.48 | 2.08 | *1.30* |

As observed for the cubic $(MgO)_4$ particle, the cubic $(MgO)_6$ particle does not appear to have any other minima on the $S_1$ surface in the explored region, as shown in table 7-12. All minima found have the same ELC of $(1 - 2)$. The TD-B3LYP results sometimes vary by 0.01 eV, but this is most likely due to the chosen (TD)DFT convergence criteria: the TD-B3LYP/def2-TZVP minima have the same energy, within two decimal places, and the TD-B3LYP/DZS minima vary by 0.01 eV in their total excited state energy. It is likely that both the def2-TZVP and the DZS minima for TD-B3LYP have only one accessible minimum, but the $S_1$ potential energy surface is shallow and due to the convergence criteria used in the calculations, two very slightly different minima result, depending on which starting structure is used. The fact that there is only one accessible minima on the $S_1$ potential energy surface (with both the B3LYP and BHLYP *xc*-functionals) might not hold true for the DZC basis set: the difference between the def2-TZVP and DZC PLE is between $0.7 - 1.0$ eV, which is not seen in the comparison of the def2-TZVP with the DZS data, suggesting that there might be another minimum on the $S_1$ surface when the DZC basis set is employed.

Finally, as with $(MgO)_4$, several transition states were found on the $S_1$ surface for many re-optimisations.

**Table 7-13:** Calculated photoluminescence energies for the hexagonal $(MgO)_9$ particle, obtained from different combinations of *xc*-functional and basis set: the model chemistry for the starting structure of the calculation is listed on the left hand side, whereas the model chemistry used for the re-optimisation is listed at the top. Italicised values are for the reference minima, the '–' sign means that this combination of model chemistries has not been tested. All values are in eV.

| $(MgO)_9$ | BHLYP / def2-TZVP | B3LYP / def2-TZVP | BHLYP / DZS | B3LYP / DZS |
|---|---|---|---|---|
| BHLYP / def2-TZVP | *3.11* | 2.78 | 2.85 | – |
| B3LYP / def2-TZVP | 3.11 | *2.78* | – | 2.24 |
| BHLYP / DZS | 3.11 | – | *2.85* | 1.95 |
| B3LYP / DZS | – | 1.73 | 2.24 | *1.51* |

When studying the hexagonal $(MgO)_9$, similarly to the hexagonal $(MgO)_6$ particle, different $S_1$ minima have been found, as seen from PLEs presented in table 7-13. The use of the def2-TZVP basis set results in more rigid potential energy surfaces compared to the smaller DZS basis set. All starting structures converge towards the same TD-BHLYP/def2-TZVP minimum with a photoluminescence energy of 3.11 eV. TD-B3LYP/def2-TZVP calculations, on the other hand, optimise to two different minima: the minimum with a photoluminescence of 2.78 eV and ELC of $(N-1)$ and another minimum, lower by 0.04 eV, which photo-luminesces at 1.73 eV and with an ELC of $(1-1)$.

As already mentioned, the use of the smaller DZS basis set can result in different minima. In addition to the TD-BHLYP/DZS with PLE of 2.85 eV, another minima with PLE of

2.24 eV is seen. The latter minima is 0.12 eV lower in energy than the former. Both minima exhibit an ELC of $(1 - 1)$.

With the TD-B3LYP/DZS model chemistry, three different $S_1$ minima can be accessed, all of which have an ELC of $(1 - 1)$. In terms of energy, the minima with a PLE of 2.24 eV is 5.03 eV lower in energy than the minima with an associated PLE at 1.51 eV, which is in turn lower in energy by 0.03 eV than the minima that de-excites an electron at 1.95 eV.

It is unclear whether the different minima obtained from the DZS basis set would all be observed experimentally. As the def2-TZVP basis set does not show this flexibility and range in different minima, it is possible that the different TD-B3LYP/DZS minima arise from the poor description of the $S_1$ surface. Furthermore, assuming these minima are not just a result of poor basis set choice, it is unclear how high the energy barriers between the different minima would be, so it cannot be said whether all minima would be accessible (when starting from the $S_0$ minimum).

What can be concluded from this small study into the size and flexibility of the particles, is that the cubic particles are rigid whereas the hexagonal particles have more flexibility. This flexibility leads to other minima on the $S_1$ surface that can be accessed from slightly different starting structures, although it is unclear as to whether any high energy barriers exist between the different minima. Extrapolating from these findings, it seems reasonable to suggest that the larger particles, in particular $(MgO)_{18}$ and larger, would not show different minima on the $S_1$ surface in the studied region, as they are larger versions of the cubic particles studied in this section. This would mean that the PLE presented at the beginning of the chapter are most likely the lowest possible PLE for the larger particles.

## 7.4   Comparison to experiment

The smaller particles are, as previously discussed, less rigid. This means that they can be found in different energetic minima. However, the larger rocksalt structures seem to converge to a PLE of about 2.1 to 2.2 eV, which is only slightly lower than the

experimental PL onset of 2.4 eV. The experimental PL peak, however, is at 3.3 eV, a value that cannot be reflected in the calculations performed by the author.

It is possible that the use of the TD-BHLYP or the TD-CAM-B3LYP approximation is simply not sufficient to predict the correct PL behaviour of the MgO nanoparticles. It would be surprising, but not impossible, that although the use of TD-CAM-B3LYP is needed to accurately describe the vertical excitation spectra, this approximation does not hold for the description of other excited state properties, possibly due to over-localising the excited electron and hole. This is discussed in more detail below.

Due to the rigidity of the large particle, extrapolated from findings in section 7.3.6, it can be concluded that it is unlikely that the larger particles studied have other minima on $S_1$ that are accessible via the ground state structure. This leads to the question of where the current computational limits are for studying the PL of MgO nanoparticles.

To understand the compatibility of the computational results with experimental observations, two questions must be asked: what physical observable is being calculated, and what property is measured experimentally? The limitations of the computational (as well as experimental) approaches to studying these properties must also be taken into account.

Firstly, the experimental spectra (figure 3.2 ii) should be analysed more closely. If all particles emitted at the same energy upon de-excitation, then only one narrow peak should be seen in the spectrum. This is not the case, presumably due to instrumental broadening, vibrational broadening and a range of particle sizes in the sample. If vibrational broadening were the only factor, then a symmetrical peak would be observed, with the peak intensity corresponding to the value attributed to the de-excitation.

The obvious question to ask next is whether the asymmetrical particle size distribution found experimentally[20] is the source of the asymmetry of the observed photoemission spectrum. The experimental particle size distribution shows that, although the average particle size is 3 nm, particles as large as 8 nm are present within the sample,[20] so it can

be said that the asymmetric peak observed is at least partly related to the particle size distribution.

However, the same study has also looked at samples with larger average particle sizes (5 nm and 10 nm) and the peak positions of the PL spectra vary in intensity but only by 0.1 eV in energy and the asymmetry of the peak does not change (figure 3.2 ii). If the particle size distribution was the only factor determining the asymmetry of the peak and the peak position, the experimentally observed PL spectra would look different for the samples with different average particle sizes, resulting in PL spectra that are shifted up or downwards in energy if the average particle size of the sample increases or decreases.

There are other sources of potential broadening of the spectra that are not related to the sample, such as instrumental broadening. This type of broadening has different sources, such as the incoming light consisting of not just the set value of λ but also small variations in the wavelength but an average value of λ. It is difficult to quantify these broadening effect, especially as a computational chemist. However, it is most likely that the experimental broadening that arises would be symmetric (either of Gaussian or Lorentzian distribution), unless some unlikely misalignment is the experimental apparatus is present. Assuming that the experiments have been performed as accurately as possible, it is very unlikely that the asymmetry of the PL peak stems from instrumental broadening.

Through exclusion of other possibilities, such as vibrational and instrumental broadening as well as particle size distribution, and the fact that the use of different electron excitation energies yield slightly different PL peaks, it appears that there is a possibility of the fact that Kasha's rule (discussed in section 1.3) does not hold true for the MgO nanoparticles investigated by the author, as observed for other particles previously[258–260]: this would mean that de-excitation does not only occur from the $S_1$ surface but also from higher-lying (singlet) states. As little spin-orbit coupling is expected in MgO nanoparticles, de-excitation from $T_1$ (or any triplet state) is unlikely. There is some experimental evidence for the fact that MgO nanoparticles exhibit non-Kasha behaviour: the experimental PL spectra should be independent of the excitation wavelength, something that is not seen experimentally. The PL peak at 3.3 eV shifts to 3.4 eV as the excitation photon increases in energy from 270 nm (4.59 eV) to 240 nm (5.17 eV). This was explained by arguing that

the peak at 3.3 eV resulted from corner de-excitation and the peak at 3.4 resulted from edge de-excitation.

From a computational chemist's point of view, the possibility that Kasha's rule may not be applicable for MgO nanoparticles has severe consequences. As discussed previously it is difficult to calculate excited state minima using TDDFT on surfaces higher than $S_1$. Furthermore, it is possible that once an electron has been excited, internal conversion (orange arrow in figure 1.3) occurs: this is a radiationless transition and is therefore difficult to study experimentally. Hence, it is possible that an electron is excited to $S_n$ with $n > 1$, the system relaxes partly and only after some relaxation, does internal conversion occur to $S_m$, with $m < n$. This process may be repeated until the nanoparticle is in the $S_1$ state, and emission occurs – or, alternatively, emission occurs from a higher-lying state. The problem, from a computational perspective, is that the complex relaxation process is completely unknown. With the cost of the calculations as they are today and the limitations of the methodology, it is just not possible to know on which potential energy surface the relaxation occurs, which internal (radiationless) processes occur and from which state emission occurs for systems as large as the ones studied in this thesis.

## 7.5   Discussion

As discussed previously in this thesis, TD-B3LYP does not correctly predict MgO excitation behaviour, due to the CT character of some of its excitations. Similarly, TD-B3LYP calculated PLEs are considerably lower than those obtained from TD-BHLYP, TD-CAM-B3LYP and experiment. A test calculation was performed to obtain the $\Lambda$ value from a $(MgO)_{24}$ excited state optimisation calculation. The $\Lambda$ value is a numerical measure of overlap between orbitals occupied in the ground and excited states, discussed in more detail in chapters 5 and 5. For comparison, the $\Lambda$ value associated with the lowest vertical excitation of an electron at the ground state structure for $(MgO)_{24}$ is 0.15, indicating that the excitation has CT character. However, at the $S_1$ optimised structure, the $\Lambda$ value decreases to 0.09, indicating that there is even less orbital overlap between the orbitals at the $S_1$ minimum. This is the reason why the TD-B3LYP data for the larger particles,

despite sharing characteristics with TD-BHLYP such as the $(1-1)$ ELC, reveals a severe underestimation of the PLE. From the data discussed in chapter 5, it was determined that the excited state has been stabilised at the ground state structure and it can be seen from the PL data presented in this chapter, that this is also true at the $S_1$ minimum.

As discussed in chapter 5, TD-BHLYP predicts the excitation energies in MgO nanoparticles to be approximately 0.5 eV higher than those found experimentally (and those calculated with TD-CAM-B3LYP), presumably de-stabilising the excited states associated with these excitations. However, this is no longer seen in the PLE data: TD-BHLYP and TD-CAM-B3LYP predict very similar PLE for the larger particles and both predict the PLEs to reach a plateau at around 2.2 eV. This plateau is consistent with the experimental observation that the PLEs are not size-dependent. The difference in Stokes shift obtained from the TD-BHLYP results are slightly (although less than 0.5 eV) higher than the results obtained using TD-CAM-B3LYP. This leads to the question of where the stabilisation of $S_1$ at the optimised $S_1$ geometry using TD-BHLYP stems from. The ESSE is consistently higher for TD-BHLYP than it is for TD-CAM-B3LYP, and this is especially noticeable for the larger particles, meaning that the $S_1$ potential energy surface as described by TD-BHLYP is steeper, and initially higher at the $S_0$ geometry. This might result in a lower TD-BHLYP-calculated $S_1$ minimum i.e. the excited state energy at the $S_1$ minimum relatively lower than at the $S_0$ minimum and therefore leads to a photoemission energy similar to that of TD-CAM-B3LYP.

On a more general note regarding TDDFT, as seen in section 5.7, the larger particles optimise with TD-BHLYP from a state in which the exciton is localised on a corner atom and edge atoms (chapter 5), to an exciton that spreads along the edge side of the particle. Although there is no clear link that has been investigated between the BHLYP *xc*-functional performance and orbital overlap, TDDFT is known to model such excitations poorly with hybrid GGA functionals (apart from functionals with significant amount of HFE), as the *xc*-energy is a description of the local density and its gradient, even though the HFE is a non-local expression. The TD-BHLYP functional is constructed with a 50% HF contribution to the exchange, but although the HFE is non-local, it only describes the exact exchange for a non-interacting system (albeit with the same density as the

interacting system). The question that remains is whether a 50% contribution of a non-local, but non-interacting expression, is a good balance to describe the optimisation process of the $S_1$ surface.

The issue remains as to why TDDFT does not predict the peak position of the PL spectrum: the experimentally observed peak is the most intense, and that peak is the $S_1 \rightarrow S_0$ vertical adiabatic de-excitation, the process that is modelled here (a $0 \rightarrow n$ vibronic de-excitation, where 0 and n are the vibronic states of the $S_1$ and $S_0$ surfaces respectively). The experimental spectrum shows a broad peak, and on either side of the highest intensity are contributions to the PL spectra that are not modelled here, such as non-vertical non-adiabatic de-excitations. The photoluminescence onset is therefore due to such de-excitation, and so the numerical agreement between the TDDFT calculations and the experimental PL onset appears to be coincidental. To model not only the most intense peak but also these other contributions, the TDDFT calculations would need to include vibronic coupling. This is technically feasible but increases the computational cost of the calculations to such an extent that it is only practical for small molecules.

As previously alluded to, it is possible that the approximations used (mainly the use of hybrid GGA *xc*-functionals) within this study are fundamentally unsuitable in describing the electronic structure near the $S_1$ minimum. Related to this, it is also possible that the $S_1$ minimum is described correctly but the barrier between that minimum and a local, higher minimum is not described correctly. The higher energy minimum could be the one from which the PL occurs experimentally, with the barrier preventing the real particle from reaching the lower $S_1$ minimum. If this barrier between two minima is not accurately described then the higher energy minima could end up being incorrectly described an on open-ended basin. Furthermore, it is possible that this barrier only arises once the particles are sufficiently large, meaning that these theoretical particles are then not representative of those studied experimentally. To test any of these hypotheses, more accurate (and therefore more expensive) calculations would be needed, or larger particles would need to be studied. The potential reasons for the failure of TDDFT in this case cannot therefore currently be tested.

Sampling limitations within TDDFT could also be the reason as to why the calculated PLE are not accurately described: it is possible (although unlikely if the rocksalt particles are as rigid as thought), that there are other $S_1$ minima that have not been found in this study. The limitation in not being able to sample higher excited states surfaces also means that it cannot be excluded that non-Kasha behaviour occurs, with the $S_n$ to $S_1$ decay failing to occur on a sufficiently fast timescale. This would blue-shift the PL peak directly. Another possibility would be that a $S_n$ to $S_1$ conversion via a conical intersection occurs, giving access to different $S_1$ minima further away from the ground state minimum. Although these last two points are possibilities, the experimental used excitation wavelength was tuned to 270 nm, which is close to the absorption onset, the $S_0$ to $S_1$ excitation, so populating a higher state than $S_1$ seems unlikely.

## 7.6   Conclusions

In this chapter, the photoluminescence energies of different MgO nanoparticles were presented and discussed. These energies were calculated using three different *xc*-functionals: B3LYP, BHLYP and CAM-B3LYP, each containing different amounts of HFE. The amount of HFE is crucial in determining an accurate description of the $S_1$ minimum, from which an electron is de-excited back to $S_0$.

It has been shown with example TD-B3LYP/def2-TZVP structures, that the ELC and optimised $S_1$ structure are directly linked. The main factor in the $S_1$ structure distortion compared to the $S_0$ optimised structure, is the number of electron centres, $n_e$: when $n_e$ is equal to one, one magnesium atom can be seen to be most distorted, increasing the bond length to the neighbouring oxygen atoms, and the rest of the particle rearranges to compensate for this distortion. As $n_e$ increases, the atoms on which the excited electron is localised, becomes less obvious in the structure, and the distortion can be seen to occur equally over the entire particle, which is a result of two factors: some atoms distort as they have more electron density and other atoms rearrange to compensate for the distortion of other atoms. This means that from the individual distortion of the atom, it cannot be said

whether that atom is distorted due to electron density gain or whether it has rearranged to accommodate another atom's distortion.

The larger particles ($n = 18, 24, 32$) all optimise to an excited state minimum which has a localised electron and hole, with the electron and hole both localising on corner sites lying on opposite ends of one edge of the particle. This is in contrast to the excited state localisation after vertical excitation at the $S_0$ minimum obtained from TD-BHLYP, where the electron and hole are in close proximity to each other. This shows that the optimisation on the $S_1$ surface corresponds to a process by which the electron and hole pair separate. In the case of the B3LYP *xc*-functional, localisation at the $S_1$ minima is found to be the same as for TD-BHLYP, although the calculations using the former are unreliable due to the strong CT-character of the excitation process. This link between poor LVEE (and possibly also PLE) predictions and poor orbital overlap has not been found for the BHLYP and CAM-B3LYP *xc*-functionals.[89,109]

Something that should be borne in mind, however, with these calculations is that they might not be representative of the experimental observations: calculated PLEs are in good agreement with the experimental PL onset by underestimating this onset by approximately 0.2 eV, although this agreement appears to be coincidental. The calculated PLEs are approximately 1 eV below the experimental peak positions. Several potential explanations have been presented to explain the disagreements between experimental and computational results.

In the unlikely situation whereby the TD-CAM-B3LYP/TD-BHLYP model of the PL from the $S_1$ surface is accurate, then it implies that Kasha's rule is not applicable to MgO nanoparticles, which makes it extremely challenging to predict the PL spectra of these particles, as emissions from many different excited surfaces down to $S_0$ would be occurring. This is computationally extremely time-consuming, if not currently intractable. Furthermore, the calculations presented here assume that no internal conversion from higher lying excited states down to $S_1$ is occurring, which may be an over-simplification of the process.

It appears that there are too many unknowns at hand to accurately model, and therefore in future predict the PL spectra of MgO particles that approach experimental size. However, computational chemistry is a field that has seen immense advances with the help of increasing computer power and more efficient implementation of (quantum) chemical codes. If this trend continues, excited state optimisations will become cheaper to perform, so that higher lying states can be studied in more detail, their predicted PLE can be calculated and a PL spectrum can be compiled. This advance would shed light on whether Kasha's rule truly is not applicable for these MgO nanoparticles.

# 8. Doped MgO particles

## 8.1 Introduction

As discussed in section 3.1.3, doping (nano)particles is an effective approach to modifying the chemical and physical properties of the particles. The effect of doping MgO nanoparticles is the subject of this preliminary study. The chosen dopants are the alkaline earth metals beryllium (Be), calcium (Ca), strontium (Sr) and barium (Ba), as well as the group 12 elements cadmium (Cd) and zinc (Zn). These dopants were chosen so as to retain a neutral particle, with all chosen dopants found as 2+ cations. Ca-, Ba- and Zn-doped MgO nanoparticles are also found experimentally. To reflect the low doping percentage found experimentally (usually below 10%, as discussed in section 3.1.3), only one Mg ion is substituted in any given system. Only $(MgO)_{24}$ and $(MgO)_{32}$ particles have been considered, as it has been shown in this thesis that these particles accurately reflect experiment at an affordable computational cost: these are also the two smallest structures with the experimentally observed rocksalt morphology. As the energetically lowest substitution occurs on corner sites, corner substitution has been studied in both the A-$Mg_{23}O_{24}$ as well as the A-$Mg_{31}O_{32}$ particles, where A denotes the dopant. Furthermore, in the case of the $(MgO)_{32}$ cluster, edge and face substitution has also been modelled.

This chapter aims to investigate whether the BHLYP *xc*-functional can reproduce experimental results of doped MgO nanoparticles, albeit with the caveat that the excitation energies might be over-estimated by as much as 0.5 eV. The CAM-B3LYP *xc*-functional has not been used here due to its computational expense, and the BHLYP *xc*-functional has been demonstrated in this thesis to be reliable in the simulation of the vertical excitation process of MgO and other inorganic nanoparticles. In essence, this chapter goes beyond chapters 5 and 7, and tests whether the approximations made in previous chapters are also suitable when considering the properties of doped particles.

The work presented here is based on preliminary results. Therefore some data sets are incomplete, and some properties considered in other chapters have not been investigated.

## 8.2   Methodology

DFT has been used to calculate the ground state structures of doped $(MgO)_{24}$ and $(MgO)_{32}$ particles with the BHLYP *xc*-functional, and TDDFT (using TD-BHLYP) employed to calculate vertical excitation energies of said structures. Furthermore, excited state relaxations on the $S_1$ surface have been performed, again using TDDFT, to obtain photoluminescence energies (PLE). The following dopants have been considered: Ba, Be, Ca, Cd, Sr and Zn. The triple-$\zeta$ basis set def2-TZVP was used for all atoms, incorporating effective core potentials for Sr and Ba.

The absorption spectra, obtained from a custom script, have all been modelled using a 0.1 eV standard deviation of the Gaussian function, in-line with studied shown in chapters 5 and 6. The character of the excitation has been analysed by evaluating the difference in the natural bond order (NBO) charges between the ground and excited states. The TURBOMOLE code has been used for all studies, and VMD for visualisation of the particles.

## 8.3   Ground state Structures

Ground state structures have been optimised by taking the optimised $(MgO)_{24}$ and $(MgO)_{32}$ particles as initial geometries. The $(MgO)_{24}$ lattice has been modified to incorporate the dopant by replacing a corner atom. In the case of the $(MgO)_{32}$ particle, one corner, one edge and one face atom have been substituted respectively, taking advantage of the cubic nature of the particle. Figure 8-1 shows the optimised corner-doped A-$Mg_{23}O_{24}$ particles overlaid on top of the pure $(MgO)_{24}$ particle. The corner, edge and face substituted A-$Mg_{31}O_{32}$ particles overlaid on the pure $(MgO)_{32}$ particle are shown in figures 8-2, 8-3 and 8-4, respectively.
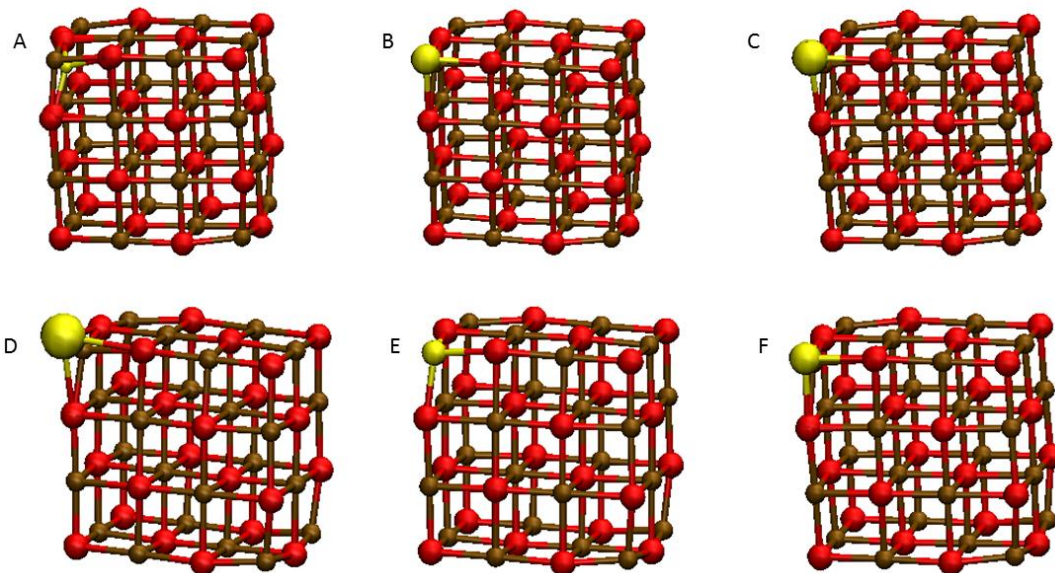
**Figure 8-1:** BHLYP/def2-TZVP optimised doped clusters A-$Mg_{23}O_{24}$ overlaid onto optimised $Mg_{24}O_{24}$, where A= Be (A), Ca (B), Sr (C), Ba (D), Zn (E) and Cd (F). Dopant is visualised as a yellow sphere, magnesium as a brown sphere and oxygen as a red sphere.

**Table 8-1:** Ionic radii, obtained from reference 261 and 262, for the ionic radius of 6-coordinated dications. All values are in Å.

| $Mg^{2+}$ | $Be^{2+}$ | $Ca^{2+}$ | $Sr^{2+}$ | $Ba^{2+}$ | $Zn^{2+}$ | $Cd^{2+}$ |
|---|---|---|---|---|---|---|
| 0.72 | 0.45 | 1.00 | 1.18 | 1.35 | 0.74 | 0.95 |

**Table 8-2:** BHLYP/def2-TZVP calculated A-O bond lengths for A-$Mg_{23}O_{24}$, where A = Mg, Be, Ca, Sr, Ba, Zn, Cd. Subscript denotes site: c for corner, e for edge, f for face and b for bulk. All values are in Å.

| | A = Mg | A = Be | A = Ca | A = Sr | A = Ba | A = Zn | A= Cd |
|---|---|---|---|---|---|---|---|
| $A_c–O_e$ | 1.906 | 1.577 | 2.166 | 2.304 | 2.428 | 1.922 | 2.130 |
| $A_c–O_e$ | 1.906 | 1.577 | 2.167 | 2.305 | 2.429 | 1.922 | 2.131 |
| $A_c–O_{e*}$ | 1.919 | 1.599 | 2.193 | 2.336 | 2.477 | 1.944 | 2.160 |

* denotes the shorter edge of the particle.

The ionic Radii, first collated by Shannon[261,262] as presented in table 8-1, are the ionic radii for a 6-coordinated, doubly positive cation, have been used to rationalise the trend seen in the ground state structures: in line with the tabulated ionic radii, Be substitution (figure 8-1-A) has a pronounced impact on bond lengths around the doped corner site: due to the significantly small size of the $Be^{2+}$ cation, it sits much closer to the neighbouring oxygen sites, inside of the rocksalt skeleton of $(MgO)_{24}$, also seen in table 8-2. Due to the size-mismatch, the neighbouring oxygen corner atoms are also displaced relative to their position in pure MgO. All other dopants have a larger ionic radius than magnesium, and therefore exhibit longer bonds with neighbouring oxygens, as seen in table 8-2. $Sr^{2+}$ and $Ba^{2+}$ and $Cd^{2+}$ doped particles also show some distortion on the neighbouring $O^{2-}$ sites as well, as seen in figure 8-1-A. The Zn-doped particle is most similar in structure to the pure MgO particle, as the $Zn^{2+}$ ion sits nearly in the same position as the $Mg^{2+}$ corner site, with only minor changes to bond lengths. The similar structures of pure $(MgO)_{24}$ and Zn-$Mg_{23}O_{24}$ arises from the fact that $Mg^{2+}$ and $Zn^{2+}$ ions have very similar ionic radii. The structural effects of the dopants are similar in corner-, edge- and face-doped A-$Mg_{31}O_{32}$, as can be seen from figures 8-2, 8-3 and 8-4, and tables 8-2, 8-3, 8-4 and 8-5.
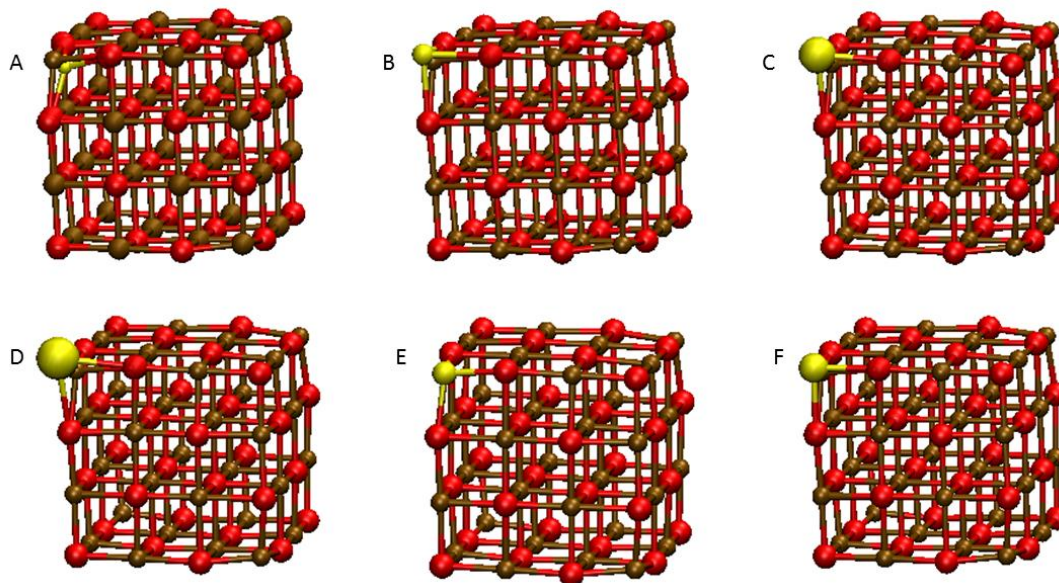
**Figure 8-2:** BHLYP/def2-TZVP optimised corner doped clusters A-$Mg_{31}O_{32}$ overlayed onto optimised $Mg_{32}O_{32}$, where A= Be (A), Ca (B), Sr (C), Ba (D), Zn (E) and Cd (F). Dopant is visualised as a yellow sphere, magnesium as a brown sphere and oxygen as a red sphere.
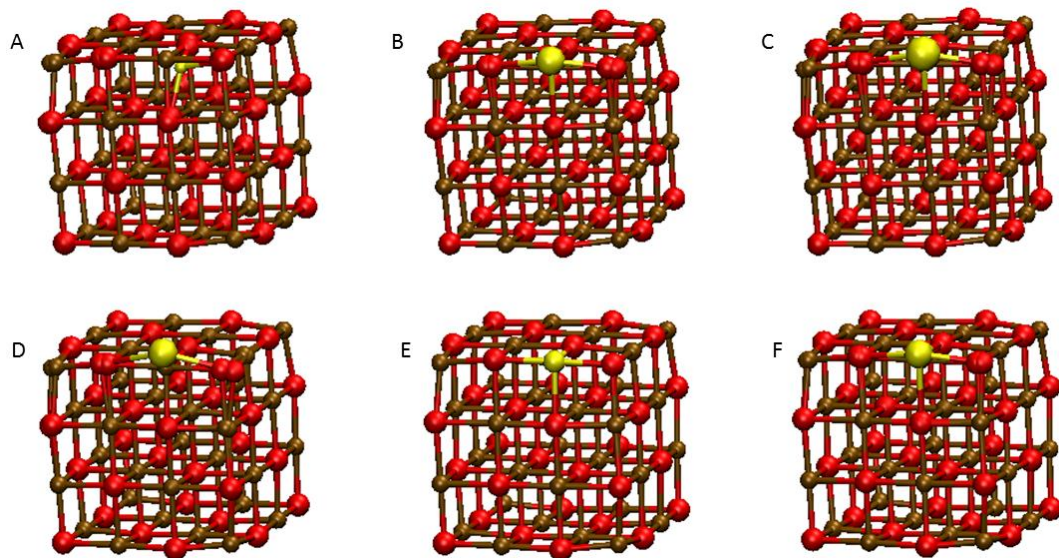


**Figure 8-3**: BHLYP/def2-TZVP optimised edge doped clusters A-$Mg_{31}O_{32}$ overlayed onto optimised $Mg_{32}O_{32}$, where A= Be (A), Ca (B), Sr (C), Ba (D), Zn (E) and Cd (F). Dopant is visualised as a yellow sphere, magnesium as a brown sphere and oxygen as a red sphere.
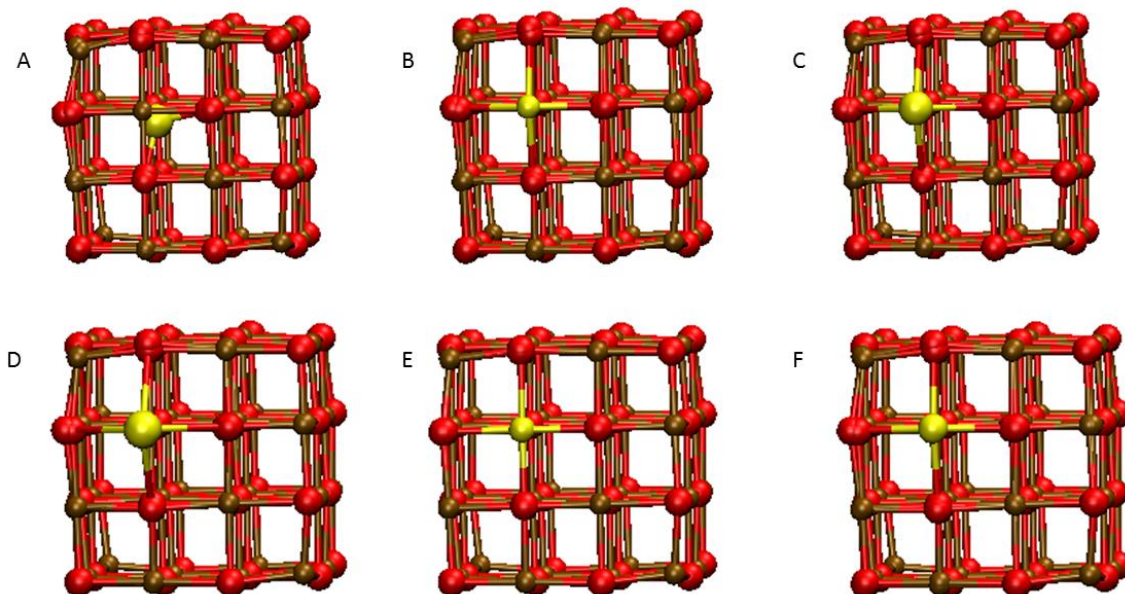
**Figure 8-4:** BHLYP/def2-TZVP optimised face doped clusters A-$Mg_{31}O_{32}$ overlayed onto optimised $Mg_{32}O_{32}$, where A= Be (A), Ca (B), Sr (C), Ba (D), Zn (E) and Cd (F). Dopant is visualised as a yellow sphere, magnesium as a brown sphere and oxygen as a red sphere.

**Table 8-3:** BHLYP/def2-TZVP A-O bond lengths for corner-doped A-$Mg_{31}O_{32}$, where A = Mg, Be, Ca, Sr, Ba, Zn, Cd. Subscript denotes site: c for corner, e for edge, f for face and b for bulk. All values are in Å.

|  | A = Mg | A = Be | A = Ca | A = Sr | A = Ba | A = Zn | A= Cd |
|---|---|---|---|---|---|---|---|
| $A_c–O_e$ | 1.915 | 1.591 | 2.179 | 2.318 | 2.449 | 1.934 | 2.145 |
| $A_c–O_e$ | 1.916 | 1.591 | 2.180 | 2.319 | 2.449 | 1.934 | 2.145 |
| $A_c–O_e$ | 1.916 | 1.591 | 2.180 | 2.318 | 2.449 | 1.934 | 2.146 |

**Table 8-4:** BHLYP/def2-TZVP A-O bond lengths for edge-doped A-$Mg_{31}O_{32}$, where A = Mg, Be, Ca, Sr, Ba, Zn, Cd. Subscript denotes site: c for corner, e for edge, f for face and b for bulk. All values are in Å.

|            | A = Mg | A = Be | A = Ca | A = Sr | A = Ba | A = Zn | A= Cd |
|------------|--------|--------|--------|--------|--------|--------|-------|
| $A_e$–$O_c$ | 1.948  | 1.538  | 2.195  | 2.324  | 2.403  | 1.938  | 2.109 |
| $A_e$–$O_e$ | 2.018  | 2.603  | 2.288  | 2.423  | 2.547  | 2.006  | 2.160 |
| $A_e$–$O_f$ | 2.014  | 1.631  | 2.288  | 2.455  | 2.656  | 2.085  | 2.317 |
| $A_e$–$O_f$ | 2.014  | 1.631  | 2.289  | 2.455  | 2.657  | 2.086  | 2.317 |

**Table 8-5:** BHLYP/def2-TZVP A-O bond lengths for face-doped A-$Mg_{31}O_{32}$, where A = Mg, Be, Ca, Sr, Ba, Zn, Cd. Subscript denotes site: c for corner, e for edge, f for face and b for bulk. All values are in Å.

|            | A = Mg | A = Be | A = Ca | A = Sr | A = Ba | A = Zn | A= Cd |
|------------|--------|--------|--------|--------|--------|--------|-------|
| $A_f$–$O_e$ | 2.069  | 2.626  | 2.271  | 2.429  | 2.586  | 2.102  | 2.239 |
| $A_f$–$O_e$ | 2.070  | 2.647  | 2.272  | 2.429  | 2.586  | 2.103  | 2.240 |
| $A_f$–$O_f$ | 1.995  | 1.592  | 2.193  | 2.344  | 2.488  | 2.023  | 2.169 |
| $A_f$–$O_f$ | 1.996  | 1.594  | 2.193  | 2.344  | 2.488  | 2.023  | 2.170 |
| $A_f$–$O_b$ | 2.069  | 1.615  | 2.598  | 3.189  | 3.555  | 2.137  | 2.526 |

It can be seen from figures 8-2 to 8-4 and tables 8-3 – 8-5 that as the coordination number of the dopant increases from three to four to five, more structural deformation of the Mg-O lattice is required to accommodate the larger dopant (apart from $Be^{2+}$). The zinc dopant is the obvious exception, with no apparent change to the structure and only minor changes to the bond lengths. Unsurprisingly, $Be^{2+}$ always moves into the lattice, rather than out of it as is the case with the other, larger, dopants, seen as e.g. in table 8-5, where the bond length between the beryllium atom and the oxygen bulk atom is smaller than the equivalent magnesium-oxygen bond length. All structures exhibit a trend that follows what would be expected from the ionic radii.

### 8.3.1  Substitution energy

Calculating the substitution energy of each dopant is interesting since it can reveal whether or not a substitution could occur naturally, i.e. whether there is an overall energy decrease. Of course, the substitution energies calculated below only offer insights into the thermodynamics of the process, i.e. no energy barriers for this process are investigated. This means that even if a substitution is favourable, it might not occur spontaneously.

Substitution energies have been calculated by taking the difference between two systems:

- The sum of the total energies of the doped clusters and the $Mg^{2+}$ ion
- The sum of the total energy of the pure MgO clusters and the dopant ion,

i.e. the difference between the starting materials and the products in equation (8-1), where $n = 24$ or 32.

$$(MgO)_n + A^{2+} \rightarrow AMg_{n-1}O_n + Mg^{2+} \tag{8-1}$$
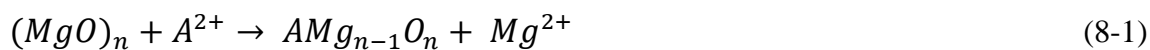
**Table 8-6:** Substitution energies of a $Mg^{2+}$ corner ion in $(MgO)_{24}$. All values are in eV.

|        | $Be^{2+}$ | $Ca^{2+}$ | $Sr^{2+}$ | $Ba^{2+}$ | $Zn^{2+}$ | $Cd^{2+}$ |
|--------|-----------|-----------|-----------|-----------|-----------|-----------|
| Corner | - 7.11    | 3.90      | 5.46      | 6.60      | - 1.59    | 1.25      |

**Table 8-7:** Substitution energies of a $Mg^{2+}$ corner, edge and face ion in $(MgO)_{32}$. Numbers in brackets show coordination numbers of the dopant. All values are in eV.

|            | $Be^{2+}$ | $Ca^{2+}$ | $Sr^{2+}$ | $Ba^{2+}$ | $Zn^{2+}$ | $Cd^{2+}$ |
|------------|-----------|-----------|-----------|-----------|-----------|-----------|
| Corner (3) | - 7.05    | 3.89      | 5.45      | 6.56      | - 1.61    | 1.21      |
| Edge (4)   | - 6.10    | 4.12      | 5.87      | 7.18      | - 1.48    | 1.31      |
| Face (5)   | - 5.77    | 4.93      | 6.99      | 8.50      | - 1.25    | 1.95      |

Tables 8-6 and 8-7 show that the substitution energy is almost independent of particle size, with all energy differences being within the uncertainty of DFT. Table 8-7 shows that as the coordination number of the dopant increases, the substitution becomes less favourable, as expected. These calculations are in agreement with the study by Sternig *et al.,*[19] which concludes that 3-coordinated sites are substituted before 4- and 5- coordinated sites. Doping MgO with $Ca^{2+}$, $Sr^{2+}$, $Ba^{2+}$ and $Cd^{2+}$ is found to be strongly endothermic, where $Cd^{2+}$ is the least endothermic substitution, presumably because $Cd^{2+}$ is most similar in size to $Mg^{2+}$. As $Zn^{2+}$ has an ionic radii that is extremely similar to that of $Mg^{2+}$, it is unsurprising that the substitution energies are small. This is in-line with the fact that Zn-doped MgO nanoparticles are studied experimentally, as discussed in section 3.1.3.3.

Despite the size-mismatch, doping MgO nanoparticles with beryllium is the most energetically favourable, which seems anomalous and is therefore discussed further in terms of cluster deformation energies.

### 8.3.1.1    Cluster deformation energies

It appears counter-intuitive that Be-doping is energetically favourable, let alone the most favourable substitution. The reasons for this are unclear, but looking at the cluster deformation energies (CDE) can give further insight into this system. The CDE is the difference in energies between:

- The total energy of the optimised doped particle, without the dopant atom, $E[Mg_{n-1}O_n{}^{2+}]_{A-Mg_{n-1}O_n}$

- The total energy of the optimised MgO particle, without the equivalent magnesium atom, $E[Mg_{n-1}O_n{}^{2+}]_{(MgO)_n}$

i.e. equation (8-2), where $n = 24$ or 32.

$$E[Mg_{n-1}O_n]_{A-Mg_{n-1}O_n} - E[Mg_{n-1}O_n]_{(MgO)_n} \qquad (8\text{-}2)$$

The CDE can shed light on whether the total energy of the particle is more or less favourable when the structure is optimised with a dopant.

**Table 8-8:** BHLYP/def2-TZVP calculated cluster deformation energies (CDE) of a $Mg^{2+}$ corner ion in $(MgO)_{24}$. All values are in eV.

|  | $Be^{2+}$ | $Ca^{2+}$ | $Sr^{2+}$ | $Ba^{2+}$ | $Zn^{2+}$ | $Cd^{2+}$ |
|---|---|---|---|---|---|---|
| Corner | 1.35 | - 0.79 | - 0.99 | - 1.08 | - 0.28 | - 0.74 |

**Table 8-9:** BHLYP/def2-TZVP calculated cluster deformation energies (CDE) of a $Mg^{2+}$ corner, edge and face ion in $(MgO)_{32}$. Numbers in brackets show coordination numbers of the dopant. All values are in eV.

|  | $Be^{2+}$ | $Ca^{2+}$ | $Sr^{2+}$ | $Ba^{2+}$ | $Zn^{2+}$ | $Cd^{2+}$ |
|---|---|---|---|---|---|---|
| Corner (3) | 1.67 | - 0.61 | - 0.83 | - 0.93 | - 0.07 | - 0.57 |
| Edge (4) | 0.54 | - 0.89 | - 1.18 | - 1.35 | - 0.13 | - 0.79 |
| Face (5) | 0.64 | - 0.65 | - 0.88 | - 0.98 | - 0.88 | - 0.81 |

Interestingly, the lattice energy is always more favourable at geometries when the lattice is optimised with a dopant, with results ranging from a 0.07 eV energy difference for the

lattice without the zinc corner dopant to a 0.93 eV difference for the lattice without the barium corner dopant, both calculated for $Mg_{31}O_{32}$ clusters. However, the presence of the beryllium dopant actually destabilises the lattice, by as much as 1.67 eV for corner doping. It seems anomalous that a destabilisation of the lattice would then lead to a stabilisation of the total energy by 7 eV when the dopant is reintroduced into the system by purely electrostatic effects from the dopant-oxygen interaction.

In contrast to the substitution energies, for the group 2 dopants, the structure of the particle is most stable when an edge magnesium atom in substituted. For the group 12 elements, face-doping results in the most stable structure.

The beryllium results appear anomalous and cannot be rationalised. To avoid potential confusions of any trends studied below, it has been decided to not study Be-doped MgO particles further.

## 8.4    Vertical excitations

As the ground state structures are now determined, attention turns to the excited state properties of these doped clusters. First, the lowest vertical excitation energies (LVEEs) of all particles are studied, before moving on to the comparison of calculated absorption spectra to available (and comparable) experimental absorption spectra for Ca-MgO, Ba-MgO and Zn-MgO nanoparticles.

### 8.4.1  Lowest vertical excitation energies

Calculating the LVEE is the first step to studying the excited state behaviour of the doped particles. The results are shown in tables 8-10 and 8-11 for the A-$Mg_{23}O_{24}$ and A-$Mg_{31}O_{32}$ particles, respectively.

**Table 8-10:** TD-BHLYP/def2-TZVP calculated lowest vertical excitation energy (LVEE) for corner doped A-$Mg_{23}O_{24}$. All values are in eV.

|  | A = Mg | A = Ca | A = Sr | A = Ba | A = Zn | A = Cd |
|---|---|---|---|---|---|---|
| LVEE | 4.96 | 4.89 | 4.84 | 4.91 | 4.85 | 3.77 |

**Table 8-11:** TD-BHLYP/def2-TZVP calculated lowest vertical excitation energy (LVEE) for corner, edge and face doped A-$Mg_{31}O_{32}$. All values are in eV.

|  | A = Mg | A = Ca | A = Sr | A = Ba | A = Zn | A = Cd |
|---|---|---|---|---|---|---|
| Corner (3) | 5.07 | 5.03 | 4.99 | 5.03 | 4.99 | 3.91 |
| Edge (4) | 5.07 | 4.87 | 4.68 | 4.74 | 4.91 | 4.24 |
| Face (5) | 5.07 | 4.93 | 4.75 | 4.78 | 4.88 | 4.37 |

Comparing the data for the corner-doped clusters from tables 8-10 and 8-11, it can be seen that for all dopants the same trend as for pure MgO nanoparticles occurs: as the particle size increase, so does the LVEE. This suggests that there is no quantum confinement, just as in pure MgO particles.

When comparing the LVEE of the differently doped A-$Mg_{31}O_{32}$ particles, as shown in table 8-11, no clear trend can be observed. For the alkaline earth dopants, as the coordination number of the dopant increases from three to four, the LVEE decreases, but increases as the coordination number of the dopant increases from four to five, although the increase is smaller in absolute terms than the decrease (following the same trend as their respective CDE). The LVEE of the group 12 dopants show opposing trends: for the zinc-doped particles, the LVEE decreases with increasing coordination number, whereas for the cadmium-doped particles, the LVEE increases with coordination number.

It should be noted that all excitations tabulated in tables 8-10 and 8-11 have non-zero oscillator strength. This means that they should all, in principle, be visible in the absorption spectrum, although possibly as low intensity excitations.

### 8.4.2  Absorption spectra

Before the character of the lowest excitation is discussed, the predicted absorption spectra of the doped $A$-$Mg_{31}O_{32}$ particles are compared to that calculated for pure $(MgO)_{32}$, as well as experimental spectra. The $A$-$Mg_{31}O_{32}$ particles are chosen over the $A$-$Mg_{23}O_{24}$ particles for this study, due to their slightly larger size and as they have more symmetry-equivalent dopant sites available. A slight disadvantage of using the larger particles, is that the $A$-$Mg_{31}O_{32}$ particles have a lower dopant concentration when compared to the $A$-$Mg_{23}O_{24}$ particles, and experimental concentration is of approximately 10% substitution[21,149,213] whereas the modelled particles have a dopant concentration of only 3%. The rigid 0.5 eV downward shift has been applied to all spectra, in-line with what has been presented for pure MgO particles in chapter 5 and other rocksalt-structured particles discussed in chapter 6. Due to the computational cost of these calculations, in particular with respect to memory requirements, only the lowest 50 excitations were modelled. This means the exact position of the higher energy peak therefore cannot be determined. This study focusses instead on the variation in absorption spectra obtained when considering different dopant positions. Furthermore, spectra have only been generated for particles where experimental data is available (i.e. $A$ = Ba, Ca, Zn).
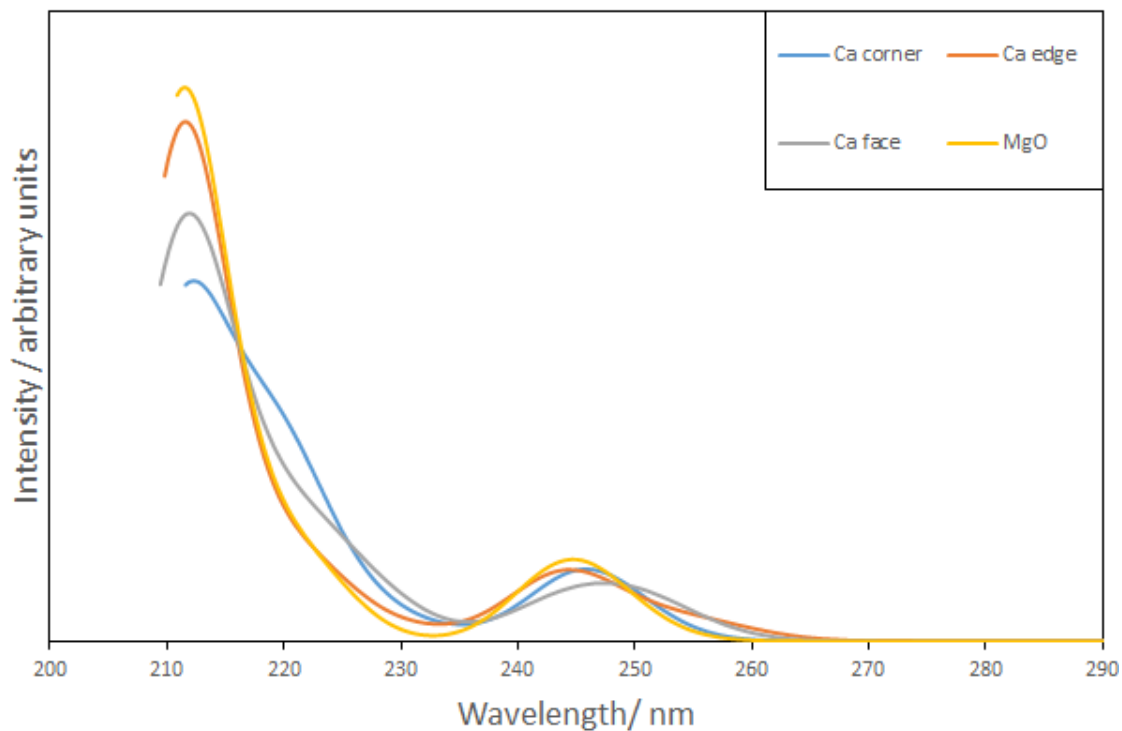
**Figure 8-5:** Calculated absorption spectra for corner-doped (blue line), edge-doped (orange line) and face-doped (grey line) $Ca-Mg_{31}O_{32}$, compared to $(MgO)_{32}$ (yellow line). A rigid red-shift of 0.5 eV and a Gaussian smearing of 0.1 eV has been applied to all spectra.

Figure 8-5 shows the absorption spectra of the differently Ca-doped particles, as well as the calculated absorption spectrum of $(MgO)_{32}$. All spectra shown look very similar to each other. Looking at the individual spectra in more detail gives insight as to which sites might have the most impact on observable properties. In the case of Ca-doping, the spectra show that edge doping has the smallest effect, with the absorption onset starting at the lowest energy (265 nm, 4.68 eV) and the peak position at approximately 245 nm (5.06 eV), when compared to the other spectra. The pure MgO absorption spectrum has a higher absorption onset (approximately 255 nm, 4.86 eV) compared to that of the edge-doped Ca-MgO particle, but the peak is positioned at the same energy of 245 nm (5.06 eV). In contrast, corner doping has the greatest effect, with a distinct shoulder appearing in the 230 – 220 nm (5.39 – 5.64 eV) energy range. A less intense shoulder appears in the same region when a face site is doped. Face-doped $Ca-Mg_{31}O_{32}$ also shows a lower absorption onset, at approximately 262 nm (4.73 eV) and a peak position at ~ 250 nm (4.96 eV).

Comparing these absorption spectra to experiment (section 3.1.3.1), it can be seen that not all experimental features are simulated. The Ca-doped MgO samples $Ca_{0.1}Mg_{0.9}O$, synthesised by Stankic *et al.,*[149] with an average size between 5 and 40 nm, exhibit a broad absorption peak around approximately 235 nm (~ 5.3 eV) and an absorption onset at 345 nm (3.59 eV). The calculated (and red-shifted) spectrum of $Ca-Mg_{31}O_{32}$ is somewhat in-line with experimental observations: the broad range of experimental particle sizes may result in a coalescence of the two predicted peaks seen in figure 8-5. However, the low absorption onset is not replicated with TDDFT. From tables 8-7, 8-8 and 8-9, it can be seen that the lowest vertical excitation energy, as predicted with TD-BHLYP, lies at 4.87 eV (4.37 eV with the 0.5 eV downward shift as explored in chapters 5 and 6), so above the experimental onset. The reason for this is unclear, although there are two possibilities. One is that the computational clusters are too small to accurately describe particles of up to 40 nm in size. Another possibility is that the dopant concentration is not high enough: Ca-doped MgO is studied experimentally at 10% and 20% substitution (compared to approximately 3% substitution in this computational study). The experimental samples with 20% substitution have a similar absorption onset as those with 10% substitution (figure 3-6), implying that the dopant concentration might not be reason for this disagreement. The experimental absorption onset of pure CaO samples is approximately 350 nm (~ 3.54 eV), giving the doped-MgO samples a lower absorption onset than pure MgO. In chapter 6, the absorption onset of pure CaO particles has been calculated to be 4.35 eV with the TD-BHLYP/def2-TZVP model chemistry, which is lower than the calculated absorption onset of the equivalent MgO particles, as well as that of the Ca-doped particles. From results discussed chapter 5, it is likely that the absorption onset needs to be lowered by 0.5 eV to represent experimental data more accurately, which would bring the absorption onset of pure CaO samples down to 3.85 eV. The gap between the calculated absorption onset and experimental absorption onset for the doped particles, and the fact that pure CaO has a lower absorption onset than MgO and Ca-doped MgO, lead to the following hypothesis: from a computational chemist's perspective, the question does arise as to whether all calcium (and other dopant) ions populate magnesium vacancies, or whether some of the dopant has phase-segregated on the MgO surface,

lowering the absorption onset by having pure CaO present on the surface of the nanoparticle.
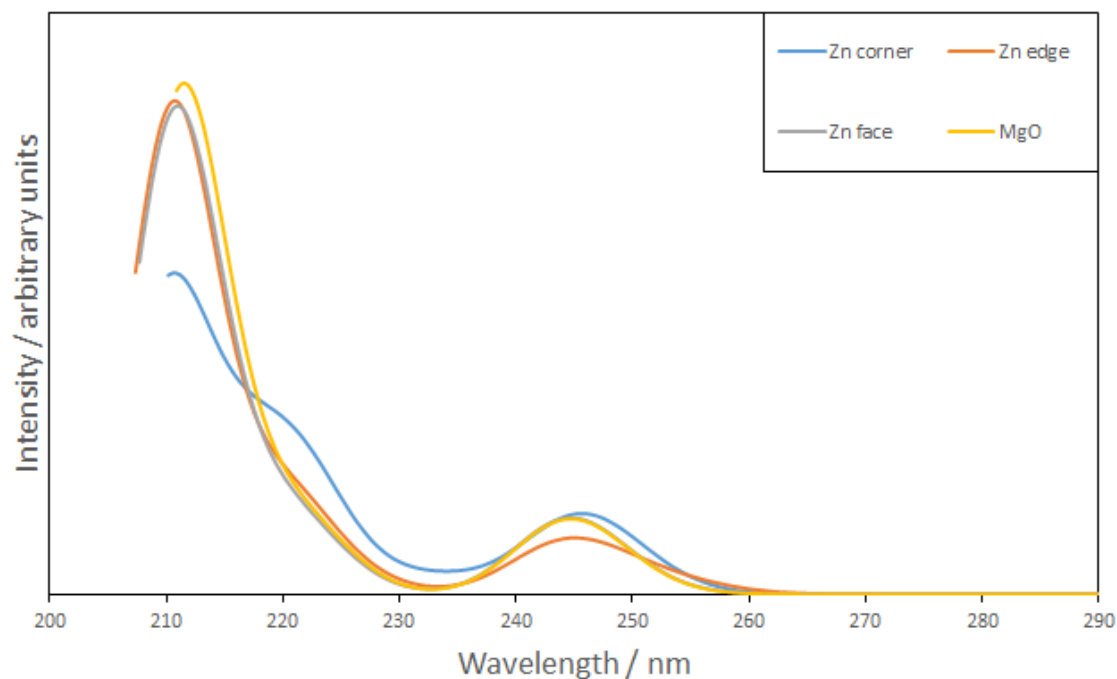


**Figure 8-6:** Calculated absorption spectra for corner-doped (blue line), edge-doped (orange line) and face-doped (grey line) $Zn\text{-}Mg_{31}O_{32}$, compared to $(MgO)_{32}$ (yellow line). A rigid red-shift of 0.5 eV and a Gaussian smearing of 0.1 eV has been applied to all spectra.

The absorption spectra for Zn-doped MgO can be seen in figure 8-6. The only real difference between that of the doped spectra and that of pure $(MgO)_{32}$ is that the corner doped particle gives rise to a shoulder for the high energy and high intensity peak at approximately 230 – 220 nm (5.39 – 5.64 eV), similar to for the predicted behaviour of the Ca corner-doped particle.

Zn-doped MgO clusters ($Zn_{0.1}Mg_{0.9}O$, particle size in the range 8 – 25 nm) exhibit a broad peak with shoulders at 335 nm (~ 3.7 eV) and 230 nm (~ 5.4 eV),[21,213] with the low energy peak again not replicated with these calculations. The experimental absorption onset for pure ZnO nanoparticles is ~ 390 nm (3.18 eV), lower than the absorption onset of pure MgO or Zn doped-MgO nanoparticles, meaning that the same logic as that discussed with

respect to Ca-doped clusters can be applied to the Zn-doped clusters: it is likely that the low absorption onset seen experimentally but not in the computed results, can be linked to the higher dopant concentration or to pure ZnO that has deposited onto the MgO surface, rather than zinc substituting for a magnesium ion.

A larger Gaussian smearing would replicate the one broad peak seen in the experimental spectra, but this would be at the expense of losing the information that the broad peak most likely stems from (at least) two different excitations.
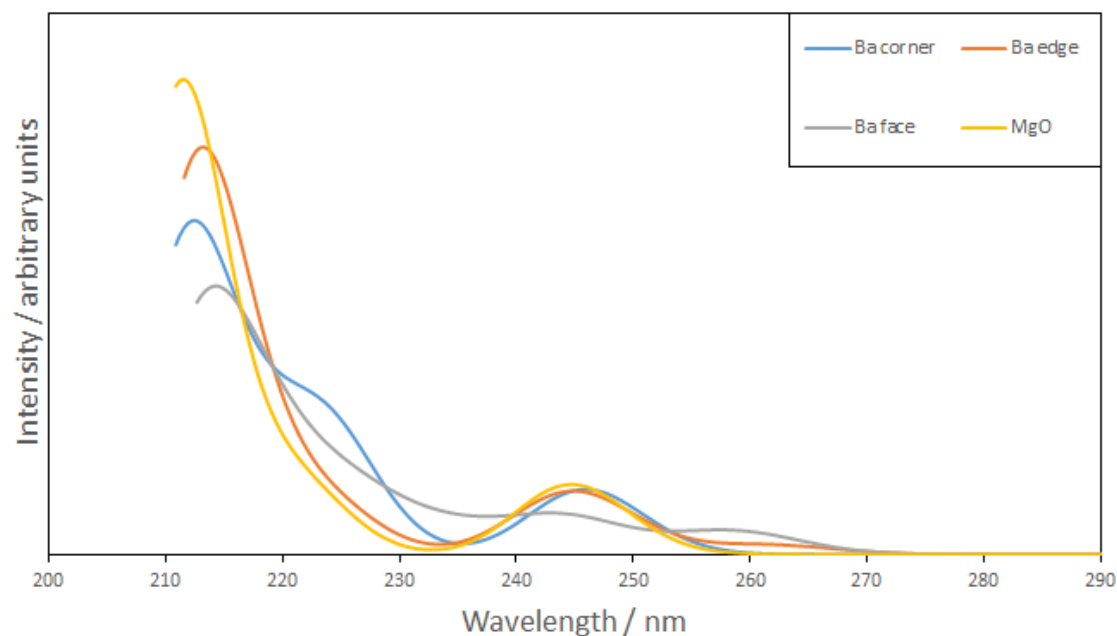


**Figure 8-7:** Calculated absorption spectra for corner-doped (blue line), edge-doped (orange line) and face-doped (grey line) Ba-$Mg_{31}O_{32}$, compared to $(MgO)_{32}$ (yellow line). A rigid red-shift of 0.5 eV and a Gaussian smearing of 0.1 eV has been applied to all spectra.

Figure 8-7 shows the different absorption spectra for the differently Ba-doped particles. Similarly to the Ca-doped and Zn-doped particles, the edge doping appears to have the least influence on the shape of the absorption spectrum. On the other hand, both face and corner doping induce significant differences in the overall appearance of the absorption spectra. Corner doping results in a distinct shoulder of the main peak in the 235 – 220 nm

(5.28 – 5.64 eV) region, as calculated for the Ca- and Zn-doped particles. In contrast to all other spectra, the Ba-face doped spectrum exhibits some intensity from 270 nm (4.59 eV) onwards, with peaks at ~ 260 nm (4.77 eV) and ~ 245 nm (5.06 eV).  Furthermore, this spectrum does not have the two well defined peaks found in all other spectra. This could be related to the fact that the barium ion is considerably larger than the magnesium ion, meaning that when a face site is substituted, a significant amount of structural rearrangement is necessary, affecting a larger part of the particle, and therefore affecting the absorption over a wider energy range.

Similarly to the observations of Ca-doped MgO particles, experimental Ba-doped MgO clusters ($Ba_{0.02}Mg_{0.98}O$, 7 nm average particle size) exhibit a broad absorption peak, with an absorption onset at approximately 350 nm (3.5 eV) and the peak at approximately 225 nm (5.5 eV).[211] Similarly to the Ca- and Zn-doped particles, the low energy absorption is not predicted in the calculated spectra. The calculated absorption onset for $Ba_{32}O_{32}$ is 3.86 eV, as seen in chapter 6, which is lower than that of the doped particles, suggesting that the hypothesis for Ca- and Zn- doped MgO nanoparticles might also be applicable to Ba-doped MgO particles.

### 8.4.3  Character of the lowest vertical excitations

As presented in chapters 5 and 6, NBO analysis can be used to study the localisation of the excited electron and hole by comparison of the atomic charges in the ground and excited state. The focus here is on the lowest vertical excitation of the $A\text{-}Mg_{31}O_{32}$ particles to aid identification of the difference the dopants and their coordination number make on the excitation characteristics.

It should be noted that only the lowest vertical excitation is analysed, but this is done for all dopants apart from Ba (and Be). The barium data has not been included as a numerical problem was found in the NBO analysis, which reported that more than one electron is involved in the excitation by having a surplus of negative charge, which accounted for

more than one electron. For this reason, it was decided that the Ba-doped particles should not be included in this analysis to avoid the risk of drawing false conclusions.

**Table 8-12:** Percentage localisation of the electron (on A and Mg sites) and hole (on O sites) of the lowest energy TD-BHLYP excitation for corner-doped A-Mg$_{31}$O$_{32}$ particles.

|            | A = Mg | A = Ca | A = Sr | A = Zn | A = Cd |
|------------|--------|--------|--------|--------|--------|
| A corner % | -      | 28.27  | 47.87  | 93.38  | 94.61  |
| Mg corner %| 17.68  | 8.98   | 5.06   | 0.71   | 0.87   |
| Mg edge %  | 72.24  | 56.16  | 40.59  | 3.03   | 2.80   |
| Mg face %  | 5.36   | 3.11   | 2.49   | 1.56   | 1.18   |
| Mg bulk %  | 4.72   | 4.47   | 4.00   | 1.32   | 0.55   |
| O corner % | 89.52  | 85.32  | 83.34  | 2.93   | 2.70   |
| O edge %   | 0.96   | 3.50   | 3.93   | 92.78  | 91.36  |
| O face %   | 3.10   | 5.34   | 7.60   | 3.43   | 5.31   |
| O bulk %   | 6.42   | 5.84   | 5.14   | 0.85   | 0.63   |

Table 8-12 shows the percentage exciton localisation per site-type in the corner-doped particles considered here. These can be separated into two different cases: the alkaline earth dopants and the group 12 dopants. The former exhibit an excitation pattern similar to that of pure MgO: an electron from a corner oxygen site is excited onto the neighbouring magnesium edge atoms. This excitation is thus a 'corner to neighbouring edge' excitation, with increased excited electron localisation on the calcium edge atom compared to the average magnesium edge atom and increased excited electron localisation on the strontium corner atom compared to the calcium corner atom. The group 12 dopants, on

the other hand, show a different pattern: an electron from an oxygen edge site is excited onto the corner dopant site, so this can be considered an 'edge to neighbouring corner' excitation. It should be noted that the alkaline earth dopants also attract significantly more excited electron density than the corresponding magnesium corner, with a dopant corner contribution of 28.27% for Ca and 47.87% for Sr. Although this is significantly smaller than the 93.38% for Zn and 94.61% for Cd, it is more than the 4.42% (17.68% divided by 4, to obtain the average magnesium corner contribution) contribution of the magnesium corner atoms in the pure MgO particle – showing that for the heavier group 2 dopants, the excited electron character becomes more like that seen for the group 12 dopants.

Figure 8-8 displays the electron density difference plot for the lowest excitation for the corner-doped particles. All corner-doped particles show a localised lowest vertical excitation, involving corner atoms and neighbouring edge atoms. Similarly to what is predicted from the NBO analysis, the electron density difference plots show that both Ca- and Sr-doped particles display a similar excitation character. As reported for pure MgO particles (discussed in section 5.7), individual magnesium edge and dopant corner contributions are not identified using density difference plots with a low isovalue. The Zn- and Cd-doped particles, however, show a different excitation character to that seen for pure MgO particles. This different excitation character has also been predicted by the NBO analysis, exhibiting an edge to corner excitation, with the excited electron almost completely localised on the dopant corner atoms. Both NBO and density difference plots show, similarly to what has been observed for pure MgO particles and other inorganic particles discussed in chapter 6, that the lowest vertical excitations cannot be described as either corner or edge excitations.
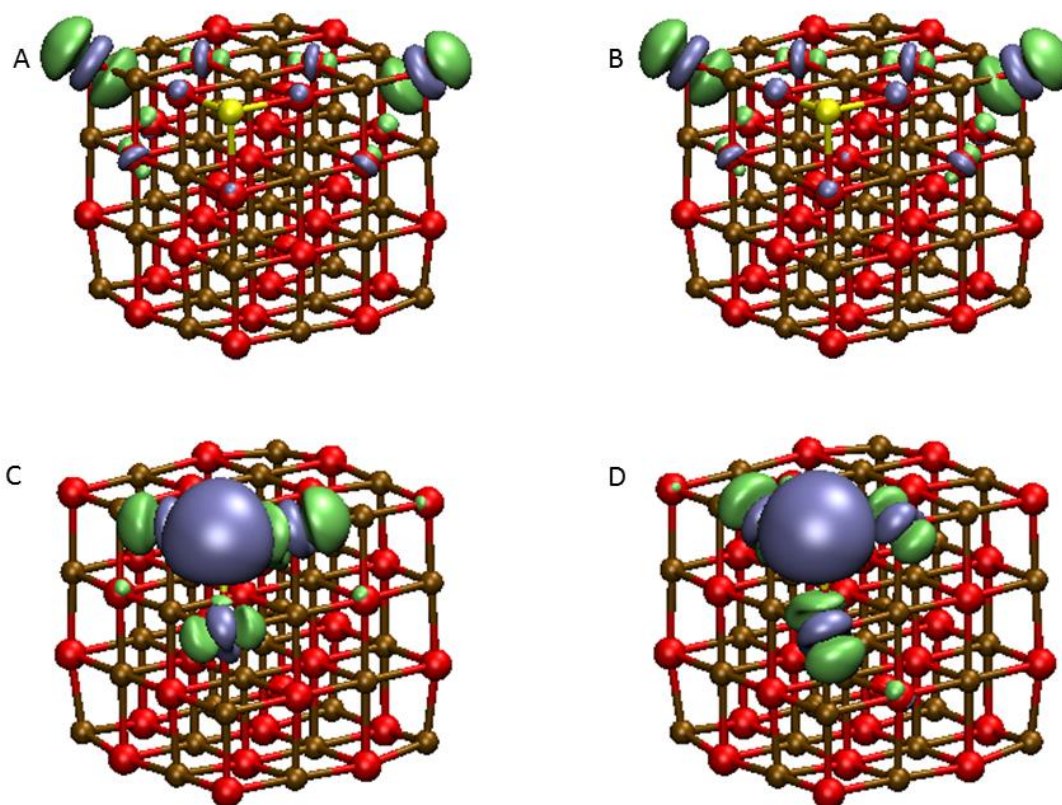
**Figure 8-8:** TD-BHLYP/def2-TZVP calculated ground and excited state electron density difference for the lowest vertical excitation for A calcium, B strontium, C zinc and D cadmium corner-doped A-$Mg_{21}O_{32}$ particles: blue isosurfaces show charge accumulation (excess of electron density in the excited state), and green show charge depletion (deficit of electron density in the excited state). An isosurface of 0.003 a.u. is used. Red spheres represent oxygen atoms, brown magnesium atoms and yellow the dopant. Equivalent figure of pure MgO can be seen in figure 5-13.

**Table 8-13:** Percentage localisation of the electron (on A and Mg sites) and hole (on O sites) of the lowest energy TD-BHLYP excitation for the differently edge-doped A-Mg$_{31}$O$_{32}$ particles.

|  | A = Mg | A = Ca | A = Sr | A = Zn | A = Cd |
|---|---|---|---|---|---|
| A edge % | - | 84.39 | 90.19 | 44.23 | 88.65 |
| Mg corner % | 17.68 | 3.49 | 1.01 | 16.08 | 2.74 |
| Mg edge % | 72.24 | 5.69 | 3.27 | 32.98 | 3.83 |
| Mg face % | 5.36 | 4.31 | 3.84 | 4.14 | 3.05 |
| Mg bulk % | 4.72 | 2.12 | 1.69 | 2.57 | 1.72 |
| O corner % | 89.52 | 89.83 | 90.53 | 76.79 | 80.56 |
| O edge % | 0.96 | 2.66 | 3.35 | 3.62 | 4.41 |
| O face % | 3.10 | 3.50 | 3.15 | 13.81 | 12.54 |
| O bulk % | 6.42 | 4.00 | 2.97 | 5.78 | 2.49 |

Similarly to what has been seen for the absorption spectra in figures 8-5, 8-6 and 8-7, edge doping appears to have only minor effects on the excitation, as can be seen in table 8-13. Pure MgO has a magnesium edge contributions of 72.24% (although only 6.02% per edge atom) and with Ca, Sr and Cd edge-doping the excited electron is localised to 84.39%, 90.19% and 88.65% on the dopant atom, respectively. This means that there is an increased electron density on one edge site, making the particle less symmetrical than in the case of the pure MgO particle. However the excitations can still be described as one of 'corner to neighbouring edge' type.

Zn-edge doping is slightly different, as only 44.23% of the excited electron is localised on the Zn dopant, with 2.75% on each magnesium edge atom (32.98% over all magnesium edge atoms). Due to the similar ionic radii of magnesium and zinc, the local environment of the oxygen corner atoms on which the hole is localised is more symmetric than in the

case of the other dopants. Therefore the excited electron delocalises on *both* zinc and magnesium edge atom.

This means that the lowest vertical excitation for each of the edge-doped particles arises from local excitations from a corner oxygen atom to the neighbouring doped edge site and, in the case of the Zn-dopant, also to the magnesium edge atoms adjacent to the oxygen corner atom on which the hole is localised.

Similarly to the NBO analysis, figure 8-9 shows that for edge-doped the $(MgO)_{32}$ particles, the charge depletion can be found mainly on the oxygen corner neighbouring the dopant site, i.e. the hole mainly localises on that oxygen corner site. The excited electron localises on the dopant site, especially in the case of the cadmium edge atom. The cadmium dopant behaves differently to the other dopants, presumably because it is a group 12 and not group 2 element, changing its electronic structure. The difference between the zinc and cadmium behaviour might be related to the different ionic radii, with that of zinc being very similar to magnesium but the difference between cadmium and magnesium being different, with cadmium having and ionic radius 32% larger than that of magnesium. As the edge site has a higher coordination number than the corner site, the difference in the localisation character between zinc and cadmium doping is more pronounced from the edge doping. Again, the density difference on the magnesium edge atoms is not identified by this analysis.
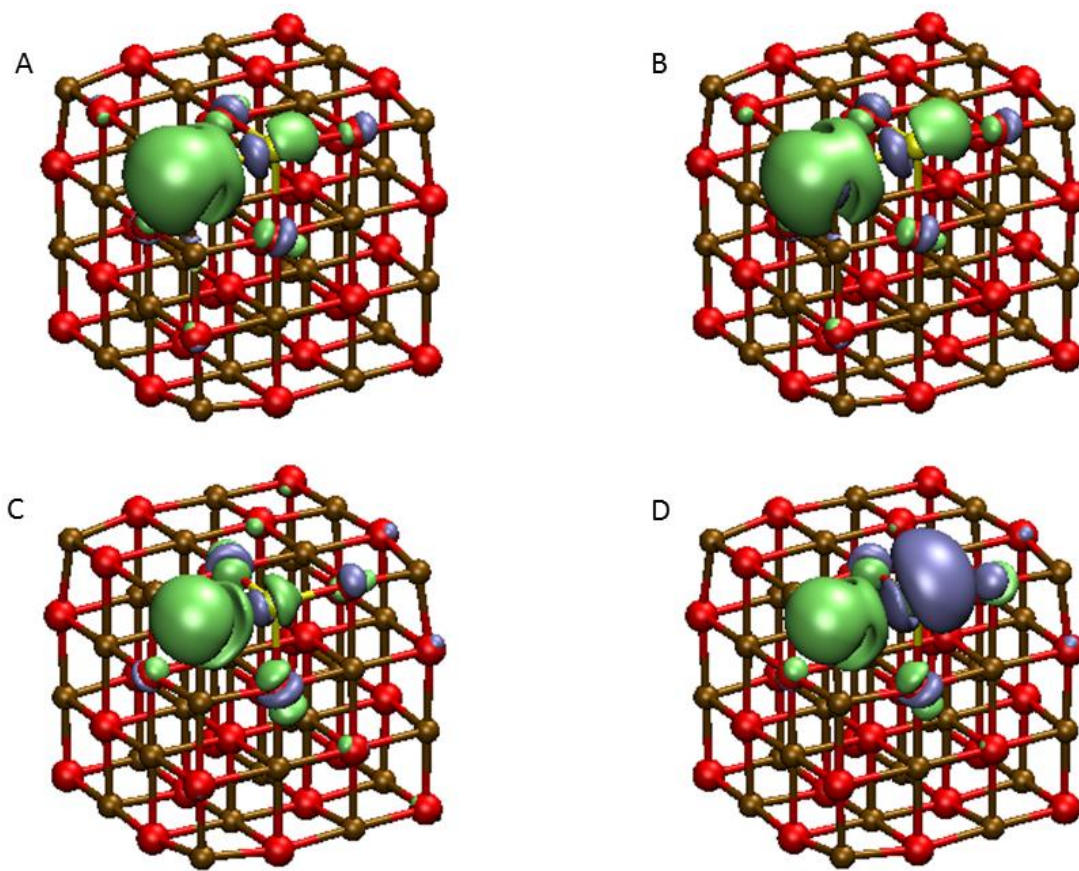
**Figure 8-9:** TD-BHLYP/def2-TZVP calculated ground and excited state electron density difference for the lowest vertical excitation for A calcium, B strontium, C zinc and D cadmium edge-doped A-$Mg_{21}O_{32}$ particles: blue isosurfaces show charge accumulation (excess of electron density in the excited state), and green show charge depletion (deficit of electron density in the excited state). An isosurface of 0.003 a.u. is used. Red spheres represent oxygen atoms, brown magnesium atoms and yellow the dopant. Equivalent figure of pure MgO can be seen in figure 5-13.

**Table 8-14:** Percentage localisation of the electron (on A and Mg sites) and hole (on O sites) of the lowest energy TD-BHLYP excitation for the differently face-doped A-Mg$_{31}$O$_{32}$ particles.

|            | A = Mg | A = Ca | A = Sr | A = Zn | A = Cd |
|------------|--------|--------|--------|--------|--------|
| A face %   | -      | 34.06  | 71.40  | 4.13   | 40.21  |
| Mg corner %| 17.68  | 8.84   | 1.90   | 81.34  | 49.18  |
| Mg edge %  | 72.24  | 50.70  | 19.88  | 9.81   | 6.55   |
| Mg face %  | 5.36   | 2.01   | 3.24   | 1.80   | 1.37   |
| Mg bulk %  | 4.72   | 4.40   | 3.58   | 2.92   | 2.68   |
| O corner % | 89.52  | 84.82  | 80.98  | 14.52  | 8.78   |
| O edge %   | 0.96   | 3.96   | 5.10   | 63.02  | 61.97  |
| O face %   | 3.10   | 4.76   | 9.34   | 18.82  | 25.25  |
| O bulk %   | 6.42   | 6.46   | 4.59   | 3.64   | 4.00   |

Table 8-14 shows the NBO-derived localisation data for the face-doped particles. It can be seen that the alkaline earth dopants have a similar effect: an electron is excited from an oxygen corner atom to neighbouring magnesium edge atoms (50.70% for Ca-doping, 19.88% for Sr-doping) and the dopant face atom (34.06% for Ca-doping, 71.40% for Sr-doping). The excited electron density on the magnesium edge and the dopant face atoms amounts to 84.76% for the Ca-doped particle and to 91.28% for the Sr-doped particle. The fact that the excited electron localises more on the strontium face atom (compared to calcium or magnesium edge atoms) is most likely due to the size mismatch of strontium and magnesium.

The group 12 dopants show a slightly different exciton localisation, namely one that involves the excitation predominantly from an oxygen edge atom (63.02% for Zn-doped and 61.97% for Cd-doped particles) with some contribution from oxygen face atoms

(18.81% for Zn-doped, 25.25% for the Cd-doped particles) to the dopant face site (40.21% for Cd-doped) and magnesium corner atoms (81.34% for Zn-doped and 49.18% for the Cd-doped particles). The difference in the localisation of the excited electron on the zinc and cadmium face atoms respectively can again be rationalised due to the size mismatch with respect to the ionic radius of magnesium. Compared to the corner doped particles, the difference in ionic radii is more relevant for face-doped particles, as the coordination number of the dopant is increased.

As has been seen with the corner-doped particles, the lowest vertical excitation of each face-doped particle is a local excitation, and can be characterised as either a 'corner to edge and face' excitation or an 'edge and face to corner and face' excitation. In both cases, all atoms involved in the excitation are on the same face of the particle.

Figure 8-10 displays the electron density differences arising from the vertical excitation for the face-doped particles. As with the previous density difference plots, the individual magnesium contributions are not identified. However, the similarity between the Ca- and Sr-doped particles is, as with the other doping sites, very clear: the hole delocalises over the oxygen corner on the same site as the dopants, as well as on some face oxygen atoms. The Zn- and Cd- doped particles show a different character to those with alkaline earth dopants in that the main sites on which the hole delocalises are the oxygen edge sites neighbouring the dopant sites, with some contribution also provided by oxygen corner sites. The magnesium corner atom nearest to the dopant site displays an accumulation of the excited electron density, which decreases as the dopant changes from Zn to Cd. At the same time the dopant contribution increases. This trend can also be seen in the NBO data.
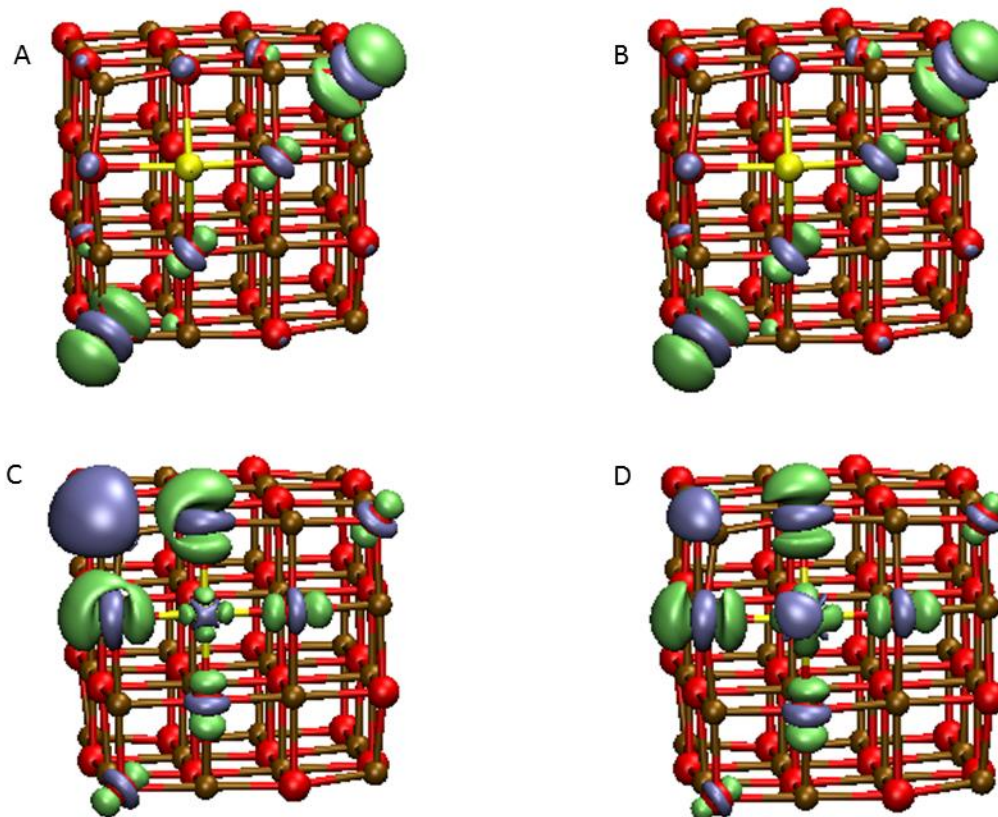
**Figure 8-10:** TD-BHLYP/def2-TZVP calculated ground and excited state electron density difference for the lowest vertical excitation for A calcium, B strontium, C zinc and D cadmium face-doped A-$Mg_{21}O_{32}$ particles: blue isosurfaces show charge accumulation (excess of electron density in the excited state), and green show charge depletion (deficit of electron density in the excited state). An isosurface of 0.003 a.u. is used. Red spheres represent oxygen atoms, brown magnesium atoms and yellow the dopant. Equivalent figure of pure MgO can be seen in figure 5-13.

The electron density difference plots (figures 8-8, 8-9 and 8-10) are in agreement with the NBO data (tables 8-12, 8-13 and 8-14), apart from the fact that the localisation of the excited electron on individual magnesium atoms is not always clear with the isosurface value chosen. However, similarly to the NBO data, both the Ca- and Sr-doped particles display a similar excitation character in the electron density difference plots. These plots demonstrate that the character of the lowest vertical excitations are centred around the dopant atom, with the excitations localised on that side of the particle.

Comparing the trends in the LVEE (table 8-11) as the coordination number of the dopant is increased with the analysis of excited electron and hole localisation analysis, it can be seen that for all dopants, apart from Zn, the more the excited electron is localised on the dopant, the lower the excitation energy. This might be related to the fact that the atoms are moved out of the lattice and are therefore able to move, and hence can lower their energy, giving rise to lower excitation energies.

For the zinc dopant, the opposite is true: the more the excited electron is localised on the zinc atom, the higher the excitation energy.

## 8.5   Photoluminescence energies

The photoluminescence energies (PLE) has also been studied for these doped particles, although the PLE results obtained for pure MgO do not agree with experimental results, as shown in chapter 7. Unfortunately, this data set is incomplete due to the extreme computational expense of these calculations. Some experimental PL data is available for doped particles, as discussed in chapter 3.

**Table 8-15:** TD-BLHYP/def2-TZVP calculated photoluminescence energies for the differently doped $A\text{-}Mg_{31}O_{32}$ particles. All values are in eV.

|        | A = Ca | A = Sr | A = Ba | A = Zn | A = Cd |
|--------|--------|--------|--------|--------|--------|
| Corner | 2.67   | 2.64   | N/A    | N/A    | N/A    |
| Edge   | 2.15   | 3.09   | 2.01   | 1.84   | 2.31   |
| Face   | N/A    | 1.93   | 1.89   | 3.27   | 2.87   |

Available data is presented in table 8-15 and shows that the dopant site has significant effects on the PLE, especially in the case for $Zn$-$Mg_{31}O_{32}$, where the PLE increases by 1.43 eV as the coordination number of the dopant is increased from four to five. This is a surprising result, as for the other doped particles, a variation of approximately only 0.5 eV can be seen when the dopant site is altered (and even less for the Ba-doped particles). The significant difference in PLE for the Zn-doped particles can be explained in the structural difference of the respective $S_1$ minima (tables 8-16 and 8-17): the optimised geometry of the edge-doped particle has a longer bond between the zinc edge atom and the oxygen corner atom of 3.098 Å (compared to 1.938 Å for the $S_0$ minimum), with a difference of more than 1 Å. The face-doped $Zn$-$Mg_{31}O_{32}$ particle, on the other hand, only displays minor changes in bond lengths (in the order of magnitude of ~ 0.1 Å). The LVEE for the edge-doped $Zn$-$Mg_{31}O_{32}$ is 4.91 eV and 4.88 eV for the face-doped one and because the face doped particle does not structurally change significantly upon relaxation on the $S_1$ surface, the PLE is close to the LVEE value (with a Stokes shift of 1.61 eV). In contrast, the edge-doped particle has a Stokes shift of 3.07 eV, reflecting the significant structural change occurring in the particle. It should be noted that no frequency analysis has been performed on these systems due to the high computational cost, which means that it is possible that some of the particles are not true minima.

**Table 8-16:** BHLYP/def2-TZVP Zn-O bond lengths for edge-doped $Zn$-$Mg_{31}O_{32}$, for the optimised ground state structure ($S_0$) and the optimised excited state structure ($S_1$). Subscript denotes site: c for corner, e for edge, f for face and b for bulk. All values are in Å.

|  | $S_0$ | $S_1$ |
|---|---|---|
| $A_e$–$O_c$ | 1.938 | 3.098 |
| $A_e$–$O_e$ | 2.006 | 1.981 |
| $A_e$–$O_f$ | 2.085 | 2.121 |
| $A_e$–$O_f$ | 2.086 | 2.122 |

**Table 8-17:** BHLYP/def2-TZVP Zn-O bond lengths for face-doped An-$Mg_{31}O_{32}$ for the optimised ground state structure ($S_0$) and the optimised excited state structure ($S_1$). Subscript denotes site: c for corner, e for edge, f for face and b for bulk. All values are in Å.

|          | $S_0$ | $S_1$ |
|----------|-------|-------|
| $A_f$–$O_e$ | 2.102 | 2.001 |
| $A_f$–$O_e$ | 2.103 | 2.004 |
| $A_f$–$O_f$ | 2.023 | 1.995 |
| $A_f$–$O_f$ | 2.023 | 1.995 |
| $A_f$–$O_b$ | 2.137 | 2.139 |

The experimental PLE are approximately 2.92 eV for Ca-doped MgO particles,[148,149,208] 2.30 eV for Ba-doped MgO particles[211] and 3.20 eV for Zn-doped particles.[21,213] Surprisingly, and in contrast to what has been seen for pure MgO particles, the calculated PLE are much closer to experimental data than expected from the results obtained from MgO, for at least one dopant site. However, as discussed in chapter 3, the photoluminescence spectra are dependent on particle size as well as the dopant concentration, making comparison with computational data extremely difficult. Furthermore, TD-BHLYP overestimates the LVEE, but underestimates the PLE (apart from in the case of face-doped Zn particles where it overestimates by 0.07 eV). This raises the question whether the agreement of the PLE is serendipity in this case, or whether the doping helps the excited electron and hole stay closer to each other (and not localise on one corner atom each, with a distance of 0.6 nm in between them), resulting in a better description of the relaxation process and therefore the $S_1$ minimum. TDDFT is known for not describing excitations that have non-local character well, and the dopant atoms might change the electronic structure such that the relaxation process on the $S_1$ potential energy surface is more local, and therefore more accurate using TDDFT. Only further work on the effect of doping on the PLE can answer this question.

**Table 8-18:** TD-BLHYP/def2-TZVP photoluminescence energies for the corner doped A-$Mg_{23}O_{24}$ particles. All values are in eV.

|         | A = Ca | A = Sr | A = Ba | A = Zn | A = Cd |
|---------|--------|--------|--------|--------|--------|
| Corner  | 2.59   | 2.55   | 2.89   | 2.66   | 1.51   |

Size-dependence and dopant concentration can be studied further by considering the PLE data for corner-doped A-$Mg_{23}O_{24}$, presented in table 8-18. The PLE difference between $(MgO)_{24}$ and $(MgO)_{32}$ is approximately 0.08 eV (seen in section 7.3.1) and the PLE data for the corner-doped particles (using Ca- and Sr-doped particles as the reference) is in-line with what has been observed for the pure MgO particles. Due to the fact that as the particle size changes but the number of dopant atoms remains the same, the effects of particle size and dopant concentration cannot be separated. However, as the PLE for the calcium and strontium corner-doped A-$Mg_{23}O_{24}$ is approximately 0.1 eV lower than the PLE for the calcium and strontium corner-doped A-$Mg_{31}O_{32}$ respectively, some educated guesses regarding the PLE trends in the A-$Mg_{31}O_{32}$ particles can be made.

**Table 8-19:** TD-BLHYP/def2-TZVP calculated photoluminescence energies for the differently doped A-$Mg_{31}O_{32}$ particles. Italicised and grey values are PLE extrapolated from the corner-doped A-$Mg_{23}O_{24}$ PLE. All values are in eV.

|        | A = Ca | A = Sr | A = Ba | A = Zn | A = Cd |
|--------|--------|--------|--------|--------|--------|
| Corner | 2.67   | 2.64   | *2.99* | *2.76* | *1.61* |
| Edge   | 2.15   | 3.09   | 2.01   | 1.84   | 2.31   |
| Face   | N/A    | 1.94   | 1.89   | 3.27   | 2.87   |

Table 8-19 shows the calculated PLE of the differently doped A-$Mg_{31}O_{32}$ particles, as well as extrapolated PLE values (for corner-doped Ba-MgO, Zn-MgO and Cd-MgO) by adding 0.1 eV to the PLE value obtained from A-$Mg_{23}O_{24}$.

Assuming that the extrapolated values are accurate, then it can be said that the PLE of the Cd-doped particles follow the same trend as the LVEE; as the coordination number of the dopant increases, so does the PLE. The PLE for both the Ca- and Ba-doped particles follow the same trend as the LVEE for the data available (a decrease in energy as the dopant coordination changes from three to four). The LVEE and PLE of Sr-doped particles do not follow the same trend, however, with the LVEE decreasing and the PLE increasing as the coordination number of the dopant increases from three to four and the PLE decreasing as the LVEE increases as the coordination number of the dopant increases from four to five. Similarly, the Zn-doped particle does not exhibit the same trend when comparing LVEE and PLE, suggesting that when the PLE does not follow the same trend as the LVEE, more substantial structural rearrangement occurs on the $S_1$ surface. Similarly to the PLE obtained for pure MgO in chapter 7, it is possible that the methodology cannot predict the PLE accurately, so it would be dangerous to over-interpret potential trends in the PLE.

## 8.6   Conclusions

It has been shown that the (TD-)BHLYP/def2-TZVP model chemistry can be used to model the absorption spectra of doped MgO particles in the region of $300 - 200$ nm ($4.13 - 6.12$ eV), especially when a rigid downward shift of 0.5 eV is applied, although the low energy absorption onset of the experimental spectra cannot be replicated. This could be due a number of reasons: the larger average sample size, larger dopant concentration, or phase separation of the dopant oxide on the MgO surface, rather than a magnesium substitution. This could be tested in the future by further calculations, e.g. by adding dopant- oxides to the surface of the magnesium particles.

The character of the excitation for the lowest vertical excitation has been studied and it can be concluded that doping alters the absorption behaviour of these particles compared to pure MgO, with edge-doping having the pronounced effect. It was also be seen that the side of the particle on which the dopant is located is also the one on which the exciton is localised. The amount the excited electron localised on the dopant can be linked directly to the LVEE value: in the case of calcium, strontium and cadmium doping, the amount the excited electron is localised on the dopant is inversely proportional to the LVEE value. In contrast, the relationship between the localisation amount of the excited electron and the LVEE value is proportional for zinc dopants.

The PLE are difficult to rationalise, and computed values are difficult to compare to experiment, as the photoluminescence spectra are strongly dependent on particle size and/or dopant concentration. However, the computed values are within 0.3 eV of those found experimentally for at least one doped site. Due to the potential unreliability of the predicted PLE values, as discussed in chapter 7, no conclusions can be drawn as to which dopant site might be prevalent experimentally. Another difficulty arises in comparing experimental and computed photoluminescence energies: in experiment, presumably a mixture of corner- edge- and face-doping can be seen, whereas the modelled particles only have one doped site.

 It would be interesting to study the photoluminescence of these doped particles further, by completing the data sets presented here, as well as having more than one dopant atom per particle. This, however, is a very large task, with varying the relative location between the dopant sites in one particle. Furthermore, changing only the particle size or dopant concentration would give some insight into the effects of particle size and dopant concentration, and would potentially help differentiate between these two phenomena. However, it is difficult to change one variable without the other in small particles. The effect of either variable on the photoluminescence (and absorption) energies would be very interesting indeed, and would aid in the comparison of calculated results to experiment.

# 9. Conclusions and perspectives

The applications of (Time-Dependent) Density Functional Theory ((TD)DFT) in chemical research have ballooned over the past decades. Ground state DFT in particular is gaining ever-increasing popularity, being applied to a greater range of systems and used to study an increasing variety of properties. However, it is critically important to benchmark results rigorously when applying computational methodologies to new areas of study or materials, ideally against experimental data. Only through such rigorous testing can advances be made: if approximations are badly applied, simulation cannot advance the knowledge of the field, and could potentially even have a detrimental effect. The B3LYP hybrid GGA exchange-correlation (*xc*)-functional is an example of a functional approximation which is broadly applied in both chemistry and chemical physics often without rigorous benchmarking – its popularity can potentially mask poor data from which invalid conclusions can be derived. Similarly, the (TD)DFT methodology is often seen as a 'black box' method but this is not the case: the researcher has to consider the approximations and their limitations before useful data can be produced and advances in the field made.

This thesis presents a novel approach to describing the excited state properties of MgO and other inorganic nanoparticles exhibiting the rocksalt structure. On the one hand, the lowest vertical excitation energies (which often correspond to the lowest optically allowed excitations) obtained from TDDFT have been benchmarked against the lowest vertical excitation energies obtained from high-level Coupled Cluster (CC) calculations for the smaller particles, and on the other hand, the TDDFT results for the larger particles have been compared to experiment. Two different approximations within (TD)DFT have been employed further to study the excitation behaviour of other inorganic nanoparticles exhibiting the rocksalt structure, in order to test whether the approximations found in this work to be suitable for MgO can also be applied to related materials with the same structure. Further to these excitation studies, the de-excitation characteristics of MgO nanoparticles have also been explored using TDDFT in terms of their photoluminescence

energies (PLEs) and the excited state minima have been studied in terms of their exciton localisation character (ELC), as well as their structural differences. Some preliminary work on doped MgO nanoparticles has also been presented, to test the suitability of TDDFT to describe their optical properties.

It has been shown that to accurately describe the lowest vertical excitation energy for MgO nanoparticles, an *xc*-functional containing a high degree of Hartree-Fock exchange (HFE), such as BHLYP, or a range-separated (long-range corrected) *xc*-functional, such as CAM-B3LYP, are needed. It has been established here that other *xc*-functionals with a low degree of HFE, such as B3LYP, severely underestimate the lowest vertical excitation energies, due to the fact that such functionals spuriously stabilise excitations with charge transfer (CT) character. This fact is the origin of why there is disagreement between results obtained with different *xc*-functionals with regard to the lowest vertical excitation energies values, with this disagreement becoming more pronounced as the particle size increases. The CT character of the excitation is characterised by poor overlap between the orbitals involved in the excitation: in the case of $(MgO)_{32}$, the excited electron is transferred from a corner oxygen atom to a corner magnesium atom upon excitation, a distance of approximately 0.6 nm. This corner to corner excitation is stabilised in energy when TD-B3LYP is employed, making it the lowest (optically allowed) transition and giving a resulting absorption spectrum that is not representative of that observed experimentally. The TD-BHLYP-calculated excitation results show that the lowest vertical excitation has a local character, with the excited electron being transferred from an oxygen corner atom to its neighbouring magnesium edge atoms upon excitation: the corner to corner excitation lies significantly higher in energy.

This link between poor orbital overlap and the spurious stabilisation of the energy of the (lowest) excited state is found not only for MgO nanoparticles, but also in other related inorganic nanoparticles exhibiting the rocksalt structure, such as CaO, SrO, BaO, MgS and MgSe. The degree to which the spurious stabilisation of the excited state energy manifests itself in these particles when using TD-B3LYP clearly correlates with the degree of delocalisation of the excited electron: as this becomes more delocalised over the entire particle, the orbital overlap increases and consequently the description of the excitation is

more accurate. Although the excitations of all of these particles are found to be badly described using TD-B3LYP, the idea that the CT character of an excitation is not binary, but more graded, arises. In contrast to the alkaline earth chalcogenides discussed above are the CdO and PbS nanoparticles with the rocksalt structure, which appear to have lowest vertical excitation energies which are similarly described using TD-B3LYP and TD-BHLYP. These two materials have excited electrons that are delocalised over the entire particle. A relationship between the excited electron delocalisation and the dielectric constant of the bulk material has been established as a potential predictive tool as to whether the use of TD-B3LYP would be suitable: particles possessing a high dielectric constant have a more delocalised excited state and therefore, the excited state description of such particles as obtained with TD-B3LYP could be expected to be reliable.

Furthermore, the suitability of TDDFT to describe the photoluminescence properties of MgO has been investigated. Similarly to the previous findings, TD-B3LYP is demonstrated to underestimate photoluminescence energies, and this underestimation becomes more pronounced as particle size increases. This is presumably linked to the original underestimation of the excitation energy: the excited state electronic structure serves as a starting point for the excited state optimisation. However, it has been shown that the description of the optimised first excited state, as obtained from TD-B3LYP and TD-BHLYP simulations, is similar in terms of the exciton localisation character, possibly explaining why TD-BHLYP (and TD-CAM-B3LYP) also underestimate the photoluminescence energies of MgO nanoparticles. The reason why TDDFT fails to predict the photoluminescence energies of MgO is unclear, but it is possible that the methodology, especially the functional approximations, are not suitable to describing the $S_1$ optimisation and the intrinsically linked photoluminescence energies.

Finally, the preliminary results obtained for the doped particles display an issue with the absorption energies: the TD-BHLYP calculated absorption onset is higher than that observed experimentally. This can be further investigated by increasing the dopant concentration in the simulated particles and/or including dopant oxide islands on top of the MgO surface. The strong dependence on the dopant site in the particle, especially for the photoluminescence energies, makes it challenging to predict how doping could be used

to tune optical properties. However, this preliminary study shows the need for further investigation of doping in these particles.

It can be concluded from the research presented in this thesis that TDDFT simulations, when suitably analysed, can be used to accurately characterise the excitation behaviour of inorganic particles, although the choice of *xc*-functional is critical, with the CAM-B3LYP *xc*-functional providing the most accurate data. In contrast, the TD-B3LYP approximation is only suitable in describing the excitation behaviour of materials with a delocalised excited electron, which is typically related to them possessing a high dielectric constant. It is important to understand the limitations of the approximations used within TDDFT, so the fact that a reliable method has been shown to be applicable to the study of MgO and other related inorganic nanoparticles is of great value.

As well as addressing these issues, the research presented here has also highlighted gaps in the current knowledge of these systems and, more generally, in our understanding of photophysical phenomena. The suitability of TDDFT in describing excitation energies is widely accepted (given suitable approximations to the *xc*-potential) and excitation spectra can be modelled with this density-based methodology extremely well. However, TDDFT is a relatively new approach to modelling photoluminescence of inorganic materials, meaning that there are many unknowns in this field. The simplest possible optimisation of the lowest excited state was attempted by taking the optimised ground state as a starting structure for the optimisation of the particle on the lowest excited potential energy surface. However, in contrast to the absorption spectra of MgO nanoparticles, their emission spectra could not be replicated with the same functional approximations. It shows that a complete understanding of the emission process in even these relatively simple systems will be a major computational undertaking.

To deepen our understanding of photoluminescence processes, the author hopes that researchers are encouraged to study the excited state properties of these particles further:

not just by optimising the structure on the $S_1$ potential energy surfaces, but also on higher lying surfaces, as well as studying internal conversion processes and possible transition states on the excited state surfaces. This may not be computationally feasible at this moment in time, but it would certainly be fascinating to elucidate the structure of these potential energy surfaces with the aim of replicating the full photoluminescence spectrum. This would shed light on the applicability of Kasha's rule in predicting the state from which photoluminescence occurs. If it happened that this rule was broken, then what other systems might display the same behaviour? Is it possible that Kasha's rule is an over-simplification? What happens in systems where spin-orbit coupling is pronounced and how would this affect the photoluminescence spectra?

There are many unanswered questions that can be posed based on the work presented here but the author certainly hopes that others with access to copious amount of patience, computational resources – and an interest in elucidating the photoluminescence behaviour of inorganic particles – engage with this area of research and challenge themselves to further develop the model of the photoluminescence spectrum of the particles studied in this thesis.

# Bibliography

1.      Bredas, J.-L. Mind the gap! *Mater. Horizons* **1,** 17–19 (2014).

2.      Shah, N.K., Ludescher, R. D. Influence of hydration on the internal dynamics of hen egg white lysozyme in the dry state. *Photochem. Photobiol.* **58,** 169–174 (1993).

3.      Gong, X., Lim, S.H., Ostrowski, J. C. & M. D., Bardeen, C. J., Bazab, G. C. Phosphorescence from iridium complexes doped into polymer blends. *J. Appl. Phys.* **95,** 948–953 (2004).

4.      Pravinata, L. C., You, Y. & Ludescher, R. D. Erythrosin B phosphorescence monitors molecular mobility and dynamic site heterogeneity in amorphous sucrose. *Biophys. J.* **88,** 3551–3561 (2005).

5.      Vayá, I., Bonancía, P., Jiménez, M. C., Markovitsi, D., Gustavsson, T., Miranda, M. A. Excited state interactions between flurbiprofen and tryptophan in drug-protein complexes and in model dyads. Fluorescence studies from the femtosecond to the nanosecond time domains. *Phys. Chem. Chem. Phys.* **15,** 4727–34 (2013).

6.      Kasha, B. Y. M. Characterization of Electronic Transitions in Complex Molecules. *Discuss. Faraday Soc.* **9,** 14–19 (1950).

7.      Botan, V., Backus, E. H. G., Pfister, R., Moretto, A., Crisma, M., Toniolo, C., Nguyen, P. H., Stock, G., Hamm, P. Energy transport in peptide helices. *Proc. Natl. Acad. Sci. U. S. A.* **104,** 12749–12754 (2007).

8.      Middleton, C. T., de la Harpe, K., Su, C., Law, Y. K., Crespo-Hernández, C. E., Kohler, B. DNA excited-state dynamics: from single bases to the double helix. *Annu. Rev. Phys. Chem.* **60,** 217–239 (2009).

9.      Choi, Charina L, Li, Hui, Olson, Andrew C K, Jain, Prashant K, Sivasankar, Sanjeevi, Alivisatos, A. P. Spatially indirect emission in a luminescent nanocrystal molecule. *Nano Lett.* **11,** 2358–2362 (2011).

10.     Greenwood, N. N. & Earnshaw, A. *Chemistry of the Elements*. (Butterworth-Heineman, 1997).

11.    Kirk-Othmer. Kirk-Othmer Encyclopedia of Chemical Technology. *Kirk-Othmer Encycl. Chem. Technol.* **15,** 622–674 (1995).

12.    Halmann, M., Frei, A. & Steinfeld, A. Magnesium Production by the Pidgeon Process Involving Dolomite Calcination and MgO Silicothermic Reduction : Thermodynamic and Environmental Analyses. *Ind. Eng. Chem. Res.* **47,** 2146–2154 (2008).

13.    Pidgeon, L. M. & Alexander, W. A. Thermal production of magnesium-pilot-plant studies on the retort ferrosilicon process. *Trans. Am. Inst. Min. Metall. Eng.* **159,** 315 – 352 (1944).

14.    Zhang, Y., Chen, H. S., Liu, B. X., Zhang, C. R., Li, X. F. & Wang, Y. C. Melting of (MgO)(n) (n=18, 21, and 24) clusters simulated by molecular dynamics. *J. Chem. Phys.* **132,** 194304–194312 (2010).

15.    Bromley, S. T., Moreira, I. D. P. R., Neyman, K. M. & Illas, F. Approaching nanoscale oxides: models and theoretical methods. *Chem. Soc. Rev.* **38,** 2657–2670 (2009).

16.    Lewis, D. W. & Catlow, C. R. A. A computational study of the role of chlorine in the partial oxidation of methane by MgO and Li/MgO. *Top. Catal.* **1,** 111–121 (1994).

17.    Arndt, S., Laugel, G., Levchenko, S. & Horn, R., Baerns, M., Scheffler, M., Schlögl, R. & Schomäcker, R. A Critical Assessment of Li/MgO-Based Catalysts for the Oxidative Coupling of Methane. *Catal. Rev.* **53,** 424–514 (2011).

18.    Hutchings, G. J., Scurrell, M. S. & Woodhouse, J. R. Oxidative coupling of methane using oxide catalysts. *Chem. Soc. Rev.* **18,** 251–283 (1989).

19.    Sternig, A., Stankic, S., Müller, M., Bernardi, J., Knözinger, E. & Diwald, O. Photoluminescent Nanoparticle Surfaces: The Potential of Alkaline Earth Oxides for Optical Applications. *Adv. Mater.* **20,** 4840–4844 (2008).

20.    Stankic, S., Müller, M., Diwald, O., Sterrer, M., Knözinger, E. & Bernardi, J. Size-dependent optical properties of MgO nanocubes. *Angew. Chem. Int. Ed. Engl.* **44,** 4917–4920 (2005).

21. Stankic, S., Sternig, A., Finocchi, F., Bernardi, J. & Diwald, O. Zinc oxide scaffolds on MgO nanocubes. *Nanotechnology* **21,** 355603–355610 (2010).

22. Hohenberg, P. & Kohn, W. Inhomogeneous Electron Gas. *Phys. Rev.* **136,** B864 – B871 (1964).

23. Kohn, W. & Sham, L. J. Self-Consistent Equations Including Exchange and Correlation Effectd. *Phys. Rev.* **140,** A1133 − A1138 (1965).

24. Schrödinger, E. An undulatory theory of the mechanics of atoms and molecules. *Phys. Rev.* **28,** 1049–1070 (1926).

25. Hartree, D. R. The Wave Mechanics of an Atom with a Non-Coulomb Central Field. Part I. Theory and Methods. *Math. Proc. Cambridge Philos. Soc.* **24,** 89–110 (1928).

26. Fock, V. Näherungsmethode zur Lösung des quantenmechanischen Mehrkörperproblems. in *Russ. Phys. Chem. Soc.* 126–148 (1930).

27. Born, M. & Oppenheimer, R. Zur quantentheorie der molekeln. *Ann. Phys.* **20,** 457–484 (1927).

28. Jensen, F. in *Introd. to Comput. Chem.* 19 (John Wiley & Sonds, Ltd, 2007).

29. Thomas, L. H. The calculation of atomic fields. *Math. Proc. Cambridge Philos. Soc.* **23,** 542–548 (1927).

30. Fermi, E. Eine statistische Methode zur Bestimmung einiger Eigenschaftern des Atoms und ihre Anwedung auf die Theorie des periofischen Systems der Elements. *Eur. Phys. J. A, Hadron. nucleii* **48,** 71–79 (1928).

31. Dirac, P. A. M. Note on Exchange Phenomena in the Thomas Atom. *Math. Proc. Cambridge Philos. Soc.* **26,** 376–385 (1930).

32. Bloch, F. Über die Quantenmechanik der Elektronen in Kristallgittern. *Zeitschrift für Phys.* **52,** 555–600 (1928).

33. Metropolis, N., Rosenbluth, A. W., Rosenbluth, M. N., Teller, A. H. & Teller, E. Equation of State Calculations by Fast Computing Machines. *J. Chem. Phys.* **21,** 1087−1092 (1953).

34.     Pauli, W. Ueber den Zusammenhang des Abschlusses der Elektronengruppen im Atom mit der Komplexstructur der Speltren. *Zeitschrift für Phys.* **31,** 765–783 (1925).

35.     Roothaan, C. C. J. New Developments in Molecular Orbital Theory. *Rev. Mod. Phys.* **32,** 69–89 (1951).

36.     Purvis, G. D. A full coupled-cluster singles and doubles model: The inclusion of disconnected triples. *J. Chem. Phys.* **76,** 1910–1918 (1982).

37.     Bartlett, R. J. Many-Body Perturbation Theory and Coupled Cluster Theory for Electron Correlation in Molecules. *Annu. Rev. Phys. Chem.* **32,** 359–401 (1981).

38.     Comeau, D. C. & Bartlett, R. J. The equation-of-motion coupled-cluster method. Applications to open- and closed-shell reference states. *Chem. Phys. Lett.* **207,** 414–423 (1993).

39.     Helgaker, T., Jorgensen, P. & Olsen, J. *Molecular Electronic-Structure Theory.* (John Wiley & Sons, Ltd, 2004).

40.     Becke, A. D. Density-functional exchange-energy approximation with correct asymptotic behaviour. *Phys. Rev.* **38,** 3098–3100 (1988).

41.     Becke, A. D. A new mixing of Hartree–Fock and local density-functional theories. *J. Chem. Phys.* **98,** 1372–1377 (1993).

42.     Rensburg, W. J. Van, Steynberg, P. J., Meyer, W. H., Kirk, M. M. & Forman, G. S. DFT Prediction and Experimental Observation of Substrate-Induced Catalyst Decomposition in Ruthenium-Catalyzed Olefin Metathesis. *J. Am. Chem. Soc.* **126,** 14332–14333 (2004).

43.     Collins, C, Dyer, M. S., Demont, A, Chater, P. A., Thomas, M. F., Darling, G. R., Claridge, J. B. & Rosseinsky, M. J. Computational prediction and experimental confirmation of B-site doping in YBa2Fe3O8. *Chem. Sci.* **5,** 1493–1505 (2014).

44.     Baerends, E. J., Gritsenko, O. V & van Meer, R. The Kohn-Sham gap, the fundamental gap and the optical gap: the physical meaning of occupied and virtual Kohn-Sham orbital energies. *Phys. Chem. Chem. Phys.* **15,** 16408–16425 (2013).

45. Marques, M.A.L, Ullrich, C.A, Nogueira, F, Rubio, A., Burke, K, Gross, E. K. U. (Eds). *Time-Dependent Density Functional Theory Series: Lecture Notes in Pysics, Vol. 706*. **706,** (Springer Berlin Heidelberg, 2006).

46. Tao, J., Perdew, J., Staroverov, V. & Scuseria, G. Climbing the Density Functional Ladder: Nonempirical Meta–Generalized Gradient Approximation Designed for Molecules and Solids. *Phys. Rev. Lett.* **91,** 3–6 (2003).

47. Perdew, J P, Ruzsinszky, A, Tao, J, Staroverov, V N, Scuseria, G E & Csonka, G. I. Prescription for the design and selection of density functional approximations: more constraint satisfaction with fewer fits. *J. Chem. Phys.* **123,** 62201–62209 (2005).

48. Maradudin, A. A. & Carr, W. J. J. Ground-State Energy of a High-Density Electron Gas. *Phys. Rev.* **133,** A371–A374 (1964).

49. Carr, W. J. J. Energy, Specific Heat, and Magnetic Properties of the Low-Density Electron Gas. *Phys. Rev.* **122,** 1437–1446 (1961).

50. Vosko, S., Wilk, L. & Nusair, M. Accurate spin-dependent electron liquid correlation energies for local spin-density calculations - a critical analysis. *Can. J. Phys.* **58,** 1200–1211 (1980).

51. Ullrich, C. A. *Time-Dependent Density-Functional Theory: Concepts and Applications*. (Oxford University Press, 2012).

52. Perdew, J., Burke, K. & Ernzerhof, M. Generalized Gradient Approximation Made Simple. *Phys. Rev. Lett.* **77,** 3865–3868 (1996).

53. Lee, C., Yang, W. & Parr, R. G. Development of the Colle-Salvetti correlation-energy formula into a functional of the electron density. *Phys. Rev. B* **37,** 785–789 (1988).

54. Polo, V., Kraka, E. & Cremer, D. Electron correlation and the self-interaction error of density functional theory. *Mol. Phys.* **100,** 1771–1790 (2002).

55. Becke, A. D. Density-functional thermochemistry. IV. A new dynamical correlation functional and implications for exact-exchange mixing. *J. Chem. Phys.* **104,** 1040–1046 (1996).

56.   Ernzerhof, M. Construction of the adiabatic connection. *Chem. Phys. Lett.* **263,** 499–506 (1996).

57.   Burke, K., Ernzerhof, M. & Perdew, J. P. The adiabatic connection method: a non-empirical hybrid. *Chem. Phys. Lett.* **265,** 115–120 (1997).

58.   Güttinger, P. Das Verhalten von Atomen im magnetischen Drehfeld. *Zeitschrift für Phys.* **73,** 169–184 (1932).

59.   Feynman, R. P. Forces in molecules. *Phys. Rev.* **56,** 340–343 (1939).

60.   Stephens, P. J., Devlin, F. J., Chabalowski, C. F. & Frisch, M. J. Ab Initio Calculation of Vibrational Absorption and Circular Dichroism Spectra Using Density Functional Force Fields. *J. Phys. Chem.* **98,** 11623–11627 (1994).

61.   Becke, A. D. Density-functional thermochemistry. III. The role of exact exchange. *J. Chem. Phys.* **98,** 5648–5652 (1993).

62.   Becke, A. D. A multicenter numerical integration scheme for polyatomic molecules. *J. Chem. Phys.* **88,** 2547–2553 (1988).

63.   Zunger, A. & Perdew, J. P. Self-interaction correction to density-functional approximations for many-electron systems. *Phys. Rev. B* **23,** 5048–5079 (1981).

64.   Yanai, T., Tew, D. P. & Handy, N. C. A new hybrid exchange–correlation functional using the Coulomb-attenuating method (CAM-B3LYP). *Chem. Phys. Lett.* **393,** 51–57 (2004).

65.   Wiggins, P., Williams, J. A. G. & Tozer, D. J. Excited state surfaces in density functional theory: a new twist on an old problem. *J. Chem. Phys.* **131,** 091101–091109 (2009).

66.   Zhao, Y., Lynch, B. J. & Truhlar, D. G. Development and Assessment of a New Hybrid Density Functional Model for Thermochemical Kinetics. *J. Phys. Chem. A* **108,** 2715–2719 (2004).

67.   Bohm, D. & Pines, D. A collective description of electron interactions. I. magnetic interactions. *Phys. Rev.* **82,** 625–634 (1951).

68.    Pines, D. & Bohm, D. A collective description of electron interactions: II. Collective vs individual particle aspects of the interactions. *Phys. Rev.* **85,** 338–353 (1952).

69.    Bohm, D. & Pines, D. A collective description of electron interactions: III. Coulomb interactions in a degenerate electron gas. *Phys. Rev.* **92,** 609–625 (1953).

70.    Furche, F. Molecular tests of the random phase approximation to the exchange-correlation energy functional. *Phys. Rev. B* **64,** 1–8 (2001).

71.    He, Y., Gräfenstein, J., Kraka, E. & Cremer, D. What correlation effects are covered by density functional theory? *Mol. Phys.* **98,** 1639–1658 (2000).

72.    Johnson, B. G., Gill, P. M. W. & Pople, J. A. The performance of a family of density functional methods. *J. Chem. Phys.* **98,** 5612–5626 (1993).

73.    Wodrich, M. D., Corminboeuf, C. & Schleyer, P. V. R. Systematic errors in computed alkane energies using B3LYP and other popular DFT functionals. *Org. Lett.* **8,** 3631–3634 (2006).

74.    Quintal, M. M., Karton, A., Iron, M. A., Boese, A. D. & Martin, J. M. L. Benchmark study of DFT functionals for late transition metal reactions. *J. Phys. Chem. A* **110,** 709–716 (2006).

75.    Sousa, S. F., Fernandes, P. A. & Ramos, M. J. General Performance of Density Functionals General Performance of Density Functionals. *J. Phys. Chem. A* **111,** 10439–10452 (2007).

76.    Boese, A. Daniel, Martin, Jan M L & Handy, N. C. The role of the basis set: Assessing density functional theory. *J. Chem. Phys.* **119,** 3005–3014 (2003).

77.    Slater, J. Atomic Shielding Constants. *Phys. Rev.* **36,** 57–64 (1930).

78.    Boys, S. F. Electronic Wave Functions. I. A General Method of Calculation for the Stationary States of Any Molecular System. *Proc. R. Soc. A Math. Phys. Eng. Sci.* **200,** 542–554 (1950).

79.    Hehre, W. J., Stewart, R. F. & Pople, J. A. Self-Consistent Molecular-Orbital Methods. I. Use of Gaussian Expansions of Slater-Type Atomic Orbitals. *J. Chem. Phys.* **51,** 2657–2664 (1969).

80. Jensen, F. in *Introd. to Comput. Chem.* (John Wiley & Sons, Ltd, 2007).

81. Hellmann, H. A New Approximation Method in the Problem of Many Electrons. *J. Chem. Phys.* **3,** 61 (1935).

82. Weigend, F. & Ahlrichs, R. Balanced basis sets of split valence, triple zeta valence and quadruple zeta valence quality for H to Rn: Design and assessment of accuracy. *Phys. Chem. Chem. Phys.* **7,** 3297 – 3305 (2005).

83. Schäfer, A., Horn, H. & Ahlrichs, R. Fully optimized contracted Gaussian basis sets for atoms Li to Kr. *J. Chem. Phys.* **97,** 2571 (1992).

84. Gunnarson, O., Lundqvist, B. I. & Lundqvist, S. Screening in a spin-polarized electron liquid. *Solid State Commun.* **11,** 149–153 (1972).

85. Jones, R. & Gunnarsson, O. The density functional formalism, its applications and prospects. *Rev. Mod. Phys.* **61,** 689–746 (1989).

86. Martin, R. M. *Electronic Structure: Basic Theory and Practical Methods.* (Cambridge University Press, 2004).

87. Tozer, D. J. & Handy, N. C. On the determination of excitation energies using density functional theory. *Phys. Chem. Chem. Phys.* 2117–2121 (2000).

88. Adamo, C. & Jacquemin, D. The calculations of excited-state properties with Time-Dependent Density Functional Theory. *Chem. Soc. Rev.* **42,** 845–56 (2013).

89. Peach, M. J. G., Benfield, P., Helgaker, T. & Tozer, D. J. Excitation energies in density functional theory: an evaluation and a diagnostic test. *J. Chem. Phys.* **128,** 044118–044125 (2008).

90. Jacquemin, D., Wathelet, V., Perpète, E. A. & Adamo, C. Extensive TD-DFT benchmark: Singlet-excited states of organic molecules. *J. Chem. Theory Comput.* **5,** 2420–2435 (2009).

91. Runge, E. & Gross, E. Density-Functional Theory for Time-Dependent Systems. *Phys. Rev. Lett.* **52,** 997–1000 (1984).

92. van Leeuwen, R. Mapping from Densities to Potentials in Time-Dependent Density-Functional Theory. *Phys. Rev. Lett.* **82,** 3863–3866 (1999).

93. Kurzweil, Y. & Baer, R. Time-dependent exchange-correlation current density functionals with memory. *J. Chem. Phys.* **121,** 8731–8741 (2004).

94. Casida, M. E. Time-dependent density-functional theory for molecules and molecular solids. *J. Mol. Struct. Theochem* **914,** 3–18 (2009).

95. Jamorski, C., Casida, M. E. & Salahub, D. R. Dynamic polarizabilities and excitation spectra from a molecular implementation of time-dependent density-functional response theory: N2 as a case study. *J. Chem. Phys.* **104,** 5134–5147 (1996).

96. Casida, M. E., Jamorski, C., Casida, K. C. & Salahub, D. R. Molecular excitation energies to high-lying bound states from time-dependent density-functional response theory: Characterization and correction of the time-dependent local density approximation ionization threshold. *J. Chem. Phys.* **108,** 4439–4449 (1998).

97. Thiele, M., Gross, E. & Kümmel, S. Adiabatic Approximation in Nonperturbative Time-Dependent Density-Functional Theory. *Phys. Rev. Lett.* **100,** 153004–153008 (2008).

98. Stein, T., Kronik, L. & Baer, R. Reliable prediction of charge transfer excitations in molecular complexes using time-dependent density functional theory. *J. Am. Chem. Soc.* **131,** 2818–2820 (2009).

99. Casida, M. E. Generalization of the optimized-effective-potential model to include electron-correlation: A variational derivation of the Sham-Schlüter equation for the exact excahnge-correlation potential. *Phys. Rev.* **51,** 2005–2013 (1995).

100. Bauernschmitt, R. & Ahlrichs, R. Treatment of electronic excitations within the adiabatic approximation of time dependent density functional theory. *Chem. Phys. Lett.* **256,** 454–464 (1996).

101. Furche, F. & Ahlrichs, R. Adiabatic time-dependent density functional methods for excited state properties. *J. Chem. Phys.* **117,** 7433–7447 (2002).

102. Heßelmann, A. & Görling, A. Blindness of the exact density response function to certain types of electronic excitations: Implications for time-dependent density-functional theory. *Phys. Rev. Lett.* **102,** 1–4 (2009).

103. Furche, F. & Ahlrichs, R. Erratum: 'Time-dependent density functional methods for excited state properties' [J. Chem. Phys. 117, 7433 (2002)]. *J. Chem. Phys.* **121,** 12772–12773 (2004).

104. Dancoff, S. M. Non-Adiabatic Meson Theory of Nuclear Forces. *Phys. Rev.* **78,** 382–385 (1950).

105. Manzhos, S., Segawa, H. & Yamashita, K. Computational dye design by changing the conjugation order: Failure of LR-TDDFT to predict relative excitation energies in organic dyes differing by the position of the methine unit. *Chem. Phys. Lett.* **527,** 51–56 (2012).

106. Dierksen, M. & Grimme, S. The Vibronic Structure of Electronic Absorption Spectra of Large Molecules: A Time-Dependent Density Functional Study on the Influence of 'Exact' Hartree Fock Exchange. *J. Phys. Chem. A* **108,** 10225–10237 (2004).

107. Laurent, A. D. & Jacquemin, D. TD-DFT benchmarks: A review. *Int. J. Quantum Chem.* **113,** 2019–2039 (2013).

108. Van Leeuwen, R. & Baerends, E. J. Exchange-correlation potential with correct asymptotic behavior. *Phys. Rev. A* **49,** 2421–2431 (1994).

109. Peach, M. J. G., Le Sueur, C. R., Ruud, K., Guillaume, M. & Tozer, D. J. TDDFT diagnostic testing and functional assessment for triazene chromophored. *Phys. Chem. Chem. Phys.* **11,** 4465–4470 (2009).

110. Peach, M. J. G. & Tozer, D. J. Illustration of a TDDFT spatial overlap diagnostic by basis function exponent scaling. *J. Mol. Struct. THEOCHEM* **914,** 110–114 (2009).

111. Peach, M. J. G. & Tozer, D. J. Overcoming low orbital overlap and triplet instability problems in TDDFT. *J. Phys. Chem. A* **116,** 9783–9789 (2012).

112. Maitra, N. T., Zhang, F., Cave, R. J. & Burke, K. Double excitations within time-dependent density functional theory linear response. *J. Chem. Phys.* **120,** 5932–5937 (2004).

113. Levine, B. G., Ko, C., Quenneville, J. & Martinez, T. J. Conical intersections and double excitations in time-dependent density functional theory. *Mol. Phys.* **104,** 1039–1051 (2006).

114. Tapavicza, E., Tavernelli, I., Rothlisberger, U., Filippi, C. & Casida, M. E. Mixed time-dependent density-functional theory/classical trajectory surface hopping study of oxirane photochemistry. *J. Chem. Phys.* **129,** 124108–124127 (2008).

115. Tapavicza, E., Meyer, A. M. & Furche, F. Unravelling the details of vitamin D photosynthesis by non-adiabatic molecular dynamics simulations. *Phys. Chem. Chem. Phys.* **13,** 20986–20998 (2011).

116. Mulliken, R. S. Electronic Population Analysis on LCAO-MO Molecular Wave Functions. IV. Bonding and Antibonding in LCAO and Valence-Bond Theories. *J. Chem. Phys.* **23,** 2343–2346 (1955).

117. Mulliken, R. S. Electronic Population Analysis on LCAOMO Molecular Wave Functions. II. Overlap Populations, Bond Orders, and Covalent Bond Energies. *J. Chem. Phys.* **23,** 1841–1846 (1955).

118. Mulliken, R. S. Electronic Population Analysis on LCAO-MO Molecular Wave Functions. III. Effects of Hybridization on Overlap and Gross AO Populations. *J. Chem. Phys.* **23,** 2338–2342 (1955).

119. Mulliken, R. S. Criteria for the Construction of Good Self-Consistent-Field Molecular Orbital Wave Functions, and the Significance of LCAO-MO Population Analysis. *J. Chem. Phys.* **36,** 3428–3439 (1962).

120. Löwdin, P.-O. On the Non-Orthogonality Problem Connected with the Use of Atomic Wave Functions in the Theory of Molecules and Crystals. *J. Chem. Phys.* **18,** 365–375 (1950).

121. Gómez-Jeria, J. S. An empirical way to correct some drawbacks of Mulliken Population Analysis. *J. Chil. Chem. Soc.* **54,** 482–485 (2009).

122. Bader, R. F. W. Everyman's derivation of the theory of atoms in molecules. *J. Phys. Chem. A* **111,** 7966–7972 (2007).

123. Bader, R. F. W. *Atoms in Molecules A Quantum Theory*. (Clarendon Press, 1994).

124. Bader, R. F. W. Quantum topology of molecular charge distributions. III. The mechanics of an atom in a molecule. *J. Chem. Phys.* **73,** 2871–2883 (1980).

125. Peach, M. J. G., Williamson, M. J. & Tozer, D. J. Influence of Triplet Instabilities in TDDFT. *J. Chem. Theory Comput.* **7,** 3578–3585 (2011).

126. Berardo, E., Hu, H.-S., Shevlin, S. A., Woodley, S. M., Kowalski, K. & Zwijnenburg, M. A. Modeling Excited States in TiO2 Nanoparticles: On the Accuracy of a TD-DFT Based Description. *J. Chem. Theory Comput.* **10,** 1189–1199 (2014).

127. Wobbe, M., Kerridge, A. & Zwijnenburg, M. A. Optical excitation of MgO nanoparticles; A computational perspective. *Phys. Chem. Chem. Phys.* **16,** 22052–22061 (2014).

128. Wobbe, M. C. C., Zwijnenburg, M. A. Chemical trends in the optical properties of rocksalt nanoparticles. *Phys. Chem. Chem. Phys.* **17,** 28892–28900 (2015).

129. Ahlrichs, R., Bär, M., Marco, H., Horn, H. & Kölmel, C. Electronic Structure calculations on workstation Computers: The Program system TURBOMOLE. *Chem. Phys. Lett.* **162,** 165–169 (1989).

130. TURBOMOLE V6.4 2012, A development of University of Karlsruhe and Forschungszentrum Karlsruhe GmbH, 1989-2007, TURBOMOLE gmbH, since 2007. (2012). at <www.turbomole.com>

131. Schmidt, M. W., Baldridge, K. K., Boatz, J. A., Elbert, S. T., Gordon, M. S., Jensen J. H., Koseki S., Matsunaga N., Nguyen K. A., Su S., Windus T. L., Dupuis, M. & M. J. A. D. General Atomic and Molecular Electronic Structure System. *J. Comput. Chem.* **14,** 1347–1363 (1993).

132. Gordon, M. S. & Schmidt, M. W. in *Adv. Electron. Struct. Theory GAMESS a Decad. later* (eds. Dykstra, C. E., Frenking, G., Kim, K. S. & Scuseria, G. E.) (Elsevier Ltd, 2005).

133. Kohut, M. DGrid. (2011). at <http://www.cpfs.mpg.de/~kohut/dgrid.html>

134. Humphrey, W., Dalke, A. & Schulten, K. VMD: Visual molecular dynamics. *J. Mol. Graph.* **14,** 33–38 (1996).

135. Anpo, M., Yamada, Y. & Kubokawa, Y. Photoluminescence and photocatalytic activity of MgO powders with co-ordinatively unsaturated surface ions. *J. Chem. Soc. Chem. Commun.* **84,** 751–764 (1986).

136. Freund, H., Kuhlenbeck, H. & Staemmler, V. Oxide surfaces. *Rep. Prog. Phys.* **59,** 283–347 (1996).

137. Henry, C. R. Surface studies of supported model catalysts. *Surf. Sci. Rep.* **31,** 231–325 (1998).

138. Baeumer, M. & Freund, H.-J. Metal deposits on well-ordered oxide films. *Prog. Surf. Sci.* **61,** 127–198 (1999).

139. Chambers, S. A. Epitaxial growth and properties of thin film oxides. *Surf. Sci. Rep.* **39,** 105–180 (2000).

140. Spoto, G., Gribov, E. N., Ricchiardi, G., Damin, A., Scarano, D., Bordiga, S., Lamberti, C. & Zecchina, A. Carbon monoxide MgO from dispersed solids to single crystals: A review and new advances. *Prog. Surf. Sci.* **76,** 71–146 (2004).

141. Fu, Q. & Wagner, T. Interaction of nanostructured metal overlayers with oxide surfaces. *Surf. Sci. Rep.* **62,** 431–498 (2007).

142. Ni, M., Leung, D. Y. C. & Leung, M. K. H. A review on reforming bio-ethanol for hydrogen production. *Int. J. Hydrogen Energy* **32,** 3238–3247 (2007).

143. Wzodarczyk, R. *et al.* Structures of the Ordered Water Monolayer on MgO (001). *J. Phys. Chem. C* **115,** 6764–6774 (2011).

144. Freund, H.-J. & Pacchioni, G. Oxide ultra-thin films on metals: new materials for the design of supported metal catalysts. *Chem. Soc. Rev.* **37,** 2224–2242 (2008).

145. Freund, H.-J., Nilius, N., Risse, T. & Schauermann, S. A fresh look at an old nano-technology: catalysis. *Phys. Chem. Chem. Phys.* **16,** 8148–8167 (2014).

146. Brena, B. & Ojama, L. Surface Effects and Quantum Confinement in Nanosized GaN Clusters: Theoretical Predictions. *J. Phys. Chem. C* **112,** 13516–13523 (2008).

147. Zecchina, A. & Stone, F. S. Reflectance Spectra of Surface States in Strontium Oxide and Barium Oxide. *J. Chem. Soc. Faraday Trans. 1* **03,** 2364–2374 (1975).

148. Stankic, S., Bernardi, J., Diwald, O. & Knözinger, E. Optical surface properties and morphology of MgO and CaO nanocrystals. *J. Phys. Chem. B* **110,** 13866–13871 (2006).

149. Stankic, S., Sterrer, M., Hofmann, P., Bernardi, J., Diwald, O. & Knözinger, E. Novel optical surface properties of Ca2+ -doped MgO nanocrystals. *Nano Lett.* **5,** 1889–1893 (2005).

150. Anderson, P. J., Horlock, R. F. & Oliver, J. F. Interaction of Water with the Magnesium Oxide Surface. *Trans.action Faraday Soc.* **61,** 2754–2762 (1965).

151. Coluccia, S., Deane, A. M. & Tench, A. J. Photoluminescent Spectra of Surface States in Alkaline Earth Oxides. *Faraday Trans. I* **74,** 2913–2922 (1978).

152. Coluccia, S., Barton, A. & Tench, A. J. Reactivity of Low-coordination Sites on the Surface of Magnesium Oxide. *J. Chem. Soc. Faraday Trans. 1* **1,** 2203–2207 (1981).

153. Moodie, A. F. & Warble, C. E. Electron microscopic investigations of MgO morphology and surfaces. *J. Cryst. Growth* **10,** 26–38 (1971).

154. Knözinger, E., Jacob, K.-H., Singh, S. & Hofmann, P. Hydroxyl groups as IR active surface probes on MgO crystallites. *Surf. Sci. Lett.* **290,** A540–A541 (1993).

155. Mageshwari, K., Mali, S. S., Sathyamoorthy, R. & Patil, P. S. Template-free synthesis of MgO nanoparticles for effective photocatalytic applications. *Powder Technol.* **249,** 456–462 (2013).

156. Müller, M., Stankic, S., Diwald, O., Knözinger, E., Sushko, P. V. & Trevisanutto, P. E., Shluger, A. L. Effect of protons on the optical properties of oxide nanostructures. *J. Am. Chem. Soc.* **129,** 12491–12496 (2007).

157. MacLean, S. G. & Duley, W. W. Photoluminescence from surface states in MgO and CaO powders. *J. Phys. Chem. Solids* **45,** 227–235 (1984).

158.  Anpo, M. & Yamada, Y. Photoluminescence and Photocatalytic activity of MgO powders. *Mater. Chem. Phys.* **18,** 465–484 (1988).

159.  Bailly, M. L., Costentin, G., Lauron-Pernot, H., Krafft, J. M. & Che, M. Physicochemical and in situ photoluminescence study of the reversible transformation of oxide ions of low coordination into hydroxyl groups upon interaction of water and methanol with MgO. *J. Phys. Chem. B* **109,** 2404–2413 (2005).

160.  Warshel, A. & Levitt, M. Theoretical studies of enzymic reactions: dielectric, electrostatic and steric stabilization of the carbonium ion in the reaction of lysozyme. *J. Mol. Biol.* **103,** 227–249 (1976).

161.  Shluger, A. L., Sushko, P. V & Kantorovich, L. N. Spectroscopy of low-coordinated surface sites : Theoretical study of MgO. *Phys. Rev. B* **59,** 2417–2430 (1999).

162.  Garrone, E., Zecchina, A. & Stone, F. S. Anionic Intermediates in Surface Processes Leading to O2- Formation on Magnesium Oxide. *J. Catal.* **62,** 396–400 (1980).

163.  Trevisanutto, P.E., Sushko, P.V., Shluger, A.L., Beck, K.M., Henyk, M., Joly, A.G. & Hess, W. P. A mechanism of photo-induced desorption of oxygen atoms from MgO nano-crystals. *Surf. Sci.* **593,** 210–220 (2005).

164.  Trevisanutto, P. E., Sushko, P. V., Beck, K. M., Joly, A. G., Hess, W. P. & Shluger, A. L. Excitation, Ionization, and Desorption : How Sub-Band Gap Photons Modify the Structure of Oxide Nanoparticles. *J. Phys. Chem. C* **113,** 1274–1279 (2009).

165.  Sushko, P. V., McKenna, K. P., Muñoz Ramo, D. , Shluger, A. L., Sternig, A., Stankic, S., Mueller, M. & Diwald, O. Photoluminescence Properties of Alkaline-Earth Oxide Nanoparticles. *ECS Trans.* **28,** 67–80 (2010).

166.  Sternig, A., Koller, D., Siedl, N., Diwald, O. & McKenna, K. Exciton Formation at Solid–Solid Interfaces: A Systematic Experimental and ab Initio Study on Compressed MgO Nanopowders. *J. Phys. Chem. C* **116,** 10103–10112 (2012).

167.  McKenna, K. P., Koller, D., Sternig, A., Siedl, N., Govind, N., Sushko, P. V. & Diwald, O. Optical properties of nanocrystal interfaces in compressed MgO nanopowders. *ACS Nano* **5,** 3003–3009 (2011).

168.  Glascock, H. H. & Hensley, E. B. Fundamental Optical Absorption, Electrical Conductivity, and Thermoelectric Power of Calcium Oxide. *Phys. Rev.* **131,** 649–652 (1963).

169.  Whited, R. C. & Walker, W. C. Exciton and Interband Spectra of Crystalline CaO. *Phys. Rev.* **188,** 1380–1384 (1969).

170.  Zecchina, A., Lofthouse, M. G. & Stone, F. S. Refelctance Spectra of Surface States in Magnesium Oxide and Calcium Oxide. *J. Chem. Soc. Faraday Trans. 1* **71,** 1476–1490 (1975).

171.  Stankic, S., Bernardi, J., Diwald, O. & Kno, E. Photoexcitation of Local Surface Structures on Strontium Oxide Grains. *J. Phys. Chem. C* **111,** 8069–8074 (2007).

172.  Rao, A. & Kearney, R. Logarithmic derivative reflectance spectra of BaO and SrO. *Phys. Status Solidi* **95,** 243–250 (1979).

173.  Kaneko, Yoshio, Koda, T. New developments in IIa-VIb (Alkaline-earth chalcogenide) binary semiconductors. *J. Cryst. Growth* **86,** 72–78 (1988).

174.  Rabah, M., Abbar, B., Al-Douri, Y., Bouhafs, B. & Sahraoui, B. Calculation of structural, optical and electronic properties of ZnS, ZnSe, MgS, MgSe and their quaternary alloy Mg1−xZnxSySe1−y. *Mater. Sci. Eng. B* **100,** 163–171 (2003).

175.  Okuyama, H., Nakano, K., Miyajima, T. & Akimoto, K. Epitaxial Growth of ZnMgSSe on GaAs Substrate by Molecular Beam Epitaxy. *Jpn. J. Appl. Phys.* **30,** L1620–L1623 (1991).

176.  Drief, F., Tadjer, a., Mesri, D. & Aourag, H. First principles study of structural, electronic, elastic and optical properties of MgS, MgSe and MgTe. *Catal. Today* **89,** 343–355 (2004).

177.  Gökoğlu, G., Durandurdu, M. & Gülseren, O. First principles study of structural phase stability of wide-gap semiconductors MgTe, MgS and MgSe. *Comput. Mater. Sci.* **47,** 593–598 (2009).

178. Freeouf, J. L. Far-ultraviolet reflectance of II-VI compounds and correlation with the Penn Phillips gap. *Phys. Rev. B* **7,** 3810–3830 (1973).

179. Dalven, R. A review of the semiconductor properties of PbTe, PbSe, PbS and PbO. *Infrared Phys.* **9,** 141–184 (1969).

180. Wang, Z. L. Functional oxide nanobelts: materials, properties and potential applications in nanosystems and biotechnology. *Annu. Rev. Phys. Chem.* **55,** 159–196 (2004).

181. Kaviyarasu, K., Manikandan, E., Paulraj, P., Mohamed, S. B. & Kennedy, J. One dimensional well-aligned CdO nanocrystal by solvothermal method. *J. Alloys Compd.* **593,** 67–70 (2014).

182. Lu, C., Guan, C., Liu, Y., Cheng, Y. & Yang, B. PbS/Polymer Nanocomposite Optical Materials with High Refractive Index. *Chem. Mater.* **17,** 2448–2454 (2005).

183. Pawar, S. B. *et al.* Facile and low cost chemosynthesis of nanostructured PbS with tunable optical properties. *Appl. Surf. Sci.* **258,** 1869–1875 (2011).

184. Cao, H., Wang, G., Zhang, S., Zhang, X. Growth and photoluminescence properties of PbS nanocubes. *Nanotechnology* **17,** 3280–3287 (2006).

185. Roessler, D. M. & Walker, W. C. Electronic Spectrum and Ultraviolet Optical Properties of Crystalline MgO. *Phys. Rev.* **159,** 733–738 (1967).

186. Whited, R. C., Flaten, C. J. & Walker, W. C. Exciton thermoreflectance of MgO and CaO. *Solid State Commun.* **13,** 1903–1905 (1973).

187. Strehlow, W. H. & Cook, E. L. Compilation of Energy Band Gaps in Elemental and Binary Compound Semiconductors and Insulators. *J. Phys. Chem. Ref. Data* **2,** 163–200 (1973).

188. Davidson, I. A., Moug, R. T., Izdebski, F., Bradford, C. & Prior, K. A. Determination of the band-gap of MgS and MgS-rich Zn1-xMgxSySe1-y alloys from optical transmission measurements. *Phys. Status Solidi Basic Res.* **247,** 1396–1398 (2010).

189. Jobst, B., Hommel, D. & Lunz, U. E0 band-gap energy and lattice constant of ternary Zn1-xMgxSe as functions of composition. *Appl. Phys. Lett.* **69,** 97–99 (1996).

190. Catlow, C. & Stoneham, A. Ionicity in Solids. *J. Phys. C. Solid State Phys.* **4321,** 4321–4338 (1983).

191. Penn, D. R. Wave-number-dependent dielectric function of semiconductors. *Phys. Rev.* **128,** 2093–2097 (1962).

192. Phillips, J. C. Covalent bond in crystals. I. Elements of a structural theory. *Phys. Rev.* **166,** 832–838 (1968).

193. Phillips, J. C. Covalent bond in crystals. II. Partially ionic binding. *Phys. Rev.* **168,** 905–911 (1968).

194. Phillips, J. C. Dielectric definition of electronegativity. *Phys. Rev. Lett.* **20,** 550–553 (1968).

195. Phillips, J. C. Ionicity of the chemical bond in crystals. *Rev. Mod. Phys.* **42,** 317–356 (1970).

196. Van Vechten, J. A. Quantum dielectric theory of electronegativity in covalent systems. I. Electronic dielectric constant. *Phys. Rev.* **182,** 891–905 (1969).

197. Henderson, A. E., Hughes, B. in *Point Defects Solids Vol. 1 Gen. Ion. Cryst.* (ed. Crawford, James H.; Slifkin, L. M.) 381–490 (Plenum Press, 1972).

198. Littlewood, P. B. The dielectric constant of cubic IV-VI compounds. *J. Phys. C Solid State Phys.* **12,** 4459–4468 (1979).

199. McFarland, E. W. & Metiu, H. Catalysis by doped oxides. *Chem. Rev.* **113,** 4391–4427 (2013).

200. Dolgov, S. A., Isakhanyan, V., Karner, T., Maaroos, A. &Nakonechnyi, S. Electron paramagnetic resonance of the [Be]+ centre in MgO:Be. *J. Phys. Condens. Matter* **15,** 6871–6878 (2003).

201. Dolgov, S. A., Isakhanyan, V., Kaerner, T., Liblik, P., Maaroos, A. & Nakonechnyi, S. Luminescence of [Be]+ centre in MgO:Be. *Radiat. Meas.* **38,** 699–702 (2004).

202. Dolgov, S. A., Feldbach, E., Kärkkänen, A., Kärner, T., Liblik, P., Maaroos, A. & Nakonechnyi, S. Low-temperature ( 4 – 295 K ) thermoluminescence of pure and Ca-doped MgO single crystals. *Phys. status solidi* **425,** 422–425 (2005).

203. Issahanyan, V., Kärner, T., Maaroos, A. & Nakonechnyi, S. Spin relaxation processes in the defect hole centres of Be doped MgO single crystals. *Phys. status solidi* **2,** 426–429 (2005).

204. Campbell, S., Cao, L. L., Cotter, M., Edgerll, R. G., Flavell, W. R., Mok, K. F. & Mackrodt, W. C. Sr segregation in doped MgO. *J. Phys. Condens. Matter* **1,** 237–239 (1989).

205. Cao, L. L., Egdell, R. G., Flavell, W. R., Mok, K. F. & Mackrodt, W. C. Surface Segregation of Sr in Doped MgO Comparison between X-Ray Photoelectron Spectroscopy and Atomistic Inoic Model Simulations. *J. Mater. Chem.* **1,** 785–788 (1991).

206. Sternig, A., Klacar, S., Bernardi, J., Stoeger-Pollach, M., Groenbeck, H. & Diwald, O. Phase Separation at the Nanoscale : Structural Properties of BaO Segregates on MgO-Based Nanoparticles. *J. Phys. Chem. C* **115,** 15853–15861 (2011).

207. Kohan, A. & Ceder, G. Tight-binding calculation of formation energies in multicomponent oxides: Application to the MgO-CaO phase diagram. *Phys. Rev. B* **54,** 805–811 (1996).

208. Mueller, M., Sternig, A., Stankic, S., Stoeger-Pollach, M., Bernardi, J., Knoezinger, E., Diwald, O. Nanoparticles as a Support : CaO Deposits on MgO Cubes. *Jounral Phys. Chem. C Lett.* **112,** 9120–9123 (2008).

209. Tran, T. B., Hayun, S., Navrotsky, A. & Castro, R. H. Transparent Nanocrystalline Pure and Ca-Doped MgO by Spark Plasma Sintering of Anhydrous Nanoparticles. *J. Am. Ceram. Soc.* **95,** 1185–1188 (2012).

210. Sternig, A., Müller, M., McCallum, M., Bernardi, J. & Diwald, O. BaO clusters on MgO nanocubes: a quantitative analysis of optical-powder properties. *Small* **6,** 582–588 (2010).

211. Sternig, A., Bernardi, J., McKenna, K. & Diwald, O. Surface-specific visible light luminescence from composite metal oxide nanocrystals. *J. Mater. Sci.* **50,** 8153–8166 (2015).

212. Ohira, T., Kawamura, M., Fukuda, M., Alvarez, K., Oezkal, B. & Yamamoto, O. Extension of the Optical Absorption Range in Zn-Doped MgO Powders and Its Effect on Antibacterial Activity. *Performance, J. Mater. Eng.* **19,** 374–379 (2010).

213. Vidic, J., Stankic, S., Haque, F., Ciric, D., Le Goffic, R., Vidy, A., Jupille, J. & Delmas, B. Selective antibacterial effects of mixed ZnMgO nanoparticles. *J. Nanoparticle Res.* **15,** 1595–1605 (2013).

214. Kantorovich, L. N., Shluger, A. L., Sushko, P. V., Gu, J., Stracke, P., Goodman, D. W., Kempter, V. Mg clusters on MgO surfaces : study of the nucleation mechanism with MIES and ab initio calculations. *Faraday Discuss.* **114,** 173–194 (1999).

215. Sterrer, M., Berger, T., Diwald, O., Knözinger, E., Sushko, P. V., Shluger, A. L. Chemistry at corners and edges: generation and adsorption of H atoms on the surface of MgO nanocubes. *J. Chem. Phys.* **123,** 64714 (2005).

216. Dong, R., Chen, X., Wang, X. & Lu, W. Structural transition of hexagonal tube to rocksalt for (MgO)3n, 2<or=n<or=10. *J. Chem. Phys.* **129,** 044705 (2008).

217. Malliavin, M.-J. & Coudray, C. Ab initio calculations on (MgO)n, (CaO)n, and (NaCl)n clusters (n=1−6). *J. Chem. Phys.* **106,** 2323–2330 (1997).

218. El-Kelany, K. E., Ferrabone, M., Rérat, M., Carbonnière, P., Zicovich-Wilson, C. M. & & Dovesi, R. The electronic structure of MgO nanotubes. An ab initio quantum mechanical investigation. *Phys. Chem. Chem. Phys.* **15,** 13296–13303 (2013).

219. Aguado, A., Ayuela, A. & Lopez, J. M. Structural and electronic properties of small neutral (MgO)n clusters. *Phys. Rev. B* **56,** 7607–7614 (1997).

220. Zhang, Y. & Chen, H. S. Thermal stability of (MgO)12 dimers. *Eur. Phys. J. D* **66,** 1–7 (2012).

221.  Haertelt, M, Fielicke, A., Meijer, G., Kwapien, K., Sierka, M., & Sauer, J. Structure determination of neutral MgO clusters--hexagonal nanotubes and cages. *Phys. Chem. Chem. Phys.* **14,** 2849–2856 (2012).

222.  Harvey, J. N. On the accuracy of density functional theory in transition metal chemistry. *Annu. Reports Sect. C* **102,** 203–226 (2006).

223.  Minenkov, Y., Singstad, Å., Occhipinti, G., Jensen, V. R. The accuracy of DFT-optimized geometries of functional transition metal compounds: a validation study of catalysts for olefin metathesis and other reactions in the homogeneous phase. *Dalt. Trans.* **41,** 5526–5541 (2012).

224.  Cazorla, C., Shevlin, S. A. Accuracy of Density Functional Theory in Prediction of Carbon Dioxide Adsorbent Materials. *Dalt. Trans.* **42,** 4670–6 (2013).

225.  Tasker, P. W. The stability of ionic crystal surfaces. *J. Phys. C Solid State Phys.* **12,** 4977–4984 (1979).

226.  Melnikov, D. & Fowler, W. Electron-phonon interaction in a spherical quantum dot with finite potential barriers: The Fröhlich Hamiltonian. *Phys. Rev. B* **64,** 245320 (2001).

227.  Berardo, E., Hu, H.-S., Kowalski, K. & Zwijnenburg, M. A. Coupled cluster calculations on TiO2 nanoclusters. *J. Chem. Phys.* **139,** 064313 (2013).

228.  Sternig, A., Stankic, S., Müller, M., Siedl, N. & Diwald, O. Surface exciton separation in photoexcited MgO nanocube powders. *Nanoscale* **4,** 7494–7500 (2012).

229.  Zwijnenburg, M. A. Optical excitations in stoichiometric uncapped ZnS nanostructures. *Nanoscale* **3,** 3780–3787 (2011).

230.  Alivisatos, A. P. Semiconductor Clusters, Nanocrystals and Quantum Dots. *Science* **271,** 933–937 (1996).

231.  Alivisatos, A. P. Perspectives on the Physical Chemistry of Semiconductor Nanocrystals. *J. Phys. Chem.* **100,** 13226–13239 (1996).

232.  Chen, W., Wang, Z., Lin, Z. & Lin, L. Absorption and luminescence of the surface states in ZnS nanoparticles. *J. Appl. Phys.* **82,** 3111–3115 (1997).

233. Inamdar, S. N., Ingole, P. P. & Haram, S. K. Determination of band structure parameters and the quasi-particle gap of CdSe quantum dots by cyclic voltammetry. *Chemphyschem* **9,** 2574–2579 (2008).

234. Kaupp, M., Schleyer, P. V. R., Stoll, H. & Preuss, H. Pseudopotential approaches to Ca, Sr, and Ba hydrides. Why are some alkaline earth MX2 compounds bent? *J. Chem. Phys.* **94,** 1360–1366 (1991).

235. Metz, B., Stoll, H. & Dolg, M. Small-core multiconfiguration-Dirac-Hartree-Fock-adjusted pseudopotentials for post-d main group elements: Application to PbH and PbO. *J. Chem. Phys.* **113,** 2563–2569 (2000).

236. Reed, A. E., Weinstock, R. B. & Weinhold, F. Natural population analysis. *J. Chem. Phys.* **83,** 735–746 (1985).

237. Whited, R. C. & Walker, W. C. Exciton spectra of CaO and MgO. *Phys. Rev. Lett.* **22,** 1428–1430 (1969).

238. Mittendorf, H. Roentgenographische und optische Untersuchungen aufgedampfter Schichten aus Erdalkalichalkogeniden. *Zeitschrift fuer Phys.* **183,** 113–129 (1965).

239. Saum, G. A., Hensley, B. Fundamental Optical Absorption in the IIA-VIB Compounds. *Phys. Rev.* **113,** 1019–1022 (1959).

240. Lunz, U. *et al.* The energy gap of epitaxial layers as a function of composition and temperature. *Semicond. Sci. Technol.* **12,** 970–973 (1999).

241. Berardo, E., Hu, H.-S., van Dam, H. J. J., Shevlin, S. A, Woodley, S. M., Kowalski, K., Zwijnenburg, M. A. Describing Excited State Relaxation and Localization in TiO 2 Nanoparticles Using TD-DFT. *J. Chem. Theory Comput.* **10,** 5538–5548 (2014).

242. Lines, M. E. Bond-orbital theory of linear and nonlinear electronic response in ionic crystals. I. Linear response. *Phys. Rev. B* **41,** 3372–3382 (1990).

243. Alkauskas, A., Broqvist, P. & Pasquarello, A. Defect levels through hybrid density functionals: Insights and applications. *Phys. Status Solidi Basic Res.* **248,** 775–789 (2011).

244. Gerosa, M., Bottani, C. E., Caramella, L., Onida, G., Di Valentin, C., Pacchioni, G. Electronic structure and phase stability of oxide semiconductors: Performance of dielectric-dependent hybrid functional DFT, benchmarked against G W band structure calculations and experiments. *Phys. Rev. B* **91,** 1–15 (2015).

245. Yang, Z., Sottile, F. & Ullrich, C. A. Simple screened exact-exchange approach for excitonic properties in solids. *Phys. Rev. B* **92,** 035202 (2015).

246. Beer, M. & Longuet-Higgins, H. C. Anomalous Light Emission of Azulene. *J. Chem. Phys.* **23,** 1390–1391 (1955).

247. Burroughes, J. H., Bradley, D. D. C., Brown, A. R., Marks, R. N., Mackay, K., Friend, R. H., Burns, P. L., Holmes, A. B. Light-emitting diodes based on conjugated polymers. *Nature* **347,** 539–541 (1990).

248. Peng, X., Manna, L., Yang, W., Wickham, J., Scher, E., Kadavanich, A., Alivisatos, A. P. Shape control of CdSe nanocrystals. *Nature* **404,** 59–61 (2000).

249. Brabec, C. J., Sariciftci, N. S. Plastic solar cells. *Adv. Funct. Mater.* **11,** 15–26 (2001).

250. Özgür, Ü., Alivov, Y. A. I., Liu, C., Teke, A., Reshchikov, M. A., Doğan, S., Avrutin, V., Cho, S. J., Morkǫ, H. A comprehensive review of ZnO materials and devices. *J. Appl. Phys.* **98,** 1–103 (2005).

251. Schäfer, A., Huber, C. & Ahlrichs, R. Fully optimized contracted Gaussian basis sets of triple zeta valence quality for atoms Li to Kr. *J. Chem. Phys.* **100,** 5829–5835 (1994).

252. Canal Neto, A., Muniz, E. P., Centoducatte, R., Jorge, F. E. Gaussian basis sets for correlated wave functions. Hydrogen, helium, first- and second-row atoms. *J. Mol. Struct. THEOCHEM* **718,** 219–224 (2005).

253. Berardo, E., Hu, H.-S., van Dam, H. J. J., Shevlin, S. A., Woodley, S. M., Kowalski, K., Zwijnenburg, M. Describing excited state relaxation and localization processes in TiO 2 nanoparticles with TD - DFT. *J. Chem. Theory Comput.* **10,** 5538–5548 (2014).

254. Zwijnenburg, M. A., Sousa, C., Illas, F. & Bromley, S. T. The fate of optical excitations in small polyhedral ZnS clusters: a theoretical study of the excitation and localization of electrons in Zn4S4 and Zn6S6. *J. Chem. Phys.* **134,** 064511 (2011).

255. Zwijnenburg, M. A., Illas, F. & Bromley, S. T. The fate of optical excitations in small hydrated ZnS clusters: a theoretical study into the effect of hydration on the excitation and localisation of electrons in Zn4S4 and Zn6S6. *Phys. Chem. Chem. Phys.* **13,** 9311–9317 (2011).

256. Zwijnenburg, M. A. Photoluminescence in semiconductor nanoparticles: an atomistic view of excited state relaxation in nanosized ZnS. *Nanoscale* **4,** 3711–3717 (2012).

257. Zwijnenburg, M. A. Excited state localisation cascades in inorganic semiconductor nanoparticles. *Phys. Chem. Chem. Phys.* **15,** 11119–11127 (2013).

258. Yanagi, K. & Kataura, H. Carbon nanotubes: Breaking Kasha's rule. *Nat. Photonics* **4,** 200–201 (2010).

259. Scuppa, S., Orian, L., Donoli, A., Santi, S. & Meneghetti, M. Anti-Kasha ' s Rule Fluorescence Emission in ( 2-Ferrocenyl ) indene Generated by a Twisted Intramolecular Charge-Transfer ( TICT ) Process. *J. Phys. Chem. A* **115,** 8344–8349 (2011).

260. Escudero, D. & Thiel, W. Exploring the Triplet Excited State Potential Energy Surfaces of a Cyclometalated Pt(II) Complex: Is There Non-Kasha Emissive Behavior? *Inorg. Chem.* **53,** 11015 – 11019 (2014).

261. Shannon, R. D. & Prewitt, C. T. Effective ionic radii in oxides and fluorides. *Acta Crystallogr. Sect. B* **25,** 925–946 (1969).

262. Shannon, R. D. Revised Effective Ionic Radii and Systematic Studies of Interatomie Distances in Halides and Chaleogenides. *Acta Crystallogr. Sect. A* **32,** 751–767 (1976).

263. Yoshimine, M. Computed Ground State Properties of BeO, MgO, CaO and SrO in Molecular Orbital Approximation. *J. Phys. Soc. Japan* **25,** 1100–1119 (1968).

# Appendix A

As discussed in section 7.3.6, it has been noticed that in some cases, the DZS basis set is a better approximation to the def2-TZVP $S_1$ minima, compared to the DSC basis set.

The hexagonal $(MgO)_6$ cluster is one example of this: Although both the TD-BHLYP/DZC and TD-BHLYP/def2-TZVP basis sets predict an $S_1$ minimum with an ELC of $(1 - 1)$, the PLE is 0.83 eV higher for the former, which appears anomalous. On the other hand, the TD-BHLYP/DZS PLE is 1.15 eV higher than the PLE of the TD-BLHYP/def2-TZVP results but the ELC of the DZS results is $(1 - 2)$, which is a different ELC to the one obtained from the def2-TZVP calculation, in-line with that would be expected from different PLE.

The cubic $(MgO)_6$ cluster is another example where the def2-TZVP and DZS data appear more in agreement with each other: with TD-BHLYP, both model chemistries predict a $(1 - 2)$ ELC, with a PLE difference of 0.27 eV. In contract, the TD-BHLYP/DZC calculation yields an ELC of $(1 - 2)$ but the PLE is 1.03 eV lower compared to the TD-BHLYP/def2-TZVP result.

Due to the absence of TD-CAM-B3LYP/DZS data, and for the sake of clarity of chapter 7, the TD-BHLYP/DZS and TD-B3LYP/DZS data is shown in this appendix rather than the main chapter.
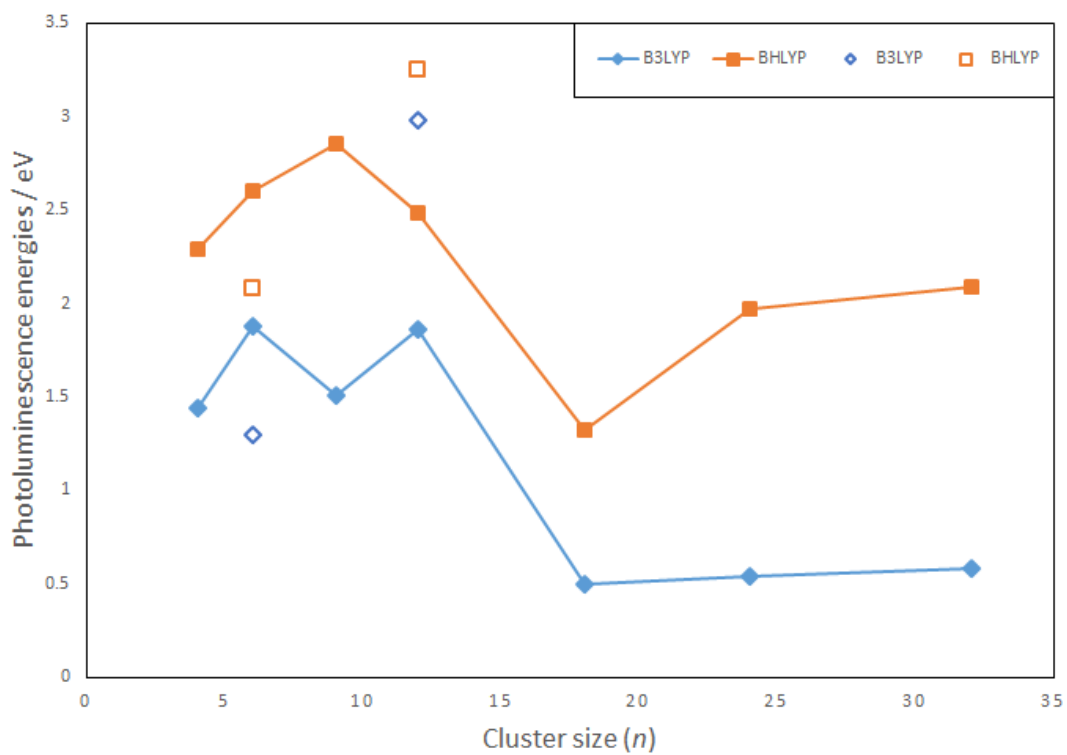
**Figure A-1:** DZS calculated photoluminescence energies, obtained using the B3LYP (blue diamonds) and BHLYP (orange squares) *xc*-functionals. Open symbols correspond to the PLE of the cubic $(MgO)_6$ and the sodalite $(MgO)_{12}$ structures.

**Table A-1:** DZS calculated photoluminescence energies, obtained using the B3LYP and BHLYP *xc*-functionals. All energies are in eV.

| | B3LYP | BHLYP |
|---|---|---|
| $(MgO)_4$ | 1.44 | 2.29 |
| $(MgO)_6$ hexagonal | 1.88 | 2.60 |
| $(MgO)_6$ cubic | 1.30 | 2.08 |
| $(MgO)_9$ | 1.51 | 2.85 |
| $(MgO)_{12}$ hexagonal | 1.86 | 2.48 |
| $(MgO)_{12}$ sodalite | 2.98 | 3.25 |
| $(MgO)_{18}$ | 0.50 | 1.32 |
| $(MgO)_{24}$ | 0.54 | 1.97 |
| $(MgO)_{32}$ | 0.58 | 2.09 |
| $(MgO)_{40}$ | 0.54 | 2.02 |
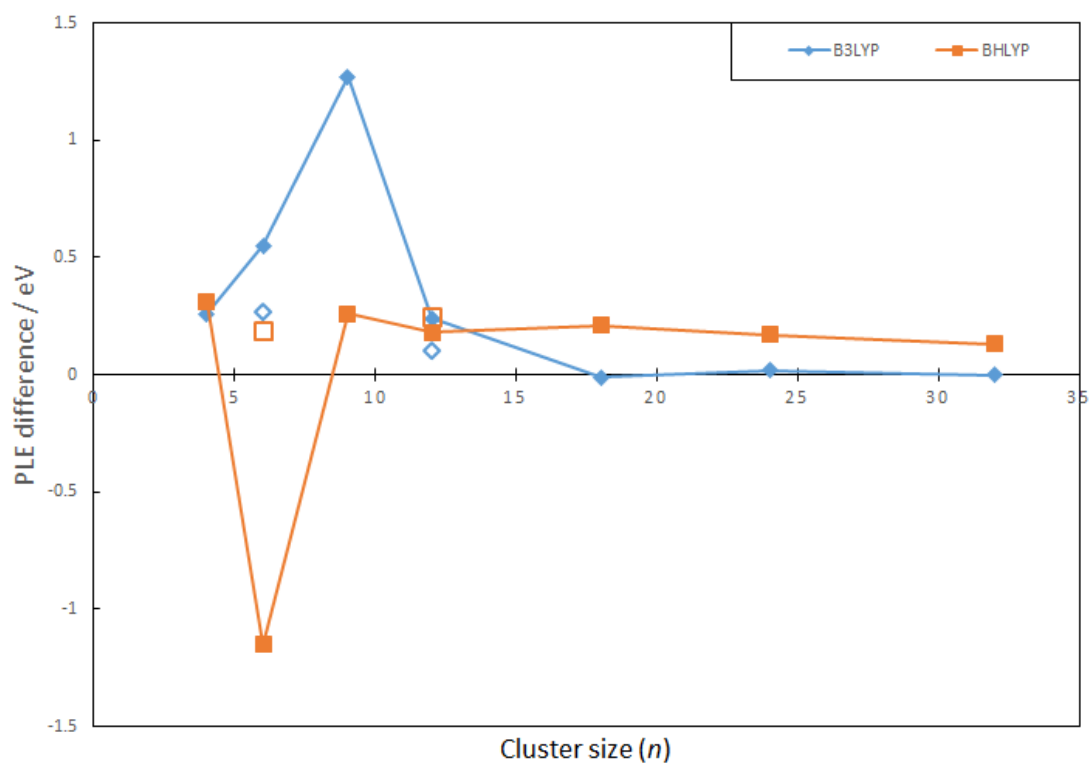
**Figure A-2:** Difference between def2-TZVP calculated PLE and DZS PLE, obtained using the B3LYP (blue diamonds) andBHLYP (orange squares). Open symbols correspond to the difference in PLE of the cubic $(MgO)_6$ and the sodalite $(MgO)_{12}$ structures.
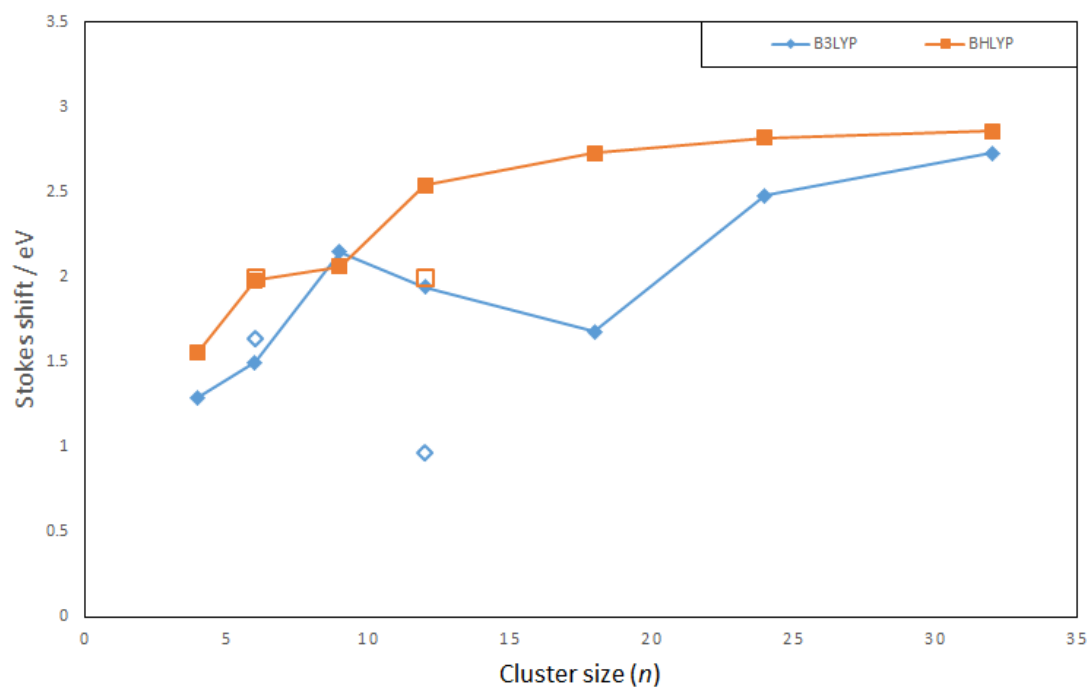
**Figure A-3:** Stokes shifts, calculated using the DZS basis sets and the B3LYP (blue diamonds) and BHLYP (orange squares) *xc*-functionals. Empty symbols represent Stokes shifts for $(MgO)_6$ cubic and $(MgO)_{12}$ sodalite structures.

**Table A-2:** Stokes shifts, calculated using the DZS basis sets and the B3LYP and BHLYP *xc*-functionals. All energies are in eV.

|  | B3LYP | BHLYP |
|---|---|---|
| $(MgO)_4$ | 1.29 | 1.56 |
| $(MgO)_6$ hexagonal | 1.50 | 1.98 |
| $(MgO)_6$ cubic | 1.64 | 2.00 |
| $(MgO)_9$ | 2.15 | 2.06 |
| $(MgO)_{12}$ hexagonal | 1.94 | 2.54 |
| $(MgO)_{12}$ sodalite | 0.97 | 2.00 |
| $(MgO)_{18}$ | 1.68 | 2.73 |
| $(MgO)_{24}$ | 2.48 | 2.82 |
| $(MgO)_{32}$ | 2.73 | 2.86 |
| $(MgO)_{40}$ | 2.77 | 2.93 |

**Table A-3:** The DZS GSDE for the B3LYP and BHLYP *xc*-functionals. All values are in eV.

|  | B3LYP GSDE | BHLYP GSDE |
|---|---|---|
| $(MgO)_4$ | 0.74 | 0.94 |
| $(MgO)_6$ hexagonal | 1.03 | 1.34 |
| $(MgO)_6$ cubic | 1.05 | 1.28 |
| $(MgO)_9$ | 1.61 | 1.33 |
| $(MgO)_{12}$ hexagonal | 1.28 | 1.65 |
| $(MgO)_{12}$ sodalite | 0.63 | 1.42 |
| $(MgO)_{18}$ | 0.80 | 1.53 |
| $(MgO)_{24}$ | 1.21 | 1.61 |
| $(MgO)_{32}$ | 1.41 | 1.68 |
| $(MgO)_{40}$ | 1.38 | 1.68 |

**Table A-4:** The DZS ESSE for the B3LYP and BHLYP *xc*-functionals. All values are in eV.

|  | B3LYP ESSE | BHLYP ESSE |
|---|---|---|
| $(MgO)_4$ | - 0.55 | - 0.62 |
| $(MgO)_6$ hexagonal | - 0.47 | - 0.64 |
| $(MgO)_6$ cubic | - 0.63 | - 0.72 |
| $(MgO)_9$ | - 0.49 | - 0.73 |
| $(MgO)_{12}$ hexagonal | - 0.66 | - 0.89 |
| $(MgO)_{12}$ sodalite | - 0.34 | - 0.58 |
| $(MgO)_{18}$ | - 0.88 | - 1.20 |
| $(MgO)_{24}$ | - 1.17 | - 1.21 |
| $(MgO)_{32}$ | - 1.32 | - 1.18 |
| $(MgO)_{40}$ | - 1.39 | - 1.25 |

**Table A-5:** Exciton localisation character (ELC) from the difference in NBO charges derived from calculations using the B3LYP and BHLYP- *xc*-functionals and DZS basis set.

|  | B3LYP | BHLYP |
|---|---|---|
| $(MgO)_4$ | $(2-2)$ | $(2-2)$ |
| $(MgO)_6$ hexagonal | $(1-2)$ | $(1-2)$ |
| $(MgO)_6$ cubic | $(1-2)$ | $(1-2)$ |
| $(MgO)_9$ | $(1-1)$ | $(2-1)$ |
| $(MgO)_{12}$ hexagonal | $(1-2)$ | $(1-3)$ |
| $(MgO)_{12}$ sodalite | $(1-2)$ | $(2-2)$ |
| $(MgO)_{18}$ | $(1-1)$ | $(1-1)$ |
| $(MgO)_{24}$ | $(1-1)$ | $(1-1)$ |
| $(MgO)_{32}$ | $(1-1)$ | $(1-1)$ |
| $(MgO)_{40}$ | $(1-1)$ | $(1-1)$ |